NONEQUILIBRIUM SELF-ENERGY FUNCTIONAL THEORY

ACCESSING THE REAL-TIME DYNAMICS OF STRONGLY CORRELATED FERMIONIC LATTICE SYSTEMS

DISSERTATION

WITH THE AIM OF ACHIEVING A DOCTORAL DEGREE
AT THE FACULTY OF MATHEMATICS, INFORMATICS AND NATURAL SCIENCES
DEPARTMENT OF PHYSICS
OF UNIVERSITY OF HAMBURG

SUBMITTED BY

FELIX HOFMANN

HAMBURG | APRIL 2016

This work was typeset in LaTeX, figures were created with matplotlib and Ti*k*Z

Acknowledgments

Felix Hofmann

Hamburg | April 2016

Abstract

The self-energy functional theory (SFT) is extended to the nonequilibrium case and applied to the real-time dynamics of strongly correlated lattice-fermions. Exploiting the basic structure of the well established equilibrium theory the entire formalism is reformulated in the language of Keldysh-Matsubara Green's functions. To this end, a functional of general nonequilibrium self-energies is constructed which is stationary at the physical point where it moreover yields the physical grand potential of the initial thermal state. Nonperturbative approximations to the full self-energy can be constructed by reducing the original lattice problem to smaller reference systems and varying the functional on the space of the respective trial self-energies, which are parametrized by the reference system's one-particle parameters. Approximations constructed in this way can be shown to respect the macroscopic conservation laws related to the underlying symmetries of the original lattice model. Assuming thermal equilibrium, the original SFT is recovered from the extended formalism. However, in the general case, the nonequilibrium variational principle comprises functional derivatives off the physical parameter space. These can be carried out analytically to derive inherently causal conditional equations for the optimal physical parameters of the reference system and a computationally realizable propagation scheme is set up. As a benchmark for the numerical implementation the variational cluster approach is applied to the dynamics of a dimerized Hubbard model after fast ramps of its hopping parameters. Finally, the time-evolution of a homogeneous Hubbard model after sudden quenches and ramps of the interaction parameter is studied by means of a dynamical impurity approximation with a single bath site. Sharply separated by a critical interaction at which fast relaxation to a thermal final state is observed, two differing response regimes can be distinguished, where the system gets trapped in prethermal intermediate states. Despite the simplicity of the reference system, good qualitative agreement with previous results of dynamical mean-field theory is found. Reminiscent of the Mott transition at zero temperature the bath site decouples from the correlated impurity site right at the critical point and this "dynamical" Mott transition can be linked to its equilibrium counterpart by studying the crossover from the case of sudden quenches to the adiabatic quasi-static dynamics. This is further investigated by considering the periodic Anderson model, where in equilibrium the presence of a Mott-type transition can be tuned via the geometrical details of the hybridization between the free conduction band and the nondispersive impurity orbitals. This characteristic also persists in the nonequilibrium case and thus strongly supports a true interrelation between both types of Mott transitions.

Kurzfassung

Die Selbstenergiefunktionaltheorie (SFT) wird für die Behandlung von Nichtgleichgewichtsproblemen verallgemeinert und auf die Realzeitentwicklung stark korrelierter Gitterfermionen angewandt. Unter Ausnutzung der grundlegenden Struktur der etablierten Gleichgewichtstheorie wird der gesamte Formalismus in der Sprache der Keldysh-Matsubara Green'schen Funktionen reformuliert. Zu diesem Zwecke wird ein Funktional der Nichtgleichgewichtsselbstenergie konstruiert, welches am physikalischen Punkt stationär ist und eben dort dem großkanonischen Potential im thermischen Anfangszustand entspricht. So können nichtperturbative Näherungen der vollen Selbstenergie konstruiert werden, indem das ursprüngliche Gitterproblem auf kleinere Bezugssysteme reduziert wird und Variationen der entsprechenden Testselbstenergien, parametrisiert durch die Einteilchenparameter des Referenzsystems, durchgeführt werden. Es zeigt sich, dass so erhaltene Näherungen die makroskopischen Erhaltungssätze respektieren, welche den zugrundeliegenden Symmetrien des ursprünglichen Gittermodels entspringen. Im Falle des thermischen Gleichgewichts reduziert sich der verallgemeinerte Formalismus auf die gewöhnliche SFT. Im allgemeinen Fall müssen allerdings Variationen berücksichtigt werden, die aus dem physikalischen Parameterraum hinausführen. Die entsprechenden Funktionalableitungen können jedoch analytisch berechnet werden, so dass kausale Bestimmungsgleichungen für die optimalen physikalischen Parameter erhalten werden und ein realisierbares, rechnergestütztes Propagationsschema aufgestellt werden kann. Als eine erste Überprüfung der numerischen Umsetzung wird der variationelle Cluster-Ansatz auf die Dynamik eines dimerisierten Hubbard-Modells angewandt, welche durch schnelle Veränderungen seiner Tunnelparameter ausgelöst wird. Schließlich wird die Zeitentwicklung eines homogenen Hubbard-Modells nach plötzlichen und endlich andauernden Einschaltvorgängen des Wechselwirkungsparameters mittels der dynamischen Störstellennäherung untersucht. Es finden sich zwei Bereiche unterschiedlichen Antwortverhaltens in denen das System je in einem präthermalen Zustand verharrt und welche durch eine kritische Wechselwirkung scharf voneinander getrennt sind. Trotz der Einfachheit des gewählten Referenzsystems stimmen die gefundenen Resultate mit jenen der dynamischen Molekularfeldtheorie qualitativ gut überein. In Analogie zum Mottübergang bei verschwindender Temperatur entkoppelt der Badplatz vollständig vom korrelierten Störstellenplatz am kritischen Punkt. Dieser "dynamische" Mottübergang kann mit seinem Gleichgewichtspendant in Verbindung gebracht werden, indem das dynamische kritische Verhalten vom Fall plötzlicher Parameteränderungen bis hin zum adiabatischen quasistatischen Fall verfolgt wird. Anhand des periodischen Anderson-Modells wird diesem Zusammenhang weiter nachgespürt. Im Gleichgewicht kann die Existenz eines Mottartigen Übergangs mittels der geometrischen Details der Hybridisierung zwischen dem freien Leitungsband und den dispersionslosen Störstellenorbitalen des Modells eingestellt werden. Dieses Charakteristikum erweist sich auch im Nichtgleichgewicht als beständig und untermauert damit zusätzlich die Vermutung einer echten Beziehung zwischen beiden Arten von Mottübergängen.

Contents

1 Introduction

A flâneur, contemplating the falling snow on a cold winter day, will most probably not observe two identically shaped snowflakes. Moreover, s/he will not be able to replicate any of the sophisticated structures s/he has discovered by freezing a tiny portion of water in his/r home's refrigerator. In fact, due to the permanently changing conditions, that falling droplets experience on their long way from high cloud layers down to earth's surface, almost endlessly many structures emerge from a quintillion of such simple molecules like that of water.

Apart from this everyday paradigm, emergent phenomena have become relevant in almost every discipline of science and examples range from genetics, where viable synthetic bacteria with a minimal genome are designed [1], via artificial intelligence, for which algorithmic realizations of neural nets are used to "teach" computers mastering challenging tasks [2], to many-body physics, where complex solids are dynamically stimulated with light-pulses to conduct electricity without any loss [3]. All of these endeavors on the one hand aim at a more fundamental understanding of basic laws of nature and emergence, but on the other hand establish the basis for future technological advances.

Of particular interest in condensed matter physics are strongly correlated materials, a prime example of which can be found among oxides of transition metals. Consider those, for which the number of electrons per unit cell is odd. According to standard band theory, but opposed to early experimental findings by Boer and Verwey [4] in 1937, such materials should be metals. To resolve this discrepancy, Mott and Peierls [5] in response suggested to include interaction effects between electrons, an idea that has been refined a decade later by Mott [6] in his work on an electron theory of metals. It took almost another fifteen years until in 1963 Hubbard [7], Gutzwiller [8] and Kanamori [9] independently proposed a many-particle model, which allowed for a systematic treatment of these nowadays called Mott insulators [10–12].

The Hubbard model contains the essential ingredients to describe both metallic as well as insulating behavior as two sides of the same coin. Electrons on a lattice may tunnel ("hop") between different atoms, but additionally repel each other due to their mutual Coulomb interaction, which, by virtue of screening, is presumed to essentially act only locally, an assumption which is generally assumed to hold e.g. for transition metal oxides. In materials with a nondegenerate half-filled valence band, for weak interactions the overall behavior is metallic and governed by almost freely moving electrons, whereas for strong interactions, two electrons residing on the same site would lead to an substantial increase in potential energy heavily reducing the electrons' mobility, and hence the material eventually becomes an insulator. Though a strong Coulomb repulsion inhibits metallic transport, electrons may still hop "virtually" and exchange information on their spin, which can lead to long-ranged antiferromagnetism [13]. By introducing impurities

into the lattice, i.e., by doping the material, one may decrease the electron density and turn an antiferromagnetic Mott insulator into a high-temperature superconductor [14]. Above all these examples, a vast variety of phenomena unfolds from the conceptually simple mechanisms captured by the Hubbard model [15], which however in many cases still elude a full understanding.

Over the recent past, laser technology has been brought to a level which allows to observe electron motion in condensed matter systems and molecules on time-scales of femto- down to a few atto-seconds [16–20]. These advances not only paved the way to excite and detect correlated many-body dynamics [21], but also to control nonequilibrium states or access new phases of the respective systems. Strong laser pulses can be utilized to excite charge carriers in a Mott insulator and temporarily drive the system into a metallic state [22–26]. Metastable states, which cannot be reached via equilibrium processes, may be dynamically stimulated. Examples are given by the uncovering of a "hidden" insulating state in a manganite not known from its equilibrium phase diagram [27] or enhanced superconductivity at room temperature in stripe ordered cuprates [28].

Starting out to the new grounds of nonequilibrium many-body dynamics raises entirely new, yet fundamental questions related to the foundations of quantum statistics [29, 30]. At first sight, unitary quantum mechanical time-evolution seems to rule out the loss of memory on the initial state, i.e., ultimately hinders the thermalization of an excited system, which clearly conflicts with both our everyday intuition but also with the basic concept of ergodicity in classical statistical mechanics. This contradiction has been realized already in the dawn of quantum mechanics and a solution has been proposed by von Neumann [31, 32]. In recent debates on thermalization it was resurrected [33] and linked to the so called eigenstate thermalization hypothesis (ETH) [34]. The ETH [35–38] states that under certain circumstances the eigenstate expectation value of a physical observable cannot be distinguished from the respective microcanonical prediction at the same energy. Although for an arbitrarily prepared state such thermal behavior is initially hidden, it will be unveiled in the course of time by dephasing. Nevertheless, thermalization may be prohibited by different causes. The dynamics of an integrable system [39] is constrained due to many conserved quantities though its relaxed state can still be described by a generalized Gibbs ensemble (GGE) [40]. A small perturbation to integrability is believed to clear the way for relaxation toward thermal equilibrium in the long-time limit, but on an emergent intermediate time-scale the system will be trapped in a so called prethermal state [41–45], which complies a statistical description by some appropriate GGE [46]. Furthermore, disorder may have a major impact on the systems ability to thermalize, since, intuitively, (many-particle) states get localized and inhibit the system from acting as its own heat bath [47–50]. Universal concepts from the equilibrium theory of phase transitions can be taken over to the nonadiabatic transient dynamics of systems driven across a phase boundary and e.g. describe the formation of defects or domains in such diverse systems as the early universe or condensed matter [51–54]. Recently, dynamical phase transitions have been in the focus of many works and some progress toward a more detailed definition of its notion has been achieved [55–58].

This sets the stage for the enormous challenge to theoretically describe and predict the

nonequilibrium behavior of strongly correlated systems and in fact considerable progress has been made at a fast pace. A rather unconventional approach to "solve" the many-body problem (out of equilibrium) is provided by experiments with trapped atoms, cooled to extremely low temperatures. In their seminal work Jaksch et al. [59] proposed a realization of the bosonic Hubbard model [60] by confining ultracold atoms in an array of counterpropagating laser beams, and as a result launched the entirely new field of quantum simulation [61–64], once dreamed of by Feynman [65, 66]. Quantum mechanical problems, which generally resist a full treatment on a classical computer, shall be mimicked by fully manipulable synthetic systems being obedient to the same description as the original problem. Ultracold fermionic atoms in an optical lattice essentially share the same energetic degrees of freedom as correlated electrons in a lattice of a solid state system as described by Hubbard like models: due to their dipole moment, atoms gather at regions of high laser intensity, where they interact via short-ranged collisions, which can be tuned arbitrarily by means of Feshbach resonances. Tunneling between different "sites" is controlled via the depth of the lattice potential, and it is thereby possible to create lattices without any defects of diverse geometries and different dimensionalities [67, 68]. Opposed to real solid state systems, the respective bandwidths correspond to intrinsic time-scales in the order of milliseconds, which, owing to an isolation from environment maintained in the range of seconds, allow for an extremely well controlled study of the nonequilibrium dynamics on long time scales and without the need for ultrafast probe techniques [69, 70]. A first implementation of the bosonic Hubbard model was achieved in 2002, for which the quantum phase transition from a superfluid to the Mott insulating phase has been observed [71]. A realization of the fermionic Hubbard model succeeded in 2005 [72] and studies on its Mott physics have been conducted thereafter [73, 74].

Over the past decade, numerous insightful experiments have been carried out in strong collaboration with theory. For bosons, controlling the superexchange coupling has been exploited to engineer ferromagnetic and antiferromagnetic spin-spin interactions [75], light-cone dynamics have been predicted and probed in one-dimensional chains [76] and periodically alternating fields have been demonstrated to allow for dynamical control of model parameters [77], which has been used to induce the superfluid to Mott insulator transition in the Bose-Hubbard model [78, 79]. Moreover, by periodically driving or "shaking" the lattice, frustrated classical magnetism has been realized [80] and artificial tunable gauge potentials have been generated which can be used to simulate lattice systems exposed to strong electromagnetic fields [81]. Microscopical techniques have been advanced to image individual atoms in real space [82–84], which will have diverse applications in observing and manipulating e.g. spin states [85] and make new cooling techniques conceivable. Lastly, though optical lattices provide pure lattice environments, controlled disorder can be implemented [86–88] allowing to tackle questions related e.g. to localization and thermalization phenomena. Concerning fermions, the decay dynamics of doubly occupied sites created within the Mott regime has been described and traced [89–91], the formation and dynamics of short ranged magnetic correlations have been addressed for different lattice geometries [92–94], which might ultimately facilitate

the revelation of mechanisms fundamental to unconventional superconductivity in the Hubbard model [95, 96] and site-resolved in-situ imaging techniques for fermionic atoms [97–99] have been used to detect Mott insulating states in real space [100]. Recently, nonergodic dynamics for strongly interacting fermions in a quasi-random lattice have been observed [101].

Apart from the ever-growing field of quantum simulation of many-body models stemming from different fields of physics, experiments with ultracold atoms (ions) have established independent applications and topics. Nonstandard Hubbard-like models e.g. with extended interactions, higher bands, density dependent tunneling and for mixtures of fermions and bosons have been proposed and realized [102]. But furthermore, they have attracted a lot interest in the field of quantum computation [103–105], with e.g. direct consequences for current encryption techniques: Shor's algorithm [106] for prime factorization on a quantum computer has very recently been implemented in a scalable fashion [107]. Finally, it is worth mentioning that many-body models cannot only be simulated in optical lattice experiments but have also been mimicked e.g. with coupled optical cavities [108, 109] or arrays of quantum dots [110].

Despite the great opportunities for quantum simulation provided by these versatile experimental techniques, all of them need theoretical guidance on the one hand, and constitute a valuable test ground for new theoretical ideas and methods on the other hand. A conceptually appealing approach to the (correlated) many-body problem is formulated by mean-field theories: a small unit of a larger lattice is embedded in an auxiliary *field* representing the remaining greater part of the whole. Certainly, nonlocal quantum fluctuations exceeding these "imaginary" building blocks of the full lattice, cannot be captured in such an approach. However, the so-called *dynamical* mean-field theory (DMFT) [111–114] accounts for all *local* fluctuations and self-consistently determines the mean-field by including the full feedback between "the part and the whole". To this end, the correlated (fermionic) lattice problem is mapped onto a single site embedded into an uncorrelated environment. More technically speaking, the DMFT assumes a completely local (i.e., momentum independent) self-energy while keeping its full frequency dependence. This approximation becomes exact in the limit of infinite coordination number and is sufficiently accurate for many three-dimensional cases or whenever the full self-energy is essentially local. The DMFT is formulated in the thermodynamic limit from the very beginning and treats local interactions nonperturbatively. It is thus well suited to capture the correlation driven metal to Mott insulator transition [115–117]. Moreover, the DMFT respects all macroscopic conservation laws for one-particle observables and the total energy in the sense of Baym and Kadanoff [118, 119], since the local impurity self-energy can be obtained from a truncated Luttinger-Ward functional.

In combination with *ab-initio* calculations, DMFT provides precious insights into properties of real materials [120]. With regard to optical lattice experiments, the DMFT has been extended to deal with bosonic lattice models [121–124]. Notable efforts have been made to also include nonlocal fluctuations, probably most straightforwardly by embedding a small cluster instead of a single site into an uncorrelated environment, comprising the cellular dynamical mean-field theory (C-DMFT) [125, 126], which however breaks the

translational symmetry of the original problem. An alternative approach, formulated in reciprocal space, is given by the dynamical cluster approximation (DCA) [127]. Furthermore, the dynamical vertex approximation (DΓA) [128] systematically includes nonlocal contributions to the self-energy by assuming locality of the two-particle vertex function (in this spirit, the DMFT would be a *one*-particle vertex approximation) and the dual fermion approach uses the DMFT as the starting point for an advanced perturbation theory [129, 130]. Crucially, over the last decade, generalizations to the nonequilibrium case have been formulated for the DMFT [131–133] and for most of its mentioned extensions [134–136], which have already been successfully applied to a number of problems [137–143]. Particularly interesting is the finding of a "dynamical Mott transition" [144]: upon suddenly switching on the Hubbard interaction from an uncorrelated initial state, two distinct response regimes, characterized by different prethermal behavior, can be found. Only at some sharply defined final interaction, rapid thermalization occurs and dynamical critical behavior is observed, i.e., a drastic change of the system's dynamical response as a function of the final state interaction. Subsequently, this has been affirmed as a rather robust phenomenon by means of various different approaches [145–147].

On the practical level, the self-consistent impurity problem, i.e., determining the time-inhomogeneous impurity self-energy, is a demanding task on its own, which gets even more complicated in nonequilibrium. In the equilibrium case, quantum Monte-Carlo (QMC) techniques are commonly used to efficiently and accurately solve the many-body impurity problem but due to a severe sign (or phase) problem can be applied only to short time propagations in nonequilibrium [148, 149]. Alternatively, perturbative approaches have been used, which however give reliable results only for strong [138] or weak [150, 151] coupling strengths and are clearly disadvantageous when it comes to describing e.g. the Mott transition, which takes place at intermediate interactions. Other favorable "solvers" rely on a Hamiltonian representation of the effective mean-field via a single impurity Anderson model (SIAM) of finite size and have been implemented in equilibrium by means of exact diagonalization (ED) methods [152, 153]. Accordingly, a systematic mapping has been suggested and realized for short times [154] and in the following has been tackled additionally by the multi-configuration time-dependent Hartree method [155] or density-matrix renormalization techniques based on matrix-product states [156]. Despite setting no limitations on the treatable parameter ranges, during the course of time successively further bath degrees of freedom have to be coupled to the impurity site in order to guarantee an appropriate mapping. More severely, already in equilibrium the *finite* bath representation of the *continuous* mean-field introduces some additional *ad-hoc* character to the DMFT self-consistency problem, which can cause a violation of thermodynamic consistency and conservation laws.

Before putting forward a "solution" to this shortcoming, it is worth mentioning quantum cluster theories [157] which share the same idea as in DMFT to replace the full self-energy with the one obtained from a solvable *reference* problem. A conceptually simple quantum cluster approach, both in and out of equilibrium, is the cluster-perturbation theory (CPT) [158–161]. Within the CPT, the infinite lattice is tiled into small clusters, which can be solved exactly by numerical means. This solution is then extended to the

full lattice by infinite-order perturbation theory with respect to the inter-cluster hopping but neglecting vertex corrections [160]. Unfortunately, the CPT in principle violates all conservation laws. Another major drawback of the CPT consists in the fact that, even for a given geometrical tiling of the lattice, the partitioning of the hopping part and hence the choice of the reference system, i.e., the starting point of the perturbative expansion is not unique. However, the nonuniqueness of the CPT construction can be turned into an advantage, if one can establish a variational prescription for finding the *optimal* starting point for the cluster-perturbation theory.

In fact, both a thermodynamical consistent replacement of the DMFT self-consistency for a *finite* bath as well as variationally optimized CPT are provided within the unifying framework of self-energy functional theory (SFT) [162]. The latter relies on the fact, that the *physical* self-energy of the full lattice problem can be obtained from a variational principle for the respective (equilibrium) grand potential when expressed as a functional of the self-energy. Moreover, there is an exact relation to lattice problems which differ only by their one-particle parameters. Decisively for the SFT, this allows to approximately evaluate the stationarity principle on a restricted subset of self-energies, stemming from small systems, which are obtained by tiling the full lattice into clusters and possibly adding uncorrelated bath degrees of freedom. These *reference* systems should be accessible to exact numerical evaluation. Depending on their precise choice, the SFT comprises such diverse and systematic approximations as the variational cluster approach (VCA) [163–165] or dynamical impurity approximations (DIA) [166] as well as combinations of both. Furthermore, in the limit of continuous baths, the DMFT and its cluster extensions are formally recovered. Just like these, any approximation constructed within the SFT is thermodynamically consistent and nonperturbative. The VCA allowed to properly describe antiferromagnetism (AF) in the original system by applying fictitious staggered magnetic fields to the reference cluster [164], has been employed to study the Mott transition in 1D system [167], and has given further insights into the Mott transition's nature in the presence of AF correlations [168]. Recent attempts toward a nonequilibrium formulation have been achieved in the steady state regime [169, 170]. Within the DIA, very precise studies of the metal to Mott insulator transition have been carried out for both single- and two-orbital Hubbard models [166, 171–174]. Furthermore, the SFT has been extended into several directions, e.g., to systems with nonlocal interactions [175], to disordered systems [176], and to bosonic systems [177–179]. However, a proper generalization to the nonequilibrium case has been lacking up to now.

With the present thesis, a nonequilibrium self-energy functional theory (NE-SFT) is constructed and applied in the same spirit as for the well established equilibrium variant. However, there are several peculiarities that have to be considered with special care. A functional of the double-time nonequilibrium self-energy has to be constructed and shown to be stationary at the physical self-energy of the system, where the value of the functional itself should ideally have a physical meaning. In the spirit of the equilibrium theory, a restricted evaluation of the functional via small reference systems, manageable by means of exact-diagonalization techniques, should be possible. This comprises to find

conditional equations, which at best allow for a causal, successive determination of the reference system's parameters. As a systematic check, the nonequilibrium DMFT should be recovered if a SIAM was chosen as a reference system. Furthermore, when evaluated for an explicitly time-*in*dependent problem, the new formalism should reduce to the familiar equilibrium SFT. Most importantly, it is essential to ask, whether approximations constructed within the NE-SFT will respect macroscopic conservation laws or rather the respective continuity equations underlying the full model. Though the construction of the self-energy functional formally makes use of the Luttinger-Ward functional, unlike DMFT the SFT is not conserving in the sense of Baym and Kadanoff [118, 119], since it cannot be understood as a re-summation of certain diagram classes. Nevertheless, by adapting the essential ideas of their seminal work, it will be possible to prove the conserving nature of the new approach.

Outline

This work is structured as follows: In Chapter 2 we review basic notions and concepts of the nonequilibrium many-particle theory as needed for the set up of the self-energy functional theory. To this end, we first introduce the correlated lattice models of interest in Sec. 2.1 and briefly present the basic mathematical framework for dealing with the many-body problem out of equilibrium in Secs. 2.2 and 2.3. Special attention is payed to the details of conservation laws expressed within the Green's functions formalism in Sec. 2.4. The following Chapter 3 is entirely devoted to the generalization of the self-energy functional theory to the nonequilibrium case. Due to the formal equivalence with the equilibrium variant of the theory, its fundamental construction can be done in close analogy to the original case as is explained in Secs. 3.1 to 3.4. However, in nonequilibrium conceptually new aspects need special consideration: in Sec. 3.5 we explain the necessity of "unphysical" variations and carry out the involved functional derivatives in Sec. 3.6. The recovery of the equilibrium SFT for explicitly time-independent problems is derived in Sec. 3.7 and the thermodynamical consistency of the theory is proven in the following Sec. 3.8. Most importantly, the issue of conserving approximations within the SFT is carefully addressed in Sec. 3.9. In Chapter 4 we turn our attention to more practical affairs and discuss an implementable propagation scheme in Sec. 4.1 as well as possible numerical easements due to certain symmetry relations in Secs. 4.2 and 4.3. To benchmark the numerical implementation the dynamics of dimerized Hubbard models following fast ramps of the hopping parameters is studied by means of the variational cluster approach (VCA) in Chapter 5. Finally, we focus on different aspects of the Mott transition in and out of equilibrium in Chapter 6, first for the Hubbard model in Secs. 6.2 and 6.3 and thereafter in two variants of periodic Anderson models in Sec. 6.4. To this end, we employ the dynamical impurity approximation (DIA), which is contrasted to Hamiltonian-based DMFT solvers in Sec. 6.5. The work is summarized in Sec. 7 where we also speculate about future improvements, applications and prospects of the nonequilibrium self-energy functional theory.

The results of this thesis have also been presented elsewhere [180–183]. For a detailed "list of publications and preprints" see page 125.

2 Nonequilibrium many-particle theory

A proper description of many-particle systems out of equilibrium is challenging in terms of several aspects. For example, though perturbative approaches might give important qualitative and even quantitative insights, they are clearly problematic for intermediate, competing parameter ranges, at which e.g. the Mott metal-insulator transition, as described by the Hubbard model, takes place. Concerning dynamics, this becomes even more crucial when parameters get modulated and all energy and time scales can become important. A more "realistic" approach should thus treat all parameters on equal footing. Green's functions are at the heart of a general, unbiased formulation of quantum many-body problems in and out of equilibrium and provide various diagrammatic techniques. Many different re-summation or truncation schemes have emerged, but also powerful functional approaches rely on Green's functions-based techniques and related diagrammatic viewpoints and have successfully been extended to describe real-time phenomena over the past decade [131–133, 136, 143, 169, 184–186]. The field of nonequilibrium Green's functions has matured over the last 50 years since the first foundations were made and subsequently advanced by merited theoreticians like Kubo [187], Matsubara [188], Schwinger [189], Keldysh [190] and Danielewicz [191]. Applications span over a wide range of diverse disciplines in theoretical physics and vivid interdisciplinary exchange has been stimulated e.g. by a recurring series of conferences [192–197]. For recent reviews, we also refer to some out of the many comprehensive books and articles [198–202].

In this chapter, we will briefly introduce the main technical aspects and notations used throughout this thesis and for the setup of the self-energy functional theory (SFT). In Sec. 2.1 we introduce the model Hamiltonians defining the actual many-body problem in nonequilibrium, which will then be addressed within the Keldysh-Matsubara formalism for Green's functions, as briefly reviewed in Secs. 2.2 and 2.3. A discussion on conservation laws, especially regarding related questions within the SFT, will follow in Sec. 2.4.

2.1 Models

Though the Hubbard model will be in the main focus of this thesis, neither the Green's functions formalism nor the SFT, as going to be introduced in chapter 3, are limited to this "simple" and paradigmatic lattice model. If not necessary or stated otherwise, we

will use the following general fermionic lattice model

$$H_{\boldsymbol{\lambda},\boldsymbol{U}}(t) = \sum_{\alpha\beta} \lambda_{\alpha\beta}(t) c_\alpha^\dagger c_\beta + \frac{1}{2} \sum_{\alpha\beta\gamma\delta} U_{\alpha\beta\delta\gamma}(t) c_\alpha^\dagger c_\beta^\dagger c_\gamma c_\delta \,, \tag{2.1}$$

where $c_\alpha^{(\dagger)}$ annihilates (creates) a fermion in a one-particle basis state, labeled by Greek indices, which typically refer to a lattice site, an orbital index and a spin-projection quantum number. For the sets of hopping and interaction parameters we write $\boldsymbol{\lambda}$ and $\boldsymbol{U}$ for short, and, whenever necessary or convenient, we indicate the dependence on those parameters by respective subscripts, e.g., $H_{\boldsymbol{\lambda},\boldsymbol{U}}$. Nontrivial real-time dynamics can be initiated by explicit time dependencies of the model parameters. Note that here and in the following we use bold symbols for matrix or vector valued quantities, e.g., $\boldsymbol{\lambda}(t)$ has elements $\lambda_{\alpha\beta}(t)$.

For practical calculations, we will mainly use the Hubbard model and though it deserves and has attracted a lot of interest on its own, we will pay some attention to the periodic Anderson model (PAM) only in comparison. Therefore, and for the sake of clarity, we will refine our notation and, as far as possible, will use the following conventions: hopping between orbitals of the same type as e.g. uncorrelated sites or correlated sites is described by parameters $\boldsymbol{T}$, whereas $\boldsymbol{V}$ denotes the hybridization between different types of orbitals, like correlated and bath sites. On-site energies are labeled by $\boldsymbol{\varepsilon}$, but might not be given explicitly, though rather implicitly contained in the site-diagonal parts of the respective hopping parameters.

To be specific, using standard notations, the Fermi-Hubbard Hamiltonian is given by

$$H(t) = \sum_{\langle ij\rangle,\sigma} T_{ij}(t) c_{i\sigma}^\dagger c_{j\sigma} + U(t) \sum_i \hat{n}_{i\uparrow}^c \hat{n}_{i\downarrow}^c \,, \tag{2.2}$$

where a fermion at site i and with spin projection $\sigma = \uparrow, \downarrow$ is annihilated (created) by $c_{i\sigma}^{(\dagger)}$, and where $\hat{n}_{i\sigma}^c = c_{i\sigma}^\dagger c_{i\sigma}$ is the density operator. Tunneling between neighboring sites $\langle ij\rangle$ is described by the hopping amplitude $T_{ij}(t)$. On the same site, fermions are subjected to the repulsive Hubbard interaction $U(t)$. In chapter 5 we will study a variant of the model with site dependent alternating (dimerized) hopping. The main attention will however be paid to its homogeneous configuration in chapter 6.

The periodic Anderson model comprises two types of orbitals per site, one of which is uncorrelated and fermions are allowed to hop between neighboring sites and a second one which is nondispersive but correlated, typically termed as "impurity". Both get coupled described by a hybridization term $\boldsymbol{V}$. In Sec. 6.4 we will discuss two different prominent cases for a hybridization on the same site or between nearest-neighbors. Using the same notation as before, the PAM's Hamiltonian reads

$$H(t) = \sum_{\langle ij\rangle,\sigma} T_{ij} c_{i\sigma}^\dagger c_{j\sigma} + \sum_{ij\sigma} V_{ij}(c_{i\sigma}^\dagger f_{j\sigma} + \text{h.c.}) + U(t) \sum_i \hat{n}_{i\uparrow}^f \hat{n}_{i\downarrow}^f \,, \tag{2.3}$$

where the orbital index was absorbed into the symbols for the creation and annihilation operators and we distinguish c-type (uncorrelated, dispersive) and f-type (correlated, nondispersive) orbitals. Here, $\hat{n}_{i\sigma}^f = f_{i\sigma}^\dagger f_{i\sigma}$ is the density operator for the f-type

fermions. For a hybridization between nearest-neighbors we have $V_{ij} = -V$ for neighboring sites i and j and zero otherwise or $V_{ij} = -V\delta_{ij}$ for an on-site hybridization.

2.2 Keldysh-Matsubara formalism

The nonequilibrium many-body problem is generally twofold. First, we shall assume that the system under consideration has initially (at time $t = t_0$) been prepared in a thermal state with inverse temperature β and chemical potential μ and suffice a statistical description via a density operator

$$\rho = \frac{\exp(-\beta\mathcal{H}(t_0))}{\text{tr}\exp(-\beta\mathcal{H}(t_0))}, \tag{2.4}$$

with $\mathcal{H}(t_0) = H(t_0) - \mu\hat{N}$, where $H(t_0)$ is the initial Hamiltonian and $\hat{N}$ the total particle-number operator. The trace is denoted by tr. Second, for times $t > t_0$ the system's time evolution shall be governed by the possibly time-dependent Hamiltonian $H(t)$. In the Heisenberg picture with respect to $\mathcal{H}(t) = H(t) - \mu\hat{N}$, an arbitrary, possibly time-dependent observable $\boldsymbol{A}(t)$ obeys the Heisenberg equation of motion

$$i\frac{\partial}{\partial t}\boldsymbol{A}_{\mathcal{H}}(t) = [\boldsymbol{A}_{\mathcal{H}}(t), \mathcal{H}_{\mathcal{H}}(t)] + i\left(\frac{\partial}{\partial t}\boldsymbol{A}(t)\right)_{\mathcal{H}}, \tag{2.5}$$

the solution of which is given by

$$\boldsymbol{A}_{\mathcal{H}}(t) = U(t_0, t)\boldsymbol{A}(t)U(t, t_0), \tag{2.6}$$

with the unitary time-evolution operator for real times t and t' [see standard textbook, e.g. 203]

$$
\begin{aligned}
U(t, t') &= \mathcal{T}\exp\left(-i\int_{t'}^{t} dt'' \mathcal{H}(t'')\right) \qquad \text{for } t > t', \\
U(t, t') &= \widetilde{\mathcal{T}}\exp\left(-i\int_{t'}^{t} dt'' \mathcal{H}(t'')\right) \qquad \text{for } t < t'.
\end{aligned}
\tag{2.7}
$$

Here, $\mathcal{T}$ ($\widetilde{\mathcal{T}}$) denotes the chronological (anti-chronological) time-ordering operator. It is important to note that we have set $\hbar \equiv 1$.

We may formally insert "complex" times in the above equations (2.7) and recognize that $\exp(-\beta\mathcal{H}(t_0)) = U(t_0 - i\beta, t_0)$ where $t_0 - i\beta$ is assumed to be a "later" time than t_0. With this, the time-dependent expectation value of the observable $\boldsymbol{A}(t)$, namely $\langle\boldsymbol{A}\rangle(t) = \text{tr}(\rho\boldsymbol{A}_{\mathcal{H}}(t))$, can be written as:

$$\langle\boldsymbol{A}\rangle(t) = \frac{\text{tr}\left(U(t_0 - i\beta, t_0)U(t_0, t)\boldsymbol{A}(t)U(t, t_0)\right)}{\text{tr}\left(U(t_0 - i\beta, t_0)U(t_0, t)U(t, t_0)\right)} \tag{2.8}$$

$$= \frac{\text{tr}\left(\mathcal{T}_{\mathcal{C}}\exp\left(-i\int_{\mathcal{C}} d\bar{z}\,\mathcal{H}(\bar{z})\right)\boldsymbol{A}(t)\right)}{\text{tr}\left(\mathcal{T}_{\mathcal{C}}\exp\left(-i\int_{\mathcal{C}} d\bar{z}\,\mathcal{H}(\bar{z})\right)\right)}. \tag{2.9}$$
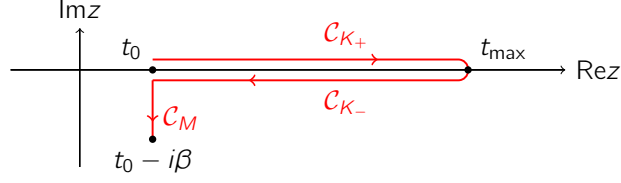
Figure 2.1: The three-branched Keldysh-Matsubara contour $\mathcal{C}$ in the complex time plane, extending up to time $t_{\max}$; $\mathcal{C}_{K_\pm}$ denotes the upper/lower branch and $\mathcal{C}_M$ the Matsubara branch. See text for further discussion.

Here, the time integration is carried out along the three-branched Keldysh-Matsubara contour $\mathcal{C}$ in the complex time plane, see Fig. 2.1, which extends from $z' = t_0$ to $z' = \infty$ along the real axis (upper Keldysh branch, $\mathcal{C}_{K_+}$) and back to $z' = t_0$ (lower Keldysh branch, $\mathcal{C}_{K_-}$) and finally from $z' = t_0$ to $z' = t_0 - i\beta$ along the imaginary axis (Matsubara branch, $\mathcal{C}_M$). We also refer to the upper and the lower branch as the Keldysh contour $\mathcal{C}_K$. For a concise notation, we define $H(z)$ for contour times z as $H(z) = H(t)$ if $z = t > t_0$ and as $H(z) = H(t_0)$ if $z = t_0 - i\tau$ with $0 \leq \tau \leq \beta$. In the same way, we define $\lambda_{\alpha\beta}(z)$ and $U_{\alpha\beta\delta\gamma}(z)$. $\mathcal{T}_\mathcal{C}$ denotes the ordering operator along the contour and, after expanding the exponential, places an operator $\mathcal{H}(z_1)$ to the left of $\mathcal{H}(z_2)$ if z_1 is "later" than z_2, where $t_0 - i\beta$ is the "latest" time. Obviously, $\mathcal{T}_\mathcal{C}$ replaces $\mathcal{T}$ on the upper and $\widetilde{\mathcal{T}}$ on the lower branch. This "unified" ordering will be essential for the application of Wick's theorem and hence a nonequilibrium perturbation theory (see Sec. 2.3.3 in the following).

When the contour ordering operator $\mathcal{T}_\mathcal{C}$ acts on $\boldsymbol{A}(t)$ in the numerator of Eq. (2.9), it places $\boldsymbol{A}(t)$ at the position $z = t$ on $\mathcal{C}$ where the expectation value is evaluated. Because the integrations along the upper and the lower branches cancel each other in the interval $t < z' < \infty$, the integration along the Keldysh branch is limited to $z' < t$ (see Fig. 2.1), and it does not matter whether $\boldsymbol{A}(t)$ is placed at $z = t$ on the upper or the lower branch of the contour. For the denominator, only the Matsubara branch contributes and results in $\mathrm{tr}\exp(-\beta\mathcal{H}(t_0))$. Additionally note that the ordering operator $\mathcal{T}_\mathcal{C}$ also involves an implicit sign stemming from the fundamental fermionic anti-commutation relations (see Appendix A.1). Let therefore $d_1(z_1)$ and $d_2(z_2)$ be two arbitrary fermionic annihilation or creation operators, then

$$\mathcal{T}_\mathcal{C}(d_1(z_1)d_2(z_2)) = \Theta_\mathcal{C}(z_1, z_2)d_1(z_1)d_2(z_2) - \Theta_\mathcal{C}(z_2, z_1)d_2(z_2)d_1(z_1)\,, \qquad (2.10)$$

where $\Theta_\mathcal{C}(z, z')$ is the Heaviside function defined on the contour, i.e., $\Theta_\mathcal{C}(z, z') = 1$ if $z \underset{\mathcal{C}}{>} z'$ (z is later on $\mathcal{C}$ than z') or zero otherwise. At equal times $\mathcal{T}_\mathcal{C}$ usually places two operators in their normal order, i.e., construction operators are placed to the left or annihilation operators. More generally, for an arbitrary set of operators $\boldsymbol{A}_i(z_i)$ composed of fermionic construction operators at arbitrary points z_i on the contour (Fig. 2.1) and

with the help of the permutation p, this can be expressed as

$$\mathcal{T}_{\mathcal{C}}(\boldsymbol{A}_1(z_1)\boldsymbol{A}_2(z_2)\ldots\boldsymbol{A}_n(z_n)) =$$
$$(-1)^P \boldsymbol{A}_{p(1)}(z_{p(1)})\boldsymbol{A}_{p(2)}(z_{p(2)})\ldots\boldsymbol{A}_{p(n)}(z_{p(n)}) , \quad (2.11)$$

such that $z_{p(1)} \underset{\mathcal{C}}{\geq} z_{p(2)} \underset{\mathcal{C}}{\geq} \ldots \underset{\mathcal{C}}{\geq} z_{p(n)}$. Here P denotes the number of minimal pairwise permutations necessary, to reobtain the original (fermionic) order.

2.3 Nonequilibrium Green's functions

To describe the dynamics of a quantum many-body system as introduced in the preceding Sec. 2.1 and specified by the parameters $\boldsymbol{\lambda}$ and $\boldsymbol{U}$, we define the elements of the contour-ordered Green's function $\boldsymbol{G}_{\boldsymbol{\lambda},\boldsymbol{U}}$ as

$$iG_{\boldsymbol{\lambda},\boldsymbol{U}}(1,2) = \langle \mathcal{T}_{\mathcal{C}} c(1)c^\dagger(2) \rangle_{\boldsymbol{\lambda},\boldsymbol{U}} . \tag{2.12}$$

The annihilation and creation operators, $c(1)$ and $c^\dagger(2)$, are given in their Heisenberg picture with respect to $\mathcal{H}_{\boldsymbol{\lambda},\boldsymbol{U}}(t)$. We use the short-hand notation $i \equiv (\alpha_i, z_i)$, i.e., $c^{(\dagger)}(i)$ has elements $c_{\alpha_i}^{(\dagger)}(z_i)$. Note that the Green's function also depends on β and μ via the initial thermal state. These dependencies are implicit in the notations.

In the following we will briefly discuss some selected properties of Green's functions or more generally of arbitrary *physical* contour functions (Sec. 2.3.1), introduce its equation of motion in different variants (Sec. 2.3.2) and review the basic notions of perturbation theory (Sec. 2.3.3). Finally, we will relate the Green's function to all relevant one-particle observables and the total energy (Sec. 2.4).

2.3.1 Selected properties

The following properties will be used in subsequent chapters. Due to their generality, we will skip their subscripts, refering to the parameters of a special type of Hamiltonian.

Parametrizations and Symmetries Whenever it comes to calculating physical real-time properties, it proves handy to eventually get rid of the compact complex-time notation. To this end we serially number the contour, namely by 1 (upper branch), 2 (lower branch) and 3 (Matsubara branch); cf. Fig. 2.1. In this representation the Green's function is decomposed into nine parts, labeled according to its time-arguments' position on the contour [198, 200], i.e.:

$$G(1,1') = \begin{pmatrix} G^{11}(1,1') & G^{12}(1,1') & G^{13}(1,1') \\ G^{21}(1,1') & G^{22}(1,1') & G^{23}(1,1') \\ G^{31}(1,1') & G^{32}(1,1') & G^{33}(1,1') \end{pmatrix} . \tag{2.13}$$

An immediate consequence of the definition of the contour-ordering is that any (two-time) contour function is unchanged by a shift of the largest time-argument on the Keldysh contour from the upper to the lower branch, i.e.,

$$
\begin{aligned}
\boldsymbol{G}(t_0 - i\tau, t^{\vee}) &= \boldsymbol{G}(t_0 - i\tau, t^{\wedge}), \\
\boldsymbol{G}(t', t^{\vee}) &= \boldsymbol{G}(t', t^{\wedge}) \text{ for } t > t',
\end{aligned}
\tag{2.14}
$$

and similarly for the first time-argument ($t^{\vee\wedge}$ denotes a time argument on the upper/lower branch at t). This symmetry relation immediately follows from the fact that the forward and backward time-evolution cancel each other after the right-most operator on the Keldysh contour (see also the discussion of Fig. 2.1).

Therefore the nine components in Eq. (2.13) are not all independent. In the following we will list basic relations between the components and at the same time introduce another common notation, which will mainly be used throughout this thesis:

(i) *lesser / greater* components

$$
G^<_{\alpha\alpha'}(t,t') = G^{12}_{\alpha\alpha'}(t,t') = +i\langle c^\dagger_{\alpha',\mathcal{H}}(t')c_{\alpha,\mathcal{H}}(t)\rangle \,,
\tag{2.15}
$$

$$
G^>_{\alpha\alpha'}(t,t') = G^{21}_{\alpha\alpha'}(t,t') = -i\langle c_{\alpha,\mathcal{H}}(t)c^\dagger_{\alpha',\mathcal{H}}(t')\rangle \,,
\tag{2.16}
$$

(ii) *retarded / advanced* components

$$
G^R_{\alpha\alpha'}(t,t') = \Theta(t - t')(G^>_{\alpha\alpha'}(t,t') - G^<_{\alpha\alpha'}(t,t')) \,,
\tag{2.17}
$$

$$
G^A_{\alpha\alpha'}(t,t') = \Theta(t' - t)(G^<_{\alpha\alpha'}(t,t') - G^>_{\alpha\alpha'}(t,t')) \,,
\tag{2.18}
$$

(iii) *hook* or *mixed* components

$$
G^{\lceil}_{\alpha\alpha'}(\tau,t') = G^{32}_{\alpha\alpha'}(t_0 - i\tau, t') = G^{31}_{\alpha\alpha'}(t_0 - i\tau, t') \,,
\tag{2.19}
$$

$$
G^{\rceil}_{\alpha\alpha'}(t,\tau') = G^{13}_{\alpha\alpha'}(t, t_0 - i\tau') = G^{23}_{\alpha\alpha'}(t, t_0 - i\tau') \,,
\tag{2.20}
$$

(iv) *Matsubara* components

$$
\begin{aligned}
G^M_{\alpha\alpha'}(\tau,\tau') = G^{33}_{\alpha\alpha'}(t_0 - i\tau, t_0 - i\tau') &= \Theta(\tau - \tau')G^>_{\alpha\alpha'}(t_0 - i\tau, t_0 - i\tau') \\
&\quad + \Theta(\tau' - \tau)G^<_{\alpha\alpha'}(t_0 - i\tau, t_0 - i\tau') \,,
\end{aligned}
\tag{2.21}
$$

which, due to the τ-independence of the initial Hamiltonian $\mathcal{H}(t_0)$, is homogeneous in imaginary time, i.e., $G^M_{\alpha\alpha'}(\tau,\tau') = G^M_{\alpha\alpha'}(\tau - \tau')$.

Due to the conjugate symmetry of the scalar product and the cyclic property of the trace, we additionally find the relations

$$
G^{\gtrless}_{\alpha\alpha'}(t,t') = -\left(G^{\gtrless}_{\alpha'\alpha}(t',t)\right)^* \,,
\tag{2.22}
$$

and

$$G_{\alpha\alpha'}^{\urcorner}(t,\tau) = G_{\alpha'\alpha}^{\ulcorner}(\beta-\tau,t)^{*}\,. \tag{2.23}$$

Note that the parametrizations and respective relations given above [Eqs. (2.14) – (2.23)] are quite general properties of any *physical* two-point functions defined on the contour, namely:

$$\boldsymbol{X}(z,z') \equiv \boldsymbol{X}^{\delta}(z)\delta_{\mathcal{C}}(z,z') + \Theta_{\mathcal{C}}(z,z')\boldsymbol{X}^{>}(z,z') + \Theta_{\mathcal{C}}(z',z)\boldsymbol{X}^{<}(z,z')\,, \tag{2.24}$$

where $\boldsymbol{X}^{\delta}$ denotes the singular part of $\boldsymbol{X}$ and $\delta_{\mathcal{C}}(z,z') = \partial_{z}\Theta_{\mathcal{C}}(z,z')$ is the delta-function on the contour, i.e., $\int_{\mathcal{C}} dz'\,\delta_{\mathcal{C}}(z,z')f(z') = f(z)$, for some single-time function $f(z)$. By definition the Green's function (2.12) does not have a singular part.

The same properties hold for the "contour-product" $\boldsymbol{X}_1 \circ \boldsymbol{X}_2$ of any two contour functions $\boldsymbol{X}_1$ and $\boldsymbol{X}_2$ if it holds for $\boldsymbol{X}_1$ and $\boldsymbol{X}_2$ individually, and thus for any analytical function f of $\boldsymbol{X}$, i.e.:

$$\boldsymbol{f}(\boldsymbol{X}) = \sum_{n} \frac{f^{(n)}(0)}{n!} \boldsymbol{X}^{\circ n}\,. \tag{2.25}$$

Note that $\boldsymbol{f}(\boldsymbol{X})$ is matrix valued since $\boldsymbol{X}$ is matrix valued. We use the notation $\boldsymbol{X}^{\circ n} = \underbrace{\boldsymbol{X} \circ \cdots \circ \boldsymbol{X}}_{n \text{ times}}$ and $\boldsymbol{X}^{\circ 0} = \boldsymbol{1}$ and the circle $\circ$ stands for the matrix product with an additional implicit integration along the contour $\mathcal{C}$, i.e., for example $(\boldsymbol{X}_1 \circ \boldsymbol{X}_2)(z,z') \equiv \int_{\mathcal{C}} d\bar{z}\,\boldsymbol{X}_1(z,\bar{z})\boldsymbol{X}_2(\bar{z},z')$. Since by setting $\hbar$ to one, time is measured in units of inverse energy, i.e., by $[E]^{-1}$, and hence the contour integration also carries the unit $[E]^{-1}$. Therefore, for a meaningful definition of f via Eq. (2.25), its argument $\boldsymbol{X}$ must have units of energy. This ensures that each $\circ$-power of $\boldsymbol{X}$ has the same unit. Accordingly the function $\boldsymbol{f}(\boldsymbol{X})$ itself carries the unit of energy $[E]$. For a list of (nonequilibrium) quantities and their respective units see Table A.1 in the appendix.

Cancellation of Keldysh integrations For arbitrary analytical functions f_i of arbitrary *physical* two-point contour functions $\boldsymbol{X}_i$, the following integral along the Keldysh branch over the equal time component of products of $\boldsymbol{f}_i(\boldsymbol{X}_i)$ vanishes, namely

$$\int_{\mathcal{C}_K} dz \left[\boldsymbol{f}_1(\boldsymbol{X}_1) \circ \boldsymbol{f}_2(\boldsymbol{X}_2) \circ \cdots \circ \boldsymbol{f}_N(\boldsymbol{X}_N)\right](z,z^+) = 0\,, \tag{2.26}$$

where z^+ is infinitesimally later than z on $\mathcal{C}$.

For a proof, we consider two arbitrary *physical* two-point contour functions $\boldsymbol{X}$ and $\boldsymbol{Y}$. By decomposing the contour integrations into their components along the branches and using the identities Eq. (2.15) and (2.16) for $\boldsymbol{X}$ and $\boldsymbol{Y}$, we find

$$\int_{\mathcal{C}_K} dz \int_{\mathcal{C}} dz'\,\boldsymbol{X}(z,z')\boldsymbol{Y}(z',z) = \int_{t_0}^{\infty} dt \int_{t_0}^{t} dt'\,\boldsymbol{X}^{>}(t,t')\boldsymbol{Y}^{<}(t',t)$$

$$+ \int_{t_0}^{\infty} dt \int_t^{\infty} dt' \, \boldsymbol{X}^<(t,t')\boldsymbol{Y}^>(t',t)$$

$$+ \int_{t_0}^{\infty} dt \int_{\infty}^{t_0} dt' \, \boldsymbol{X}^<(t,t')\boldsymbol{Y}^>(t',t)$$

$$+ \int_{\infty}^{t_0} dt \int_{t_0}^{\infty} dt' \, \boldsymbol{X}^>(t,t')\boldsymbol{Y}^<(t',t)$$

$$+ \int_{\infty}^{t_0} dt \int_{\infty}^{t} dt' \, \boldsymbol{X}^>(t,t')\boldsymbol{Y}^<(t',t)$$

$$+ \int_{\infty}^{t_0} dt \int_{t}^{t_0} dt' \, \boldsymbol{X}^<(t,t')\boldsymbol{Y}^>(t',t)$$

$$+ \int_{t_0}^{\infty} dt \int_0^{\beta} d\tau' \boldsymbol{X}^<(t,t_0-i\tau')\boldsymbol{Y}^>(t_0-i\tau',t)$$

$$+ \int_{\infty}^{t_0} dt \int_0^{\beta} d\tau' \boldsymbol{X}^<(t,t_0-i\tau')\boldsymbol{Y}^>(t_0-i\tau',t)\,.$$

Now, collecting all terms with identical integrands, we easily obtain

$$\int_{\mathcal{C}_K} dz \int_{\mathcal{C}} dz' \, \boldsymbol{X}(z,z')\boldsymbol{Y}(z',z) = 0\,. \tag{2.27}$$

Since any product of contour functions and also any analytical function of contour functions is again a contour function, this directly proves Eq. (2.26). This property will be of importance for functionals of contour functions in later chapters.

2.3.2 Equations of motion

The equation of motion for the one-particle Green's function (2.12) is deduced from the Heisenberg equations (2.5) for the construction operators, which read as:

$$
\begin{aligned}
i\partial_z c_{\alpha,\mathcal{H}}(z) &= \sum_{\beta} h_{\alpha\beta}(z)c_{\beta,\mathcal{H}}(z) + \left[c_{\alpha,\mathcal{H}}(z), H_{0,\boldsymbol{U};\mathcal{H}}(z)\right]\,, \\
i\partial_z c_{\alpha,\mathcal{H}}^{\dagger}(z) &= -\sum_{\beta} c_{\beta,\mathcal{H}}^{\dagger}(z)h_{\beta\alpha}(z) - \left[H_{0,\boldsymbol{U};\mathcal{H}}(z), c_{\alpha,\mathcal{H}}^{\dagger}(z)\right]\,,
\end{aligned}
\tag{2.28}
$$

where for brevity we defined $h_{\alpha\beta}(z) \equiv \lambda_{\alpha\beta}(z)-\mu\delta_{\alpha\beta}$. The first summand originates from the respective commutator with $H_{\boldsymbol{\lambda},0}-\mu\hat{N}$ and gives rise to another one-particle Green's function when applying the time derivative to Eq. (2.12) whereas the second term leads to a higher Green's function. The latter again obeys an equation of motion involving even higher Green's functions and one is finally left with a hierarchy of equations of motion for Green's functions of arbitrary order [204, 205]. However, the equations of motion for $\boldsymbol{G}_{\boldsymbol{\lambda},\boldsymbol{U}}$ can be cast into a closed form by defining the *self-energy* via

$$
\begin{aligned}
(\boldsymbol{\Sigma}_{\boldsymbol{\lambda},\boldsymbol{U}} \circ \boldsymbol{G}_{\boldsymbol{\lambda},\boldsymbol{U}})_{\alpha\alpha'}(z,z') &\equiv (-i)\langle \mathcal{T}_{\mathcal{C}}\left(\left[c_{\alpha,\mathcal{H}}(z), H_{0,\boldsymbol{U};\mathcal{H}}(z)\right] c_{\alpha',\mathcal{H}}^{\dagger}(z')\right)\rangle\,, \\
(\boldsymbol{G}_{\boldsymbol{\lambda},\boldsymbol{U}} \circ \boldsymbol{\Sigma}_{\boldsymbol{\lambda},\boldsymbol{U}})_{\alpha\alpha'}(z,z') &\equiv (-i)\langle \mathcal{T}_{\mathcal{C}}\left(c_{\alpha,\mathcal{H}}(z)\left[H_{0,\boldsymbol{U};\mathcal{H}}(z'), c_{\alpha',\mathcal{H}}^{\dagger}(z')\right]\right)\rangle\,,
\end{aligned}
\tag{2.29}
$$

and thus read as

$$
\begin{aligned}
\left(i \overrightarrow{\partial}_z - \boldsymbol{h}(z)\right) \boldsymbol{G}_{\boldsymbol{\lambda},\boldsymbol{U}}(z,z') &= \delta_{\alpha\alpha'}\delta_{\mathcal{C}}(z,z') + \left(\boldsymbol{\Sigma}_{\boldsymbol{\lambda},\boldsymbol{U}} \circ \boldsymbol{G}_{\boldsymbol{\lambda},\boldsymbol{U}}\right)(z,z'), \\
\boldsymbol{G}_{\boldsymbol{\lambda},\boldsymbol{U}}(z,z') \left(-i \overleftarrow{\partial}_{z'} - \boldsymbol{h}(z)\right) &= \delta_{\alpha\alpha'}\delta_{\mathcal{C}}(z,z') + \left(\boldsymbol{G}_{\boldsymbol{\lambda},\boldsymbol{U}} \circ \boldsymbol{\Sigma}_{\boldsymbol{\lambda},\boldsymbol{U}}\right)(z,z'),
\end{aligned}
\tag{2.30}
$$

where the time derivative formally acts either from right or from the left as indicated by the superscript arrows. By setting $\boldsymbol{U} = 0$ in Eqs. (2.29) and (2.30) the inverse of the "free" Green's function is obtained as

$$
G^{-1}_{\boldsymbol{\lambda},0;\alpha\alpha'}(z,z') = \delta_{\mathcal{C}}(z,z') \left(\delta_{\alpha\alpha'}(\pm i) \overset{\rightleftarrows}{\partial}_{z'} - h_{\alpha\alpha'}(z')\right).
\tag{2.31}
$$

Note that the matrix inverse refers to both one-particle basis indices and time variables (see also the definition of the inverse of a two-point contour function in Eq. A.6).

Dyson equation

With the free Green's function (2.31) at hand the equations of motion (2.30) are easily recast in the following form

$$
\begin{aligned}
\left[(\boldsymbol{G}^{-1}_{\boldsymbol{\lambda},0} - \boldsymbol{\Sigma}_{\boldsymbol{\lambda},\boldsymbol{U}}) \circ \boldsymbol{G}_{\boldsymbol{\lambda},\boldsymbol{U}}\right]_{\alpha\alpha'}(z,z') &= \delta_{\alpha\alpha'}\delta_{\mathcal{C}}(z,z') \\
&= \left[\boldsymbol{G}_{\boldsymbol{\lambda},\boldsymbol{U}} \circ (\boldsymbol{G}^{-1}_{\boldsymbol{\lambda},0} - \boldsymbol{\Sigma}_{\boldsymbol{\lambda},\boldsymbol{U}})\right]_{\alpha\alpha'}(z,z').
\end{aligned}
\tag{2.32}
$$

By multiplying with $\boldsymbol{G}_{\boldsymbol{\lambda},0}$ from either the left or the right, we therewith obtain two equivalent Dyson equations:

$$
\begin{aligned}
\boldsymbol{G}_{\boldsymbol{\lambda},\boldsymbol{U}}(z,z') &= \boldsymbol{G}_{\boldsymbol{\lambda},0}(z,z') + \left[\boldsymbol{G}_{\boldsymbol{\lambda},0} \circ \boldsymbol{\Sigma}_{\boldsymbol{\lambda},\boldsymbol{U}} \circ \boldsymbol{G}_{\boldsymbol{\lambda},\boldsymbol{U}}\right](z,z'), \\
\boldsymbol{G}_{\boldsymbol{\lambda},\boldsymbol{U}}(z,z') &= \boldsymbol{G}_{\boldsymbol{\lambda},0}(z,z') + \left[\boldsymbol{G}_{\boldsymbol{\lambda},\boldsymbol{U}} \circ \boldsymbol{\Sigma}_{\boldsymbol{\lambda},\boldsymbol{U}} \circ \boldsymbol{G}_{\boldsymbol{\lambda},0}\right](z,z'),
\end{aligned}
\tag{2.33}
$$

the formal solution of which can be written as

$$
\boldsymbol{G}_{\boldsymbol{\lambda},\boldsymbol{U}}(z,z') = \left(\boldsymbol{G}^{-1}_{\boldsymbol{\lambda},0} - \boldsymbol{\Sigma}_{\boldsymbol{\lambda},\boldsymbol{U}}\right)^{-1}(z,z').
\tag{2.34}
$$

However, the self-energy is generally not known exactly and approximations are needed. Perturbation theory can either provide truncated expansions for the self-energy or motivate functional relations, as we will briefly review in the following section.

2.3.3 Perturbation theory

By switching to the interaction picture, the Green's function [Eq. 2.12] can be cast into the following form [see also Eq. 2.9]

$$
iG_{\boldsymbol{\lambda},\boldsymbol{U};\alpha\alpha'}(z,z') = \frac{\langle \mathcal{T}_{\mathcal{C}} e^{-i\int_{\mathcal{C}} dz'' \, \mathcal{H}_{0,U}(z'')} c_\alpha(z) c^\dagger_{\alpha'}(z') \rangle_{\boldsymbol{\lambda},0}}{\langle \mathcal{T}_{\mathcal{C}} e^{-i\int_{\mathcal{C}} dz'' \, \mathcal{H}_{0,U}(z'')} \rangle_{\boldsymbol{\lambda},0}},
\tag{2.35}
$$

where the time dependencies of all operators are due to $\mathcal{H}_{\boldsymbol{\lambda},0}$ only. Likewise, the expectation value $\langle\cdots\rangle_{\boldsymbol{\lambda},0} = \operatorname{tr}(\rho_{\boldsymbol{\lambda},0}\cdots)$ is defined via the free density operator $\rho_{\boldsymbol{\lambda},0} = \exp\left(-\beta\mathcal{H}_{\boldsymbol{\lambda},0}\right)/\operatorname{tr}\exp\left(-\beta\mathcal{H}_{\boldsymbol{\lambda},0}\right)$. Hence, Wick's theorem applies and therewith the standard techniques of perturbation theory [198, 206] can be exploited. It is important to note that besides free expectation values also a single ordering principle for all operators involved in correlation functions is a prerequisite for Wick's theorem to hold. Thus, the Keldysh-Matsubara bookkeeping of contour quantities is not only handy but also necessary for the setup of a nonequilibrium diagrammatic perturbation theory. As in the equilibrium case, by expanding the exponentials in Eq. (2.35), the interacting Green's function $\boldsymbol{G}_{\boldsymbol{\lambda},U}$ can be expressed as an infinite series of free Green's functions $\boldsymbol{G}_{\boldsymbol{\lambda},0}$ and all diagrammatic rules know from Matsubara Green's functions can be easily generalized to nonequilibrium Green's functions. Furthermore, this expansion motivates the definition of a functional $\widehat{\boldsymbol{G}}_U[\boldsymbol{G}_0]$ of some two-time contour function $\boldsymbol{G}_0$, which yields the full *physical* Green's function when evaluated a the free *physical* Green's function, i.e., $\boldsymbol{G}_{\boldsymbol{\lambda},U} = \widehat{\boldsymbol{G}}_U[\boldsymbol{G}_{\boldsymbol{\lambda},0}]$. Note that here and in the following functionals are indicated by a hat. Since $\widehat{\boldsymbol{G}}_U$ only depends on the interaction $\boldsymbol{U}$ and the free Green's function explicitly, but not on the one-particle parameters of the system, it is called *universal*. However, considering strong correlations, a "direct" perturbative expansion around the noninteracting limit seems at least questionable. Besides complications concerning convergence, most importantly, expansions in terms of "bare" propagators $\boldsymbol{G}_0$ might result in approximations that do not respect the conservation laws of the underlying full problem. An alternative to this is prescribed by "self-consistent renormalization", namely by partially summing certain (infinite) subclasses of diagrams. To this end, two observations are essential. First, when expanding the full Green's function into an infinite set of diagrams made up of "free propagators" and "interaction vertices", the full Green's function can be identified as again implicitly contained in the expansion, i.e., can be factored out, which symbolically reads as

$$ (2.36) $$

Here, a double line represents the full Green's function $\boldsymbol{G}$ and a single line stands for the free Green's function. The remaining part, indicated by a shaded semicircle, can be identified with the respective self-energy $\boldsymbol{\Sigma}$. Hence note that this is nothing but the Dyson equation (2.33), namely $\boldsymbol{G} = \boldsymbol{G}_0 + \boldsymbol{G}_0 \circ \boldsymbol{\Sigma} \circ \boldsymbol{G}$. A second observation concerns the self-energy itself. All contributing diagrams can essentially be classified into two different types: (i) those, which can be thought of some simpler diagram, where another self-energy diagram has been "inserted" or which can be "cut" into simpler self-energy diagrams and (ii) those, where this is not possible. The latter ones are called "skeleton diagrams". Intriguingly, the second class is sufficient to describe the entire self-energy, by simply replacing all bare propagators $\boldsymbol{G}_0$ by their full counterparts $\boldsymbol{G}$, pictorially termed as "dressing" the diagram. Thus, the self-energy $\boldsymbol{\Sigma}$ can be expressed as the sum

of all *dressed self-energy skeleton diagrams*, i.e.,

$$\mathbf{\Sigma} = \quad = \quad + \quad + \quad + \cdots \tag{2.37}$$

where dashed lines represent the interaction $\mathbf{U}$. Via the expansion (2.37) the self-energy can be defined as an universal functional of the full (interacting) Green's function, namely $\widehat{\mathbf{\Sigma}}_{U}[\mathbf{G}]$, which parametrically depends on the system's interaction parameter only. Independently of its first definition (2.29) and (2.33), the system's self-energy can be reobtained when evaluating the functional $\widehat{\mathbf{\Sigma}}_{U}$ at the respective Green's function, and thus:

$$\mathbf{\Sigma}_{\boldsymbol{\lambda},U} = \widehat{\mathbf{\Sigma}}_{U}[\mathbf{G}_{\boldsymbol{\lambda},U}] \,. \tag{2.38}$$

This provides a self-consistent perturbation theory, since $\mathbf{\Sigma}_{\boldsymbol{\lambda},U}$ can be calculated in an approximate fashion by truncating the series (2.37), but still depends on the full Green's function which at the same time has to fulfill the respective Dyson equation (2.33).

2.4 Observables and conservation laws

Finally, we relate nonequilibrium Green's functions to prevalent one- and two-particle observables and comment on their respective conservation laws in a Hubbard-like model. Later, this will be used for the important discussion on conservation laws within the framework of the SFT (cf. Sec. 3.9).

2.4.1 One-particle observables

Any one-particle observable can generally be expressed as

$$\boldsymbol{A}(t) = \sum_{\alpha\beta} a_{\alpha\beta}(t) c_{\alpha}^{\dagger} c_{\beta} \,, \tag{2.39}$$

which immediately allows us to relate the respective expectation value to the one-particle Green's function [Eq. 2.12] via

$$\langle \boldsymbol{A} \rangle_{\boldsymbol{\lambda},\boldsymbol{U}}(t) = -i \operatorname{tr} \left(\boldsymbol{a}(t) \boldsymbol{G}_{\boldsymbol{\lambda},\boldsymbol{U}}(t, t^{+}) \right) \,. \tag{2.40}$$

Its equation of motion is readily obtained from the equation of motion for the Green's function (i.e., from Eqs. (2.30); see also Ref. [200]). We easily find:

$$\partial_t \langle \boldsymbol{A} \rangle_{\boldsymbol{\lambda},\boldsymbol{U}}(t) = \operatorname{tr} \left(\boldsymbol{a}(t) \left[\boldsymbol{G}_{\boldsymbol{\lambda},\boldsymbol{U}}, \boldsymbol{\lambda} \right](t, t^{+}) \right) + \operatorname{tr} \left(\boldsymbol{a}(t) \left[\boldsymbol{G}_{\boldsymbol{\lambda},\boldsymbol{U}} \,\substack{\circ\\\circ}\, \boldsymbol{\Sigma}_{\boldsymbol{\lambda},\boldsymbol{U}} \right](t, t^{+}) \right) \,, \tag{2.41}$$

where $[\cdot, \cdot]$ is the commutator and $[\cdot \,\substack{\circ\\\circ}\, \cdot]$ indicates that besides the commutator a contour integration along the inner time-arguments is implied.

It's worth mentioning different special cases for the coefficient matrix $\boldsymbol{a}$, namely for which the observable $\boldsymbol{A}$ equals the ...

$$\ldots \text{kinetic energy} \quad \Leftrightarrow \quad a_{i\sigma,j\sigma'} = \delta_{\sigma\sigma'}\lambda_{ij,\sigma} \quad \text{or just} \quad a_{\alpha\beta} = \lambda\alpha\beta \tag{2.42}$$

$$\begin{aligned}&\ldots \text{particle number}\\&\ldots \text{spin in } \eta \text{ direction}\end{aligned} \quad \Leftrightarrow \quad a_{i\sigma,j\sigma'} = \delta_{ij}a_{\sigma\sigma'} \text{ with } \begin{aligned}a_{\sigma,\sigma'} &= \delta_{\sigma\sigma'}\\a_{\sigma,\sigma'} &= \tfrac{1}{2}\sigma^{(\eta)}_{\sigma\sigma'}\end{aligned}. \tag{2.43}$$

Here, as before, i refers to the sites of the lattice model, $\sigma, \sigma' = \uparrow, \downarrow$ to the spin degrees of freedom, and $\boldsymbol{\sigma}^{(\eta)}$ stands for the three Pauli matrices, with $\eta \in \{x, y, z\}$.

For the occupation number and the spin, it is interesting to express the integral quantities $\boldsymbol{A}$ in terms of sums over their local constituents $\boldsymbol{A}_i$, i.e., as $\boldsymbol{A} = \sum_i \boldsymbol{A}_i$. For these, the equation of motion [Eq. 2.41] becomes

$$\partial_t \langle \boldsymbol{A}_i \rangle_{\boldsymbol{\lambda},\boldsymbol{U}}(t) = \sum_{\sigma\sigma'} a_{\sigma\sigma'} \left[\boldsymbol{G}_{\boldsymbol{\lambda},\boldsymbol{U}}, \boldsymbol{\lambda} \right]_{ii,\sigma'\sigma}(t, t^+)$$

$$+ \sum_{\sigma\sigma'} a_{\sigma\sigma'} \left[\boldsymbol{G}_{\boldsymbol{\lambda},\boldsymbol{U}} \,\substack{\circ\\\circ}\, \boldsymbol{\Sigma}_{\boldsymbol{\lambda},\boldsymbol{U}} \right]_{ii,\sigma'\sigma}(t, t^+). \tag{2.44}$$

For a Hubbard-type model with local interaction, the second commutator vanishes identically. Equation (2.44) thus attains the form of a continuity equation where the first commutator represents the divergence of the charge current or spin current. It vanishes if summed over all sites i due the cyclic property of the trace, and we are left with $\partial_t \langle \boldsymbol{A} \rangle_{\boldsymbol{\lambda},\boldsymbol{U}}(t) = 0$, i.e., conservation of the total particle number or spin.

One should note, that whenever observables are calculated from approximated Green's functions via Eq. (2.40), the fact whether the second term in Eq. (2.44) does or does not vanish within the respective approximation serves as a condition if the particular conservation laws are preserved, i.e., generally

$$\langle \boldsymbol{A}_i \rangle_{\boldsymbol{\lambda},\boldsymbol{U}}(t) \text{ conserved} \quad \Leftrightarrow \quad \sum_{\sigma\sigma'} a_{\sigma\sigma'} \left[\boldsymbol{G}_{\boldsymbol{\lambda},\boldsymbol{U}} \,\substack{\circ\\\circ}\, \boldsymbol{\Sigma}_{\boldsymbol{\lambda},\boldsymbol{U}} \right]_{ii,\sigma'\sigma}(t, t^+) = 0. \tag{2.45}$$

2.4.2 Energy

Two important examples for two-particle observables that can actually be obtained from the single-particle Green's function and the self-energy are the interaction energy E_{int} as well as the closely related (local) double occupancy $d_i = \langle \hat{n}^c_{i\uparrow} \hat{n}^c_{i\downarrow} \rangle$, the first of which is defined as [cf. Eq. 2.1]

$$E_{\text{int}}(t) = \langle H_{0,\boldsymbol{U}}(t) \rangle = \frac{1}{2} \sum_{\alpha\beta\gamma\delta} U_{\alpha\beta\delta\gamma}(t) \langle c^\dagger_\alpha(t) c^\dagger_\beta(t) c_\gamma(t) c_\delta(t) \rangle. \tag{2.46}$$

For a local Hubbard-type interaction parameter in a model with spatial- and spin-degrees of freedom, i.e., $U_{\alpha\beta\gamma\delta} = U_{i\sigma,j\sigma',l\lambda,k\lambda'} = U_i \delta_{ij}\delta_{jl}\delta_{lk}\delta_{\lambda\sigma}\delta_{\lambda'\sigma'}$, this becomes

$$E_{\text{int}}(t) = \frac{1}{2} \sum_{i\sigma\sigma'} U_i(t) \langle c^\dagger_{i\sigma}(t) c^\dagger_{i\sigma'}(t) c_{i\sigma'}(t) c_{i\sigma}(t) \rangle = \frac{1}{2} \sum_{i\sigma} U_i(t) \langle c^\dagger_{i\sigma}(t) c^\dagger_{i\bar{\sigma}}(t) c_{i\bar{\sigma}}(t) c_{i\sigma}(t) \rangle$$

$$= \sum_i U_i(t) \langle \hat{n}^c_{i\uparrow} \hat{n}^c_{i\downarrow} \rangle = \sum_i U_i(t) d_i(t), \tag{2.47}$$

i.e., the interaction energy is basically given by the double occupancy multiplied by the interaction parameter. From the definition of the self-energy [Eq. 2.29] and with the commutator $\left[c_\alpha, H_{0,U}\right]$ and its complex conjugate [cf. Eqs. A.4] we obtain

$$(\boldsymbol{\Sigma}_{\boldsymbol{\lambda},\boldsymbol{U}} \circ \boldsymbol{G}_{\boldsymbol{\lambda},\boldsymbol{U}})_{\alpha\alpha'}(t,t^+) = -\frac{i}{2}\sum_{\beta\gamma\delta} U_{[\alpha,\beta]\delta\gamma}(t)\langle c^\dagger_{\alpha'}(t)c^\dagger_\beta(t)c_\delta(t)c_\gamma(t)\rangle\,, \tag{2.48}$$

$$(\boldsymbol{G}_{\boldsymbol{\lambda},\boldsymbol{U}} \circ \boldsymbol{\Sigma}_{\boldsymbol{\lambda},\boldsymbol{U}})_{\alpha\alpha'}(t,t^+) = -\frac{i}{2}\sum_{\beta\gamma\delta} U_{\delta\gamma[\alpha',\beta]}(t)\langle c^\dagger_\delta(t)c^\dagger_\gamma(t)c_\alpha(t)c_\beta(t)\rangle\,, \tag{2.49}$$

where we used the short-hand notation $U_{[\alpha,\beta]\delta\gamma} = U_{\alpha\beta\delta\gamma} - U_{\beta\alpha\delta\gamma}$ as well as the symmetry $U_{\alpha\beta\delta\gamma} = U_{\beta\alpha\gamma\delta}$. After a short calculation, this eventually yields

$$\begin{aligned} E_{\mathrm{int}}(t) &= -\frac{i}{2}\,\mathrm{tr}\left((\boldsymbol{\Sigma}_{\boldsymbol{\lambda},\boldsymbol{U}} \circ \boldsymbol{G}_{\boldsymbol{\lambda},\boldsymbol{U}})(t,t^+)\right) = -\frac{i}{2}\,\mathrm{tr}\left((\boldsymbol{G}_{\boldsymbol{\lambda},\boldsymbol{U}} \circ \boldsymbol{\Sigma}_{\boldsymbol{\lambda},\boldsymbol{U}})(t,t^+)\right) \\ &= -\frac{i}{4}\,\mathrm{tr}\left((\boldsymbol{\Sigma}_{\boldsymbol{\lambda},\boldsymbol{U}} \circ \boldsymbol{G}_{\boldsymbol{\lambda},\boldsymbol{U}} + \boldsymbol{G}_{\boldsymbol{\lambda},\boldsymbol{U}} \circ \boldsymbol{\Sigma}_{\boldsymbol{\lambda},\boldsymbol{U}})(t,t^+)\right). \end{aligned} \tag{2.50}$$

If the self-energy is not directly accessible, the interaction energy can also be calculated via the time derivative of the Green's function, as can be seen from the equation of motion [Eq. 2.30]:

$$E_{\mathrm{int}}(t) = \frac{1}{4}\,\mathrm{tr}\left(\partial_t \boldsymbol{G}_{\boldsymbol{\lambda},\boldsymbol{U}}(t,t') - \partial_{t'} \boldsymbol{G}_{\boldsymbol{\lambda},\boldsymbol{U}}(t,t')\right)_{t'=t^+} - \frac{1}{2}E_{\mathrm{kin}}(t) + \frac{1}{2}\mu\hat{N}(t)\,, \tag{2.51}$$

where $\hat{N}(t) = \sum_i \hat{n}^c_i(t)$ is the total particle number.

Let us again discuss the conservation laws for the case of the total energy. Therefore, recall that the kinetic part of the energy $E_{\mathrm{kin}}(t) = \langle H_{\boldsymbol{\lambda},0}(t)\rangle$, according to Eq. (2.42), can be written as

$$E_{\mathrm{kin}}(t) = -i\,\mathrm{tr}\left(\boldsymbol{\lambda}(t)\boldsymbol{G}_{\boldsymbol{\lambda},\boldsymbol{U}}(t,t^+)\right). \tag{2.52}$$

In the following, we will skip the indices $\boldsymbol{\lambda}$ and $\boldsymbol{U}$ and write $\boldsymbol{G}$ and $\boldsymbol{\Sigma}$ for brevity.

The total energy of the system is $E_{\mathrm{tot}}(t) \equiv \langle H(t)\rangle = E_{\mathrm{kin}}(t) + E_{\mathrm{int}}(t)$. In the following, we assume that the interaction parameters $\boldsymbol{U}$ are time-independent (see also the discussion on the next page, following after Eq. 2.56). Using $\partial_t E_{\mathrm{tot}}(t) = \langle \partial_t H(t)\rangle$, this immediately implies the energy-balance relation:

$$\frac{\partial E_{\mathrm{tot}}(t)}{\partial t} = \sum_{\alpha\beta} \frac{\partial \lambda_{\alpha\beta}(t)}{\partial t}\langle c^\dagger_\alpha(t)c_\beta(t)\rangle\,. \tag{2.53}$$

Next, we express both the left-hand side and the right-hand side of Eq. (2.53) in terms of $\boldsymbol{\Sigma}$ and $\boldsymbol{G}$. Using the equation of motion again, the time derivatives of $E_{\mathrm{kin}}(t)$ and $E_{\mathrm{int}}(t)$ can be computed. From Eq. (2.52) we get:

$$\begin{aligned} \frac{\partial E_{\mathrm{kin}}(t)}{\partial t} &= \mathrm{tr}\left(\boldsymbol{\lambda}(t)\,[\boldsymbol{G},\boldsymbol{\lambda}]\,(t,t^+)\right) + \mathrm{tr}\left(\boldsymbol{\lambda}(t)\,[\boldsymbol{G}\,\overset{\circ}{,}\,\boldsymbol{\Sigma}]\,(t,t^+)\right) - i\,\mathrm{tr}\left(\frac{\partial\boldsymbol{\lambda}(t)}{\partial t}\boldsymbol{G}(t,t^+)\right) \\ &= \mathrm{tr}\left(\boldsymbol{\lambda}(t)\,[\boldsymbol{G}\,\overset{\circ}{,}\,\boldsymbol{\Sigma}]\,(t,t^+)\right) - i\,\mathrm{tr}\left(\frac{\partial\boldsymbol{\lambda}(t)}{\partial t}\boldsymbol{G}(t,t^+)\right). \end{aligned} \tag{2.54}$$

Here the first term in the first line vanishes due the cyclic property of the trace. Exploiting once more the equation of motion as well as its complex conjugate, we find:

$$\frac{\partial E_{\mathrm{kin}}(t_1)}{\partial t_1} = i \sum_{\alpha_1} \int d2 \left(\left(\frac{\partial}{\partial t_1} G(1,2) \right) \Sigma(2,1^+) + \Sigma(1,2) \frac{\partial}{\partial t_1} G(2,1^+) \right)$$

$$- i \operatorname{tr} \left(\frac{\partial \boldsymbol{\lambda}(t_1)}{\partial t_1} \boldsymbol{G}(t_1, t_1^+) \right) . \quad (2.55)$$

Note that the last summand just equals the right-hand side of Eq. (2.53). This equation can easily be combined with the time derivative of the interaction energy [Eq. 2.50]. After applying the product rule, the energy-balance relation [Eq. 2.53] is expressed as [119]:

$$-\frac{3}{4} \sum_{\alpha_1} \int d2 \frac{\partial}{\partial t_1} \left(\Sigma(1,2) G(2,1^+) + G(1,2) \Sigma(2,1^+) \right)$$

$$+ \sum_{\alpha_1} \int d2 \left(\frac{\partial \Sigma(1,2)}{\partial t_1} G(2,1^+) + G(1,2) \frac{\partial \Sigma(2,1^+)}{\partial t_1} \right) = 0 . \quad (2.56)$$

Again, it turns out that this equation is trivially obeyed e.g. for the Hubbard model [Eq. 2.2] due to its symmetries. However, if approximations for the self-energy and the Green's function are used for the calculation of the total energy, this is far from obvious, and hence Eq. (2.56) serves as a conditional equation to check whether an approximative treatment of the full lattice problem follows the respective energy conservation law or if it doesn't.

Discussion

For the preceding derivation, we assumed the interaction parameters as time-independent, i.e., $\boldsymbol{U} = \mathrm{const}$. In case of a time-dependent interaction $\boldsymbol{U}(t)$ (and assuming the one-particle parameters as constant for a moment), the energy-balance relation will involve a two-particle correlation function,

$$\frac{\partial E_{\mathrm{tot}}(t)}{\partial t} = \frac{1}{2} \sum_{\alpha\beta\gamma\delta} \frac{\partial U_{\alpha\beta\delta\gamma}(t)}{\partial t} \langle c_\alpha^\dagger(t) c_\beta^\dagger(t) c_\gamma(t) c_\delta(t) \rangle , \quad (2.57)$$

which cannot (easily) be expressed in terms of $\boldsymbol{\Sigma}$ and $\boldsymbol{G}$. Therefore, without further approximations, it is impossible to set up (and prove) a general energy balance equation in the same spirit.

An exception worth mentioning is a time dependence of the simple form $U_{\alpha\beta\delta\gamma}(t) = \kappa(t) U_{\alpha\beta\delta\gamma}$ where we furthermore assume the existence of some function $\varphi(t)$, such that $\kappa(t) = (\dot\varphi(\varphi^{-1}(t)))^{-1}$ with $\dot\varphi(t) \equiv \partial_t \varphi(t) \neq 0$. In this case, the time dependence can be shifted to the one-particle parameters by a transformation of the time scale:[*] $H(t) \mapsto$

---

[*] for the following we use: $\dot\varphi(t)\kappa(\varphi(t)) = \dot\varphi(t)(\dot\varphi(\varphi^{-1}(\varphi(t))))^{-1} = \dot\varphi(t)(\dot\varphi(t))^{-1} = 1$, i.e., the prefactor of the Hamiltonian's interaction part becomes time independent

$\widetilde{H}(t) = \dot{\varphi}(t) H(\varphi(t))$ and $|\widetilde{\psi}(t)\rangle = |\psi(\varphi(t))\rangle$ which leaves the Schrödinger equation form invariant:

$$(i\partial_t - \widetilde{H}(t))|\widetilde{\psi}(t)\rangle = \dot{\varphi}(t)(i\partial_\varphi - H(\varphi))|\psi(\varphi)\rangle = 0 \,. \tag{2.58}$$

We furthermore note, that in fact in most cases, after some initial modulation of the parameters to stimulate nontrivial real-time dynamics, these will be held constant and instead of a more general balance of energies, we will be interested in a strict conservation of the total energy only, i.e., $\partial_t E_{\text{tot}} = 0$ should hold as soon as the model parameters are not explicitly time-dependent any more. Nevertheless, when the self-energy and the Green's function are given via some approximative scheme, the conditional equation (2.56) has to be fulfilled in the same manner, in order for the respective approximation to be energy-conserving.

3 Nonequilibrium self-energy functional theory

The general task for describing the dynamics of an interacting many-body problem is to solve the Green's function's equation of motion, or equivalently the corresponding Dyson's equation (as discussed in chapter 2). In general, already for rather simple systems its full solution cannot be found since the respective self-energy is not known exactly. However, solving Dyson's equation self-consistently can be equivalently recast into a variational problem for the model's grand potential expressed as a functional of the self-energy. Though this seems to be of little use at first sight, since the problem remains utterly complex, this *self-energy functional* in fact has several beneficial properties which allow to relate the full lattice problem to a numerically solvable, small reference problem. This idea is at the very heart of the self-energy functional theory (SFT), first formulated in equilibrium by Potthoff [162]. The following chapter is entirely devoted to its generalization to the nonequilibrium case.

The first sections are rather preparatory and, due to the formal equivalence of the Green's function formalism in and out of equilibrium, can be presented in close analogy to the equilibrium SFT. To this end we first introduce the Luttinger-Ward functional and review its essential properties in Sec. 3.1, which will then be used to construct the dynamical variational principle of the nonequilibrium SFT in Sec. 3.2. A prescription for constructing approximations follows in Sec. 3.3 and as a special case we will show the relation to nonequilibrium DMFT in Sec. 3.4. Apart from that, there are several peculiarities which exclusively arise for the nonequilibrium variant of the SFT. It turns out that opposed to the equilibrium case the space of variational parameters has to be "enlarged" in the sense that variations off the physical manifold have to be incorporated, as we discuss in Sec. 3.5. For an evaluation of the variational principle on the space of physical parameters an analytical evaluation of the respective functional derivatives will be beneficial and carried out in Sec. 3.6. The relation to the underlying equilibrium theory is worked out in Sec. 3.7 and thermodynamical consistency is surveyed subsequently in Sec. 3.8. Finally, and most importantly, we will carefully discuss the conserving nature and possible drawbacks in Sec. 3.9.

3.1 Luttinger-Ward functional

The nonequilibrium Luttinger-Ward functional $\widehat{\Phi}_U[\boldsymbol{G}]$ can be defined by means of all-order perturbation theory in close analogy to the equilibrium case [207]. It is obtained as the limit of the infinite series of closed renormalized skeleton diagrams (see also Sec. 2.3.3), and is thus given as a functional of the contour-ordered Green's function:

$$-\beta\widehat{\Phi}_U[\boldsymbol{G}] \;=\; \vcenter{\hbox{}} \;+\; \vcenter{\hbox{}} \;+\; \vcenter{\hbox{}} \;+\; \cdots \tag{3.1}$$

Usually the skeleton-diagram expansion cannot be summed up to get a closed form for $\widehat{\Phi}_U[\boldsymbol{G}]$, and the explicit functional dependence is unknown even for the most simple types of interactions like the Hubbard interaction. As an alternative to the diagrammatic definition of the Luttinger-Ward functional, a nonequilibrium path-integral formalism may be used for an entirely nonperturbative construction. Again, this can be done analogously to the equilibrium case [208]. Both variants allow to derive the following four properties that will be used extensively for constructing the nonequilibrium SFT:

(i) The Luttinger-Ward functional vanishes in the noninteracting limit:

$$\widehat{\Phi}_U[\boldsymbol{G}] \equiv 0 \quad \text{for} \quad \boldsymbol{U} = 0\,, \tag{3.2}$$

since there is no zeroth-order diagram.

(ii) The functional derivative of the Luttinger-Ward functional with respect to its argument is:

$$\frac{\delta\widehat{\Phi}_U[\boldsymbol{G}]}{\delta G(1,2)} = \frac{1}{\beta}\widehat{\Sigma}_U[\boldsymbol{G}](2,1)\,. \tag{3.3}$$

Diagrammatically, the functional derivative corresponds to the removal of a propagator from each of the Φ diagrams. Taking care of topological factors [207], one ends up with the skeleton-diagram expansion of the self-energy (2.37) which gives the self-energy as a functional of the Green's function $\widehat{\Sigma}_U[\boldsymbol{G}]$, and when evaluated at the exact ("physical") Green's function $\boldsymbol{G}_{\lambda,U}$ yields the physical self-energy $\boldsymbol{\Sigma}_{\lambda,U} = \widehat{\Sigma}_U[\boldsymbol{G}_{\lambda,U}]$ (cf. Eq. 2.38). In Sec. 2.3.3, this relation was refered to as the starting point for self-consistent perturbative expansions of $\widehat{\Sigma}_U[\boldsymbol{G}]$. In fact, this truncation of the series is typically done on the level of the Luttinger-Ward functional and the actual self-energy approximation is provided by Eq. (3.3) and consequently termed as "Φ-derivable". Intriguingly, such approximations are conserving in the sense of Baym and Kadanoff [118, 119]. We will come back to this fact in greater detail in Sec. 3.9.

(iii) Since any diagram in the series depends on $\boldsymbol{U}$ and on $\boldsymbol{G}$ *only*, the Luttinger-Ward functional is "universal", i.e., it is independent of $\boldsymbol{\lambda}$. Two systems with the same interaction $\boldsymbol{U}$ but different one-particle parameters $\boldsymbol{\lambda}$ and $\boldsymbol{\lambda}'$ are described by the same Luttinger-Ward functional. This implies that the functional $\widehat{\boldsymbol{\Sigma}}_{\boldsymbol{U}}[\boldsymbol{G}]$ is universal, too, as we already noted in Sec. 2.3.3.

(iv) If evaluated at the physical Green's function $\boldsymbol{G}_{\boldsymbol{\lambda},\boldsymbol{U}}$ of the system with Hamiltonian $H_{\boldsymbol{\lambda},\boldsymbol{U}}$, the Luttinger-Ward functional provides a quantity

$$\Phi_{\boldsymbol{\lambda},\boldsymbol{U}} = \widehat{\Phi}_{\boldsymbol{U}}[\boldsymbol{G}_{\boldsymbol{\lambda},\boldsymbol{U}}]\,, \tag{3.4}$$

which depends on the initial equilibrium state of the system only, as contributions from the Keldysh branch cancel each other (for details, see Eq. 2.26). $\Phi_{\boldsymbol{\lambda},\boldsymbol{U}}$ is related to the grand potential of the system via the expression

$$\Omega_{\boldsymbol{\lambda},\boldsymbol{U}} = \Phi_{\boldsymbol{\lambda},\boldsymbol{U}} + \frac{1}{\beta}\,\mathrm{Tr}\ln\left(\boldsymbol{G}_{\varepsilon_0,0}^{-1} \circ \boldsymbol{G}_{\boldsymbol{\lambda},\boldsymbol{U}}\right) - \frac{1}{\beta}\,\mathrm{Tr}(\boldsymbol{\Sigma}_{\boldsymbol{\lambda},\boldsymbol{U}} \circ \boldsymbol{G}_{\boldsymbol{\lambda},\boldsymbol{U}})\,. \tag{3.5}$$

Here, the trace also involves an integration along the entire contour and is defined as

$$\mathrm{Tr}\,\boldsymbol{A} = \sum_\alpha \int_{\mathcal{C}} dz\, A_{\alpha\alpha}(z, z^+)\,. \tag{3.6}$$

With the trivial inverse Green's function (cf. Eq. 2.31)

$$G_{\varepsilon_0,0;\alpha\alpha'}^{-1}(z, z') = \delta_{\alpha\alpha'}\delta_{\mathcal{C}}(z, z')\left(i\partial_{z'} + \mu - \varepsilon_0\right)\,, \tag{3.7}$$

the term $\boldsymbol{G}_{\varepsilon_0,0}^{-1}\circ\boldsymbol{G}_{\boldsymbol{\lambda},\boldsymbol{U}}$ carries energy units, and the principal branch of the logarithm $\ln\left(\boldsymbol{G}_{\varepsilon_0,0}^{-1} \circ \boldsymbol{G}_{\boldsymbol{\lambda},\boldsymbol{U}}\right)$ is well defined for any ε_0 (cf. Eq. 2.25 and the related discussion). For $\varepsilon_0 \to \infty$, it represents a regularization of the ill-defined expression $\ln\boldsymbol{G}_{\boldsymbol{\lambda},\boldsymbol{U}}$. In particular, we find that this is related to the grand potential,

$$\Omega_{\boldsymbol{\lambda},\boldsymbol{0}} = \frac{1}{\beta}\,\mathrm{Tr}\ln\left(\boldsymbol{G}_{\varepsilon_0,0}^{-1} \circ \boldsymbol{G}_{\boldsymbol{\lambda},\boldsymbol{0}}\right)\Big|_{\varepsilon_0\to\infty}\,, \tag{3.8}$$

in the noninteracting case (see also Eq. 3.5). It will be omitted in the following as it does not affect the following results of interest. Equation (3.5) can be derived using a coupling-constant integration [207] or by integrating over the chemical potential μ [208]. The proof is completely analogous to the equilibrium case.

3.2 Dynamical variational principle

We assume the functional $\widehat{\boldsymbol{\Sigma}}_{\boldsymbol{U}}[\boldsymbol{G}]$ is invertible *locally* to construct the Legendre transform of the Luttinger-Ward functional:

$$\widehat{F}_{\boldsymbol{U}}[\boldsymbol{\Sigma}] = \widehat{\Phi}_{\boldsymbol{U}}[\widehat{\boldsymbol{G}}_{\boldsymbol{U}}[\boldsymbol{\Sigma}]] - \frac{1}{\beta}\,\mathrm{Tr}(\boldsymbol{\Sigma} \circ \widehat{\boldsymbol{G}}_{\boldsymbol{U}}[\boldsymbol{\Sigma}])\,. \tag{3.9}$$

Here, $\widehat{\boldsymbol{G}}_U[\widehat{\boldsymbol{\Sigma}}_U[\boldsymbol{G}]] = \boldsymbol{G}$. With Eq. (3.3) one has:

$$\frac{\delta \widehat{F}_U[\boldsymbol{\Sigma}]}{\delta \Sigma(1,2)} = -\frac{1}{\beta} \widehat{G}_U[\boldsymbol{\Sigma}](2,1) \, . \tag{3.10}$$

We now define the self-energy functional as:

$$\widehat{\Omega}_{\boldsymbol{\lambda},U}[\boldsymbol{\Sigma}] = \frac{1}{\beta} \operatorname{Tr} \ln \left(\boldsymbol{G}_{\boldsymbol{\lambda},0}^{-1} - \boldsymbol{\Sigma} \right)^{-1} + \widehat{F}_U[\boldsymbol{\Sigma}] \, , \tag{3.11}$$

For any analytical function of contour functions (2.25) we immediately have

$$\frac{\delta \operatorname{Tr}(f(\boldsymbol{X}))}{\delta \boldsymbol{X}(1,2)} = f'(\boldsymbol{X})(2,1^+) \, , \tag{3.12}$$

and thus the functional derivative of (3.11) is:

$$\frac{\delta \widehat{\Omega}_{\boldsymbol{\lambda},U}[\boldsymbol{\Sigma}]}{\delta \boldsymbol{\Sigma}} = \frac{1}{\beta} \left(\boldsymbol{G}_{\boldsymbol{\lambda},0}^{-1} - \boldsymbol{\Sigma} \right)^{-1} - \frac{1}{\beta} \widehat{\boldsymbol{G}}_U[\boldsymbol{\Sigma}] \, . \tag{3.13}$$

The equation

$$\widehat{\boldsymbol{G}}_U[\boldsymbol{\Sigma}] = \left(\boldsymbol{G}_{\boldsymbol{\lambda},0}^{-1} - \boldsymbol{\Sigma} \right)^{-1} \tag{3.14}$$

is a (highly nonlinear) conditional equation for the self-energy of the system $H_{\boldsymbol{\lambda},U}$. Equations (2.33) and (2.38) show that it is satisfied by the physical self-energy $\boldsymbol{\Sigma} = \boldsymbol{\Sigma}_{\boldsymbol{\lambda},U}$. Note that the left-hand side of Eq. (3.14) is independent of $\boldsymbol{\lambda}$ but depends on $\boldsymbol{U}$ (due to the universality of $\widehat{\boldsymbol{G}}_U[\boldsymbol{\Sigma}]$), while the right-hand side is independent of $\boldsymbol{U}$ but depends on $\boldsymbol{\lambda}$ via $\boldsymbol{G}_{\boldsymbol{\lambda},0}^{-1}$.

The obvious problem of finding a solution of Eq. (3.14) is that there is no closed form for the functional $\widehat{\boldsymbol{G}}_U[\boldsymbol{\Sigma}]$. Solving Eq. (3.14) is equivalent, however, to a search for the stationary point of the grand potential as a functional of the self-energy:

$$\frac{\delta \widehat{\Omega}_{\boldsymbol{\lambda},U}[\boldsymbol{\Sigma}]}{\delta \boldsymbol{\Sigma}} = 0 \, . \tag{3.15}$$

This equation is the starting point for nonequilibrium self-energy functional theory.

Note that, while there are various symmetry relations between the elements $\Sigma_{\alpha\alpha'}(z,z')$ of the self-energy at different times z and z', the elements of $\boldsymbol{\Sigma}$ have to be treated as *independent of each other* for the functional differentiation to ensure the equivalence of the variational principle Eq. (3.15) with the fundamental Dyson equation Eq. (3.14). As will become clear below, the stationarity with respect to some of the variational directions just ensures the correct symmetry relations between the elements of $\Sigma_{\alpha\alpha'}(z,z')$, while the other variational directions fix the actual value of $\Sigma_{\alpha\alpha'}(z,z')$.
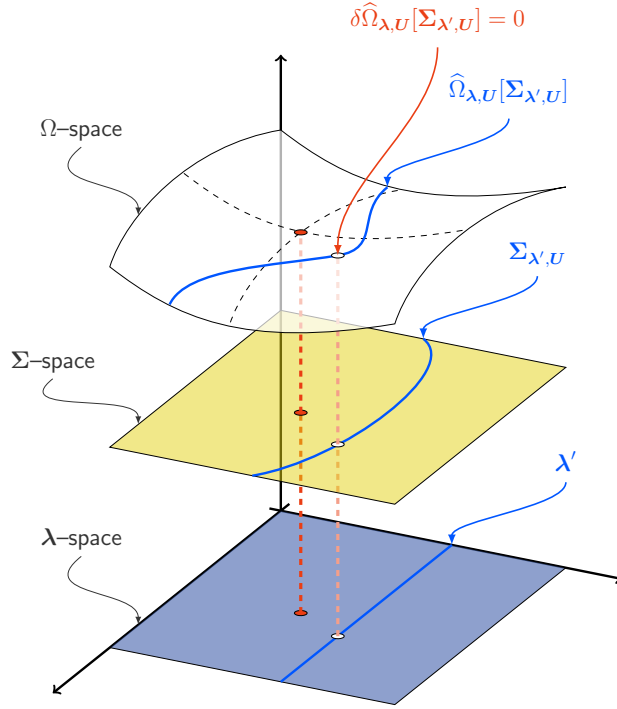
Figure 3.1: Variation of the self-energy functional $\widehat{\Omega}_{\boldsymbol{\lambda},\boldsymbol{U}}$ on the restricted space of trial self-energies $\boldsymbol{\Sigma}_{\boldsymbol{\lambda'},\boldsymbol{U}}$, spanned by a certain reference system characterized by its one particle parameters $\boldsymbol{\lambda'}$. For a detailed discussion, see text.

3.3 Constructing approximations

Even though the Luttinger-Ward functional and its Legendre transform $\widehat{F}_{\boldsymbol{U}}[\boldsymbol{\Sigma}]$ are generally unknown, it is possible to evaluate the self-energy functional Eq. (3.11) exactly on a certain subspace of self-energies: To this end we compare the self-energy functional of the original system with the self-energy functional of a reference system, given by a Hamiltonian $H' \equiv H_{\boldsymbol{\lambda'},\boldsymbol{U}}$, which differs from the original Hamiltonian $H_{\boldsymbol{\lambda},\boldsymbol{U}}$ only in its one-particle parameters $\boldsymbol{\lambda'}$, but shares its interaction part. Here and in the following, primed quantities refer to the reference system. The respective self-energy functional is

$$\widehat{\Omega}_{\boldsymbol{\lambda'},\boldsymbol{U}}[\boldsymbol{\Sigma}] = \frac{1}{\beta}\operatorname{Tr}\ln\left(\boldsymbol{G}_{\boldsymbol{\lambda'},0}^{-1} - \boldsymbol{\Sigma}\right)^{-1} + \widehat{F}_{\boldsymbol{U}}[\boldsymbol{\Sigma}]\,. \tag{3.16}$$

Since $\widehat{F}_{\boldsymbol{U}}[\boldsymbol{\Sigma}]$ is universal, we can eliminate $\widehat{F}_{\boldsymbol{U}}[\boldsymbol{\Sigma}]$ and write

$$\widehat{\Omega}_{\boldsymbol{\lambda},\boldsymbol{U}}[\boldsymbol{\Sigma}] = \widehat{\Omega}_{\boldsymbol{\lambda'},\boldsymbol{U}}[\boldsymbol{\Sigma}] + \frac{1}{\beta}\operatorname{Tr}\ln\left(\boldsymbol{G}_{\boldsymbol{\lambda},0}^{-1} - \boldsymbol{\Sigma}\right)^{-1} - \frac{1}{\beta}\operatorname{Tr}\ln\left(\boldsymbol{G}_{\boldsymbol{\lambda'},0}^{-1} - \boldsymbol{\Sigma}\right)^{-1}\,. \tag{3.17}$$

The previous expression is still exact, but the self-energy functional for the reference system is not available in a closed form, even for very simple cases, as e.g. the atomic

limit of the Hubbard model. However, we can nevertheless make use of Eq. (3.17), if both the exact self-energy $\boldsymbol{\Sigma}_{\boldsymbol{\lambda}',U}$ and the self-energy functional of the reference system, evaluated at the exact self-energy, i.e., $\widehat{\Omega}_{\boldsymbol{\lambda}',U}[\boldsymbol{\Sigma}_{\boldsymbol{\lambda}',U}] = \Omega_{\boldsymbol{\lambda}',U}$, are accessible. Using Dyson's equation (2.33) for the reference system, we find for the self-energy functional of the original system if evaluated at a trial self-energy taken from the reference system and parametrized by the set of variational parameters $\boldsymbol{\lambda}'$:

$$\widehat{\Omega}_{\boldsymbol{\lambda},U}[\boldsymbol{\Sigma}_{\boldsymbol{\lambda}',U}] = \Omega_{\boldsymbol{\lambda}',U} + \frac{1}{\beta} \operatorname{Tr} \ln \left(\boldsymbol{G}_{\boldsymbol{\lambda},0}^{-1} - \boldsymbol{\Sigma}_{\boldsymbol{\lambda}',U} \right)^{-1} - \frac{1}{\beta} \operatorname{Tr} \ln \left(\boldsymbol{G}_{\boldsymbol{\lambda}',U} \right) . \qquad (3.18)$$

This shows that an exact evaluation of the general nonequilibrium self-energy functional is possible on the restricted space of trial self-energies spanned by any reference system with the same interaction part, provided that the contour-ordered self-energy and Green's function as well as the initial-state grand potential of the reference system can be computed exactly.

The time-dependent optimal variational parameters $\boldsymbol{\lambda}'_{\mathrm{opt}}(z)$ have to be determined via the Euler equation (for a schematic illustration see Fig. 3.1):

$$\left. \frac{\delta \widehat{\Omega}_{\boldsymbol{\lambda},U}[\boldsymbol{\Sigma}_{\boldsymbol{\lambda}',U}]}{\delta \boldsymbol{\lambda}'(z)} \right|_{\boldsymbol{\lambda}'(z)=\boldsymbol{\lambda}'_{\mathrm{opt}}(z)} = 0 . \qquad (3.19)$$

We thus have (approximate) access to the initial-state grand potential $\widehat{\Omega}_{\boldsymbol{\lambda},U}[\boldsymbol{\Sigma}_{\boldsymbol{\lambda}'_{\mathrm{opt}},U}]$ as well as to the final-state dynamics via the one-particle Green's function

$$\boldsymbol{G}^{\mathrm{SFT}} \equiv (\boldsymbol{G}_{\boldsymbol{\lambda},0}^{-1} - \boldsymbol{\Sigma}_{\boldsymbol{\lambda}'_{\mathrm{opt}},U})^{-1} \qquad (3.20)$$

on the Keldysh branch. The choice of the reference system specifies the type of approximation. Approximations generated in this way are nonperturbative by construction.

The Hamiltonian $H_{\boldsymbol{\lambda}',U}$ of the reference system must have the same interaction part as the one of the original system and, for any practical application, must allow for an exact calculation of the trial self-energy $\boldsymbol{\Sigma}_{\boldsymbol{\lambda}',U}$ and of the Green's function $\boldsymbol{G}_{\boldsymbol{\lambda}',U}$ by analytical or numerical means. Typically, this is achieved by cutting the original lattice into disconnected clusters with a small number of sites L_c (Fig. 3.2). To enlarge the number of variational degrees of freedom locally without changing the interaction part, a number L_b of uncorrelated "bath sites" may be coupled to each of the reference system's correlated sites via a finite hybridization. To formally assure equal Hilbert space dimensions in the original and in the reference system, bath sites are included in the original system as well but without a coupling to the physical sites (Fig. 3.2). In the case of a local (Hubbard-type) interaction and for sufficiently small L_c and L_b, the reference system can be treated by exact-diagonalization techniques. This comprises rather different approximations like the variational cluster approach (VCA) with a finite number of correlated sites but without any additional bath sites ($0 < L_c < \infty$, $L_b = 0$) or the dynamical impurity approximation (DIA), for which a finite number of bath sites is coupled to a single correlated site ($L_c = 1$, $0 < L_b < \infty$). We will apply both approximations in chapter 5 or 6 respectively.

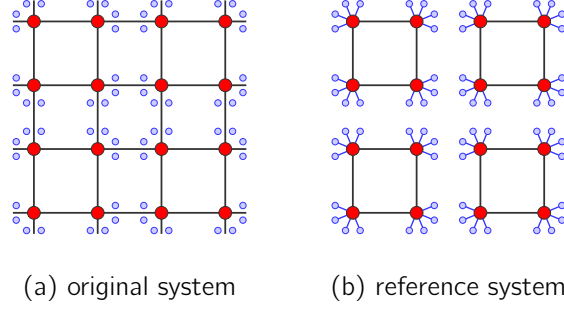(a) original system   (b) reference system

Figure 3.2: Schematic representation of (a) the original system and of (b) a generic reference system. Large red circles: correlated sites with Hubbard-like local interaction U. Small blue circles: uncorrelated "bath" sites, i.e., $U = 0$. Bold black lines: intra-cluster hopping. Thin blue lines: hybridization, i.e., hopping between correlated and bath sites in the reference system. Note that in the original system (a) bath sites are decoupled from the correlated ones. Their presence is helpful for formal reasons to ensure equal Hilbert space dimensions in (a) and (b).

3.4 Relation to dynamical mean-field theory

Nonequilibrium dynamical mean-field theory is recovered within the SFT framework when we choose the reference system as a set of completely decoupled correlated sites ($L_c = 1$) with an infinite number of bath sites ($L_b = \infty$), i.e., as a set of decoupled single-impurity Anderson models. For $L_c = 1$ the trial self-energies are local, i.e., diagonal with respect to the spatial indices, and the Euler equation (3.19) thus explicitly reads as:

$$
\begin{aligned}
0 &= \frac{\delta \widehat{\Omega}_{\boldsymbol{\lambda},U}[\boldsymbol{\Sigma}_{\boldsymbol{\lambda}',U}]}{\delta \boldsymbol{\lambda}'(z)} \\
&= \frac{1}{\beta} \sum_{i,\sigma_1\sigma_2} \int_{\mathcal{C}} dz_1 dz_2 \left(\left(\boldsymbol{G}_{\boldsymbol{\lambda},0}^{-1} - \boldsymbol{\Sigma}_{\boldsymbol{\lambda}',U} \right)^{-1} - \boldsymbol{G}_{\boldsymbol{\lambda}',U} \right)_{ii,\sigma_1\sigma_2} (z_1, z_2) \times \\
&\qquad\qquad\qquad\qquad\qquad \times \frac{\delta \Sigma_{\boldsymbol{\lambda}',U;ii,\sigma_2\sigma_1}(z_2, z_1^+)}{\delta \boldsymbol{\lambda}'(z)} \, . \quad (3.21)
\end{aligned}
$$

Equation (3.21) would be trivially satisfied if the bracket in the integrand vanished, which would be nothing but the standard self-consistency equation of DMFT [113, 131, 132]. Thus any solution of the (nonequilibrium) DMFT represents a stationary point of the SFT – provided that the DMFT self-energy can be represented as the self-energy $\boldsymbol{\Sigma}_{\boldsymbol{\lambda}',U}$ of a single-impurity Anderson Hamiltonian with single-particle (bath) parameters $\boldsymbol{\lambda}'$. The representability of the DMFT action by an actual impurity Hamiltonian with $L_b = \infty$ is not straightforward to see for nonequilibrium Green's functions but can be shown under rather general conditions [154].

When one considers finite single-impurity models with a small number of bath orbitals, the bracket in Eq. (3.21) will in general not vanish because the discrete pole structure of
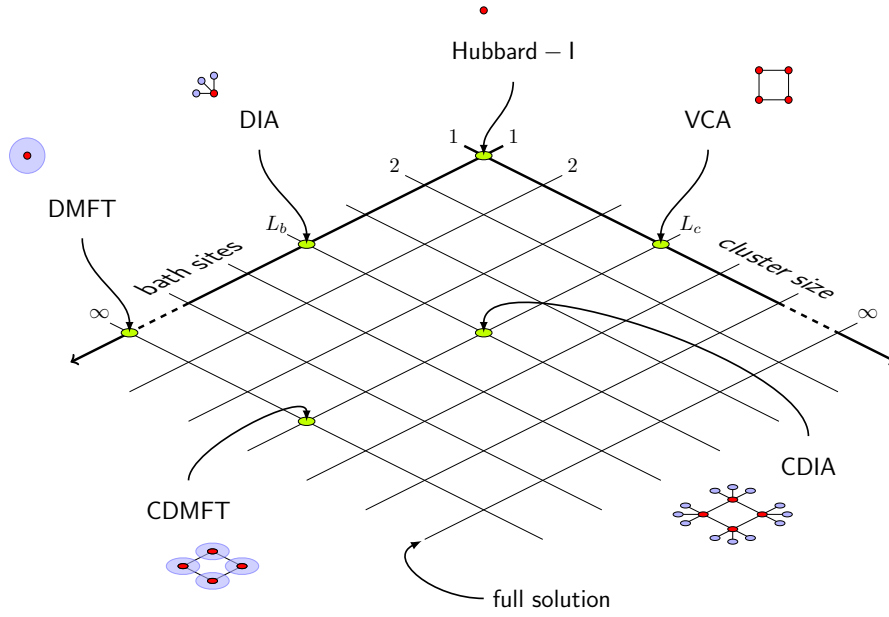
Figure 3.3: Summary of various approximations accessible within the SFT by choice of the reference system. The most simplest one represented by the Hubbard-I approximation is attained by a single correlated site $L_c = 1$. By considering larger clusters $L_c > 1$ this is extended to variational cluster approaches (VCA). Coupling a finite set of uncorrelated bath sites $L_b > 0$ to the single correlated site yields dynamical impurity approximations (DIA) and in the limit of a continuous bath $L_b \to \infty$ the DMFT is recovered. A combination of both leads to the cellular variants of the DIA or the DMFT. For reference clusters as large as the original system, the full solution is formally contained in the space of variational parameters, as indicated by the most right line at $L_c \to \infty$. For the small pictograms representing the reference system the same convention as in Fig. 3.2 is used and the blue shaded circles stand for continuous baths.

the impurity Green's function cannot be reconciled with the branch cuts of the Green's function for the original model. Due to the presence of the projector $\delta\Sigma_{\boldsymbol{\lambda}'}/\delta\boldsymbol{\lambda}'$, however, stationarity of the self-energy functional is nevertheless possible. This allows to generate nonperturbative and consistent approximations to DMFT by solving reference systems with a few degrees of freedom only. In the equilibrium case, this has been shown to be a highly efficient strategy (see, e.g., Refs. [171, 174]). Furthermore, we shall note that by choosing a cluster of correlated sites coupled to a continuous bath, the above arguments extend to the cellular DMFT (C-DMFT) in complete analogy.

3.5 Physical and transverse variations

The variational problem, Eq. (3.19), is posed on the whole contour $\mathcal{C}$, i.e., the self-energy functional must be stationary with respect to variations of the parameters $\boldsymbol{\lambda}'(z)$

separately on the Matsubara branch and on both branches of the Keldysh contour. This generates one imaginary-time and two independent real-time Euler equations which are obtained by writing $\widehat{\Omega}_{\boldsymbol{\lambda},\boldsymbol{U}}[\boldsymbol{\Sigma}_{\boldsymbol{\lambda}',\boldsymbol{U}}] \equiv \widehat{\Omega}_{\boldsymbol{\lambda},\boldsymbol{U}}[\boldsymbol{\Sigma}_{\boldsymbol{\lambda}'_{\vee},\boldsymbol{\lambda}'_{\wedge},\boldsymbol{\lambda}'_{\mathrm{M}},\boldsymbol{U}}]$ as a functional of the single particle parameters $\boldsymbol{\lambda}_{\vee\wedge}(t)$ on the upper/lower branch of the contour (for real t), as well as of the parameters $\boldsymbol{\lambda}'_{\mathrm{M}}(t_0 - i\tau)$ on the Matsubara branch. Using a simple transformation of variables,

$$
\begin{aligned}
\boldsymbol{\lambda}'_{\mathrm{phys}}(t) &= \frac{1}{2}(\boldsymbol{\lambda}'_{\vee}(t) + \boldsymbol{\lambda}'_{\wedge}(t)) \,, \\
\boldsymbol{\lambda}'_{\mathrm{trans}}(t) &= \frac{1}{2}(\boldsymbol{\lambda}'_{\vee}(t) - \boldsymbol{\lambda}'_{\wedge}(t)) \,,
\end{aligned}
\tag{3.22}
$$

the real-time equations become equivalent to

$$
\frac{\delta\widehat{\Omega}_{\boldsymbol{\lambda},\boldsymbol{U}}[\boldsymbol{\Sigma}_{\boldsymbol{\lambda}'_{\mathrm{phys}},\boldsymbol{\lambda}'_{\mathrm{trans}},\boldsymbol{\lambda}'_{\mathrm{M}},\boldsymbol{U}}]}{\delta\boldsymbol{\lambda}'_{\mathrm{phys/trans}}(t)} = 0 \,.
\tag{3.23}
$$

The separation into variations with respect to $\boldsymbol{\lambda}'_{\mathrm{phys}}$ ("physical variations") and $\boldsymbol{\lambda}'_{\mathrm{trans}}$ ("transverse variations") has a simple motivation: In the end, we are only interested in solutions of the Euler equation by a physical parameter set $\boldsymbol{\lambda}'(z)$, i.e., one that corresponds to an actual *Hamiltonian*. These parameters must thus satisfy $\boldsymbol{\lambda}'_{\vee}(t) = \boldsymbol{\lambda}'_{\wedge}(t)$, i.e., $\boldsymbol{\lambda}'_{\mathrm{trans}}(t) = 0$. In addition, $\boldsymbol{\lambda}'_M(t_0 - i\tau)$ must not depend on imaginary time (this is discussed in Sec. 3.7). Transverse variations $\delta\boldsymbol{\lambda}'_{\mathrm{trans}}(t) \neq 0$ shift the parameters away from the physical manifold, while physical variations remain therein.

Let us first consider variations of $\boldsymbol{\lambda}'_{\mathrm{phys}}(t)$. Interestingly, one can show that the self-energy functional is always stationary with respect to physical variations when evaluated at a physical parameter set, which satisfies $\boldsymbol{\lambda}'_{\mathrm{trans}}(t) = 0$, i.e.,

$$
\left.\frac{\delta\widehat{\Omega}_{\boldsymbol{\lambda},\boldsymbol{U}}[\boldsymbol{\Sigma}_{\boldsymbol{\lambda}'_{\mathrm{phys}},\boldsymbol{\lambda}'_{\mathrm{trans}},\boldsymbol{\lambda}'_{\mathrm{M}},\boldsymbol{U}}]}{\delta\boldsymbol{\lambda}'_{\mathrm{phys}}(t)}\right|_{\boldsymbol{\lambda}'_{\mathrm{trans}}(t)=0} = 0 \,.
\tag{3.24}
$$

To prove Eq. (3.24), we first recall that any function of contour functions (2.25) is unchanged when the largest time-argument on the Keldysh contour is shifted from the upper to the lower branch, see Eq. (2.14). Furthermore, with Eq. (2.26) it is easy to see that in the expression (3.5) for the trace all integrations over the Keldysh branch cancel for any function with the symmetry (2.14) [see also Eq. 2.25]. Thus the self-energy functional (3.11), when evaluated at physical parameters, depends on the Matsubara part of $\boldsymbol{\Sigma}_{\boldsymbol{\lambda}',\boldsymbol{U}}$ only. This immediately implies the stationarity condition (3.24).

Stationarity with respect to physical variations locally restricts the solution to the physical manifold. Thus, a second equation is needed to fix the solution within the physical manifold. This "second" equation is given by the condition that the self-energy functional be stationary with respect to the transverse variations, if evaluated at a physical parameter set:

$$
\left.\frac{\delta\widehat{\Omega}_{\boldsymbol{\lambda},\boldsymbol{U}}[\boldsymbol{\Sigma}_{\boldsymbol{\lambda}'_{\mathrm{phys}},\boldsymbol{\lambda}'_{\mathrm{trans}},\boldsymbol{\lambda}'_{\mathrm{M}},\boldsymbol{U}}]}{\delta\boldsymbol{\lambda}'_{\mathrm{trans}}(t)}\right|_{\boldsymbol{\lambda}'_{\mathrm{trans}}(t)=0} = 0 \,.
\tag{3.25}
$$

Equation (3.25) is the central equation of the nonequilibrium SFT.

Let us stress once more that the functional derivative with respect to $\boldsymbol{\lambda}'_{\text{trans}}(t)$ is a derivative into a "nonphysical" direction in parameter space. This has important conceptual consequences for the numerical evaluation of the theory. In the vast majority of previous *equilibrium* SFT studies, the grand potential $\widehat{\Omega}_{\boldsymbol{\lambda},U}[\boldsymbol{\Sigma}_{\boldsymbol{\lambda}',U}]$ has been computed for different (static) parameter sets $\boldsymbol{\lambda}'$, and algorithms to find a stationary point of a multi-dimensional scalar function $\boldsymbol{\lambda}' \mapsto \widehat{\Omega}_{\boldsymbol{\lambda},U}[\boldsymbol{\Sigma}_{\boldsymbol{\lambda}',U}]$ have been employed (see Ref. [209], for example). In the nonequilibrium case, a similar strategy would require to work explicitly with Green's functions that are defined with a different Hamiltonian for the forward and backward time-evolution. A more convenient strategy, which is worked out in the following, is to carry out the functional derivative analytically and to solve the resulting Euler equation by numerical means. The analytical expressions for the functional derivatives are then given by higher order correlation functions evaluated at the physical parameters.

3.6 Evaluation of the Euler equation

We focus on Eq. (3.18) again and perform the functional derivative in Eq. (3.19) analytically. This is most conveniently done by considering the variational parameters as functions of the contour variable, i.e., $\boldsymbol{\lambda}'(z)$ with $z \in \mathcal{C}$, instead of treating $\boldsymbol{\lambda}_{\vee\wedge}(t)$ and $\boldsymbol{\lambda}_{\text{M}}(t_0 - i\tau)$ separately.

Using the chain rule, we find:

$$\frac{\delta\widehat{\Omega}_{\boldsymbol{\lambda},U}[\boldsymbol{\Sigma}_{\boldsymbol{\lambda}',U}]}{\delta\lambda'_{\alpha_1\alpha_2}(z)} = \text{Tr}\left(\frac{\delta\widehat{\Omega}_{\boldsymbol{\lambda},U}[\boldsymbol{\Sigma}_{\boldsymbol{\lambda}',U}]}{\delta\boldsymbol{\Sigma}_{\boldsymbol{\lambda}',U}} \circ \frac{\delta\boldsymbol{\Sigma}_{\boldsymbol{\lambda}',U}}{\delta\lambda'_{\alpha_1\alpha_2}(z)}\right). \tag{3.26}$$

The first factor is given by Eq. (3.13) but can be rewritten in a more convenient way. We define the difference between the one-particle parameters of the original and of the reference system as

$$\boldsymbol{\Lambda}(z) = \boldsymbol{\lambda}(z) - \boldsymbol{\lambda}'(z), \tag{3.27}$$

which immediately leads to the following relation of the respective free Green's functions [see Eq. 2.31]

$$G_{\boldsymbol{\lambda}',0}^{-1}(1,2) = G_{\boldsymbol{\lambda},0}^{-1}(1,2) + \delta_{\mathcal{C}}(z_1,z_2)\Lambda_{\alpha_1\alpha_2}(z_2). \tag{3.28}$$

With this and with Dyson's equation for the reference system we get

$$\begin{aligned}G_{\boldsymbol{\lambda},0}^{-1}(1,2) - \Sigma_{\boldsymbol{\lambda}',U}(1,2) &= G_{\boldsymbol{\lambda}',0}^{-1}(1,2) - \delta_{\mathcal{C}}(z_1,z_2)\Lambda_{\alpha_1\alpha_2}(z_2) - \Sigma_{\boldsymbol{\lambda}',U}(1,2) \\ &= G_{\boldsymbol{\lambda}',U}^{-1}(1,2) - \delta_{\mathcal{C}}(z_1,z_2)\Lambda_{\alpha_1\alpha_2}(z_2).\end{aligned} \tag{3.29}$$

Plugged into the definition of the SFT Green's function, Eq. (3.20), we get the following Dyson-like equation [cf. Eqs. 2.33 and 2.34]

$$\boldsymbol{G}^{\text{SFT}} = \boldsymbol{G}_{\boldsymbol{\lambda}',U} + \boldsymbol{G}_{\boldsymbol{\lambda}',U}\boldsymbol{\Lambda} \circ \boldsymbol{G}^{\text{SFT}}, \tag{3.30}$$

which constitutes the nonequilibrium cluster-perturbation theory [160]. One may formally resort the perturbative expansion of the preceding Eq. (3.30), i.e.,

$$\boldsymbol{G}^{\mathrm{SFT}} = \boldsymbol{G}_{\boldsymbol{\lambda}',\boldsymbol{U}} + \boldsymbol{G}_{\boldsymbol{\lambda}',\boldsymbol{U}}\boldsymbol{\Lambda}\circ\boldsymbol{G}_{\boldsymbol{\lambda}',\boldsymbol{U}} + \boldsymbol{G}_{\boldsymbol{\lambda}',\boldsymbol{U}}\boldsymbol{\Lambda}\circ\boldsymbol{G}_{\boldsymbol{\lambda}',\boldsymbol{U}}\boldsymbol{\Lambda}\circ\boldsymbol{G}_{\boldsymbol{\lambda}',\boldsymbol{U}} + \dots \tag{$\star$}$$

$$= \boldsymbol{G}_{\boldsymbol{\lambda}',\boldsymbol{U}} + \boldsymbol{G}_{\boldsymbol{\lambda}',\boldsymbol{U}}\left[\boldsymbol{\Lambda} + \boldsymbol{\Lambda}\circ\boldsymbol{G}_{\boldsymbol{\lambda}',\boldsymbol{U}}\boldsymbol{\Lambda} + \dots\right]\circ\boldsymbol{G}_{\boldsymbol{\lambda}',\boldsymbol{U}}$$

$$= \boldsymbol{G}_{\boldsymbol{\lambda}',\boldsymbol{U}} + \boldsymbol{G}_{\boldsymbol{\lambda}',\boldsymbol{U}}\left[\boldsymbol{\Lambda} + \boldsymbol{\Lambda}\circ\left(\boldsymbol{G}_{\boldsymbol{\lambda}',\boldsymbol{U}} + \boldsymbol{G}_{\boldsymbol{\lambda}',\boldsymbol{U}}\boldsymbol{\Lambda}\circ\boldsymbol{G}_{\boldsymbol{\lambda}',\boldsymbol{U}} + \dots\right)\boldsymbol{\Lambda}\right]\circ\boldsymbol{G}_{\boldsymbol{\lambda}',\boldsymbol{U}}$$

$$\overset{(\star)}{=} \boldsymbol{G}_{\boldsymbol{\lambda}',\boldsymbol{U}} + \boldsymbol{G}_{\boldsymbol{\lambda}',\boldsymbol{U}}\left[\boldsymbol{\Lambda} + \boldsymbol{\Lambda}\circ\boldsymbol{G}^{\mathrm{SFT}}\boldsymbol{\Lambda}\right]\circ\boldsymbol{G}_{\boldsymbol{\lambda}',\boldsymbol{U}}\,, \tag{3.31}$$

and define the T-matrix as

$$\boldsymbol{Y}_{\boldsymbol{\lambda}',\boldsymbol{\lambda},\boldsymbol{U}}(z_1,z_2) = \boldsymbol{\Lambda}(z_1)\delta_{\mathcal{C}}(z_1,z_2) + \boldsymbol{\Lambda}(z_1)\boldsymbol{G}^{\mathrm{SFT}}(z_1,z_2)\boldsymbol{\Lambda}(z_2)\,, \tag{3.32}$$

to arrive at the related Lippmann-Schwinger equation

$$\boldsymbol{G}^{\mathrm{SFT}} = \boldsymbol{G}_{\boldsymbol{\lambda}',\boldsymbol{U}} + \boldsymbol{G}_{\boldsymbol{\lambda}',\boldsymbol{U}}\circ\boldsymbol{Y}_{\boldsymbol{\lambda}',\boldsymbol{\lambda},\boldsymbol{U}}\circ\boldsymbol{G}_{\boldsymbol{\lambda}',\boldsymbol{U}}\,. \tag{3.33}$$

This eventually yields

$$\frac{\delta\widehat{\Omega}_{\boldsymbol{\lambda},\boldsymbol{U}}[\boldsymbol{\Sigma}_{\boldsymbol{\lambda}',\boldsymbol{U}}]}{\delta\boldsymbol{\Sigma}_{\boldsymbol{\lambda}',\boldsymbol{U}}} = \frac{1}{\beta}\boldsymbol{G}_{\boldsymbol{\lambda}',\boldsymbol{U}}\circ\boldsymbol{Y}_{\boldsymbol{\lambda}',\boldsymbol{\lambda},\boldsymbol{U}}\circ\boldsymbol{G}_{\boldsymbol{\lambda}',\boldsymbol{U}} \tag{3.34}$$

for the first factor in Eq. (3.26).

To evaluate the second factor, the Dyson equation for the reference system is used once more to get $\boldsymbol{\Sigma}_{\boldsymbol{\lambda}',\boldsymbol{U}} = \boldsymbol{G}_{\boldsymbol{\lambda}',0}^{-1} - \boldsymbol{G}_{\boldsymbol{\lambda}',\boldsymbol{U}}^{-1}$. The $\boldsymbol{\lambda}'$-dependence of the inverse free Green's function is simple and given by $G_{\boldsymbol{\lambda}',0}^{-1}(1,2) = \delta_{\mathcal{C}}(z_1,z_2)\delta_{\alpha_1,\alpha_2}i\partial_{z_2} - \delta_{\mathcal{C}}(z_1,z_2)(\lambda'_{\alpha_1\alpha_2}(z_2) - \delta_{\alpha_1\alpha_2}\mu)$ [see Eq. 2.31]. We thus get:

$$\frac{\delta\Sigma_{\boldsymbol{\lambda}',\boldsymbol{U}}(3,4)}{\delta\lambda'_{\alpha_1\alpha_2}(z_1)} = -\delta_{\mathcal{C}}(z_3,z_4)\delta_{\alpha_3\alpha_1}\delta_{\mathcal{C}}(z_4,z_1)\delta_{\alpha_4\alpha_2}$$

$$+ \iint d5d6\, G_{\boldsymbol{\lambda}',\boldsymbol{U}}^{-1}(3,5)\frac{\delta G_{\boldsymbol{\lambda}',\boldsymbol{U}}(5,6)}{\delta\lambda'_{\alpha_1\alpha_2}(z_1)}G_{\boldsymbol{\lambda}',\boldsymbol{U}}^{-1}(6,4)\,. \tag{3.35}$$

The functional derivative of the Green's function is straightforwardly obtained by making use of the properties of the time ordering operator and the exponential function and reads

$$\frac{\delta G_{\boldsymbol{\lambda}',\boldsymbol{U}}(5,6)}{\delta\lambda_{\alpha_1\alpha_2}(z_3)} = G_{\boldsymbol{\lambda}',\boldsymbol{U}}(5,6)\, G_{\boldsymbol{\lambda}',\boldsymbol{U}}(2,1^+)\Big|_{z_2=z_1} - G_{\boldsymbol{\lambda}',\boldsymbol{U}}^{(2)}(5,2,1^+,6)\Big|_{z_2=z_1}\,, \tag{3.36}$$

where $\boldsymbol{G}_{\boldsymbol{\lambda}',\boldsymbol{U}}^{(2)}$ is the two-particle Green's function of the reference system.

Combining this with Eq. (3.34), we finally get the derivative of the self-energy functional with respect to $\boldsymbol{\lambda}'(z_1)$ in the form:

$$\frac{\delta\widehat{\Omega}_{\boldsymbol{\lambda},\boldsymbol{U}}[\boldsymbol{\Sigma}_{\boldsymbol{\lambda}',\boldsymbol{U}}]}{\delta\lambda'_{\alpha_1\alpha_2}(z_1)} = -\frac{1}{\beta}\iint d3d4\, Y_{\boldsymbol{\lambda}',\boldsymbol{\lambda},\boldsymbol{U}}(4,3)\, L_{\boldsymbol{\lambda}',\boldsymbol{U}}(3,2,1^+,4)\Big|_{z_2=z_1}\,, \tag{3.37}$$

where

$$L_{\boldsymbol{\lambda}',\boldsymbol{U}}(1,2,3,4) = G_{\boldsymbol{\lambda}',\boldsymbol{U}}(2,4)G_{\boldsymbol{\lambda}',\boldsymbol{U}}(1,3)$$
$$- G_{\boldsymbol{\lambda}',\boldsymbol{U}}(1,4)G_{\boldsymbol{\lambda}',\boldsymbol{U}}(2,3) + G^{(2)}_{\boldsymbol{\lambda}',\boldsymbol{U}}(1,2,3,4) \quad (3.38)$$

is the two-particle (four-point) vertex function with external legs.

Therewith, we have the Euler equation of the nonequilibrium SFT

$$K^{(0)}[\boldsymbol{\lambda}']_{\alpha_2\alpha_1}(t_1) := \iint d3\,d4\, Y_{\boldsymbol{\lambda}'_{\mathrm{opt}},\boldsymbol{\lambda},\boldsymbol{U}}(4,3)\, L_{\boldsymbol{\lambda}'_{\mathrm{opt}},\boldsymbol{U}}(3,2,1^+,4)\Big|_{z_2=z_1=t_1} = 0\,, \quad (3.39)$$

which after the functional derivative with respect to $\boldsymbol{\lambda}'$ has been carried out, can be evaluated on the *physical* parameter-space, made explicit by the dependence on the *physical* time t_1 in the above equation. This result will be needed both for the numerical determination of the stationary point and for working out the relation between nonequilibrium and conventional equilibrium SFT. Note that for brevity we defined a new functional $\boldsymbol{K}^{(0)}[\boldsymbol{\lambda}'] = -\beta\delta\widehat{\Omega}_{\boldsymbol{\lambda},\boldsymbol{U}}[\boldsymbol{\Sigma}_{\boldsymbol{\lambda}',\boldsymbol{U}}]/\delta\boldsymbol{\lambda}'$.

3.7 Thermal equilibrium and initial state

Nonequilibrium SFT reduces to the conventional equilibrium formalism for a system where $\boldsymbol{\lambda}(z)$ and $\boldsymbol{U}(z)$ are constant on the entire contour $\mathcal{C}$, i.e., for the case $H(t) = \mathrm{const.} = H(t_0)$. To prove this fact explicitly, we have to show that a stationary point of the equilibrium SFT functional, which determines *time-independent* optimal parameters $\boldsymbol{\lambda}'_{\mathrm{opt}}$, is also a stationary point of the more general nonequilibrium Euler equation (3.19), i.e., of Eq. (3.39), when $\boldsymbol{\lambda}(z)$ and $\boldsymbol{U}(z)$ are constant.

Equilibrium SFT is obtained from the more general nonequilibrium formalism by restricting the functional (3.18) to the Matsubara branch of the contour, and furthermore, by considering time-independent and physical variations only, i.e., the trial self-energy $\boldsymbol{\Sigma}_{\boldsymbol{\lambda}',\boldsymbol{U}}$ is obtained as the Matsubara self-energy of a Hamiltonian with constant parameters $\boldsymbol{\lambda}'$, and the parameters are varied to make $\widehat{\Omega}_{\boldsymbol{\lambda},\boldsymbol{U}}[\boldsymbol{\Sigma}_{\boldsymbol{\lambda}',\boldsymbol{U}}]$ stationary. In the language of the more general nonequilibrium SFT formalism, those variations correspond to a variation $\delta\boldsymbol{\lambda}(z)$ which is constant along the whole contour, i.e.,

$$\frac{\partial\widehat{\Omega}_{\boldsymbol{\lambda},\boldsymbol{U}}[\boldsymbol{\Sigma}_{\boldsymbol{\lambda}',\boldsymbol{U}}]}{\partial\boldsymbol{\lambda}'} = \int_{\mathcal{C}} dz\, \frac{\delta\widehat{\Omega}_{\boldsymbol{\lambda},\boldsymbol{U}}[\boldsymbol{\Sigma}_{\boldsymbol{\lambda}',\boldsymbol{U}}]}{\delta\boldsymbol{\lambda}'(z)}\,. \quad (3.40)$$

Note that the integrations over the upper and lower branch of the Keldysh contour cancel, as discussed in connection with Eq. (3.24) and shown for Eq. (2.26). We now suppose that the original Hamiltonian is time-independent, and that $\boldsymbol{\lambda}'_{\mathrm{opt}}$ is a solution of the equilibrium SFT formalism, i.e., the single variational equation $\partial\widehat{\Omega}_{\boldsymbol{\lambda},\boldsymbol{U}}[\boldsymbol{\Sigma}_{\boldsymbol{\lambda}',\boldsymbol{U}}]/\partial\boldsymbol{\lambda}'|_{\boldsymbol{\lambda}'_{\mathrm{opt}}} = 0$ is satisfied.

To see that the parameters $\boldsymbol{\lambda}'_{\mathrm{opt}}$ also represent a solution of the nonequilibrium SFT, we must show that all other variations, including physical, transverse, and Matsubara

ones, vanish as well. For this it is sufficient to show that the general variational equation becomes time-translationally invariant, i.e., that the expression

$$
\left. \frac{\delta\widehat{\Omega}_{\boldsymbol{\lambda},U}[\boldsymbol{\Sigma}_{\boldsymbol{\lambda}',U}]}{\delta\boldsymbol{\lambda}'(z)} \right|_{\boldsymbol{\lambda}'(z)=\boldsymbol{\lambda}'_{\text{opt}}}
\tag{3.41}
$$

does not depend on z.

Consider a time z on the Matsubara branch first. Invariance under translations of imaginary time is most easily seen from the explicit expression (3.37) for the variational derivative: For $z_1 = t_0 - i\tau_1$, the integrals in Eq. (3.37) reduce to the Matsubara branch. Furthermore, the two functions $\boldsymbol{L}$ and $\boldsymbol{Y}$ in the integrand are translationally invariant in imaginary time as they are evaluated at τ-independent parameters $\boldsymbol{\lambda}'$. More precisely, we can write $\boldsymbol{L}(\tau_3, \tau_1, \tau_1^+, \tau_4) \equiv \tilde{\boldsymbol{L}}(\tau_3 - \tau_1, \tau_4 - \tau_1)$ and $\boldsymbol{Y}(\tau_3, \tau_4) \equiv \tilde{\boldsymbol{Y}}(\tau_3 - \tau_4)$ with functions $\tilde{\boldsymbol{L}}$ and $\tilde{\boldsymbol{Y}}$ that are anti-periodic under $\tau \to \tau + \beta$. After a shift of variables it is easily seen that the integral in Eq. (3.37) does not depend on z_1.

For z_1 on the Keldysh branch, on the other hand, time-translational invariance of Eq. (3.41) can be seen from a Lehmann representation (or spectral representation) of the functions $\boldsymbol{L}$ and $\boldsymbol{Y}$. The explicit calculation is more tedious and presented in the following. To this end, we start with Eq. (3.37) and make all contour integrations explicit:

$$
-\beta \frac{\delta\widehat{\Omega}_{\boldsymbol{\lambda},U}[\boldsymbol{\Sigma}_{\boldsymbol{\lambda}',U}]}{\delta\lambda'_{\alpha_1\alpha_2}(t_1)} =
$$

$$
= \int d3 \int d4 \; Y_{\boldsymbol{\lambda}',\boldsymbol{\lambda},U}(4,3) L_{\boldsymbol{\lambda}',U}(3,2,1^+,4) \Big|_{z_2=z_1=t_1}
$$

$$
= \sum_{\alpha_3\alpha_4} \int dz_3 \, Y_{43}^{\delta}(z_3) L_{3214}(z_3, t_1, t_1^+, z_3^+)
\tag{3.42}
$$

$$
+ \sum_{\alpha_3\alpha_4} \int_{t_0}^{t_1} dt_3 \int_{t_0}^{t_3} dt_4 \, Y_{43}^{<}(t_4, t_3) L_{3214}^{3>}(t_3, t_1, t_1^+, t_4)
\tag{3.43}
$$

$$
+ \sum_{\alpha_3\alpha_4} \int_{t_0}^{t_1} dt_3 \int_{t_3}^{t_1} dt_4 \, Y_{43}^{>}(t_4, t_3) L_{3214}^{3<}(t_3, t_1, t_1^+, t_4)
\tag{3.44}
$$

$$
- \sum_{\alpha_3\alpha_4} \int_{t_0}^{t_1} dt_3 \int_{t_0}^{t_1} dt_4 \, Y_{43}^{<}(t_4, t_3) L_{3214}^{2>}(t_3, t_1, t_1^+, t_4)
\tag{3.45}
$$

$$
- \sum_{\alpha_3\alpha_4} \int_{t_0}^{t_1} dt_3 \int_{t_0}^{t_1} dt_4 \, Y_{43}^{>}(t_4, t_3) L_{3214}^{2<}(t_3, t_1, t_1^+, t_4)
\tag{3.46}
$$

$$
+ \sum_{\alpha_3\alpha_4} \int_{t_0}^{t_1} dt_3 \int_{t_3}^{t_1} dt_4 \, Y_{43}^{<}(t_4, t_3) L_{3214}^{1>}(t_3, t_1, t_1^+, t_4)
\tag{3.47}
$$

$$
+ \sum_{\alpha_3\alpha_4} \int_{t_0}^{t_1} dt_3 \int_{t_0}^{t_3} dt_4 \, Y_{43}^{>}(t_4, t_3) L_{3214}^{1<}(t_3, t_1, t_1^+, t_4)
\tag{3.48}
$$

$$
- i \sum_{\alpha_3\alpha_4} \int_{t_0}^{t_1} dt_3 \int_{0}^{\beta} d\tau_4 \, Y_{43}^{>}(t_0 - i\tau_4, t_3) L_{3214}^{2<}(t_3, t_1, t_1^+, t_0 - i\tau_4)
\tag{3.49}
$$

$$+ i \sum_{\alpha_3 \alpha_4} \int_{t_0}^{t_1} dt_3 \int_0^\beta d\tau_4 \, Y_{43}^>(t_0 - i\tau_4, t_3) L_{3214}^{1<}(t_3, t_1, t_1^+, t_0 - i\tau_4) \qquad (3.50)$$

$$- i \sum_{\alpha_3 \alpha_4} \int_0^\beta d\tau_3 \int_{t_0}^{t_1} dt_4 \, Y_{43}^<(t_4, t_0 - i\tau_3) L_{3214}^{2>}(t_0 - i\tau_3, t_1, t_1^+, t_4) \qquad (3.51)$$

$$+ i \sum_{\alpha_3 \alpha_4} \int_0^\beta d\tau_3 \int_{t_0}^{t_1} dt_4 \, Y_{43}^<(t_4, t_0 - i\tau_3) L_{3214}^{1>}(t_0 - i\tau_3, t_1, t_1^+, t_4) \qquad (3.52)$$

$$- \sum_{\alpha_3 \alpha_4} \int_0^\beta d\tau_3 \int_0^{\tau_3} d\tau_4 \, Y_{43}^<(t_0 - i\tau_4, t_0 - i\tau_3) L_{3214}^{1>}(t_0 - i\tau_3, t_1, t_1^+, t_0 - i\tau_4) \quad (3.53)$$

$$- \sum_{\alpha_3 \alpha_4} \int_0^\beta d\tau_3 \int_{\tau_3}^\beta d\tau_4 \, Y_{43}^>(t_0 - i\tau_4, t_0 - i\tau_3) L_{3214}^{1<}(t_0 - i\tau_3, t_1, t_1^+, t_0 - i\tau_4) \,. \quad (3.54)$$

Here we have split up the T-matrix $\boldsymbol{Y}$ into a singular, lesser and greater part (see Eq. 2.24):

$$\boldsymbol{Y}_{\boldsymbol{\lambda'},\boldsymbol{\lambda},\boldsymbol{U}}(z_1, z_2) = \boldsymbol{\Lambda}(z_1)\delta_{\mathcal{C}}(z_1, z_2) + \boldsymbol{\Lambda}(z_1)\boldsymbol{G}^{\mathrm{SFT}}(z_1, z_2)\boldsymbol{\Lambda}(z_2) \qquad (3.55)$$

$$=: \boldsymbol{Y}_{\boldsymbol{\lambda'},\boldsymbol{\lambda},\boldsymbol{U}}^\delta(z_1)\delta_{\mathcal{C}}(z_1, z_2) + \Theta_{\mathcal{C}}(z_1, z_2)\boldsymbol{Y}_{\boldsymbol{\lambda'},\boldsymbol{\lambda},\boldsymbol{U}}^>(z_1, z_2)$$

$$+ \Theta_{\mathcal{C}}(z_2, z_1)\boldsymbol{Y}_{\boldsymbol{\lambda'},\boldsymbol{\lambda},\boldsymbol{U}}^<(z_1, z_2) \,. \qquad (3.56)$$

For the two-particle vertex function $\boldsymbol{L}_{\boldsymbol{\lambda'},\boldsymbol{U}}$ [Eq. 3.38], the notation $L^{i \gtrless}(z_3, z_1, z_1^+, z_4)$ indicates that z_1 is the i-th time on the contour and that z_3 is a later/earlier contour-time than z_4. Note that we write $L_{3214}^{i\gtrless}$ which is short for $L_{\alpha_3 \alpha_2 \alpha_1 \alpha_4}^{i\gtrless}$ and that the indexing with the parameters $\boldsymbol{\lambda'}$ and $\boldsymbol{U}$ has been suppressed for brevity.

To evaluate the above integrations in equilibrium, we express the T-matrix via its spectral representation [206] with the respective spectral function $\boldsymbol{A}^Y$, i.e.,

$$\boldsymbol{Y}^\gtrless(z_1, z_2) = i \int d\omega \, e^{-i\omega(z_1 - z_2)} f^\gtrless(\omega) \boldsymbol{A}^Y(\omega) \,, \qquad (3.57)$$

with $f^<(\omega) = f(\omega)$ and $f^>(\omega) = f(\omega) - 1$ and where $f(\omega)$ is the Fermi function. This also implies

$$f^>(\omega) = -e^{\omega\beta} f^<(\omega) \,. \qquad (3.58)$$

For the two-particle vertex function we choose the Lehmann representation by insert-

ing the completeness relation $\mathbf{1} = \sum_m |m\rangle \langle m|$ between all operators. We find

$$L^{3>}(3, 2, 1^+, 4)_{z_2 = z_1} =$$
$$\sum_{mnkl} \Big[- P_{3214}^{mnkl} e^{-\beta E_m} e^{-\beta E_k} e^{i(E_m + E_k - E_n - E_l)z_1} e^{i(E_n - E_m)z_3} e^{i(E_l - E_k)z_4}$$
$$+ \tilde{P}_{3214}^{mnkl} e^{-\beta E_m} e^{-\beta E_k} e^{i(E_m - E_n)z_3} e^{i(E_n - E_m)z_4}$$
$$- Q_{3214}^{mnkl} e^{-\beta E_m} e^{i(E_m - E_k)z_1} e^{i(E_k - E_l)z_3} e^{i(E_l - E_m)z_4} \Big], \qquad (3.59)$$

$$L^{3<}(3, 2, 1^+, 4)_{z_2 = z_1} =$$
$$\sum_{mnkl} \Big[- P_{3214}^{mnkl} e^{-\beta E_m} e^{-\beta E_k} e^{i(E_m + E_k - E_n - E_l)z_1} e^{i(E_n - E_m)z_3} e^{i(E_l - E_k)z_4}$$
$$- \tilde{P}_{3214}^{mnkl} e^{-\beta E_n} e^{-\beta E_k} e^{i(E_m - E_n)z_3} e^{i(E_n - E_m)z_4}$$
$$+ \tilde{Q}_{3214}^{mnkl} e^{-\beta E_m} e^{i(E_m - E_k)z_1} e^{i(E_l - E_m)z_3} e^{i(E_k - E_l)z_4} \Big], \qquad (3.60)$$

and similar expressions for $L^{1\gtrless}$ and $L^{2\gtrless}$. For the amplitudes we used the short-hand notations:

$$P_{3214}^{mnkl} = \frac{(-i)^2}{Z^2} \langle m|c_1^\dagger|n\rangle \langle n|c_3|m\rangle \langle k|c_2|l\rangle \langle l|c_4^\dagger|k\rangle, \qquad (3.61)$$

$$\tilde{P}_{3214}^{mnkl} = \frac{(-i)^2}{Z^2} \langle m|c_3|n\rangle \langle n|c_4^\dagger|m\rangle \langle k|c_1^\dagger|l\rangle \langle l|c_2|k\rangle, \qquad (3.62)$$

$$Q_{3214}^{mnkl} = \frac{(-i)^2}{Z^2} \langle m|c_1^\dagger|n\rangle \langle n|c_2|k\rangle \langle k|c_3|l\rangle \langle l|c_4^\dagger|m\rangle, \qquad (3.63)$$

$$\tilde{Q}_{3214}^{mnkl} = \frac{(-i)^2}{Z^2} \langle m|c_1^\dagger|n\rangle \langle n|c_2|k\rangle \langle k|c_4^\dagger|l\rangle \langle l|c_3|m\rangle, \qquad (3.64)$$

where $Z = \text{tr}(\exp(-\beta \mathcal{H}'(t_0)))$ is the partition function.

Let us first focus on those terms involving only greater and lesser parts of $\boldsymbol{Y}_{\boldsymbol{\chi}', \boldsymbol{\lambda}, U}$ [Eqs. 3.43 – 3.54] and evaluate them for each amplitude [Eqs. 3.61 – 3.64] separately. For this purpose we write all summands (3.43) – (3.54) in the compact form

$$i \sum_{\alpha_3 \alpha_4} \sum_{mnkl} \sum_X \int d\omega \, f(\omega) A_{43}^Y(\omega) X_{3214}^{mnkl} \mathcal{R}_{mnkl}^X(\omega, t_1). \qquad (3.65)$$

To this end, we have made use of Eq. (3.58) and factored out all common terms for each combination of amplitudes X_{3214}^{mnkl}, where X stands for $P, \tilde{P}, Q$, or $\tilde{Q}$. The remaining exponential factors, resulting from the time-evolution operator and the density matrix when introducing the Lehmann representation, and the two time integrations along the different branches are collected in the term $\mathcal{R}_{mnkl}^X(\omega, t_1)$ for each X. As an example, we give an expression for $\mathcal{R}_{mnkl}^Q(\omega, t_1)$ in the following and tag each summand according to

its origin in the above expression for $-\beta\delta\widehat{\Omega}_{\boldsymbol{\lambda},\boldsymbol{U}}[\boldsymbol{\Sigma}_{\boldsymbol{\lambda}',\boldsymbol{U}}]/\delta\lambda'_{\alpha_1\alpha_2}(t_1)$:

$$\mathcal{R}^Q_{mnkl}(\omega,t_1) =$$
$$- e^{-\beta E_m}\left(-\mathcal{I}^Q_{c'} + \mathcal{I}^Q_{a'} + \mathcal{I}^Q_{b_1} - \mathcal{I}^Q_a\right) \qquad\qquad\text{(from 3.43)}$$
$$+ e^{-\beta(E_l-\omega)}\left(-\mathcal{I}^Q_c + \mathcal{I}^Q_{b_1} + \mathcal{I}^Q_{b_2} - \mathcal{I}^Q_a\right) \qquad\qquad\text{(from 3.46)}$$
$$- e^{-\beta E_k}\left(-\mathcal{I}^Q_c + \mathcal{I}^Q_{b_2} + \mathcal{I}^Q_{c'} - \mathcal{I}^Q_{a'}\right) \qquad\qquad\text{(from 3.47)}$$
$$+ \left(e^{-\beta E_m} - e^{-\beta(E_l-\omega)}\right)\left(\mathcal{I}^Q_{b_1} - \mathcal{I}^Q_a\right) \qquad\qquad\text{(from 3.49)}$$
$$+ \left(e^{-\beta E_k} - e^{-\beta(E_l-\omega)}\right)\left(\mathcal{I}^Q_{b_2} - \mathcal{I}^Q_a\right) \qquad\qquad\text{(from 3.52)}$$
$$+ \left[\left(e^{-\beta E_m} - e^{-\beta E_k}\right)\mathcal{I}^Q_{a'} + \left(e^{-\beta E_k} + e^{-\beta(E_l-\omega)}\right)\mathcal{I}^Q_a\right]\,. \qquad\text{(from 3.53)}$$

Here, the results of the different integrals are given by:

$$\mathcal{I}^Q_a := \mathcal{I}^Q_{a,mnkl}(\omega,t_1) = \frac{1}{E_l - E_m - \omega}\frac{1}{E_k - E_l + \omega}e^{i(E_m-E_k)(t_1-t_0)}\,, \qquad (3.66)$$

$$\mathcal{I}^Q_{a'} := \mathcal{I}^Q_{a',mnkl}(\omega,t_1) = \frac{1}{E_l - E_m - \omega}\frac{1}{E_k - E_m}e^{i(E_m-E_k)(t_1-t_0)}\,, \qquad (3.67)$$

$$\mathcal{I}^Q_{b_1} := \mathcal{I}^Q_{b_1,mnkl}(\omega,t_1) = \frac{1}{E_l - E_m - \omega}\frac{1}{E_k - E_l + \omega}e^{i(E_m-E_l+\omega)(t_1-t_0)}\,, \qquad (3.68)$$

$$\mathcal{I}^Q_{b_2} := \mathcal{I}^Q_{b_2,mnkl}(\omega,t_1) = \frac{1}{E_l - E_m - \omega}\frac{1}{E_k - E_l + \omega}e^{i(E_l-E_k-\omega)(t_1-t_0)}\,, \qquad (3.69)$$

$$\mathcal{I}^Q_c := \mathcal{I}^Q_{c,mnkl}(\omega) = \frac{1}{E_l - E_m - \omega}\frac{1}{E_k - E_l + \omega}\,, \qquad (3.70)$$

$$\mathcal{I}^Q_{c'} := \mathcal{I}^Q_{c',mnkl}(\omega) = \frac{1}{E_l - E_m - \omega}\frac{1}{E_k - E_m}\,. \qquad (3.71)$$

By collecting prefactors, we find that all explicitly t_1-dependent parts drop out and that only those containing $\mathcal{I}^Q_c$ and $\mathcal{I}^Q_{c'}$ contribute. Analogous calculations lead to the same result for P, $\tilde{P}$ and $\tilde{Q}$, and we thus conclude:

$$\mathcal{R}^X_{mnkl}(\omega,t_1) = \mathcal{R}^X_{mnkl}(\omega) \quad \forall X\,. \qquad (3.72)$$

The singular part $\sum_{\alpha_3\alpha_4}\int dz_3\, Y^\delta_{43}(z_3)L_{3214}(z_3,t_1,t_1^+,z_3^+)$ [Eq. 3.42] is evaluated straightforwardly and also turns out to be independent of the time t_1. This completes the proof.

For a general nonequilibrium situation with $H(t) \neq$ const. the above argument can be used to show that the causality principle is satisfied by the nonequilibrium SFT: Satisfying the general variational equation (3.19) for all variations of $\boldsymbol{\lambda}'(t_0 - i\tau)$ on the Matsubara branch requires that the optimal parameters on the Matsubara branch are τ-independent and must be given by a solution of the equilibrium SFT. This shows that the description of the initial state is independent from the final-state dynamics.

We also note that, as in the equilibrium case, the self-energy functional evaluated at the stationary point, $\widehat{\Omega}_{\boldsymbol{\lambda},\boldsymbol{U}}[\boldsymbol{\Sigma}_{\boldsymbol{\lambda}'_{\mathrm{opt}},\boldsymbol{U}}]$, has a clear physical meaning: It represents the (approximate) grand potential of the initial thermal state. Provided that there are several

stationary points for a given set of (time-dependent) parameters of the original system, the one with the lowest grand potential in the initial state describes the thermodynamically stable initial state and the emerging final-state dynamics. Furthermore, provided that the same type of reference system is considered, the (approximate) description of the initial state is on equal footing with the one for the final state. Concluding, the nonequilibrium SFT is a true extension of the equilibrium SFT.

3.8 Internal consistency

The SFT provides access to time-dependent expectation values of arbitrary one-particle observables as well as to the grand potential of the initial thermal state. An *exact* relation between both quantities can be derived by formally extending the grand canonical density operator to the whole Keldysh-Matsubara contour, such that the partition function reads as $Z_{\boldsymbol{\lambda},\boldsymbol{U}} = \text{tr}(\mathcal{T}_{\mathcal{C}} e^{-i \int_{\mathcal{C}} dz\, \mathcal{H}_{\boldsymbol{\lambda},\boldsymbol{U}}(z)})$ (see also discussion in Sec. 2.3). The grand potential $\Omega_{\boldsymbol{\lambda},\boldsymbol{U}} = -\beta^{-1} \ln Z_{\boldsymbol{\lambda},\boldsymbol{U}}$ then becomes a functional of the (contour)-time dependent single-particle parameters of the model. We now consider an arbitrary one-particle observable of the form $\boldsymbol{A}(z) = \sum_{\alpha\beta} a_{\alpha\beta}(z) c_\alpha^\dagger c_\beta$ (cf. Eq. 2.39) which couples linearly to the Hamiltonian $H_{\boldsymbol{\lambda},\boldsymbol{U}}(z) = H^{(0)}_{\boldsymbol{\lambda},\boldsymbol{U}}(z) + \lambda_A(z)\boldsymbol{A}(z)$ via a time-dependent parameter $\lambda_A(z)$. The set of one-particle parameters $\boldsymbol{\lambda}(z)$ comprises $\lambda_A(z)$ as well as the remaining parameters $\widetilde{\boldsymbol{\lambda}}(z)$. Then, the expectation value of $\boldsymbol{A}(z)$ can be obtained via the linear-response relation

$$\langle \boldsymbol{A}(z) \rangle_{\boldsymbol{\lambda},\boldsymbol{U}} = -i\beta \left. \frac{\delta \Omega_{\boldsymbol{\lambda},\boldsymbol{U}}}{\delta \lambda_A(z)} \right|_{\lambda_A(z)=0} , \tag{3.73}$$

where only the variational derivative in the "transverse" but not in the "physical" contributes, as discussed in Sec. 3.5.

On the other hand the expectation value may be computed from the one-particle Green's function as:

$$\langle \boldsymbol{A}(z) \rangle_{\boldsymbol{\lambda},\boldsymbol{U}} = -i \, \text{tr}\left(\boldsymbol{a}(z) \boldsymbol{G}_{\boldsymbol{\lambda},\boldsymbol{U}}(z,z^+) \right) . \tag{3.74}$$

The SFT provides approximate expressions for the grand potential as well as for the expectation value. However, one can show that these approximations are consistent, i.e.:

$$\left. \frac{\delta \widehat{\Omega}_{\boldsymbol{\lambda},\boldsymbol{U}}[\boldsymbol{\Sigma}_{\boldsymbol{\lambda}'_{\text{opt}},\boldsymbol{U}}]}{\delta \lambda_A(z)} \right|_{\lambda_A(z)=0} = \frac{1}{\beta} \, \text{tr}\left(\boldsymbol{a}(t) \boldsymbol{G}^{\text{SFT}}(z,z^+) \right) , \tag{3.75}$$

where $\boldsymbol{G}^{\text{SFT}}$ is the SFT Green's function [see Eq. 3.20]. Here $\widehat{\Omega}_{\boldsymbol{\lambda},\boldsymbol{U}}[\boldsymbol{\Sigma}_{\boldsymbol{\lambda}'_{\text{opt}},\boldsymbol{U}}]$ is the grand potential at the optimal parameters of the reference system which still can be considered as a functional of the time-dependent parameters of the original system and of $\lambda_A(z)$ in particular. Eq. (3.75) represents a generalization of the "thermodynamical consistency" that has been shown in the context of the equilibrium formalism already [210].

To prove Eq. (3.75), we note that its left-hand side has a twofold dependence on $\lambda_A(z)$: (i) via the free Green's function of the original model, $\boldsymbol{G}_{\boldsymbol{\lambda},0}^{-1}$, which enters the second term in Eq. (3.18), and (ii) via the optimized parameters $\boldsymbol{\lambda}'_{\text{opt}}(z)$ which depend on the time-dependent parameters in the final state of the original system. Consequently, there are two terms resulting from the derivative:

$$\frac{\delta\widehat{\Omega}_{\boldsymbol{\lambda},U}[\boldsymbol{\Sigma}_{\boldsymbol{\lambda}'_{\text{opt}},U}]}{\delta\lambda_A(z)} = \text{tr}\left(\frac{\delta\widehat{\Omega}_{\boldsymbol{\lambda},U}[\boldsymbol{\Sigma}_{\boldsymbol{\lambda}'_{\text{opt}},U}]}{\delta\boldsymbol{\lambda}'_{\text{opt}}} \circ \frac{\delta\boldsymbol{\lambda}'_{\text{opt}}}{\delta\lambda_A(z)}\right)$$
$$+ \text{tr}\left(\frac{\delta\widehat{\Omega}_{\boldsymbol{\lambda},U}[\boldsymbol{\Sigma}_{\boldsymbol{\lambda}'_{\text{opt}},U}]}{\delta\boldsymbol{\lambda}} \circ \frac{\delta\boldsymbol{\lambda}}{\delta\lambda_A(z)}\right). \quad (3.76)$$

Internal consistency is achieved because of the stationarity of the self-energy functional at $\boldsymbol{\lambda}'_{\text{opt}}(z)$, which implies that the first term must vanish. Using Eqs. (3.11) and (3.12), the functional derivative with respect to $\boldsymbol{\lambda}(z)$ in the second term is found to be:

$$\frac{\delta\widehat{\Omega}_{\boldsymbol{\lambda},U}[\boldsymbol{\Sigma}_{\boldsymbol{\lambda}'_{\text{opt}},U}]}{\delta\boldsymbol{\lambda}(z)} = \frac{1}{\beta}\boldsymbol{G}^{\text{SFT}}(z,z^+). \quad (3.77)$$

The second factor $\delta\boldsymbol{\lambda}/\delta\lambda_A$ yields $\boldsymbol{a}(t)$, which proves Eq. (3.75).

3.9 Conservation laws

Approximations cannot be expected *a priori* to respect fundamental conservation laws that result from the invariance of the Hamiltonian under certain continuous groups of unitary transformations. In fact, conservation of the total particle number, the total spin or the total energy are certainly violated within simple non-self-consistent or non-variational schemes such as the nonequilibrium cluster-perturbation theory – apart from certain highly symmetric situations such as given by the Hubbard model on a bipartite lattice at half-filling [160, 211, 212]. A general theory for real-time dynamics must therefore address the question under which conditions an approximation is conserving.

With respect to self-consistent perturbative approximations, this question has been answered by Baym and Kadanoff [118, 119]: A diagrammatic approximation is defined by a certain truncation of the skeleton-diagram expansion of the self-energy, which yields the self-energy as a functional of the Green's function; see Eq. (3.3) and the discussion thereafter. Combined with Dyson's equation, which provides an independent relation between self-energy and Green's function, the problem can be solved using an iterative and self-consistent approach. A perturbative approximation is found to be conserving if the (truncated) skeleton-diagram expansion of the self-energy is obtained as the functional derivative of an approximate Luttinger-Ward functional that itself is constructed by truncations and re-summations within diagrammatic weak-coupling perturbation theory, i.e., the self-energy must be "Φ-derivable". Approximations constructed in this way are conserving.

Contrary, approximations generated within the framework of the SFT are nonperturbative and do not rely on diagrammatic re-summations. While the Luttinger-Ward functional is essential for the construction of the SFT, and while the SFT self-energy is obtained as its functional derivative, approximations are generated in a very different way as compared to perturbation theory. Namely, instead of truncating the Luttinger-Ward functional diagrammatically, it is restricted to a sub-manifold of self-energies generated by some (simpler) reference system.

Note that the DMFT, as the most prominent approximation in this context, represents an exception. DMFT can be understood as an approximation generated within the SFT framework (see Sec. 3.4). At the same time, DMFT is a Φ-derivable approximation in the spirit of Baym and Kadanoff as it can be constructed diagrammatically from a truncated Luttinger-Ward functional involving local propagators only.

In the following we will modify and adapt the essential ideas of Baym and Kadanoff to analyze under which circumstances an *arbitrary* approximation constructed within the SFT framework is conserving. The important point observed by Baym and Kadanoff is that the fundamental conservation laws, reformulated in terms of the self-energy and the Green's function, result from invariances of the Luttinger-Ward functional under appropriate gauge transformations of the Green's function:

$$
\begin{aligned}
0 &= \delta \widehat{\Phi}_U[\boldsymbol{G}_{\boldsymbol{\lambda},U}] \\
&= \frac{1}{\beta} \operatorname{Tr} \left(\boldsymbol{\Sigma}_{\boldsymbol{\lambda},U} \circ \delta \boldsymbol{G}_{\boldsymbol{\lambda},U} \right) .
\end{aligned}
\tag{3.78}
$$

Within SFT, the self-energy functional is in fact constructed with the help of the Luttinger-Ward functional, see Eqs. (3.9) and (3.11). However, it does not inherit its gauge invariance. Nevertheless, the Euler equation provides the analog of Eq. (3.78) at the stationary point:

$$
\begin{aligned}
0 &= \delta \widehat{\Omega}_{\boldsymbol{\lambda}',U}[\boldsymbol{\Sigma}_{\boldsymbol{\lambda}',U}]\Big|_{\boldsymbol{\lambda}'=\boldsymbol{\lambda}'_{\mathrm{opt}}} \\
&= \frac{1}{\beta} \operatorname{Tr} \left(\left(\boldsymbol{G}^{\mathrm{SFT}} - \boldsymbol{G}_{\boldsymbol{\lambda}',U} \right) \circ \delta \boldsymbol{\Sigma}_{\boldsymbol{\lambda}',U} \right)\Big|_{\boldsymbol{\lambda}'=\boldsymbol{\lambda}'_{\mathrm{opt}}} ,
\end{aligned}
\tag{3.79}
$$

i.e., by construction the variation of the grand potential $\widehat{\Omega}_{\boldsymbol{\lambda},U}[\boldsymbol{\Sigma}_{\boldsymbol{\lambda}',U}]$ with respect to an *arbitrary* set of one-particle parameters of the reference system $\boldsymbol{\lambda}'$ vanishes, if evaluated at the optimal parameters. Thus, the goal is to identify a certain class of parameter variations which generates, via Eq. (3.79), the necessary conditions on the SFT Green's function and the self-energy from which the conservation laws derive, namely Eqs. (2.45) and (2.56).

3.9.1 Particle number and spin conservation

Within SFT the real-time dynamics of one-particle observables (cf. Sec. 2.4.1) is determined by the approximate Green's function $\boldsymbol{G}^{\mathrm{SFT}}$, as given by Eq. (3.20), i.e.,

$$
\langle \boldsymbol{A} \rangle(t) = -i \operatorname{tr} \left(\boldsymbol{a}(t) \boldsymbol{G}^{\mathrm{SFT}}(t, t^+) \right) .
\tag{3.80}
$$

The SFT self-energy is the self-energy of a reference system with one-particle parameters $\boldsymbol{\lambda}'$. Both are taken at optimal parameter values $\boldsymbol{\lambda}'_{\text{opt}}$ satisfying the SFT Euler equation, Eq. (3.19). Thus, in accordance with Eq. (2.45), our goal is to show that

$$\sum_{\sigma\sigma'} a_{\sigma\sigma'} \left[\boldsymbol{G}^{\text{SFT}} \, {}^{\circ}_{\circ} \, \boldsymbol{\Sigma}_{\boldsymbol{\lambda}'_{\text{opt}},U} \right]_{ii,\sigma'\sigma} (t, t^+) = 0 \,. \tag{3.81}$$

This would be sufficient to ensure that an approximation constructed within the SFT framework respects the conservation of particle number and spin even locally.

To this end we consider the following gauge transformations of the one-particle parameters of the reference system $\boldsymbol{\lambda}' \mapsto \bar{\boldsymbol{\lambda}}'$,

$$\begin{aligned}
\boldsymbol{\varepsilon}'(z) &\mapsto & \bar{\boldsymbol{\varepsilon}}'(z) = \boldsymbol{\varepsilon}'(z) - \partial_z \boldsymbol{\chi}(z) \,, \\
\boldsymbol{T}'(z) &\mapsto & \bar{\boldsymbol{T}}'(z) = e^{i\boldsymbol{\chi}(z)} \boldsymbol{T}'(z) e^{-i\boldsymbol{\chi}(z)} \,,
\end{aligned} \tag{3.82}$$

where $\boldsymbol{\varepsilon}'$ denotes the (spatially) diagonal part of $\boldsymbol{\lambda}'$ and $\boldsymbol{T}'$ its off-diagonal part. The gauge transformation is generated by a spatially diagonal contour function $\boldsymbol{\chi}$ of the form

$$\chi_{ij,\sigma\sigma'}(z) = \delta_{ij} \chi_i(z) a_{\sigma\sigma'} \,. \tag{3.83}$$

To ensure a Hermitian reference system, $\boldsymbol{\chi}$ must be real but can be chosen arbitrary in other respects. Note that $\boldsymbol{\chi}$ commutes with $\boldsymbol{\varepsilon}'$, which will become important later. This is trivially satisfied in the case $A_i = n_i$ [cf. Eq. 2.43], and also holds in the case $A_i = S_i^{(\eta)}$ [cf. Eq. 2.43], provided that $\boldsymbol{\varepsilon}'$ is independent of spin indices. The latter is a necessary condition to ensure total spin conservation *in the reference system.*

The next step is to show that the above gauge transformation of the one-particle parameters $\boldsymbol{\lambda}'$ implies that the exact Green's function $\boldsymbol{G}' \equiv \boldsymbol{G}_{\boldsymbol{\lambda}',U}$ and the exact self-energy $\boldsymbol{\Sigma}' \equiv \boldsymbol{\Sigma}_{\boldsymbol{\lambda}',U}$ of the reference system transform as:

$$\boldsymbol{G}'(z_1, z_2) \mapsto \bar{\boldsymbol{G}}'(z_1, z_2) = e^{i\boldsymbol{\chi}(z_1)} \boldsymbol{G}'(z_1, z_2) e^{-i\boldsymbol{\chi}(z_2)} \,, \tag{3.84}$$

and

$$\boldsymbol{\Sigma}'(z_1, z_2) \mapsto \bar{\boldsymbol{\Sigma}}'(z_1, z_2) = e^{i\boldsymbol{\chi}(z_1)} \boldsymbol{\Sigma}'(z_1, z_2) e^{-i\boldsymbol{\chi}(z_2)} \,. \tag{3.85}$$

We first note that Eq. (3.84) implies Eq. (3.85), which is verified by referring to the (exact) skeleton-diagram expansion $\bar{\boldsymbol{\Sigma}}' = \hat{\boldsymbol{\Sigma}}_U[\bar{\boldsymbol{G}}']$ [cf. Eq. 2.37 and 2.38]: Inserting the transformed $\bar{\boldsymbol{G}}'$, the phase factors of the incoming and the outgoing propagators cancel at each internal vertex. Only at the two links for the external legs the phase factors do not find a counterpart. This leaves us with the two phase factors at the transformed self-energy in Eq. (3.85). In order to verify Eq. (3.84), it is sufficient to show that the transformed Green's function and the transformed self-energy satisfy the equation of motion for the transformed parameters:

$$i\partial_{z_1} \bar{\boldsymbol{G}}'(z_1, z_2) = \delta_{\mathcal{C}}(z_1, z_2) + \bar{\boldsymbol{\lambda}}'(z_1) \bar{\boldsymbol{G}}'(z_1, z_2) + (\bar{\boldsymbol{\Sigma}}' \circ \bar{\boldsymbol{G}}')(z_1, z_2) \,. \tag{3.86}$$

To verify this, we first compute the left-hand side of Eq. (3.86):

$$i\partial_{z_1}\bar{\boldsymbol{G}}'(z_1, z_2) = e^{i\boldsymbol{\chi}(z_1)}i\partial_{z_1}\boldsymbol{G}'(z_1, z_2)e^{-i\boldsymbol{\chi}(z_2)}$$
$$- (\partial_{z_1}\boldsymbol{\chi}(z_1))e^{i\boldsymbol{\chi}(z_1)}\boldsymbol{G}'(z_1, z_2)e^{-i\boldsymbol{\chi}(z_2)}. \quad (3.87)$$

To treat the second term on the right-hand side of Eq. (3.86), we distinguish between (spatially) diagonal and off-diagonal parts of the one-particle parameters and apply the respective transformation laws, Eq. (3.82). This yields:

$$\bar{\boldsymbol{\lambda}}'(z_1)\bar{\boldsymbol{G}}'(z_1, z_2)$$
$$= \bar{\boldsymbol{\varepsilon}}'(z_1)\bar{\boldsymbol{G}}'(z_1, z_2) + \bar{\boldsymbol{T}}'(z_1)\bar{\boldsymbol{G}}'(z_1, z_2)$$
$$= \boldsymbol{\varepsilon}'(z_1)e^{i\boldsymbol{\chi}(z_1)}\boldsymbol{G}'(z_1, z_2)e^{-i\boldsymbol{\chi}(z_2)} + e^{i\boldsymbol{\chi}(z_1)}\boldsymbol{T}'(z_1)e^{-i\boldsymbol{\chi}(z_1)}e^{i\boldsymbol{\chi}(z_1)}\boldsymbol{G}'(z_1, z_2)e^{-i\boldsymbol{\chi}(z_2)}$$
$$- (\partial_{z_1}\boldsymbol{\chi}(z_1))e^{i\boldsymbol{\chi}(z_1)}\boldsymbol{G}'(z_1, z_2)e^{-i\boldsymbol{\chi}(z_2)}$$
$$= e^{i\boldsymbol{\chi}(z_1)}\boldsymbol{\lambda}'(z_1)\boldsymbol{G}'(z_1, z_2)e^{-i\boldsymbol{\chi}(z_2)} - (\partial_{z_1}\boldsymbol{\chi}(z_1))e^{i\boldsymbol{\chi}(z_1)}\boldsymbol{G}'(z_1, z_2)e^{-i\boldsymbol{\chi}(z_2)}. \quad (3.88)$$

In the last step we made use of the commutativity of $\boldsymbol{\varepsilon}'$ and $\boldsymbol{\chi}$. The second terms in Eq. (3.87) and in Eq. (3.88) cancel each other. Finally, we have $(\bar{\boldsymbol{\Sigma}}' \circ \bar{\boldsymbol{G}}')(z_1, z_2) = e^{i\boldsymbol{\chi}(z_1)}(\boldsymbol{\Sigma}' \circ \boldsymbol{G}')(z_1, z_2)e^{-i\boldsymbol{\chi}(z_2)}$ and $\delta_{\mathcal{C}}(z_1, z_2) = e^{i\boldsymbol{\chi}(z_1)}\delta_{\mathcal{C}}(z_1, z_2)e^{-i\boldsymbol{\chi}(z_2)}$. Thus, collecting all terms, plugging these into Eq. (3.86) and canceling the phase factors $e^{i\boldsymbol{\chi}(z_1)}$ and $e^{-i\boldsymbol{\chi}(z_2)}$, we conclude that the transformed equation of motion is solved by the transformed Green's function and self-energy if the original one was solved by the original quantities.

A first-order variation of the one-particle parameters of the reference system, given by $\delta\boldsymbol{\chi}(z)$ leads to the following first-order variation of the self-energy (cf. Eq. (3.85)):

$$\delta\boldsymbol{\Sigma}'(z_1, z_2) = i\delta\boldsymbol{\chi}(z_1)\boldsymbol{\Sigma}'(z_1, z_2) - i\boldsymbol{\Sigma}'(z_1, z_2)\delta\boldsymbol{\chi}(z_2). \quad (3.89)$$

This leads to a first-order variation $\delta\widehat{\Omega}_{\boldsymbol{\lambda},\boldsymbol{U}}[\boldsymbol{\Sigma}_{\boldsymbol{\lambda}',\boldsymbol{U}}]$ which vanishes for optimal values of the variational parameters $\boldsymbol{\lambda}'$, provided that the variation $\delta\boldsymbol{T}' = i\delta\boldsymbol{\chi}\boldsymbol{T}' - i\boldsymbol{T}'\delta\boldsymbol{\chi}$ and $\delta\boldsymbol{\varepsilon}' = -\partial_z\delta\boldsymbol{\chi}$ of the reference parameters induced by Eq. (3.82) are chosen to be part of our variational space. We insert Eq. (3.89) into the SFT Euler equation, as given by Eq. (3.79), and use Eq. (3.83) to get

$$0 = \beta\delta\widehat{\Omega}_{\boldsymbol{\lambda},\boldsymbol{U}}[\boldsymbol{\Sigma}_{\boldsymbol{\lambda}',\boldsymbol{U}}]\Big|_{\boldsymbol{\lambda}'=\boldsymbol{\lambda}'_{\text{opt}}}$$
$$= -i\sum_{i,\sigma\sigma'}\int_{\mathcal{C}}dz\, a_{\sigma\sigma'}\Big(\Big[\boldsymbol{G}^{\text{SFT}} \overset{\circ}{,} \boldsymbol{\Sigma}_{\boldsymbol{\lambda}'_{\text{opt}},\boldsymbol{U}}\Big]$$
$$+ \Big[\boldsymbol{G}_{\boldsymbol{\lambda}'_{\text{opt}},\boldsymbol{U}} \overset{\circ}{,} \boldsymbol{\Sigma}_{\boldsymbol{\lambda}'_{\text{opt}},\boldsymbol{U}}\Big]\Big)_{ii,\sigma'\sigma}(z, z^+)\delta\chi_i(z). \quad (3.90)$$

Since this holds for arbitrary first-order variations $\delta\chi_i(z)$, the term $\sum_{\sigma\sigma'} a_{\sigma\sigma'}(\cdots)$ must vanish. Consider the second term in the bracket: The condition $\sum_{\sigma\sigma'} a_{\sigma\sigma'}[\boldsymbol{G}_{\boldsymbol{\lambda}'_{\text{opt}},\boldsymbol{U}} \overset{\circ}{,} \boldsymbol{\Sigma}_{\boldsymbol{\lambda}'_{\text{opt}},\boldsymbol{U}}]_{ii,\sigma'\sigma}(z, z^+) = 0$ is just equivalent with local particle-number and spin conservation *in the reference system* [see Eq. 2.45]. Therefore, *if* this is satisfied, the first term

in the bracket must vanish as well, i.e., Eq. (3.81) is inferred. It is quite intuitive that particle-number and spin conservation is respected by an approximation within the SFT only if it is exactly satisfied for the reference system that has been chosen to specify the approximation. We conclude that within the SFT particle-number and spin conservation is proliferated from the reference system, where it must hold exactly, to the original system, where it holds when formulated with the approximate SFT Green's function and self-energy.

The conservation laws are ensured by stationarity of the SFT grand potential with respect to the parameter variations defined by Eq. (3.82). Note that $\boldsymbol{\varepsilon}'$ and $\boldsymbol{T}'$ are not varied independently, i.e., particle-number and spin conservation requires stationarity with respect to variations along certain *directions* in the parameter space. In particular, complex hopping-parameter variations must be taken into account. Stationarity with respect to other directions can, of course, be imposed additionally.

The calculations above also show that conservation of the *total* particle-number and the *total* spin are respected with site-independent variations, i.e., with a site-independent $\chi_i(z) = \chi(z)$ only. For the case of the particle number, this is equivalent with an arbitrarily time-dependent but *spatially homogeneous* variation of the on-site energies only as the phase factors in the transformation law for the off-diagonal parameters cancel each other. Analogously, the total spin is conserved within SFT if an arbitrarily time-dependent but *spatially homogeneous* magnetic field coupling to the total spin of the reference system is treated as a variational parameter.

3.9.2 Energy conservation

The case of energy conservation is more elaborate. This is related to the fact that the SFT is a variational approach which focuses on one-particle quantities, i.e., on the variational optimization of the one-particle self-energy and thus of the one-particle Green's function, while the interaction part of the total energy is a two-particle quantity. Fortunately, it can be expressed in terms of the one-particle Green's function and self-energy using the equation of motion, as we discussed in Sec. 2.4.2. We can therefore proceed analogously to particle-number and spin conservation and again try to make use of the ideas of Baym and Kadanoff [118, 119]. Complications are nevertheless to be expected and found in fact.

Adopting Eqs. (2.50) and (2.52), the kinetic (and potential) energy $E_{\mathrm{kin}}(t)$ and the interaction energy $E_{\mathrm{int}}(t)$ when evaluated within the SFT read

$$E_{\mathrm{kin}}(t) = -i \operatorname{tr}\left(\boldsymbol{\lambda}'_{\mathrm{opt}}(t)\boldsymbol{G}^{\mathrm{SFT}}(t,t^+)\right), \tag{3.91}$$

$$E_{\mathrm{int}}(t) = -\frac{i}{4}\operatorname{tr}\left((\boldsymbol{\Sigma}_{\boldsymbol{\lambda}'_{\mathrm{opt}},\boldsymbol{U}} \circ \boldsymbol{G}^{\mathrm{SFT}} + \boldsymbol{G}^{\mathrm{SFT}} \circ \boldsymbol{\Sigma}_{\boldsymbol{\lambda}'_{\mathrm{opt}},\boldsymbol{U}})(t,t^+)\right). \tag{3.92}$$

An approximation constructed within the SFT will respect energy balance if Eq. (2.56) holds but with $\boldsymbol{\Sigma}$ replaced by $\boldsymbol{\Sigma}_{\boldsymbol{\lambda}'_{\mathrm{opt}},\boldsymbol{U}}$ and with $\boldsymbol{G}$ replaced by $\boldsymbol{G}^{\mathrm{SFT}}$. Thus, the goal is to find a class of transformations of the one-particle parameters such that their corresponding first-order variations around the stationary point generate the mentioned

equation (2.56) as the SFT Euler equation. In principle, this can be achieved with

$$\boldsymbol{\lambda}'(z) \mapsto \bar{\boldsymbol{\lambda}}'(z) = i(1 - \dot{\theta}^{-1/2})\partial_z + \frac{i}{4}\dot{\theta}^{-3/2}\ddot{\theta} + \dot{\theta}^{1/2}\boldsymbol{\lambda}'(\theta) \,, \tag{3.93}$$

where $\theta(z)$ is an arbitrary real function on the contour with $\partial_z\theta(z) \neq 0$ which describes a transformation of the time scale. Note that due to the term $\propto \partial_z$ the action of $\bar{\boldsymbol{\lambda}}'(z)$ is nonlocal in time. This is a severe complication if $\bar{\boldsymbol{\lambda}}'(z)$ should represent parameters of an actual impurity Hamiltonian, as discussed in Sec. 3.9.3 below. It is nevertheless illustrative to see how energy conservation can be derived if the self-energy functional is stationary under the variations defined by Eq. (3.93).

The time-dependent transformation of the one-particle parameters induces a corresponding transformation of the exact Green's function $\boldsymbol{G}' \equiv \boldsymbol{G}_{\boldsymbol{\lambda}',U}$ and of the exact self-energy $\boldsymbol{\Sigma}' \equiv \boldsymbol{\Sigma}_{\boldsymbol{\lambda}',U}$ of the reference system. For $\boldsymbol{G}'$ we have:

$$\boldsymbol{G}'(z_1, z_2) \mapsto \bar{\boldsymbol{G}}'(z_1, z_2) = \dot{\theta}_1^{1/4}\boldsymbol{G}'(\theta_1, \theta_2)\dot{\theta}_2^{1/4} \,, \tag{3.94}$$

where the short hand notation $\theta_1 = \theta(z_1)$ and $\dot{\theta}_1 = \partial_{z_1}\theta(z_1)$ etc. is used. Via the skeleton-diagram expansion $\boldsymbol{\Sigma}' = \widehat{\boldsymbol{\Sigma}}_U[\boldsymbol{G}']$ [cf. Eq. 2.37], this induces the following transformation of the self-energy:

$$\boldsymbol{\Sigma}'(z_1, z_2) \mapsto \bar{\boldsymbol{\Sigma}}'(z_1, z_2) = \dot{\theta}_1^{3/4}\boldsymbol{\Sigma}'(\theta_1, \theta_2)\dot{\theta}_2^{3/4} \,. \tag{3.95}$$

Namely, any internal vertex at time z_i connects to four propagators and thereby collects a factor $\dot{\theta}_i$ by which the implicit z_i integration can be transformed into a θ_i integration. The factors $\dot{\theta}_1^{3/4}$ and $\dot{\theta}_2^{3/4}$ in Eq. (3.95) result from the three incoming and outgoing propagators at the two "external" vertices. Now, Eq. (3.94) is verified by showing that the asserted expression for the transformed Green's function $\bar{\boldsymbol{G}}'(z_1, z_2)$ together Eq. (3.95) satisfies the equation of motion for transformed one-particle parameters, Eq. (3.93). Again, a proof for this is given in the following. To verify the transformed equation of motion,

$$i\partial_{z_1}\bar{\boldsymbol{G}}'(z_1, z_2) = \delta_{\mathcal{C}}(z_1, z_2) + \bar{\boldsymbol{\lambda}}'(z_1)\bar{\boldsymbol{G}}'(z_1, z_2) + (\bar{\boldsymbol{\Sigma}}' \circ \bar{\boldsymbol{G}}')(z_1, z_2) \,, \tag{3.96}$$

we first compute the left-hand side:

$$\begin{aligned}
i\partial_{z_1}\bar{\boldsymbol{G}}'(z_1, z_2) &= i\partial_{z_1}\left(\dot{\theta}_1^{1/4}\boldsymbol{G}'(\theta_1, \theta_2)\dot{\theta}_2^{1/4}\right) \\
&= \frac{i}{4}\dot{\theta}_1^{-3/4}\ddot{\theta}_1\boldsymbol{G}'(\theta_1, \theta_2)\dot{\theta}_2^{1/4} + i\dot{\theta}_1^{5/4}\partial_{\theta_1}\boldsymbol{G}'(\theta_1, \theta_2)\dot{\theta}_2^{1/4} \\
&= \dot{\theta}_1^{3/4}\left(\frac{i}{4}\dot{\theta}_1^{-3/2}\ddot{\theta}_1\boldsymbol{G}'(\theta_1, \theta_2) + i\dot{\theta}_1^{1/2}\partial_{\theta_1}\boldsymbol{G}'(\theta_1, \theta_2)\right)\dot{\theta}_2^{1/4} \,. \tag{3.97}
\end{aligned}$$

For the second summand on the right hand side of Eq. (3.96) and using Eq. (3.93) we

find:

$$
\begin{aligned}
\bar{\boldsymbol{\lambda}}'&(z_1)\bar{\boldsymbol{G}}'(z_1, z_2) \\
&= \left(i(1 - \dot{\theta}_1^{-1/2})\partial_z + \frac{i}{4}\dot{\theta}_1^{-3/2}\ddot{\theta}_1 + \dot{\theta}_1^{1/2}\boldsymbol{\lambda}'(\theta_1) \right) \dot{\theta}_1^{1/4}\boldsymbol{G}'(\theta_1, \theta_2)\dot{\theta}_2^{1/4} \\
&= \left(\frac{i}{4}(1 - \dot{\theta}_1^{-1/2})\dot{\theta}_1^{-3/4}\ddot{\theta}_1 + \frac{i}{4}\dot{\theta}_1^{-5/4}\ddot{\theta}_1 + \dot{\theta}_1^{3/4}\boldsymbol{\lambda}'(\theta_1) + i(1 - \dot{\theta}_1^{-1/2})\dot{\theta}_1^{5/4}\partial_{\theta_1} \right) \times \\
&\quad \times \boldsymbol{G}'(\theta_1, \theta_2)\dot{\theta}_2^{1/4} \\
&= \dot{\theta}_1^{3/4}\left(\frac{i}{4}\dot{\theta}_1^{-3/2}\ddot{\theta}_1\boldsymbol{G}'(\theta_1, \theta_2) + i\dot{\theta}_1^{1/2}\partial_{\theta_1}\boldsymbol{G}'(\theta_1, \theta_2) \right)\dot{\theta}_2^{1/4} \\
&\quad - \dot{\theta}_1^{3/4}\Big(i\partial_{\theta_1}\boldsymbol{G}'(\theta_1, \theta_2) - \boldsymbol{\lambda}'(\theta_1)\boldsymbol{G}'(\theta_1, \theta_2) \Big)\dot{\theta}_2^{1/4}. \tag{3.98}
\end{aligned}
$$

Combining both equations leaves us with the following expression:

$$
\begin{aligned}
i\partial_{z_1}\bar{\boldsymbol{G}}'(z_1, z_2) - \bar{\boldsymbol{\lambda}}'(z_1)\bar{\boldsymbol{G}}'(z_1, z_2) = \\
\dot{\theta}_1^{3/4}\Big(i\partial_{\theta_1}\boldsymbol{G}'(\theta_1, \theta_2) - \boldsymbol{\lambda}'(\theta_1)\boldsymbol{G}'(\theta_1, \theta_2) \Big)\dot{\theta}_2^{1/4}. \tag{3.99}
\end{aligned}
$$

Furthermore, using the substitution rule, we find both, $(\bar{\boldsymbol{\Sigma}}' \circ \bar{\boldsymbol{G}}')(z_1, z_2) = \dot{\theta}_1^{3/4}(\boldsymbol{\Sigma}' \circ \boldsymbol{G}')(\theta_1, \theta_2)\dot{\theta}_2^{1/4}$ and $\delta(z_1, z_2) = \dot{\theta}_1\delta(\theta_1, \theta_2) = \dot{\theta}_1^{3/4}\delta(\theta_1, \theta_2)\dot{\theta}_2^{1/4}$. Thus, assembling all parts and cancel-ling the factors $\dot{\theta}_1^{3/4}$ and $\dot{\theta}_2^{1/4}$ completes the proof.

With this, we can now consider the first-order variations of $\boldsymbol{\Sigma}'$ [Eq. 3.95] induced by the transformation (3.93), namely $\delta\boldsymbol{\Sigma}' = \delta\boldsymbol{\Sigma}'(\theta_1, \theta_2)/\delta\theta|_{\theta=z} \circ \delta\theta$, are given by:

$$
\begin{aligned}
\delta\Sigma'(2, 1) = \int_{\mathcal{C}} dz &\left[\frac{3}{4}\Sigma'(2, 1)\left(\frac{\partial}{\partial z_2}\delta_{\mathcal{C}}(z_2 - z) \right) + \frac{3}{4}\Sigma'(2, 1)\left(\frac{\partial}{\partial z_1}\delta_{\mathcal{C}}(z_1 - z) \right) \right. \\
&\left. + \left(\frac{\partial}{\partial z_2}\Sigma'(2, 1) \right)\delta_{\mathcal{C}}(z_2 - z) + \left(\frac{\partial}{\partial z_1}\Sigma'(2, 1) \right)\delta_{\mathcal{C}}(z_1 - z) \right]\delta\theta(z). \tag{3.100}
\end{aligned}
$$

Inserting this into the Euler equation in its variational form, i.e., Eq. (3.79), integrating

by parts and exploiting the δ-functions, we are left with:

$$
\begin{aligned}
0 = \ & \beta\delta\widehat{\Omega}_{\boldsymbol{\lambda},U}[\boldsymbol{\Sigma}_{\boldsymbol{\lambda}',U}]\Big|_{\boldsymbol{\lambda}'=\boldsymbol{\lambda}'_{\mathrm{opt}}} \\
= \ & \Bigg\{ \int_{\mathcal{C}} dz_1 \left[-\frac{3}{4}\sum_{\alpha_1}\int d2\, \frac{\partial}{\partial z_1}\Big(\Sigma_{\boldsymbol{\lambda}',U}(1,2)G^{\mathrm{SFT}}(2,1^+) + G^{\mathrm{SFT}}(1,2)\Sigma_{\boldsymbol{\lambda}',U}(2,1^+)\Big) \right. \\
& + \sum_{\alpha_1}\int d2\, \left(\left(\frac{\partial}{\partial z_1}\Sigma_{\boldsymbol{\lambda}',U}(1,2)\right)G^{\mathrm{SFT}}(2,1^+) + G^{\mathrm{SFT}}(1,2)\frac{\partial}{\partial z_1}\Sigma_{\boldsymbol{\lambda}',U}(2,1^+)\right) \\
& + \frac{3}{4}\sum_{\alpha_1}\int d2\, \frac{\partial}{\partial z_1}\Big(\Sigma_{\boldsymbol{\lambda}',U}(1,2)G_{\boldsymbol{\lambda}',U}(2,1^+) + G_{\boldsymbol{\lambda}',U}(1,2)\Sigma_{\boldsymbol{\lambda}',U}(2,1^+)\Big) \\
& - \left. \sum_{\alpha_1}\int d2\, \left(\left(\frac{\partial}{\partial z_1}\Sigma_{\boldsymbol{\lambda}',U}(1,2)\right)G_{\boldsymbol{\lambda}',U}(2,1^+) + G_{\boldsymbol{\lambda}',U}(1,2)\frac{\partial}{\partial z_1}\Sigma_{\boldsymbol{\lambda}',U}(2,1^+)\right) \right] \times \\
& \times \delta\theta(z_1) \Bigg\}_{\boldsymbol{\lambda}'=\boldsymbol{\lambda}'_{\mathrm{opt}}} .
\end{aligned}
\tag{3.101}
$$

At the stationary point, this holds for all variations $\delta\theta(z_1)$. Hence, the term in the square brackets must vanish. We assume that the energy-balance relation is satisfied *in the reference system* as expressed by Eq. (2.56), with $\boldsymbol{\Sigma} \equiv \boldsymbol{\Sigma}_{\boldsymbol{\lambda},U}$ replaced by $\boldsymbol{\Sigma}_{\boldsymbol{\lambda}',U}$ and with $\boldsymbol{G} \equiv \boldsymbol{G}_{\boldsymbol{\lambda},U}$ replaced by $\boldsymbol{G}_{\boldsymbol{\lambda}',U}$. This implies that the last two terms in Eq. (3.101) vanish and therewith the first two terms in the square bracket must vanish which is just equivalent with total-energy balance within the SFT. We conclude that within the SFT the energy-conservation law is proliferated from the reference system to the original system, if stationarity of the self-energy functional under the variations defined by Eq. (3.93) can be enforced.

3.9.3 Energy conservation — revised

However, there are two important points that need further discussion. First, we recall that the interaction parameters have been assumed as constant when we derived the energy balance relation in Sec. 2.4.2. In a subsequent discussion, we argued that for many relevant cases, we will be interested in a conservation of energy *after* the system has been excited by a (short) time-dependent modulation of the parameters, i.e., a possible violation of the energy balance will be relevant only over a short initial period of time. However, it is worth mentioning that taking into account an *explicit* time-dependence of the one-particle parameters, as has been done in Sec. 2.4.2, now actually proves essential since for the reference system we have to expect a nontrivial time-dependency for the optimal parameter also *after* the stimulation of the system has elapsed. Moreover, since the conservation laws are proliferated from the reference system, an energy balance relation also in presence of some time-dependent one-particle parameters has to be valid.

The second point to be discussed is that according to the presence of the contour derivative ∂_z in the transformation law Eq. (3.93), time-nonlocal one-particle parameters of the reference system are generated by a generic transformation of the time scale $\theta(z)$.

Within the present (Hamiltonian) formalism, time-nonlocal parameters $\boldsymbol{\lambda}'(z_1, z_2)$ must be generated effectively by considering additional bath degrees of freedom in the reference system, i.e., $\boldsymbol{\lambda}'(z_1, z_2)$ must be understood as a corresponding hybridization function

$$\boldsymbol{\lambda}'(z_1, z_2) = \boldsymbol{V}'(z_1)\boldsymbol{G}'_0(z_1, z_2)\boldsymbol{V}'(z_2)\,, \tag{3.102}$$

where $\boldsymbol{G}'_0$ is the noninteracting bath Green's function and $\boldsymbol{V}'$ the hybridization matrix element. However, a time-nonlocal term of the form ∂_z can presumably not be represented with the help of a *finite* number of bath degrees of freedom (see also Ref. [154] for a discussion). On the other hand, with the consideration of a *continuum* of bath sites one is essentially restricted to DMFT or to cellular DMFT as approximations that can be constructed within the SFT framework. This conflicts with the original intention to construct variational and consistent approximations using reference systems with a few degrees of freedom only which are accessible to an exact-diagonalization technique.

However, the argument can also be turned by stating that the degree to which energy conservation is violated within an SFT-based approximation can be controlled systematically by increasing the number of variational degrees of freedom in the reference system. Adding bath degrees of freedom, for example, is expected to substantially improve the degree to which energy conservation is respected.

Another option is to enforce energy conservation. As the SFT is a variational approach, energy conservation can easily be imposed as an additional constraint that is used to fix the time-dependence of one of the variational parameters. This represents an *ad hoc* but physically motivated modification of the original theory by which the search for optimal values of the remaining variational parameters is confined to a subspace where $E_{\text{tot}} = \text{const}$. Here, $E_{\text{tot}} = E_{\text{tot}}[\boldsymbol{\lambda}'](z)$ is given by Eqs. (3.91) and (3.92). The SFT variational principle, Eq. (3.19), is replaced by

$$\frac{\delta}{\delta\boldsymbol{\lambda}'(z)}\Big(\widehat{\Omega}_{\boldsymbol{\lambda},\boldsymbol{U}}[\boldsymbol{\Sigma}_{\boldsymbol{\lambda}',\boldsymbol{U}}] - \int_{\mathcal{C}_K} dz'\xi(z')E_{\text{tot}}[\boldsymbol{\lambda}'](z')\Big) = 0\,, \tag{3.103}$$

with the constraint

$$E_{\text{tot}}[\boldsymbol{\lambda}'](z) - \text{const.} = 0\,, \tag{3.104}$$

where $\xi(z)$ is a Lagrange multiplier on the Keldysh branch $\mathcal{C}_K$. Alternatively, for driven systems with an explicitly time-dependent Hamiltonian, one may impose Eq. (2.56), again formulated in terms of $\boldsymbol{G}^{\text{SFT}}$ and $\boldsymbol{\Sigma}_{\boldsymbol{\lambda}',\boldsymbol{U}}$, as a constraint. Again, variations in the transverse direction must be considered (i.e., $\boldsymbol{\lambda}_+(t) = -\boldsymbol{\lambda}_-(t)$), followed by an evaluation on the physical manifold (i.e., $\boldsymbol{\lambda}_+(t) = \boldsymbol{\lambda}_-(t)$, $\xi_+ = \xi_-$), as discussed in Sec. 3.5. Furthermore, Eqs. (3.104) and (3.103) have an inherent causal structure analogous to the full SFT equations and may thus be solved by a similar propagation algorithm as going to be discussed in Sec. 4.1.

4 Numerical implementation

In the following, we will put forward a numerical implementation of the nonequilibrium self-energy functional theory, which is by far more complex than its equilibrium variant. In Sec. 4.1 we will derive a stable and reliable propagation scheme for the optimal time-dependent parameters of the reference system and give minimal benchmark results for both the VCA as well as the DIA with reference systems consisting of two sites only in both cases (i.e., $L_c = 2, L_b = 0$ for the VCA and $L_c = 1, L_b = 1$ for the DIA). In the following sections we will briefly mention technical aspects which will allow for a more efficient implementation, namely symmetry relations between elements of higher Green's functions and hence of the self-energy functional's derivatives in Sec. 4.2 and furthermore on restrictions of the actual set of required variational parameters in Sec. 4.3.

4.1 Propagation scheme

With the *time-dependent* Euler equation (3.39) we are facing a profound root-finding problem of formally infinite dimensions. However, the SFT variational principle is inherently causal which allows us to determine the optimal parameters at a given time on a discrete time grid, without affecting the results at previous grid times, and then proceed to the next time. This causality is most easily seen when discussing Eq. (3.37): The integrals over z_3 and z_4 extend over the entire contour $\mathcal{C}$ but can be confined to times which are (physically) earlier than $t_{\max} = t_1$ (cf. Fig. 2.1). If one or both times are located beyond t_1, the later time can be shifted from the upper to the lower branch (or vice versa) without altering the contour ordering (see Sec. 2.3.1), and the respective contributions to the integral cancel. Thus, at time t_1, all quantities in the Euler equation (3.39) and therewith the parameter $\boldsymbol{\lambda}'_{\mathrm{opt}}(t_1)$ itself depend on parameters at earlier times only.

Unfortunately, a straightforward numerical solution of the Euler equation (3.39) turns out to be impossible. The optimal parameters, determined by standard root-finding techniques, quickly accumulate a large error after a few time steps only such that a reasonable solution cannot be found in this way. Generally, for a functional depending parametrically on time, which is evaluated on a finite time grid and the parameters of which are varied only at the very last instant of time, we expect the explicit dependence of the variation of the functional on the time step Δt to scale as $(\Delta t)^n$ with $n \geq 1$,
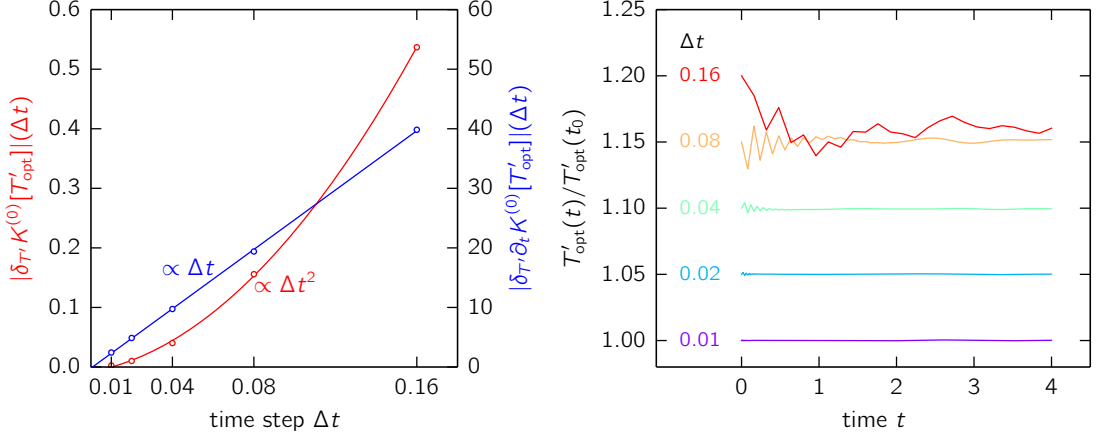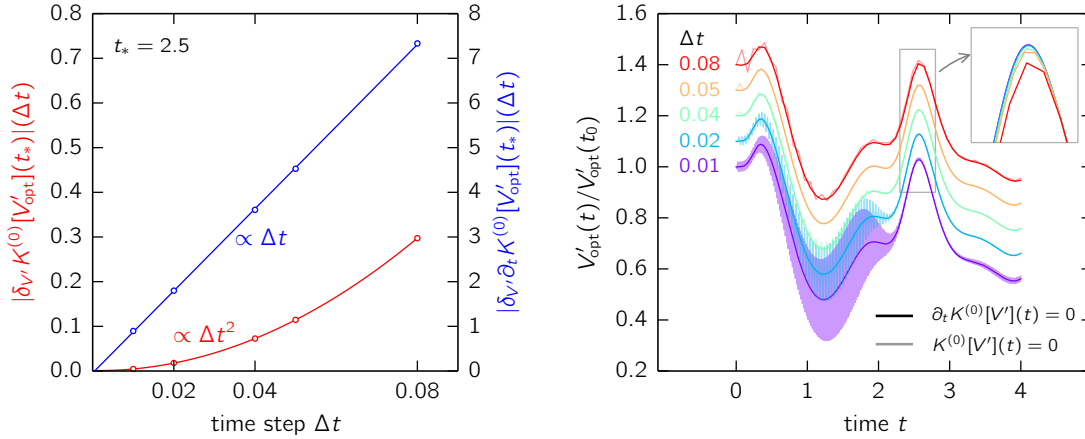

Figure 4.1: Test of the numerical implementation for the time-propagation with the VCA. The system is a one-dimensional chain of 100 sites at $\beta = 6$ and held at equilibrium with $U = 4$. As a reference system a two-site cluster is used. *Left*: Δt dependence of the Jacobian of $\boldsymbol{K}^{(0)}[\boldsymbol{\lambda}'](t)$ (red, left ordinate axis) and of $\partial_t \boldsymbol{K}^{(0)}[\boldsymbol{\lambda}'](t)$ (blue, right ordinate axis). Note that the ordinate axes' scales differ by one orders of magnitude. Results are independent of the time t and the Jacobians are evaluated at the initial time step. *Right:* Time dependence of the optimal parameters, obtained as the roots of $\partial_t \boldsymbol{K}^{(0)}[\boldsymbol{\lambda}'](t) = 0$ [Eq. (4.2)] for different Δt; those for $\boldsymbol{K}^{(0)}[\boldsymbol{\lambda}'](t) = 0$ could not be stabilized and diverged after only a few time steps. The ordinate axis refers to the result for $\Delta t = 0.01$; results for larger Δt are constantly shifted by multiples of 0.05.

since for an infinitesimally fine grid variations at a single instant of time would reduce to variations on a null set, and thus the variation of the functional must vanish.

If one aims to solve Eq. (3.39) at a given time t, keeping the solution $\boldsymbol{\lambda}'_{\text{opt}}$ fixed at earlier times, the variation $\delta_{\boldsymbol{\lambda}'(t)} \boldsymbol{K}^{(0)}[\boldsymbol{\lambda}'_{\text{opt}}](t)$ of the parameters at the last time-step will scale as $(\Delta t)^2$, if the whole implementation is based on an equidistant time-grid Δt. This is verified numerically in Figs. 4.1 and 4.2 (both left) for two special cases within both the VCA as well as the DIA (as described in the figure caption). This scaling is independent of the quadrature rules used in solving the time integrals (if the accuracy of those scales as $(\Delta t)^2$ or better). Hence the observed $(\Delta t)^2$ scaling is in fact due to the Jacobian $\delta_{\boldsymbol{\lambda}'(t)} \boldsymbol{K}^{(0)}[\boldsymbol{\lambda}'_{\text{opt}}](t)$ itself and turned out to be detrimental for the stability of the algorithm for practically reasonable choices of Δt.

Fortunately, this problem can be overcome by requiring the *time derivative* of $\boldsymbol{K}^{(0)}[\boldsymbol{\lambda}'](t)$ [see Eq. (3.39)] to vanish for all times $t > t_0$ and by fixing the initial conditions at t_0 by Eq. (3.39). Hence, instead of solving the Euler equation (3.39) for all times, we rather

Figure 4.2: Test of the numerical implementation for the time-propagation with the DIA. The system is a one-dimensional chain of 40 sites at $\beta = 6$ and the interaction is ramped from $U_{\text{ini}} = 1$ to $U_{\text{fin}} = 4$ within $\Delta t_{\text{ramp}} = 0.4$. *Left*: Δt dependence of the Jacobians (same as for VCA, see Fig. 4.1) evaluated at the time $t_* = 2.5$. *Right:* Time dependence of the optimal parameters within DIA. Results are obtained as the roots of both $\boldsymbol{K}^{(0)}[\boldsymbol{\lambda}'](t) = 0$ and $\partial_t \boldsymbol{K}^{(0)}[\boldsymbol{\lambda}'](t) = 0$ [see Eqs. (4.2) and (4.3)] for different Δt. The ordinate axis refers to the result for $\Delta t = 0.01$; results for larger Δt are constantly shifted by multiples of 0.1. The inset centered at $t_* = 2.5$ shows how the (unshifted) results converge with smaller time steps.

consider

$$\boldsymbol{K}^{(0)}[\boldsymbol{\lambda}'](t)\Big|_{\boldsymbol{\lambda}'=\boldsymbol{\lambda}'_{\text{opt}}} = 0\,, \qquad \text{for } t = t_0\,, \tag{4.1a}$$

$$\partial_t \boldsymbol{K}^{(0)}[\boldsymbol{\lambda}'](t)\Big|_{\boldsymbol{\lambda}'=\boldsymbol{\lambda}'_{\text{opt}}} = 0\,, \qquad \text{for } t > t_0\,. \tag{4.1b}$$

As can be seen in Figs. 4.1 and 4.2 (both left), the dependence on Δt is only linear in this case. This greatly improves the accuracy of the parameter optimization and allows us to trace the optimal variational parameters as a function of time. As a simple numerical check, one may consider the *equilibrium* problem. The expected time *in*dependence of the optimal variational parameters is indeed found for sufficiently small Δt, see Fig. 4.1 (right). In Fig. 4.2 we additionally show and compare some nontrivial dynamics of the optimal parameter of the DIA induced by a ramp of the interaction and as obtained from the roots of both $\boldsymbol{K}^{(0)}[\boldsymbol{\lambda}'](t)$ and $\partial_t \boldsymbol{K}^{(0)}[\boldsymbol{\lambda}'](t)$ (see the figure's caption for details).

According to Eq. (3.39), the time derivative $\partial_t \boldsymbol{K}^{(0)}[\boldsymbol{\lambda}'](t)$ can be obtained from the corresponding equations of motion for the four-point vertex function $\boldsymbol{L}_{\boldsymbol{\lambda}',\boldsymbol{U}}$. There are two qualitatively different dependencies on t: The first one results from the boundary terms due to the time-ordering operator comprised by all Green's functions. Contributions from this one cancel out when taking the time derivative. The second one is the explicit dependence of the annihilator and the creator on the external time t_1. This is
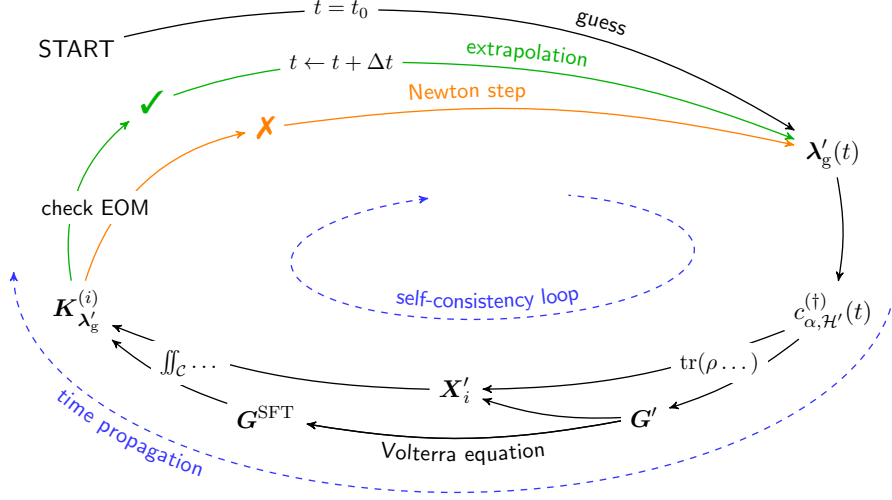
Figure 4.3: Sketch of the propagation algorithm for the optimal parameters. Note that $\boldsymbol{X}'_i$ is short for $\boldsymbol{L}' = \boldsymbol{X}'_0$ and $\boldsymbol{M}' = \boldsymbol{X}'_1$. See text for discussion.

governed by the Heisenberg equation of motion [cf. Eq. 2.28]. Commuting the operators with the one-particle part of the Hamiltonian simply results in matrix products with $\boldsymbol{\lambda}'$ while commuting with the interacting part gives rise to higher-order products of annihilators and creators which we denote by ψ or $\psi^\dagger$, respectively: $\left[c(1), H'_1(1)\right] \equiv \psi(1)$ and $\left[H'_1(1), c^\dagger(1)\right] \equiv \psi^\dagger(1)$ [see also Eqs. 2.28 and (A.4)]. Thus, the time derivative of $\boldsymbol{K}^{(0)}[\boldsymbol{\lambda}'](t)$ acquires the form:

$$\partial_t \boldsymbol{K}^{(0)}[\boldsymbol{\lambda}'](t) = \left[\boldsymbol{K}^{(0)}[\boldsymbol{\lambda}'](t), \boldsymbol{\lambda}'(t)\right] + \boldsymbol{K}^{(1)}[\boldsymbol{\lambda}'](t) \,, \tag{4.2}$$

where we have used Eq. (3.39), i.e.,

$$K^{(0)}[\boldsymbol{\lambda}']_{\alpha_2\alpha_1}(t_1) = \iint d3\,d4\, Y_{\boldsymbol{\lambda}',\boldsymbol{\lambda},\boldsymbol{U}}(4,3)\, L_{\boldsymbol{\lambda}',\boldsymbol{U}}(3,2,1^+,4)\Big|_{z_2=z_1=t_1} \,, \tag{4.3}$$

and where

$$K^{(1)}[\boldsymbol{\lambda}']_{\alpha_2\alpha_1}(t_1) = \iint d3\,d4\, Y_{\boldsymbol{\lambda}',\boldsymbol{T},\boldsymbol{U}}(4,3)\, M_{\boldsymbol{\lambda}',\boldsymbol{U}}(3,2,1^+,4)\Big|_{z_2=z_1=t_1} \,, \tag{4.4}$$

with

$$M_{\boldsymbol{\lambda}',\boldsymbol{U}}(3,2,1^+,4) = L_{\boldsymbol{\lambda}',\boldsymbol{U}}(3,2,1^+_\psi,4) - L_{\boldsymbol{\lambda}',\boldsymbol{U}}(3,2_\psi,1^+,4) \,. \tag{4.5}$$

The subscript ψ indicates that c and $c^\dagger$ are replaced by ψ and $\psi^\dagger$ in the respective correlation function. For example, $iG_{\boldsymbol{\lambda}',\boldsymbol{U}}(1_\psi,2) = \langle \mathcal{T}_\mathcal{C} \psi(1) c^\dagger(2)\rangle_{\boldsymbol{\lambda}',\boldsymbol{U}}$.

The algorithm for the numerical implementation of the SFT in the general nonequilibrium case [Eq. (4.1)] is sketched in Fig. 4.3. The following steps are performed at each time step:

(i) At a given time t and for certain guessed parameters $\boldsymbol{\lambda}'_{\mathrm{g}}(t)$, we propagate $c^\dagger_\alpha(t)$ and $c_\alpha(t)$ for all relevant orbitals α by a time step Δt and store their respective representations in the occupation-number basis. For small cluster sizes, this is straightforward. Therewith, arbitrary correlation functions can be calculated for arbitrary times on the contour up to the time t. While the single particle Green's function $\boldsymbol{G}'$ can be updated from time step to time step and kept in the storage, the higher correlation functions $\boldsymbol{L}'$ and $\boldsymbol{M}'$ have to be recalculated on-the-fly for *any* time step and after any update of $\boldsymbol{\lambda}'_{\mathrm{g}}(t)$, because of the external time t. Symmetries can be exploited to reduce the actual number of elements that have to be calculated and are listed separately in Sec. 4.2.

(ii) The SFT Green's function $\boldsymbol{G}^{\mathrm{SFT}}$ is obtained from the CPT equation (3.30), which can be cast in the form of a Volterra equation of second kind: $(\boldsymbol{1}-\boldsymbol{G}_{\boldsymbol{\lambda}',\boldsymbol{U}}\boldsymbol{\Lambda})\circ\boldsymbol{G}^{\mathrm{SFT}} = \boldsymbol{G}_{\boldsymbol{\lambda}',\boldsymbol{U}}$. The latter is solved up to time t by standard techniques (cf. Refs. [213–216]). Here, we exploit the translational symmetries of $\boldsymbol{\Lambda}$ and of $\boldsymbol{G}^{\mathrm{SFT}}$ by Fourier transformation with respect to the super-lattice.

(iii) The correlation functions $\boldsymbol{L}'$, $\boldsymbol{M}'$ and $\boldsymbol{G}^{\mathrm{SFT}}$, are then used to calculate both $\boldsymbol{K}^{(0)}[\boldsymbol{\lambda}'](t)$ and $\boldsymbol{K}^{(1)}[\boldsymbol{\lambda}'](t)$ via Eqs. (4.3) and (4.4). For the initial time t_0, only those integrations contribute where both times are on the Matsubara branch. For any later time, the mixed and Keldysh integrations have to be carried out, too. Results for the integrals from earlier time steps cannot be recycled, due to the external time t appearing in the correlation functions $\boldsymbol{L}'$ and $\boldsymbol{M}'$. For both, the integrations involved in the Euler equation (4.1) as well as in the Volterra equation, we use high-order integration schemes, like the Newton-Cotes rules or the Gregory rules [215, 217], to allow for large $\Delta\tau$ and large Δt steps. This in principle necessitates to consider the same high-order integration schemes for the time-evolution operator.*

(iv) Generally, the initial guess $\boldsymbol{\lambda}'_{\mathrm{g}}(t)$ will not be a root of Eqs. (4.1), and must therefore be updated. The standard way of doing this, is to apply Newton's method.

---

* For a real-time propagation also the time-evolution operator can be implemented in a high-order scheme, e.g., by making use of techniques suggested by Alvermann and Fehske [218]. This either makes it necessary to know the respective Hamilton operator explicitly at *unequally* spaced times within the propagation time interval, as needed for Gaussian quadrature, or to extrapolate beyond the time interval to past times for the application of "extended" open Newton-Cotes formulas [217]. The first case is not feasible here, since our algorithm works on an equidistant time grid. The second, however, turned out to be highly unstable for any integration scheme of higher order than the trapezoidal rule. This might be due to Runge's phenomenon [219, 220]. Another explanation could be the following: changing the value of the considered parameter at the last time affects the shape of the fitted function for *all* nodes, and hence implicitly induces some acausal propagation which spoils a stable propagation. This could be bypassed by simultaneously optimizing parameters at all nodes involved in the actual fit which would causally fix only the parameters at the "earliest" of these nodes. This however would increase the numerical effort for each optimization and had its own problems when we tried it. However, leaving these difficulties as a side-remark their solution was beyond the scope of the present work and we could obtain satisfying results already with our implementation.

This, however, requires the knowledge of the (inverse of the) functional's Jacobian $\delta_{\boldsymbol{\lambda}'(t_0)}\boldsymbol{K}^{(0)}[\boldsymbol{\lambda}'](t_0)$ or $\delta_{\boldsymbol{\lambda}'(t)}\partial_t\boldsymbol{K}^{(0)}[\boldsymbol{\lambda}'](t)$ respectively. Both, the implementation of an analytical expression for the Jacobian or a direct numerical evaluation via finite difference methods are rather costly options and thus not feasible. We thus employ Broyden's method [221, 222], which provides increasingly improved updates for the (inverse of the) Jacobian during the course of the Newton iteration, starting from an initial guess for both, the root as well as the Jacobian itself. However, at the initial time we evaluate the Jacobian numerically by finite differences at some guessed parameter. This improves the success and the speed of the method significantly. At later times, we extrapolate both the optimal parameter as well as the inverse Jacobian of $\partial_t\boldsymbol{K}^{(0)}[\boldsymbol{\lambda}'](t)$ to again start the Broyden iteration from an accurate initial guess - with this, we reliably find the roots of the respective functional after only one to three iterations per time step. Concerning the equilibrium case, it is worth mentioning that to the best of our knowledge, all previous SFT studies evaluated the grand potential $\widehat{\Omega}_{\boldsymbol{T},\boldsymbol{U}}[\boldsymbol{\Sigma}_{\boldsymbol{V}',\boldsymbol{U}}]$ [cf. Eq. 3.18] (and possibly its derivatives [171]) directly to search for stationary points. Throughout this thesis we instead determine the equilibrium solution by evaluating its derivative analytically and look for the roots of $\boldsymbol{K}^{(0)}[\boldsymbol{\lambda}'](t_0)$ by solving Eq. (4.1a).

Finally, we would like to add an important remark regarding the solution of Eq. (4.1b). As Eq. (4.2) contains $\boldsymbol{\lambda}'(t)$ explicitly, a first naive approach would be to guess an "optimal" value $\boldsymbol{\lambda}'_{\mathrm{g}}(t)$, calculate $\boldsymbol{K}^{(0)}[\boldsymbol{\lambda}'_{\mathrm{g}}](t)$ and $\boldsymbol{K}^{(1)}[\boldsymbol{\lambda}'_{\mathrm{g}}](t)$, plug these into Eq. (4.2), solve the resulting equation $0 = \left[\boldsymbol{K}^{(0)}[\boldsymbol{\lambda}'_{\mathrm{g}}](t),\boldsymbol{\lambda}'(t)\right] + \boldsymbol{K}^{(1)}[\boldsymbol{\lambda}'_{\mathrm{g}}](t)$ for a new $\boldsymbol{\lambda}'(t)$, update both functionals and iterate this procedure until convergence. However, there are two complications. First, close to the optimal point, $\boldsymbol{K}^{(0)}[\boldsymbol{\lambda}'](t)$, and hence also $\boldsymbol{K}^{(1)}[\boldsymbol{\lambda}'](t)$ must vanish and therefore solving Eq. (4.2) for $\boldsymbol{\lambda}'(t)$ will get more and more unstable. Second, for a guessed parameter it is unlikely that the corresponding functionals will be compatible with Eq. (4.2), i.e., that a solution is existing at all. For this to be the case, e.g., $\boldsymbol{K}^{(1)}[\boldsymbol{\lambda}'_g](t)$ has to be trace-less, since it otherwise could not equal a commutator of two other matrices. Indeed, in our numerics this requirement is not met in general. More generally, Eqs. (4.2) and (4.1) can be understood as a special case of Sylvester's equation, namely $\boldsymbol{AX} - \boldsymbol{XB} = \boldsymbol{C}$, which has a unique solution for any matrix $\boldsymbol{C}$, if and only if the matrices $\boldsymbol{A}$ and $\boldsymbol{B}$ have distinct spectra (see Refs. [223–225]). In our case, this is clearly not the case, which is why we cannot expect a unique solution (or any solution at all), for some $\boldsymbol{K}^{(1)}[\boldsymbol{\lambda}'_g](t)$ as obtained for an arbitrarily guessed optimal parameter. A way out would be to not solve Eq. (4.1) directly, but minimize the norm of the left-hand side, which then, in any case, again suffers from the first complication.

4.2 Symmetries of contour Green's functions

In the following, we list some useful symmetries of all relevant (higher) contour Green's functions that arise in the context of the SFT Euler equations (4.1), namely $\boldsymbol{L}'_{\boldsymbol{\lambda}',\boldsymbol{U}}$ in the expression for $\boldsymbol{K}^{(0)}[\boldsymbol{\lambda}'](t)$ (4.3) and $\boldsymbol{M}_{\boldsymbol{\lambda}',\boldsymbol{U}}$ in the expression for $\boldsymbol{K}^{(1)}[\boldsymbol{\lambda}'](t)$ (4.4).

Note that we use the same notation as was introduced for Eqs. (3.42) to (3.54). In the following we will skip any labeling with regard to the reference system, since the listed properties are of general validity.

Keldysh components

$$G^{\gtrless}(3,4) = -G^{\gtrless}(4,3)^* \tag{4.6}$$

$$L^{3\gtrless}(3,2,1^+,4) = -L^{1\gtrless}(4,1,2^+,3)^* \tag{4.7}$$

$$L^{2\gtrless}(3,2,1^+,4) = -L^{2\gtrless}(4,1,2^+,3)^* \tag{4.8}$$

$$M^{3\gtrless}(3,2,1^+,4) = M^{1\gtrless}(4,1,2^+,3)^* \tag{4.9}$$

$$M^{2\gtrless}(3,2,1^+,4) = M^{2\gtrless}(4,1,2^+,3)^* \tag{4.10}$$

Mixed components

$$G^{\neg}(3,4) = G^{\ulcorner}(\beta-4,3)^* \tag{4.11}$$

$$L^{2\neg}(3,2,1^+,4) = L^{1\ulcorner}(\beta-4,1,2^+,3)^* \tag{4.12}$$

$$L^{2\ulcorner}(3,2,1^+,4) = L^{1\neg}(4,1,2^+,\beta-3)^* \tag{4.13}$$

$$M^{2\neg}(3,2,1^+,4) = -M^{1\ulcorner}(\beta-4,1,2^+,3)^* \tag{4.14}$$

$$M^{2\ulcorner}(3,2,1^+,4) = -M^{1\neg}(4,1,2^+,\beta-3)^* \tag{4.15}$$

Matsubara components

$$G^{1\gtrless}(4,3) = -G^{1\gtrless}(\beta-3,\beta-4)^* \tag{4.16}$$

$$L^{1\gtrless}(3,2,1^+,4) = -L^{1\gtrless}(\beta-4,1,2^+,\beta-3)^* \tag{4.17}$$

$$M^{1\gtrless}(3,2,1^+,4) = M^{1\gtrless}(\beta-4,1,2^+,\beta-3)^* \tag{4.18}$$

where in all cases z_1 and z_2 are on the Keldysh branch. Note that we used compact notations like e.g. $G^{(2),2\neg}(3,2,1^+,4) = G^{(2),2<}_{\alpha_3\alpha_2\alpha_1\alpha_4}(t_3,t_2,t_1^+,\tau_4)$, and $G(\beta-2,1) = G_{\alpha_2\alpha_1}(\beta-\tau_2,t_1)$.

Also note that the above symmetries have direct implications for $\boldsymbol{K}^{(i)}[\boldsymbol{\lambda}'](t)$ with $i \in \{0,1\}$, namely

$$\boldsymbol{K}^{(i)}[\boldsymbol{\lambda}'](t)^\dagger = -(-1)^i \boldsymbol{K}^{(i)}[\boldsymbol{\lambda}'](t)\,, \tag{4.19}$$

i.e., $\boldsymbol{K}^{(0)}[\boldsymbol{\lambda}'](t)$ is *skew-hermitian* and $\boldsymbol{K}^{(1)}[\boldsymbol{\lambda}'](t)$ is *hermitian*, at any time t. These can be directly deduced from Eqs. (4.3) and (4.4) and their explicit forms given by Eqs. (3.42) to (3.54).

4.3 Modifying variational degrees of freedom

Generally, one should considering variations of *all* one-particle parameters of the reference system. However, one might be confident with only varying a certain subset of parameters, while keeping others fixed, though this would clearly spoil the strict respectation of one-particle conservation laws (cf. Sec. 3.9.1). On the other hand, due to the

symmetry transformations which lead to the inherently conserving nature of the SFT, not all parameters have to be considered for variation, but their time-dependencies can be absorbed in other parameters' time-dependencies. In the following, we will comment on both cases, which might be useful for the implementation or when running the computer code for a given set of variational parameters.

4.3.1 Varying a subset of parameters

Let $\{\xi'_i\}_i$ be a subset of parameters of the reference system's Hamiltonian parameters (e.g., on-site energies, certain hopping parameters, or a parametrization of elements), i.e., for certain elements α, β we have $\lambda'_{\alpha\beta} = \lambda'[\boldsymbol{\xi}']_{\alpha\beta}$. By means of the chain rule, we directly obtain

$$
\begin{aligned}
-\beta \frac{\delta \widehat{\Omega}_{\boldsymbol{T},\boldsymbol{U}}[\boldsymbol{\Sigma}_{\boldsymbol{\lambda}'[\boldsymbol{\xi}']},\boldsymbol{U}]}{\delta \xi'_i(z)} &= \sum_{\alpha\beta} (-\beta) \frac{\delta \widehat{\Omega}_{\boldsymbol{T},\boldsymbol{U}}[\boldsymbol{\Sigma}_{\boldsymbol{\lambda}'},\boldsymbol{U}]}{\delta \lambda'_{\alpha\beta}(z)} \frac{\partial \lambda'_{\alpha\beta}(z)}{\partial \xi'_i(z)} \\
&= \sum_{\alpha\beta} K^{(0)}_{\boldsymbol{\lambda}';\beta\alpha}(z) \frac{\partial \lambda'_{\alpha\beta}(z)}{\partial \xi'_i(z)} \\
&= \mathrm{tr}\left(\boldsymbol{K}^{(0)}_{\boldsymbol{\lambda}'}(z) \frac{\partial \boldsymbol{\lambda}'(z)}{\partial \xi'_i(z)} \right) =: \bar{K}^{(0)}[\boldsymbol{\xi}']_i(z)\,,
\end{aligned}
\tag{4.20}
$$

i.e., a new functional $\bar{\boldsymbol{K}}^{(0)}$ which is just derived from the original functional $\boldsymbol{K}^{(0)}$ by "projection" onto the subspace of the $\boldsymbol{\xi}'$-parameters. In principle the same holds true also for the time-derivative of $\boldsymbol{K}^{(0)}$, though a little care should be taken concerning the last Eq. (4.20) since the projection matrix $\delta\boldsymbol{\lambda}'/\delta\boldsymbol{\xi}'$ may be explicitly time-dependent. However, it turns out that this is only the case if variations of the phase or the absolute value of a complex parameter are considered, which nevertheless might be disadvantageous due to possible discontinuities of the phase of a parameter (due to sign changes) and we hence only consider real and imaginary parts of elements of $\boldsymbol{\lambda}'$ as variational parameters.

4.3.2 Symmetry relations at stationarity

More importantly, not all parameters have to be varied, but some sets of variational parameters are equivalent via the gauge transformations [Eq. 3.82] introduced in Sec. 3.9 in the context of one-particle conservation laws within the SFT and which read as

$$
\begin{aligned}
\varepsilon'_{i\sigma}(z) &\mapsto \quad \bar{\varepsilon}'_{i\sigma}(z) = \varepsilon'_{i\sigma}(z) - \partial_z \chi_{i\sigma}(z)\,, \\
T'_{ij\sigma}(z) &\mapsto \quad \bar{T}'_{ij\sigma}(z) = e^{i\chi_{i\sigma}(z)} T'_{ij\sigma}(z) e^{-i\chi_{j\sigma}(z)}\,,
\end{aligned}
\tag{4.21}
$$

where $\boldsymbol{T}'$ denotes the off-diagonal part of $\boldsymbol{\lambda}'$ while $\boldsymbol{\varepsilon}'$ stands for the respective (spatially) diagonal elements.

In Sec. 3.9 we already realized that the self-energy functional itself is not generally invariant under these transformations and we have to introduce a new functional dependence on the transformed set of parameters, namely $\widehat{\Omega}_{\boldsymbol{T},\boldsymbol{U}}[\bar{\boldsymbol{\lambda}}'] = \widehat{\Omega}_{\boldsymbol{T},\boldsymbol{U}}[\boldsymbol{\lambda}'[\bar{\boldsymbol{\lambda}}']]$, where

$\widehat{\Omega}_{\boldsymbol{T},\boldsymbol{U}}[\boldsymbol{\lambda}'] \equiv \widehat{\Omega}_{\boldsymbol{T},\boldsymbol{U}}[\boldsymbol{\Sigma}_{\boldsymbol{\lambda}',\boldsymbol{U}}]$ for brevity. Let's again reexamine the gauge transformation's consequences for the Euler equation. Applying the chain rule, we immediately get

$$\frac{\delta\widehat{\Omega}_{\boldsymbol{T},\boldsymbol{U}}[\boldsymbol{\lambda}']}{\delta T'_{ij\sigma}(z)} = \frac{\delta\widehat{\bar{\Omega}}_{\boldsymbol{T},\boldsymbol{U}}[\bar{\boldsymbol{\lambda}}']}{\delta \bar{T}'_{ij\sigma}(z)} e^{i(\chi_{i\sigma}(z)-\chi_{j\sigma}(z))}\,, \tag{4.22}$$

and

$$\frac{\delta\widehat{\Omega}_{\boldsymbol{T},\boldsymbol{U}}[\boldsymbol{\lambda}']}{\delta \varepsilon'_{i\sigma}(z)} = \frac{\delta\widehat{\bar{\Omega}}_{\boldsymbol{T},\boldsymbol{U}}[\bar{\boldsymbol{\lambda}}']}{\delta \bar{\varepsilon}'_{i\sigma}(z)} \delta_{\mathcal{C}}(z,0)\,, \tag{4.23}$$

which thus implies

$$\left.\frac{\delta\widehat{\Omega}_{\boldsymbol{\lambda},\boldsymbol{U}}[\boldsymbol{\Sigma}_{\boldsymbol{\lambda}',\boldsymbol{U}}]}{\delta\boldsymbol{\lambda}'(z)}\right|_{\boldsymbol{\lambda}'(z)=\boldsymbol{\lambda}'_{\mathrm{opt}}(z)} = 0 \quad\Leftrightarrow\quad \left.\frac{\delta\widehat{\Omega}_{\boldsymbol{\lambda},\boldsymbol{U}}[\boldsymbol{\Sigma}_{\boldsymbol{\lambda}',\boldsymbol{U}}]}{\delta\boldsymbol{\lambda}'(z)}\right|_{\boldsymbol{\lambda}'(z)=\bar{\boldsymbol{\lambda}}'_{\mathrm{opt}}(z)} = 0\,, \tag{4.24}$$

i.e., there is an equivalence relation between different optimal points $\boldsymbol{\lambda}'_{\mathrm{opt}}(z)$ and $\bar{\boldsymbol{\lambda}}'_{\mathrm{opt}}(z)$ via the gauge transformation of Eq. (4.21).

To further illustrate the consequences for a practical implementation, let's make a special choice, namely

$$\chi_{i\sigma}(z) = \int_0^z \mathrm{d}\bar{z}\,(\varepsilon'_{i\sigma}(\bar{z}) - \varepsilon'_{i\sigma}(0))\,, \tag{4.25}$$

which, when plugged into Eq. (4.21) leads to

$$\begin{aligned}
\varepsilon'_{i\sigma}(z) &\mapsto \bar{\varepsilon}'_{i\sigma}(z) = \varepsilon'_{i\sigma}(0) \\
T'_{ij\sigma}(z) &\mapsto \bar{T}'_{ij\sigma}(z) = e^{i\int_0^z \mathrm{d}\bar{z}\,(\varepsilon'_{i\sigma}(\bar{z})-\varepsilon'_{i\sigma}(0))} T'_{ij\sigma}(z) e^{-i\int_0^z \mathrm{d}\bar{z}\,(\varepsilon'_{j\sigma}(\bar{z})-\varepsilon'_{j\sigma}(0))}\,.
\end{aligned} \tag{4.26}$$

Thus, all time dependencies of on-site energies of the reference system can be absorbed in a complex phase of the nonlocal hopping (or hybridization) parameters, i.e., all on-site energies can be determined at the initial time t_0 and subsequently can be kept fixed while only variations of complex hopping amplitudes have to be considered.

Though the explicit results for the time-dependent optimal parameters would clearly differ after such a gauge transformation, the SFT Green's function and the optimal reference system's self-energy would only acquire a phase factor (see Sec. 3.9) which however does not affect the actual values of the time-dependent expectation values of physical observables (cf. definitions in Sec. 2.4).

5 Dynamics in dimerized Hubbard models

As a first benchmark of the numerical implementation developed in the previous chapter, we focus on two concrete examples for the application of the nonequilibrium variational cluster approach (VCA). To this end, we consider the one-dimensional dimerized Hubbard model at half-filling and at different interaction strengths and study (fast) ramps of the hopping parameters.

Figure 5.1 provides an illustration of the initial and of the final states as well as of the reference systems: In both cases, the system is initially in the thermal state of a dimerized Hubbard model specified by some inverse temperature β. In case (a), this state is generated by an initial Hamiltonian which consists of decoupled two-site clusters. Hence, the initial state is a simple valence-bond state with nearest-neighbor correlations and reduced translational symmetries. The intra-cluster hopping $T_{\text{intra}} = 1$ fixes energy and time units. In case (b), the clusters with $T_{\text{intra}} = 1$ are weakly coupled by an inter-cluster hopping $T_{\text{inter}} = 0.2$.

In case (a), the final-state dynamics after the ramp is governed by the full Hubbard Hamiltonian where the initially disconnected clusters are linked by a final inter-cluster hopping $T_{\text{inter}} = 1$. This is a highly nontrivial example where the system should build up longer-ranged nonlocal correlations and entanglement in the course of time. In case (b) the final-state Hamiltonian is basically the same as the Hamiltonian specifying the initial state but with the important difference that the nearest-neighbor hopping $T_{\text{inter}} = 1$ now connects clusters that are shifted by one lattice constant. This example is also highly nontrivial as it corresponds to a sudden switch between Hamiltonians describing states with well-developed but incompatible valence bonds where the entanglement and the spin correlations must reorganize between two different local situations.

Both examples have been in the focus of recent experiments where the redistribution of antiferromagnetic correlations between different bonds and for different ramp times [94] as well as the topological properties of Bloch bands in optical lattices [226] for the uncorrelated variant of the model [227, 228] were studied.

The VCA, as a cluster mean-field approximation, can only partly cover the expected final-state dynamics. Here, our main intention is to discuss some numerical issues and to demonstrate that the VCA can be implemented successfully and yields reasonable results (which can in principle be improved systematically by going to larger cluster sizes).
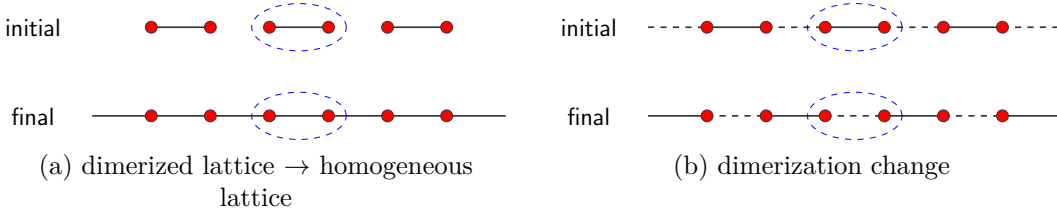
Figure 5.1: Illustration of initial and final states for both (a) the ramp from a dimerized configuration to a homogeneous lattice as well as (b) change of the dimerization. Black solid lines indicate a nearest-neighbor intra- or inter-cluster hopping, $T_{\text{intra}} = 1$ or $T_{\text{inter}} = 1$. Black dashed lines: $T_{\text{inter}} = 0.2$. Correlated sites are represented by red filled dots. The reference system used for the VCA calculations is indicated by a representative two-site reference cluster highlighted as the blue dashed ellipse.

5.1 Variational cluster approach — numerical setup

As a reference system we have chosen as set of simple, disconnected clusters consisting of two sites each, indicated by the blue dashed lines in Fig. 5.1. No additional bath degrees of freedom have been added. Thus, the only possible variational parameters are the intra-cluster hopping T' and the on-site energies ε'_i in the reference system, though the latter are already fixed by the model's symmetries at half-filling.

We have tested the computer code in several trivial limits. Furthermore, for the equilibrium case our data for different U and β and for a *homogeneous* lattice are fully consistent with those obtained previously for $\beta \to \infty$ in Ref. [167] using a completely different algorithm.

Calculations for the systems sketched in Fig. 5.1 have been performed at inverse temperature $\beta = 10$ which, on the level of the approximation employed, is already representative of the zero-temperature limit as has been checked by varying β. Using fifth-order integration schemes on the Matsubara branch, converged results are obtained with $\Delta\tau = 0.1$. On the Keldysh branch we are limited to the trapezoidal rule only since the implementation of higher-order schemes for the evaluation of the time-propagation operator gives rise to numerical instabilities (see Sec. 4.1, footnote on page 55). Converged results are obtained for a time step of $\Delta t = 0.02$, and a maximum propagation time of $t_{\text{max}} = 10$ is easily achieved with a desktop computer. To get converged results with respect to the spatial extension of the one-dimensional lattice, it is sufficient to consider systems with $L = 100$ sites (using periodic boundary conditions). We stimulate the system's dynamics by short ramps lasting for $\Delta t_{\text{ramp}} = 0.5$ and for a ramp profile $r(t) = (1 - \cos(\pi t/\Delta t_{\text{ramp}}))/2$ with continuous first-order derivatives at the joints at $t = 0$ and $t = \Delta t_{\text{ramp}}$. This has been recognized to stabilize the algorithm significantly as opposed to using sudden quenches of the hopping parameters.

(a) dimerized lattice → homogeneous lattice

(b) dimerization change
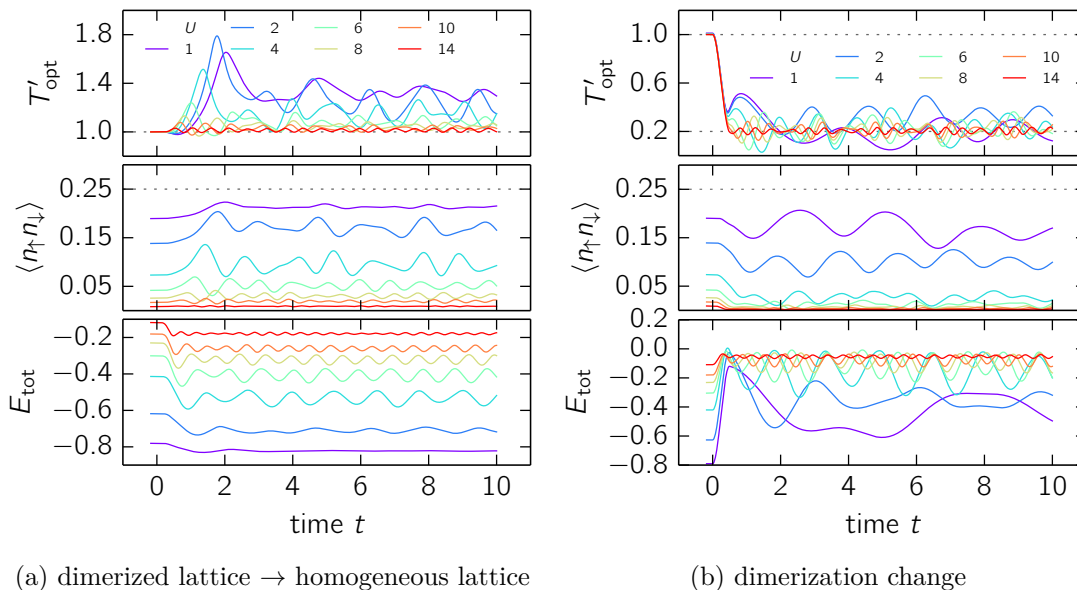
Figure 5.2: Time dependencies of the optimal hopping T'_{opt} of the two-site reference cluster, the double occupancy and the total energy $E_{\mathrm{tot}}(t) = \langle H(t) \rangle$ for different U and for the two different ramps of the hopping parameters of the original system (see Fig. 5.1, (a) and (b)). See text for discussion.

5.2 Results

Results are shown in Fig. 5.2. We first discuss case (a). For $t = 0$, the optimal value of the variational parameter is found as $T'_{\mathrm{opt}} = T_{\mathrm{intra}} = 1$ (dotted line). In fact, this had to be expected since, for the given problem, the self-energy of the reference system equals the full self-energy [cf. Eq. 3.20] and thus the VCA is exact in the initial state. This represents another nontrivial check of our algorithm.

For $t > 0$ we find that T'_{opt} becomes time-dependent, i.e., the reference system adjusts itself to the parameter ramp in a time-dependent way to optimally describe the dynamics of the original system. In the limit of infinitely large clusters where VCA formally becomes exact, one would expect $T'_{\mathrm{opt}}(t)$ to become constant after a certain relaxation time. As seen in the figure, this relaxation of the optimal variational parameter, and also of the double occupancy, takes place on a short time scale given by one or two inverse hoppings. With a reference cluster of two sites only, however, some finite-size effects must be tolerated. These show up indeed as oscillations of $T'_{\mathrm{opt}}(t)$ around an average value after the relaxation process. For weak U, where the physics is governed by the hopping part of the Hamiltonian, this average is by about 30% higher than the initial value $T_{\mathrm{intra}} = 1$. With increasing U, the final average value of $T'_{\mathrm{opt}}(t)$ is seen to decrease and approaches unity for $U \to \infty$. This is plausible since for weak U the fermion system is more itinerant and thus an increased hopping parameter in the reference system is

necessary to (at least partially) compensate for the missing inter-cluster hopping in the reference system while for strong U this is less important as the physics is more local.

Similar arguments can be used to explain the time dependence of the double occupancy. For $t = 0$, there is a strong U dependence of $\langle n_\uparrow n_\downarrow \rangle$, which is exactly reproduced by the VCA. For $t > 0$, the double occupancy quickly relaxes to a higher value (apart from significant finite-size oscillations) as the system becomes more itinerant due to the additional physical inter-cluster hopping. The effect is strongest for weak U.

For case (b), finite-size effects are generally somewhat stronger, see Fig. 5.2(b). Still the main trends are clear and plausible: As the inter-cluster hopping is weak, the initial values of T'_{opt} and of $\langle n_\uparrow n_\downarrow \rangle$ are close to those of case (a). For $t > 0$, the relaxation process takes place on essentially the same time scale of one or two inverse hoppings. However, one now expects that the optimal intra-cluster hopping adjusts to a value close to $T_{\text{inter}} = 0.2$, i.e., close to the physical hopping parameter (see final state in Fig. 5.1(b)). This is in fact seen (dotted line in Fig. 5.2(b)). The decrease of the final average value of the double occupancy with increasing U is understood in the same way as in case (a).

Note that the geometrical structure of the reference system is the same for the initial and the final state, see Fig. 5.1. Given this, we expect that the description of the initial state is better than that of the final state in the case of the dimerization change. We have also performed calculations using a reference system that is shifted by one lattice constant for both, the initial and the final state. In this case, one expects that the VCA description of the final-state dynamics is more accurate than for the initial state. The calculations (not shown) yield unphysical results in this case with a diverging optimal intra-cluster hopping after one to two inverse hoppings, depending somewhat on U. This demonstrates the crucial importance of an accurate description of the initial state for the subsequent real-time dynamics. A sudden switch of the geometrical structure of the reference system at $t = 0$, which follows the dimerization change of the original system, would be a legitimate choice and would result in a superior approximation. This, however, requires a substantially higher numerical effort as more than a single two-site cluster must be considered as a building block in the calculation which is beyond the scope of the present work.

In both cases, (a) and (b), there is a fairly good conservation of the total energy right after the ramp (recall that $\Delta t_{\text{ramp}} = 0.5$) with some remaining finite-size oscillations but no long-time drift. Note that, *a priori*, this could not have been expected as a matter of course, since strict energy conservation within SFT can only be ensured by variations *nonlocal* in time, which would correspond to the optimization of infinitely many bath-degrees of freedom (see Sec. 3.9.3 for a detailed discussion).

In case (a) and for all interaction strengths, we find that the total energy decreases after the ramp (see Fig. 5.2(a)). This implies that the increase of the total energy due to the heating of the system during the ramp is overcompensated by the energy decrease that is induced by the coupling of the different isolated clusters via $H_{T_{\text{inter}},0}$ and the corresponding lowering of the kinetic energy. In case (b) the total energy increases for all U after the ramp (see Fig. 5.2(b)). Since the initial and the final Hamiltonians are

identical apart from a translation by one lattice constant, they have the same ground-state energies. The observed increase of the total energy must therefore be exclusively due to the heating of the system during the ramp.

Despite the simple two-site reference system used here, the resulting real-time dynamics is in fact completely different from a mere superposition of oscillations with frequencies that are characteristic for the finite reference system. Namely, the variational embedding of the cluster rather allows to describe the relaxation of the system to a new stationary final state. Depending on the system, on the type of process studied and on the model parameters, however, the final state does show some unphysical oscillations which are caused by the small size of the reference system and which must be tolerated at the given approximation level.

6 Static and dynamical Mott transitions

As preliminary discussed, lattice systems of strongly correlated fermions as described by (generalized) Hubbard-like models (cf. Sec. 2.1) exhibit diverse emergent phenomena such as insulating behavior caused by strong local Coulomb repulsion. For weak interactions fermions essentially move freely through the lattice and the system behaves metallic. Tunneling processes may lead to doubly occupied sites, which at strong interactions are energetically unfavorable. At zero temperature and at half filling, where there is one particle per site on average, this leads to a suppression of the fermions' motion above some critical value of the interaction U_c where the system becomes a (paramagnetic) insulator. A remainder of this quantum phase transition can be observed as a first-order phase transition (from a bad metal to a bad insulator) also for finite temperatures up to some critical value T_c. In equilibrium detailed studies on the phase diagram of this Mott transition has been conducted e.g. with DMFT [113]. Recently, there has been renewed theoretical interest in such a Mott transition in the context of real-time dynamics following a quantum quench [144–147].

Suddenly changing (quenching) the interaction parameter of the Hubbard model has been realized to initiate intriguing nontrivial dynamics. Starting from a noninteracting initial state, at weak final interactions, thermalization is delayed and the system gets trapped in a so called prethermal metastable state [42]. On the other hand, for strong final interactions, relaxation to a thermal state is again impeded by (damped) collapse-and-revival oscillations which are characteristic for the atomic limit. Both regimes are well separated by a sharp transition at a distinct final interaction U_c^{dyn}, at which a fast decay toward thermal equilibrium takes place, as was first found within nonequilibrium DMFT [144]. This "dynamical Mott transition" has subsequently been studied e.g. for ramps instead of quenches and for different dimensions by using various methods [145–147, 229].

However, a relation between both the "dynamical transition" at U_c^{dyn} and the conventional equilibrium Mott transition at $U = U_c(T)$ and temperature T is far from obvious. Firstly, U_c^{dyn} is found at about half the size of $U_c(0)$ in all studies [145–147, 229]. Secondly, within the dynamical mean-field approach, after the quench to U_c^{dyn}, the system is

found in a thermal state at temperature $T_\star$ which turns out to be more than an order of magnitude higher than the critical temperature T_c for the equilibrium Mott transition, above which the metallic and the insulating states are smoothly connected and a proper distinction is barely possible [144, 214]. Thus, due to the large parametric distance of $(U_c^{\mathrm{dyn}}, T_\star)$ and $(U_c(T_c), T_c)$ in the equilibrium phase diagram, an obvious relation of both phenomena does not obtrude itself.

On the other hand, quenching the interaction represents a rather harsh excitation and a substantial heating of the system in the final state has to be somewhat expected. Using the time-dependent Gutzwiller variational method, Sandri et al. [229] studied U-ramps instead of sudden quenches and found a well-defined U_c^{dyn} for any duration Δt_{ramp} of the ramp. Interestingly, in the limit $\Delta t_{\mathrm{ramp}} \to \infty$, where the ramp can be considered as a quasi-stationary thermodynamical process, the "critical" interaction U_c^{dyn} approaches $U_c \equiv U_c(T = 0)$, which in fact suggests some link between the "dynamical" and the "static" Mott transition.

Another possible interrelation has been observed by Schiró and Fabrizio [145]: in equilibrium the metal to Mott insulator transition is known to turn into a crossover for any finite doping leading away from half-filling. In the mean-field approach employed by the authors, right at the critical interaction U_c^{dyn} the quasi-particle weight vanishes nonanalytically in its long-time limit after the undoped system has been excited by a sudden quench. Interestingly, away from half-filling, this nonanalyticity is washed out and only a crossover from the weak- to the strong-interaction regime can be found. This in fact can be regarded as a key feature of the (doping-driven) Mott transition (in equilibrium) and its persistence also in the nonequilibrium case suggests another link between both critical phenomena.

An entirely new aspect will be brought into play by extending the same question to models with more than just a single orbital, for which the Mott transition is expected to depend on additional parameters. Only a few nonequilibrium DMFT studies have been carried out beyond the single-orbital case [133, 139, 230] but did not concern the Mott phenomenology. However, recent studies by means of the time-dependent slave-boson mean-field approach revealed a much more complicated scenario for the dynamical Mott transition in the two-band Hubbard model though an exhausting analysis on its parameter dependencies is still lacking.

Here, we will focus on two variants of the periodic Anderson model (PAM) (see also Sec. 2.1), which entails uncorrelated sites connected by some finite hopping and hybridized with correlated but nondispersive orbitals. In case this hybridization acts only locally, the model exhibits a smooth crossover from a hybridization band insulator at $U = 0$ to a strongly correlated Kondo insulator for strong U. On the contrary, as suggested by Huscroft et al. [231] and affirmed by different methods [232–234], for a hybridization V of nearest neighbors, there is a quantum-critical point U_c at $T = 0$: the conduction-electron system stays metallic while the localized-electron system undergoes a Mott transition at U_c. Close to the critical point, Held and Bulla [233] could show the equivalence of the PAM and the Hubbard model by means of linearized DMFT [235]. In particular, they found a vanishing quasi-particle weight upon approaching the crit-

ical interaction from the "metallic" side and could identify a characteristic V^2-scaling of U_c. Contrary, in case of an on-site hybridization they argued that $U_c = \infty$. Van Dongen et al. [234] related the presence of this Mott-type transition in the model with nearest-neighbor hybridization to the absence of the Kondo effect in the limit of strong coupling (weak hybridization). In momentum space, the hybridization vanishes at the Fermi surface of the half-filled noninteracting model, whereas the local hybridization is constant in reciprocal space and hence promotes the formation of Kondo singlets in the strong coupling limit. Moreover, it turns out that any small deviation from the strict nearest-neighbor configuration turns the transition into a sharp crossover. So far, this has not been studied in the nonequilibrium domain. It will be thus interesting to see, whether this "tunability" of the Mott scenario for the PAM will persist also in the dynamics initiated by changes of the interaction strength and in strong analogy with the Hubbard model. This would in fact support the conjecture of some link between the dynamic and the static transition.

In the following chapter we will present studies related to the previously discussed cases and give further insights on the "dynamical Mott transition" by means of the nonequilibrium extension of the two-site dynamical impurity approximation (DIA). The latter proves sufficient to cover the basic aspects of the nontrivial dynamics following a quench or ramps of the interaction in the half-filled paramagnetic Hubbard model [144, 145]. Right at the critical point, the DIA favors a final state which is reminiscent of the Mott insulator in equilibrium at zero temperature, which we first examine for quenches starting from a free initial state in Sec. 6.3.1. By means of ramps of different duration, we trace this behavior till close to the adiabatic response regime in Sec. 6.3.2 and find a dependence of the critical interaction on the ramp duration which is in line with previous studies [229]. We repeat the same analysis for both variants of the PAM in its paramagnetic state at half-filling in Sec. 6.4. Though unrelated with regard to the precise physical content, the obtained results also serve as a basis for comparison of the DIA to Hamiltonian-based solvers DMFT [154–156] in Sec. 6.5. All of this is however preceded by a short technical section (Sec. 6.1) on implementational details of the two-site DIA as applied to the present problems and succeeded by a discussion on the well explored equilibrium Mott transition in the Hubbard model in Sec. 6.2.

6.1 Dynamical impurity approximation — numerical setup

For the Hubbard model as well as for both variants of the PAM, we have computed their equilibrium properties as well as their time evolutions initiated by quenches and ramps of the interaction $U(t)$ by means of the dynamical impurity approximation (DIA). In particular, we have considered the simplest compatible reference system, which consists of a single correlated site ($L_c = 1$) with only one bath site ($L_b = 1$) coupled to it via the time dependent hybridization parameter $V'(t)$. At half-filling its Hamiltonian reads

$$H_{\boldsymbol{V'},U}(t) = V'(t) \sum_{i\sigma} (c_{i\sigma}^{\dagger} f_{i\sigma} + \text{h.c.}) + U(t) \sum_i \hat{n}_{i\uparrow}^f \hat{n}_{i\downarrow}^f, \qquad (6.1)$$

(a) Hubbard model   (b) PAM with nearest-neighbor hybridization   (c) PAM with on-site hybridization   (d) set of DIA reference systems
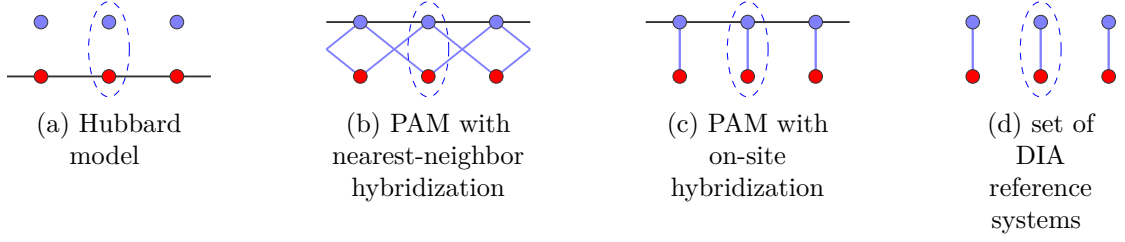
Figure 6.1: Illustration of (a) the Hubbard model, the PAM with (b) nearest-neighbor or with (c) on-site hybridization, and a set of (d) reference systems within the two-site DIA. Black lines represent hoppings between the same type of orbitals, i.e., either between correlated sites (red filled dots) or between uncorrelated sites (blue filled dots). Blue lines stand for the hybridizations which couple correlated and uncorrelated sites. The fundamental building blocks of the reference system are highlighted by dotted blue ellipses in all cases.

where we used the same standard notation as in Sec. 2.1 and time-evolutions as well as expectation values are calculated with respect to $\mathcal{H}_{\boldsymbol{V'},\boldsymbol{U}}(t) = H_{\boldsymbol{V'},\boldsymbol{U}}(t) - \mu(t)\hat{N}^f$ with $\mu(t) = U(t)/2$ (cf. Sec. 2.2). Note that the labeling of the orbitals follows the one used for the PAM, i.e., c-type orbitals are uncorrelated whereas correlated impurities are denoted as f-type orbitals. Contrary, in the single-band Hubbard model c-type operators refer to correlated sites. However, this should not cause any major confusion and we will use the f-/c-labeling explicitly only in Sec. 6.4. For an illustration of all models and the reference system, see Fig. 6.1.

Interestingly, for the two-site reference model [Eq. 6.1] the self-energy is known analytically at zero temperature in equilibrium [236], and reads:

$$\Sigma_{\boldsymbol{V'},\boldsymbol{U}}(\omega) = \frac{U^2}{8}\left(\frac{1}{\omega - 3V'} + \frac{1}{\omega + 3V'}\right), \tag{6.2}$$

where ω is a complex frequency. The quasi-particle weight, generally defined as $Z = \left(1 - \partial_\omega \operatorname{Re}\Sigma(\omega + i0^+)\big|_{\omega=0}\right)^{-1}$, is thus directly obtained as

$$Z = \frac{36V'^2}{36V'^2 + U^2}. \tag{6.3}$$

and we easily calculate the two limits of weak and strong interactions, i.e.,

$$Z\big|_{U \ll V'} \propto 1 \qquad \text{and} \tag{6.4}$$

$$Z\big|_{U \gg V'} \propto 36\frac{V'^2}{U^2}, \tag{6.5}$$

which will be of use for the following discussion.

For our calculations, in all cases, we considered a one-dimensional lattice of 40 sites with periodic boundary conditions, which is sufficient to ensure numerically converged

results. Choosing a one-dimensional system is convenient for numerical reasons. It is important to note, however, that the lattice dimension and geometry enters the DIA only via the free density of states (DOS). Moreover, we expect that results essentially depend on the variance of the DOS only [166]. For the Hubbard model on an one-dimensional lattice this is $\Delta_{\mathrm{1D}} = \sqrt{2}\,T$. Energy (and time) units are fixed by setting $T = 1$. Calculations have been performed for different inverse temperatures β, which set the length of the Matsubara branch in Eq. (4.1). All integrations over imaginary time τ have been carried out using accurate fifth-order numerical integration schemes with step sizes varying from $\Delta\tau = 0.05$ for larger β to $\Delta\tau = 0.1$ for smaller β. For the real-time propagation and all integrations along both Keldysh branches, however, we are again limited to the trapezoidal rule (see Sec. 4.1, footnote on page 55). Sufficiently converged time propagations are obtained for time steps $\Delta t \leq 0.05$ for maximum times up to $t_{\mathrm{max}} \leq 26$.

6.2 Equilibrium Mott transition

Before the real-time dynamics of the Hubbard model can be analyzed within the two-site DIA, a proper initial state has to prepared, that is, the equilibrium variational problem [Eq. (3.19) at $t = t_0$, i.e., Eq. (4.1a)] has to be solved. As a benchmark for our numerical method in the initial state (cf. Sec. 4.1) and as a starting point for the real-time dynamics, in this section we reproduce and discuss the known equilibrium results for a two-site reference system, as depicted in Fig. 6.1(d).

Results for the optimal hybridization parameter V'_{opt} are shown in Fig. 6.2(a). The on-site energies of the correlated and of the bath site could be used as additional variational parameters, but here they are fixed due to particle-hole symmetry at half-filling, as we already anticipated in Eq. (6.1). Starting from small β and weak interaction U, one can easily perform a global search to obtain a solution of Eq. (4.1a). The full T–U phase diagram is then explored using a local search based on Broyden's method [221, 222], starting from the solution at a nearby point in the phase diagram. By increasing β, i.e., lowering the temperature, we find three solutions for certain values of U, indicating the coexistence of a metallic solution with large V'_{opt}, which connects to the weak-U limit, an insulating one with small V'_{opt}, connected to the strong-U limit, and a third solution with intermediate V'_{opt}, which is thermodynamically unstable (see below).

In Fig. 6.2(b) we additionally present the double occupancies for the respective optimal solutions. In the coexistence region the double occupancy, like the optimal hybridization, has three branches. The branch for which $\langle \hat{n}^c_\uparrow \hat{n}^c_\downarrow \rangle$ increases with increasing U corresponds to the thermodynamical unstable solution since here $\partial\langle \hat{n}^c_\uparrow \hat{n}^c_\downarrow \rangle / \partial U = \partial^2\Omega(\beta, U)/\partial U^2 > 0$, violating a thermodynamical stability condition. This violation stems from the mean field character of the DIA and resembles the familiar example of the van der Waals equation, which predicts negative compressibilities for real gases in a certain critical region. In fact, the system undergoes a first-order phase transition at a critical interaction, the value of which can be inferred from a Maxwell construction [237], as shown in the inset of Fig. 6.2(b): a jump of the double occupancy is inserted at the critical interaction U_{c},
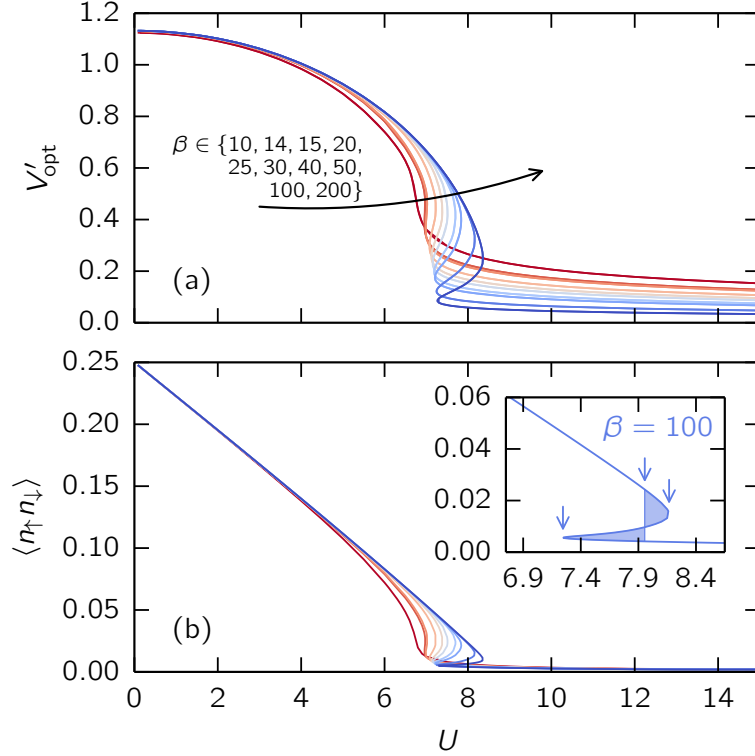
Figure 6.2: (a) Optimal variational parameter V'_{opt} as a function of the interaction for different inverse temperatures increasing from $\beta = 10$ (red curve) to $\beta = 200$ (blue curve), and (b) the respective double occupancies. The inset in (b) shows the Maxwell construction for $\beta = 100$: The mid arrow indicates the value for U_c, the outer arrows point at the spinodal points, which define the region where metallic and insulating solutions coexist.

determined by requiring that the shaded areas on both sides of the jump be equal. In addition, the lower and upper boundaries of the coexistence region, U_{c1} and U_{c2}, can be read off at the spinodal points of the curve [see outmost arrows in Fig. 6.2(b)].

Results for different temperatures are collected in the phase diagram shown in Fig. 6.2. Metallic and insulating solutions coexist in a triangular-shaped region, bounded by the curves $U_{c1}(T)$ and $U_{c2}(T)$. Within the coexistence region, there is a line $U_c(T)$ of first-order transitions terminating in a second-order critical end point at the temperature T_c. For temperatures above T_c the Mott metal-insulator transition is no longer sharply defined but a smooth crossover only. Extrapolating our data to $T = 0$, we find $U_{c1}(0) \approx 7.28 \approx 5.15\Delta_{1D}$ and $U_c(0) = U_{c2}(0) \approx 8.59 \approx 6.07\Delta_{1D}$, both of which fall within a range of results obtained earlier for other lattices (where the variance of the density of states has been used as energy unit) [166]. The value of $U_{c2}(0)$ obtained within the DIA for the Bethe lattice is in remarkably good agreement with DMFT+NRG [238] ($U_c(0) = 5.88$).
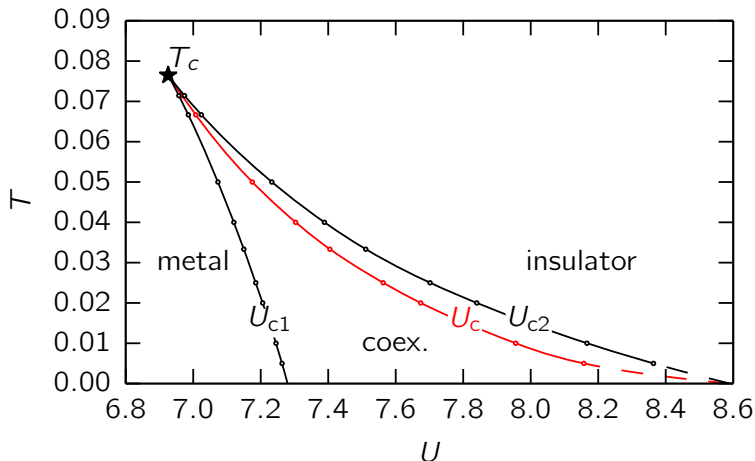
Figure 6.3: Phase diagram of the Mott transition in the half-filled Hubbard model on a one-dimensional lattice as obtained from the DIA with a two-site reference system. Below the critical temperature T_c metallic solutions exist up to interactions $U \leq U_{c2}$, insulating solutions exist down to $U \geq U_{c1}$, and in between both coexist. Red line: first-order phase boundary $U_c(T)$.

The value obtained for the critical temperature, $T_c \approx 0.077 \approx 0.054\Delta_{1D}$, is more sensitive to the lattice geometry as is obvious when comparing with the result $T_c \approx 0.03$ that is obtained by the two-site DIA for a semi-elliptical DOS of unit variance [166]. T_c also increases by more than 50% when adding more bath sites but already for three bath sites there is quantitative agreement with full DMFT results [171].

We conclude that the present implementation of the two-site DIA reproduces the known results for the Mott transition obtained earlier where the phase diagram has been constructed from the explicit calculation of the grand potential. As compared to the full DMFT solution, the two-site approximation captures the correct physics qualitatively, i.e., the equilibrium phase diagram has exactly the same topology. Quantitatively, U_{c2} is predicted quite accurately while U_{c1} is over- and T_c is underestimated. For the present study, we will nevertheless restrict ourselves to the two-site approximation since the computational effort is considerably higher for the nonequilibrium case. More importantly, nonequilibrium calculations with more than a single bath site are not easily stabilized numerically with the present implementation.

6.3 Dynamical Mott transition

In the following we will discuss the real-time dynamics of the Hubbard model induced by sudden quenches or ramps of the interaction starting from a "free" initial state to arbitrary final interactions $U_{\text{fin}} > 0$. Within the SFT the optimal parameters of the reference system are undefined for a free system due to the vanishing self-energy. For

practical reasons we therefore consider initial states with $U_{\text{ini}} = 0.01$.

We furthermore choose $\beta = 10$. Essentially, this corresponds to a zero-temperature initial state: As concerns the reference system, there is hardly any change in the optimal hybridization parameter with temperature in the limit $U \to 0$, as can be seen from Fig. 6.2(a). The remaining temperature dependence via the noninteracting Green's function of the original system [see Eq. 3.18] is very weak for lower temperatures. Consequently, there is hardly any temperature dependence seen in the nonequilibrium results. This has been verified numerically (up to $\beta \leq 40$).

The interaction is switched from U_{ini} to U_{fin} via $U(t) = U_{\text{ini}} + (U_{\text{fin}} - U_{\text{ini}})r(t)$ by either quenching,

$$r(t) = \Theta(t) \,, \tag{6.6}$$

or conducting cosine-shaped ramps of different duration Δt_{ramp}, i.e.,

$$r(t) = (1 - \cos(\pi t/\Delta t_{\text{ramp}}))/2 \,. \tag{6.7}$$

Both cases will be discussed successively in the next two subsections.

6.3.1 Interaction quenches

Following the time evolution after a quench, we find two qualitatively different response patterns for weak and strong final interactions, which are well separated by a sharp transition point at a critical interaction $U_{\text{c}}^{\text{dyn}} \approx 4.61$. Results are presented in Fig. 6.4, where we show the time dependence of the optimal hybridization parameter, the double occupancy, and the total energy. Moreover, in Fig. 6.5 we show for any time-dependent quantity $Q(t)$ the time average

$$\overline{Q} = \lim_{t \to \infty} \frac{1}{t} \int_0^t dt' \, Q(t') \,, \tag{6.8}$$

and the fluctuations

$$\overline{\Delta Q} = \overline{(Q - \overline{Q})^2}^{\frac{1}{2}} \,. \tag{6.9}$$

Let us first focus on *weak* quenches, i.e., $U_{\text{fin}} < U_{\text{c}}^{\text{dyn}}$. For the optimal hybridization parameter $V_{\text{opt}}'(t)$ we observe a quick drop to smaller values within approximately one inverse hopping, followed by moderate oscillations around some constant value, see Fig. 6.4 (top left). For final interactions $U_{\text{fin}} \lesssim 4$, the long-time average of the optimal hybridization slightly decreases with increasing U_{fin} (Fig. 6.5, top).

On the same short time scale, the double occupancy decays from its noninteracting initial value, i.e., the Coulomb repulsion quickly suppresses doubly occupied sites. For final interactions $U_{\text{fin}} \gtrsim 3$ we find a strong initial drop and pronounced periodic recurrences. However, these shift to later and later times upon increasing U_{fin}. In addition, small regular oscillations around some value close to zero become apparent, see Fig. 6.4 (middle left).
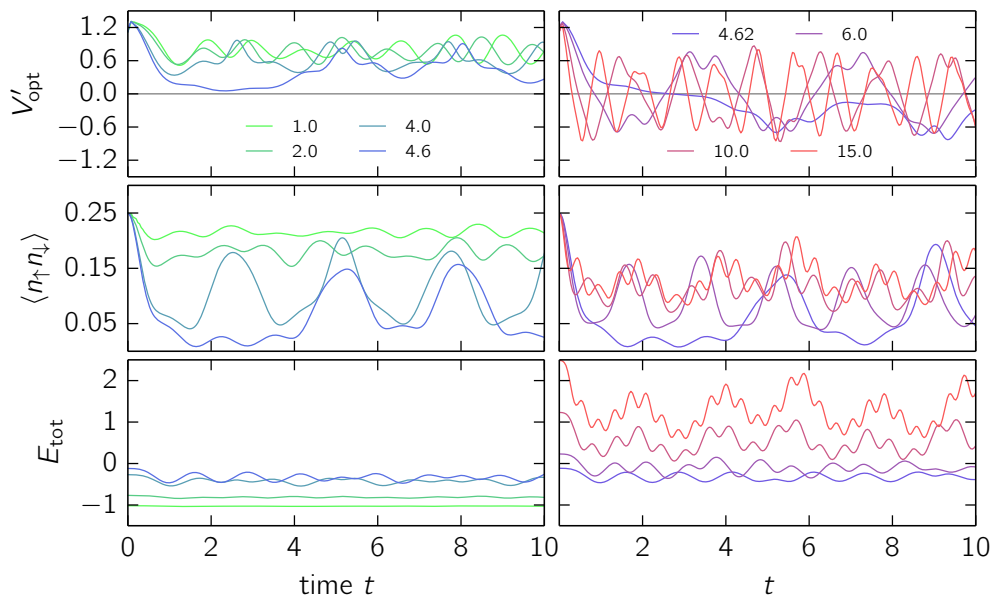
Figure 6.4: Time dependencies of the optimal hybridization V'_{opt}, the double occupancy $\langle n_\uparrow n_\downarrow \rangle$ and the total energy E_{tot} for interaction quenches starting from $U_{\mathrm{ini}} = 0.01$ to different U_{fin} (see color labels). Left: weak-coupling regime, $U_{\mathrm{fin}} < U_{\mathrm{c}}^{\mathrm{dyn}}$. Right: strong-coupling regime, $U_{\mathrm{fin}} > U_{\mathrm{c}}^{\mathrm{dyn}}$.

The exact value of the total energy right after the quench (at $t = t_0^+$) is given by the expectation value of the Hamiltonian in the noninteracting initial state, $E_{\mathrm{tot}}(t_0^+) = E_{\mathrm{kin}}(t_0) + U_{\mathrm{fin}}/4$, which increases linearly with the final interaction. For weak quenches we find that this value is relatively well conserved, apart from a small drop of the time-averaged value, and some moderate oscillatory behavior for increased quench size (Fig. 6.5, bottom). By comparison with a thermal ensemble for the same interaction U_{fin}, i.e., by comparing with equilibrium two-site DIA calculations, we can thus ascribe an effective temperature T_{eff} to the long-time averages, namely by demanding that $\overline{E_{\mathrm{tot}}} = E_{\mathrm{tot}}^{\mathrm{eq}}(T_{\mathrm{eff}})$. The effective temperature increases from $T_{\mathrm{eff}} \approx 0.12$ for $U_{\mathrm{fin}} = 1$ to $T_{\mathrm{eff}} \approx 0.28$ for $U_{\mathrm{fin}} = 4$ (see Fig. 6.6). The corresponding thermal value for the double occupancy roughly agrees with the respective time-averaged value (see Fig. 6.5, middle). This is in agreement with the prethermalization scenario [42, 144] observed in DMFT calculations.

We now turn to *strong* quenches, i.e., $U_{\mathrm{fin}} > U_{\mathrm{c}}^{\mathrm{dyn}}$. Here the time-dependent behavior of the system drastically differs from that in the regime of weak quenches. For $U_{\mathrm{fin}} \gtrsim 6$ we find a quite regular oscillatory behavior for all relevant quantities. A Fourier analysis of the oscillations in the double occupancy reveals that oscillations occur with frequencies approximately given by U_{fin}, as shown in Fig. 6.7, i.e., the characteristic frequency for collapse-and-revival oscillations in the atomic limit. On top of this, there are slow beatings, which probably should be ascribed to finite-size effects and which appear to be independent of the interaction. In the long-time limit, the double occupancy slowly
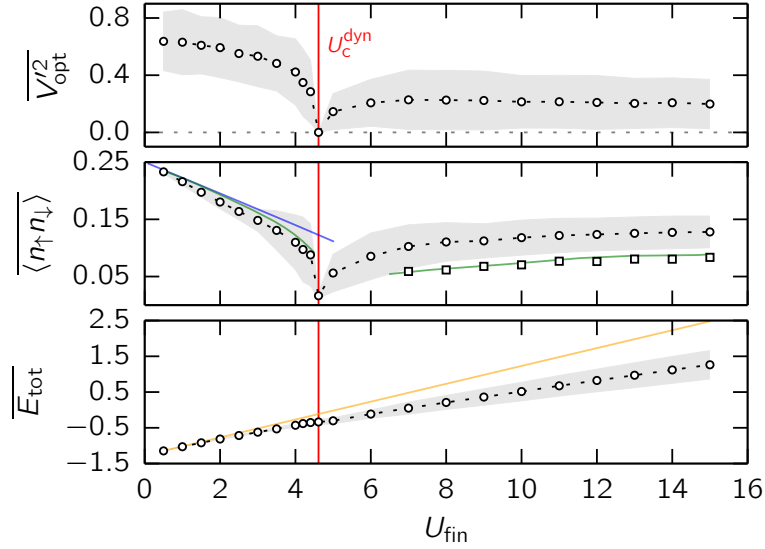
Figure 6.5: Long-time averages (points) and fluctuations (shaded areas) of the optimal hybridization V'^2_{opt}, the double occupancy $\langle n_\uparrow n_\downarrow \rangle$ and the total energy E_{tot}. Red lines: critical interaction U_c^{dyn} separating weak- and strong-coupling regime. Blue line: equilibrium values of the double occupancy at zero temperature. Green lines: thermal values of the double occupancy, which in the weak-coupling regime almost coincide with the long-time average, but in the strong-coupling regime match the minima of the double-occupancy oscillations (squares). Orange line: total energy right after the quench.

increases with U_{fin}. However, it does not reach its free value (i.e., $\langle \hat{n}^c_\uparrow \hat{n}^c_\downarrow \rangle_0 = 0.25$) again, as perturbative arguments would suggest [144], i.e., the two-site approximation seems to underestimate the actual double occupancy in the strong-coupling limit (see Fig. 6.5, middle).

The optimal hybridization parameter strongly oscillates around zero, see Fig. 6.4 (top right). Recall that in equilibrium and for strong interactions the quasi-particle weight (for a two-site system) is given by $36V'^2/U^2$ [see Eq. 6.5] so that strong collapses and revivals of the *square* of the optimal parameter would correspond to an oscillatory behavior of the Fermi-surface discontinuity, as has been observed in DMFT calculations [144]. In Fig. 6.5 (top) we therefore show the long-time behavior of $V'^2_{\text{opt}}(t)$. With increasing interactions U_{fin} we find that both the average and the fluctuations quickly saturate.

For strong final interactions, conservation of total energy becomes rather poor and, compared to the weak-coupling case, the time-averaged value differs more significantly from the exact value. Nevertheless, we may again compare the long-time average to an appropriate thermal value to extract the effective temperature T_{eff}. As compared to the weak-coupling regime, the effective temperatures are roughly an order of magnitude higher and, apart from an offset, scale linearly with U_{fin} (see Fig. 6.6). Interestingly, from this we find thermal values of the double occupancy which in fact coincide with the

overall minima of its time-dependent oscillations, see Fig. 6.5 (middle). This is again in line with the DMFT results [144].

We now focus on the dynamics close to the *critical* point $U_c^{\rm dyn} \approx 4.61$, see Fig. 6.8. In this regime the behavior of $V'_{\rm opt}(t)$ for $U_{\rm fin} \lesssim U_c^{\rm dyn}$ and $U_{\rm fin} \gtrsim U_c^{\rm dyn}$ becomes very similar: Within two inverse hoppings, the optimal hybridization strength decays to almost zero, but then revives to positive values for $U_{\rm fin} \lesssim U_c^{\rm dyn}$ and shows slow oscillations with relatively large amplitude. The same dynamics, but with opposite sign of the optimal parameter at long times, is observed for $U_{\rm fin} \gtrsim U_c^{\rm dyn}$. This is accompanied by a decay of the double occupancy down to almost zero ($\langle \hat{n}_\uparrow^c \hat{n}_\downarrow^c \rangle \approx 0.016$), followed by strong revivals which are in phase with $V'_{\rm opt}(t)$. As discussed for the weak-quench regime, these oscillations shift to later and later times for quenches closer and closer to the critical value. Finally, right at the critical point, no revivals are observed, i.e., the bath dynamically *decouples*, and $V'_{\rm opt}(t)$ remains zero up to the longest simulated times. For $U_{\rm fin} = U_c^{\rm dyn}$ the double occupancy merely shows weak oscillates around its long-time average.

We conclude that, within the two-site DIA, the dynamical Mott transition is described as a sharp transition characterized by *critical* behavior in the $U_{\rm fin}$-dependence of the quantities shown in Fig. 6.5. One may speculate that in calculations with more bath degrees of freedom in the DIA, some of them would decouple (at low energies) whereas others would remain connected to the correlated impurity (at high energies). Nevertheless, even on the level of the two-site approximation, there is a surprisingly good agreement of the critical interaction with results from the DMFT [144] ($U_{c,{\rm DMFT}}^{\rm dyn} \approx 3.2$) and the Gutzwiller ansatz [239] ($U_{c,{\rm Gutzw}}^{\rm dyn} \approx 3.3$) when comparing with the value rescaled by the variance of the one-dimensional DOS, i.e, with $U_c^{\rm dyn} \approx 4.61 \approx 3.26\Delta_{\rm 1D}$.

Within the DMFT [144] a rapid thermalization is found at $U_{\rm fin} = U_c^{\rm dyn}$, and the thermalized state is characterized as a bad metal. Opposed to this, within the two-site DIA, a complete decoupling of the bath site right at the critical point implies that the final state is described on the level of the Hubbard-I approximation [7]. Note that therewith the
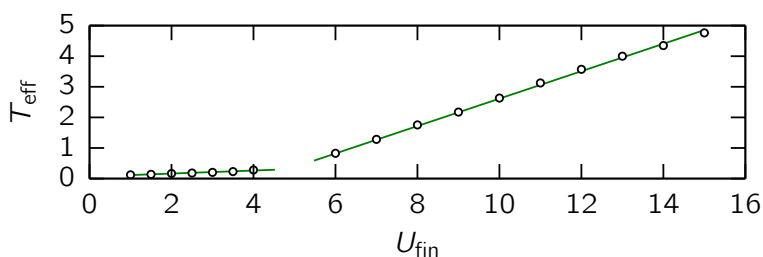
Figure 6.6: Effective temperatures of the thermal state obtained from equating the total energy in the long time average with values obtained from an equilibrium calculation (see text above). Note that the straight lines are only a guide to the eye and especially for weak interactions the trend might not be exactly linear.
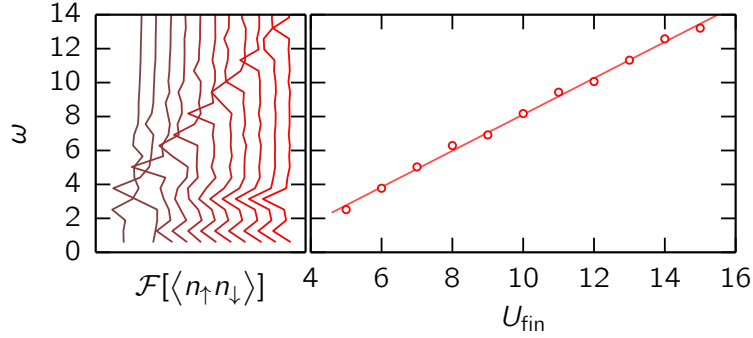
Figure 6.7: Left: Fourier transform ($\mathcal{F}$) of the double occupancy. Plots have been shifted for better visibility. Right: linear dependence of the dominant frequency on the final interaction U_{fin} in the strong coupling regime $U_{\text{fin}} > U_c^{\text{dyn}}$. Note the interaction-independent small beating frequencies (left).

dynamical Mott transition is very similar to the equilibrium Mott transition at zero temperature which is also characterized by a vanishing hybridization to the bath site. In both cases, the Hubbard-I approximation must be seen as a comparatively crude description of the bad metal or Mott insulator, and one cannot expect a fully consistent picture on this level. In the nonequilibrium case, for example, the determination of the effective temperature by comparison with equilibrium two-site DIA calculations via $\overline{E_{\text{tot}}} = E_{\text{tot}}^{\text{eq}}(T_{\text{eff}})$ yields $T_{\text{eff}} \approx 0.3$. The resulting thermal double occupancy of $\langle \hat{n}_\uparrow^c \hat{n}_\downarrow^c \rangle \approx 0.1$, however, turns out too large as compared with the time average $\overline{\langle \hat{n}_\uparrow^c \hat{n}_\downarrow^c \rangle} \approx 0.016$. A better agreement is found when estimating T_{eff} by comparing with the Hubbard-I solution, where the bath site is decoupled. This yields $T_{\text{eff}} \approx 0.6$ and $\langle \hat{n}_\uparrow^c \hat{n}_\downarrow^c \rangle \approx 0.02$. However, at finite temperatures, the Hubbard-I solution is only metastable. One may summarize that for the final state at $U_{\text{fin}} = U_c^{\text{dyn}}$, our findings more resemble the predictions of the Gutzwiller approach [239] rather than those of the DMFT.

6.3.2 Ramps of the interaction

The dynamical Mott transition is reminiscent of the conventional equilibrium Mott transition but occurs at about half the respective critical interaction and at a high effective temperature. Therefore, an interesting question is whether the two phenomena are related at all. One route to study this question is to consider a ramp with a finite duration rather than an instantaneous quench of the interaction as has been done using the Gutzwiller approach in Ref. [229]. Ramping the interaction in a short time from U_{ini} to U_{fin} will make contact to the results found for a sudden quench. On the other hand, for ramps with infinite duration, i.e., if the interaction is changed adiabatically rather than suddenly, the system evolves along paths within the equilibrium phase diagram and will cross the line of equilibrium transitions (see Fig. 6.3). In fact, assuming that
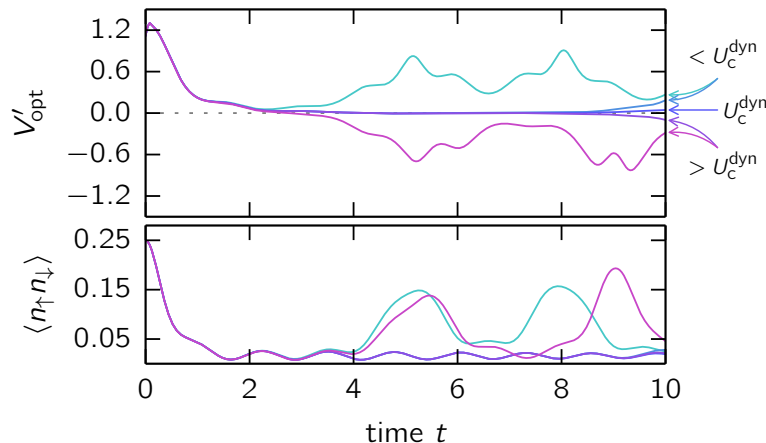
Figure 6.8: Dynamical decoupling of the bath site at the critical point ($U_{\text{fin}} = U_{\text{c}}^{\text{dyn}}$) (top) and the corresponding dynamics of the double occupancy (bottom). Additional curves: dynamics for final interactions differing by less than 0.3% from $U_{\text{c}}^{\text{dyn}}$. Note the strong impact upon tiny changes of U_{fin} indicating a *sharp* transition between the two regimes.

there is a critical interaction for any ramp time Δt_{ramp} at all, one should expect that, with increasing Δt_{ramp}, the critical interaction crosses over from $U_{\text{c}}^{\text{dyn}} \approx 4.61$ (sudden quench) to $U_{\text{c}2} \approx 8.59$ ($T = 0$), since starting from a zero-temperature initial state, an adiabatic process will result in a zero-temperature final state.

To test our expectation we therefore consider a sequence of (cosine-shaped) ramps with different duration Δt_{ramp}, see Eq. (6.7). Here we are limited to finite propagation times, $t_{\text{max}} \leq 25$, for practical reasons. Nevertheless, this allows us to study the relevant critical behavior for ramp times up to $\Delta t_{\text{ramp}} \leq 20$.

We begin the discussion for ramps of different speed but to the same final interaction $U_{\text{fin}} = 12$, starting from the same initial state that has also been considered for the quenches discussed in section 6.3.1. As a measure of adiabaticity of the process we compare the total energy as a function of the interaction *during* the ramp with the corresponding equilibrium result. This is shown in Fig. 6.9 where the time-dependent value of the total energy $E_{\text{tot}}(t)$ during the ramp is plotted against the instantaneous value $U(t)$ of the interaction. The resulting function $E_{\text{tot}}(U)$ can be compared with the equilibrium total energy (dashed line) as well as with the total energy after a sudden quench (straight line).

We find that for short ramps the total energy increases linearly during the ramp up to intermediate interaction strengths but then changes to sublinear behavior. For longer ramps, this linear regime shrinks. With increasing ramp duration the curves $E_{\text{tot}}(U)$ finally converge to the equilibrium result, i.e., to the U-dependence of the ground-state energy. For ramp times $\Delta t_{\text{ramp}} \gtrsim 15$, the process is almost perfectly adiabatic.
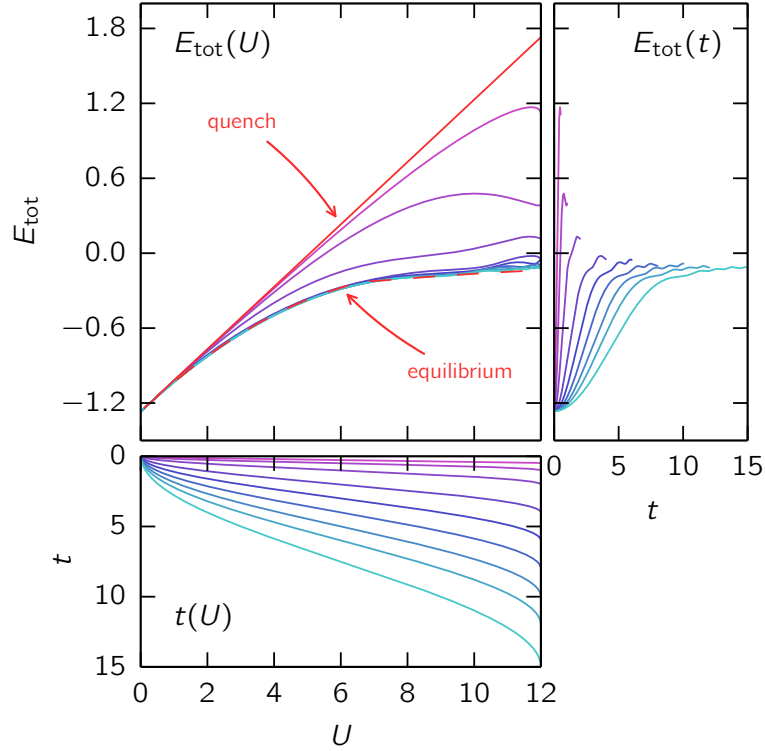
Figure 6.9: Check of adiabaticity for ramps of the interaction from $U_{\mathrm{ini}} = 0.01$ to $U_{\mathrm{fin}} = 12$ with different ramp times ($\Delta t_{\mathrm{ramp}} \in \{0.5, 1, 2, 4, 6, 8, 10, 12, 15\}$, colored from purple to cyan). The total energy during the ramp is plotted as a function of the instantaneous interaction (top left), i.e., $E_{\mathrm{tot}}(U) \equiv E_{\mathrm{tot}}(t(U))$, as obtained from the inverse of (cosine) ramp profile $U(t)$, Eq. (6.7), (bottom) and from the time-dependent total energy $E_{\mathrm{tot}}(t)$ (right). The results are contrasted with the total energy after a quench (straight red line) and the equilibrium energy at the same final interaction (dashed red line).

Independent of the ramp duration, we find essentially the same distinction between a weak- and a strong-coupling regime that has been discussed for the case of a sudden quench. The two regimes are sharply separated by a critical interaction $U_{\mathrm{c}}^{\mathrm{dyn}} = U_{\mathrm{c}}^{\mathrm{dyn}}(\Delta t_{\mathrm{ramp}})$ which depends on the ramp duration (see discussion below).

With increasing ramp time the dynamics becomes more well-behaved in the sense that energy conservation becomes almost perfect for weak final interactions and is strongly improved in the strong-coupling case. As an example, in Fig. 6.10, we show the time dependencies of the optimal hybridization, of the double occupancy and of the total energy for different U_{fin} which are located below, right at, and above the dynamical critical interaction $U_{\mathrm{c}}^{\mathrm{dyn}} \approx 8.02$ for a ramp with $\Delta t_{\mathrm{ramp}} = 7$. Note that the process is clearly nonadiabatic. For $U_{\mathrm{fin}} \leq U_{\mathrm{c}}^{\mathrm{dyn}}$ we find that there are almost no oscillations of the optimal hybridization parameter after the ramp is completed. The same holds
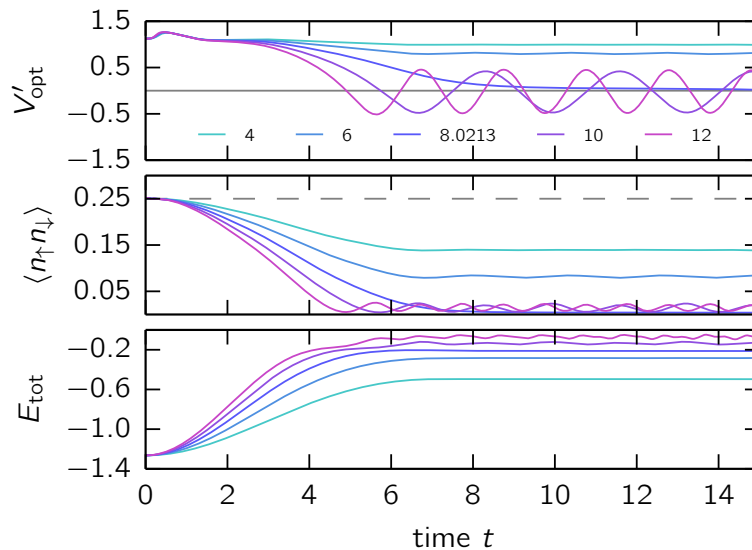
Figure 6.10: Time dependencies of the optimal hybridization V'_{opt}, the double occupancy $\langle n_\uparrow n_\downarrow \rangle$ and the total energy E_{tot} (from top to bottom) for ramps of the interaction with $\Delta t_{\mathrm{ramp}} = 7$, starting from $U_{\mathrm{ini}} = 0.01$ to different U_{fin} (as indicated in the top panel) in the weak- and the strong-coupling regime as well as right at the dynamical critical point.

true for the double occupancy. Its (time-averaged) value after the ramp only slightly increases with increasing final interaction after having reached a minimum (close to zero) right at the critical point. This already indicates proximity to an adiabatic process where the double occupancy would just follow its equilibrium value, i.e., where it would monotonically decrease with increasing final interactions [see Fig. 6.2(b)].

We also obtain reasonable results for the time-dependent momentum distribution $n(k,t)$ and, contrary to the study of quench dynamics, can therefore more comprehensively focus on the question of thermalization. In Fig. 6.11, we show three different examples for the final-state dynamics of $n(k,t)$, exemplary for the weak- (Fig. 6.11(a)) and for the strong-coupling case (Fig. 6.11(b)) as well as for $U_{\mathrm{fin}} = U_{\mathrm{c}}^{\mathrm{dyn}}$ (Fig. 6.11(c)). We again consider ramps with $\Delta t_{\mathrm{ramp}} = 7$. The initial state is characterized by a sharp Fermi-surface discontinuity, which is slightly washed out by the finite temperature ($\beta = 10$) that has been assumed for practical reasons. As mentioned above, however, this does not affect the final-state dynamics significantly. The final state that is reached in the long-time limit either shows a sharp jump of $n(k,t)$ at the Fermi surface (in case of $U_{\mathrm{fin}} < U_{\mathrm{c}}^{\mathrm{dyn}}$) or collapse-and-revival oscillations ($U_{\mathrm{fin}} > U_{\mathrm{c}}^{\mathrm{dyn}}$). This is very similar to the DMFT results in the quench case [144]. Right at the critical point ($U_{\mathrm{fin}} = U_{\mathrm{c}}^{\mathrm{dyn}}$) we also find fast thermalization immediately after the ramp is completed toward a hot thermal distribution. Comparing with Hubbard-I equilibrium calculations, we find an effective temperature of $T_{\mathrm{eff}} \approx 0.5$, see Figs. 6.11(c) and 6.11(d). Note that this is somewhat

(a) $U_{\mathrm{fin}} < U_{\mathrm{c}}^{\mathrm{dyn}}$ (b) $U_{\mathrm{fin}} > U_{\mathrm{c}}^{\mathrm{dyn}}$ (c) $U_{\mathrm{fin}} = U_{\mathrm{c}}^{\mathrm{dyn}}$ (d) relative error for fits
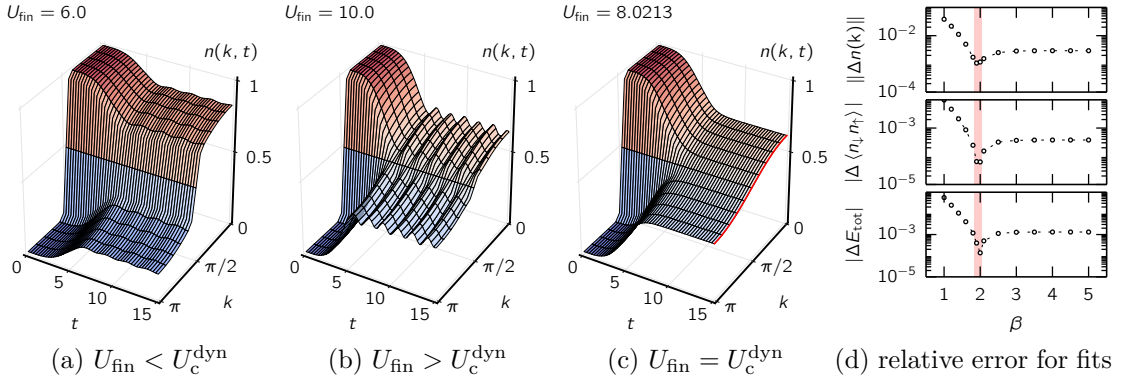
Figure 6.11: Time dependent momentum distribution for a ramp with $\Delta t_{\mathrm{ramp}} = 7$ ending at different interactions (a) below, (b) above and (c) right at the critical point. Precise numbers are given in the top left corner of each plot. For the latter the long-time average of the momentum distribution is fitted with an equilibrium distribution within the Hubbard-I approximation (red line). Relative errors of fits for the momentum distribution, the double occupancy and the total energy (from top to bottom) at different temperatures are shown in (d), an error estimate for the effective temperature $T_{\mathrm{eff}} \approx 0.5$ is indicated by a red shaded area.

lower than the effective temperature that had been obtained for the quench ($T_{\mathrm{eff}} \approx 0.6$).

Let us finally come back to the original motivation to study ramps of the interaction. We consider ramps with various durations bridging the limit of an instantaneous quench $\Delta t_{\mathrm{ramp}} = 0$ and the adiabatic limit $\Delta t_{\mathrm{ramp}} \to \infty$. For each ramp time, we have performed a series of calculations with different U_{fin} to extract the respective value of the dynamical critical interaction $U_{\mathrm{c}}^{\mathrm{dyn}}$. The latter is indeed well defined in the whole Δt_{ramp}-regime. Its dependence on the ramp time for $\Delta t_{\mathrm{ramp}} \leq 20$ is shown in Fig. 6.12.

$U_{\mathrm{c}}^{\mathrm{dyn}}$ monotonically increases with Δt_{ramp} and seems to approach the value of the critical interaction $U_{\mathrm{c2}} \approx 8.59$ for the zero-temperature Mott transition, as obtained by the two-site DIA (cf. Sec. 6.2). However, the convergence turns out to be very slow. We also cannot fully exclude that the low but nonzero initial-state temperature has some effect on the result expected for $\Delta t_{\mathrm{ramp}} \to \infty$ and that, even for a perfectly adiabatic process, the final-state effective temperature becomes nonzero which would imply that $U_{\mathrm{c}}^{\mathrm{dyn}}$ converges to a somewhat lower value. Nevertheless, the results indeed clearly indicate that the dynamical Mott transition and the equilibrium Mott transition are related phenomena which are smoothly connected – at least within the two-site DIA. The same conclusion can be drawn from the results of the Gutzwiller calculations [229] which, however, suffer from additional oscillations of the critical interaction when increasing the ramp duration. This effect is absent in the two-site DIA and presumably an artifact of the Gutzwiller method.
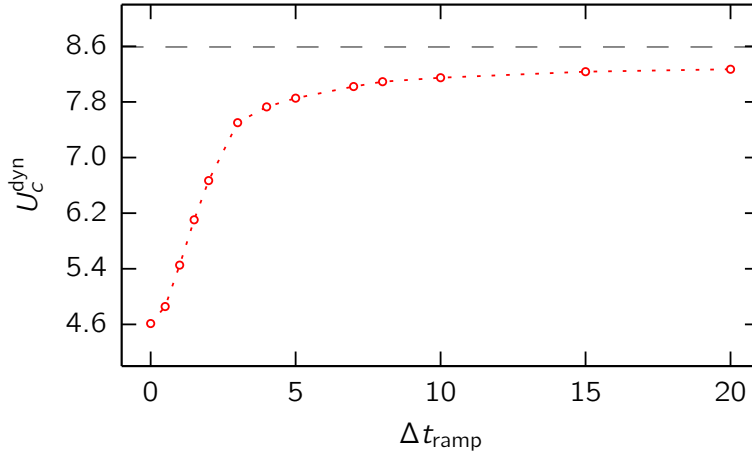
Figure 6.12: Dynamical critical interaction U_c^{dyn} as a function of the ramp time Δt_{ramp} determined for cosine-shaped ramps starting from $U_{\mathrm{ini}} = 0.01$. The equilibrium value $U_{c2}(0) \approx 8.59$ for the critical interaction at zero temperature is indicated by a gray dashed line.

6.4 Tunable Mott transitions in periodic Anderson models

In the following we will discuss both cases of the periodic Anderson model (see Eq. 2.3), where we first consider a hybridization between nearest-neighbors for which $V_{ij} = -V$ for neighboring sites i and j and zero otherwise [see Fig. 6.1(b)] and thereafter turn over to a site-local hybridization, i.e., $V_{ij} = -V \delta_{ij}$ [see Fig. 6.1(c)]. For the following discussion we will essentially adapt the structure of the preceding section for the Hubbard model and will refer back wherever convenient.

6.4.1 Equilibrium case

As before (see Sec. 6.2), for small β and small U the optimal parameter V'_{opt} is easily found by a global search and can then be traced throughout the entire β–U parameter space. Exemplary results for the optimal reference system's hybridization parameter V'_{opt} for $V = 0.866$ in the original system (i.e., $V^2 \approx 0.75$) and a representative range of interactions are shown in Fig. 6.13(a). Upon lowering the temperature, i.e., increasing β, three coexisting solution for V'_{opt} are found for certain values of U, indicating a phase transition of first order.

Though its strong resemblance with the Mott transition in the Hubbard model (see Sec. 6.2), to better understand the details of the transition in the two-orbital model, we extrapolate the results for V'_{opt} to zero temperature: for small U the optimal parameters become independent of temperature and converge to a constant value, whereas for large U, carrying out the $T \to 0$ limit we find $V'_{\mathrm{opt}} \to 0$. Thus, at some intermediate value $U_c(T = 0)$ the bath site decouples, i.e., V'_{opt} vanishes.
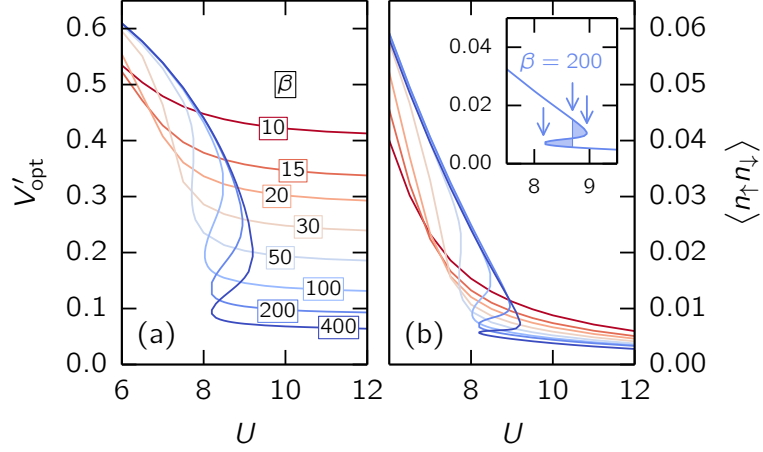
Figure 6.13: Equilibrium results for a PAM with nearest-neighbor hybridization with $V = 0.866$ (i.e., $V^2 \approx 0.75$): (a) optimal parameters for different inverse temperatures β (for numbers see boxes) and (b) corresponding double occupancies (in the f-orbitals). The inset in (b) shows the Maxwell construction for $\beta = 200$: the mid arrow indicates the value for U_c, the outer arrows point at the spinodal points, which bound the region where metallic and insulating solutions coexist.

The orbital selective character of the transition is straightforwardly discussed with the help of the (frequency dependent) spectral function as given by

$$\boldsymbol{A}(\omega) = -\frac{1}{\pi} \lim_{\eta \searrow 0} \operatorname{Im} \boldsymbol{G}(\omega + i\eta). \tag{6.10}$$

Here, $\boldsymbol{G}(\omega) = L^{-1} \sum_k \boldsymbol{G}(k, \omega)$, denotes a general Green's function and the sum runs over all lattice momenta. This expression can be evaluated directly within the DIA at $\boldsymbol{G} = \boldsymbol{G}^{\mathrm{DIA}} = (\boldsymbol{G}_{T,V,0}^{-1} - \boldsymbol{\Sigma}_{V'_{\mathrm{opt}},U})^{-1}$ [cf. Eq. 3.20], since the self-energy of the reference system is known analytically from Eq. (6.2) and can be evaluated at the optimal parameter V'_{opt}. To this end, we also exploit the lattice's translational symmetry to obtain the k-dependent dispersion

$$\varepsilon(k) = \begin{pmatrix} T(k) & V(k) \\ V(k) & 0 \end{pmatrix}, \tag{6.11}$$

with $T(k) = -2T\cos(ka)$ and $V(k) = 2V\cos(ka)$ for the nearest-neighbor hybridization (see Fig. 6.1(b)), or $V(k) = V$ for the on-site hybridization respectively (see Fig. 6.1(c)), which eventually leads to

$$\boldsymbol{G}^{\mathrm{DIA}}(k, \omega) = \begin{pmatrix} \omega - T(k) & -V(k) \\ -V(k) & \omega - \Sigma'_{\mathrm{opt}}(\omega) \end{pmatrix}^{-1}. \tag{6.12}$$
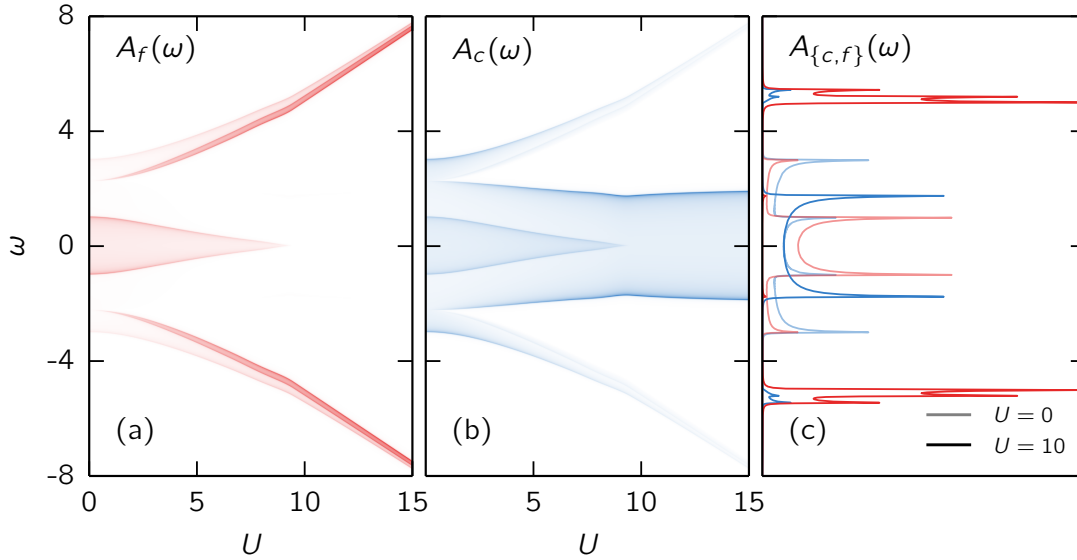
Figure 6.14: Density plots of spectral densities for both (a) the correlated (impurity) f-type orbitals and (b) the uncorrelated (conducting) c-type orbitals, for different frequencies ω and different interactions U at zero temperature $T = 0$. Cuts along lines with constant interactions $U = 0$ and $U = 10$ are shown in (c), indicated by the shading of the lines. The nearest-neighbor hybridization has magnitude $V = 0.866$. See text for discussion.

For practical calculations we have used a finite but small $\eta = 0.01$, which causes an artificial broadening of the delta poles in the spectral density [Eq. 6.10]. Results for $V = 0.866$ are shown in Fig. 6.14.

In the noninteracting case we find two superimposed tight-binding like bands of different width for both the f- and c-type spectral densities $A_f(\omega) \equiv A_{ff}(\omega)$ and $A_c(\omega) \equiv A_{cc}(\omega)$ with the same compact support, as can be seen from the shaded plots in Fig. 6.14(c) (note that in Fig. 6.14(a) the smallest values of $A_f(\omega)$ are not well resolved with the present color gradient). For finite U the two poles of the self-energy at $\omega = \pm 3V'_{\text{opt}}$ [Eq. 6.2] translate into a a three-peak structure of $A_f(\omega)$ with two Hubbard-like peaks located at $\omega \approx \pm U/2$ and the central quasi-particle resonance at $\omega = 0$. Upon increasing U, i.e., for reduced V'_{opt} [cf. Fig. 6.13(a)], spectral weight gets transferred from the central peak into the outer Hubbard peaks, until finally at $U_c \approx 9.46$, where $V'_{\text{opt}} \to 0$, the poles of the self-energy merge at $\omega = 0$ and a finite Mott gap is established in the f-electron's spectral density A_f. This resembles the Mott metal-insulator transition in the half-filled single-band Hubbard model as e.g. discussed in Sec. 6.2. However, simultaneously the weight of the induced Hubbard peaks in the c-type spectral density gradually gets suppressed and for interactions $U > U_c$ the c-type spectrum is dominated by a tight-binding-like dispersion of width $W \approx 4T$ leading to an overall metallic behavior of the system even for strong U (see Fig. 6.14(c), blue plot for $U = 10$).
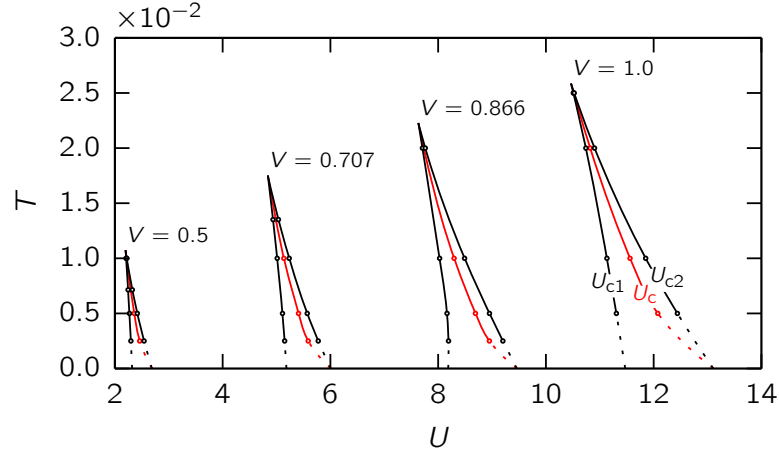
Figure 6.15: Triangular shaped phase diagrams of the Mott-like transition of the f-electron system in the half-filled PAM with different nearest-neighbor hybridizations V. Below some critical temperature metallic solutions persist up to interactions $U \leq U_{c2}$, insulating solutions arise for $U \geq U_{c1}$ (black lines), and in between both coexist. Red line: the first-order phase boundary $U_c(T)$. Extrapolations of all results down to zero temperature are indicated by dashed lines.

With this, we now turn back to finite temperatures and additionally consider the double occupancy for the respective optimal solutions, as depicted in Fig. 6.13(b), which as well shows three different branches in the coexistence region. Again, those solutions violating the thermodynamical stability condition $\partial \langle \hat{n}_\uparrow^f \hat{n}_\downarrow^f \rangle / \partial U = \partial^2 \Omega / \partial U^2 < 0$ have to be excluded via a Maxwell construction: the middle branch of the double occupancy is eliminated in favor of a jump at an appropriate interaction $U_c(\beta)$ [see inset of Fig. 6.13(b)]. The spinodal points of the curve set the lower and upper boundaries of the coexistence region, U_{c1} and U_{c2}.

Results for different temperatures and several values of V are shown in the phase diagrams depicted in Fig. 6.15. For all values of the hybridization V we find a triangular-shaped region, bounded by the curves $U_{c1}(T)$ and $U_{c2}(T)$, in between of which lies the first-order transition line $U_c(T)$ and which intersect at the critical temperature T_c, where the transition is of second order. Below T_c, metallic solutions for the f-electron system exist up to $U \leq U_{c2}$ whereas insulating solutions arise for $U \geq U_{c1}$, as has been discussed for the Hubbard model in the preceding section 6.2. This equivalence has been observed in DMFT calculations [232] and derived within the linearized DMFT [233]. In particular, Held and Bulla [233] found an approximate V^2-scaling of the critical interaction for the nearest-neighbor PAM at zero temperature which is recovered within our calculations, as shown in Fig. 6.16. However, they also suggested the same scaling law for the critical temperature, whereas our data rather yield a linear scaling $T_c \propto V$ [see Fig. 6.16(a)]. In fact the linearized DMFT is formulated at zero temperature and one thus might at least
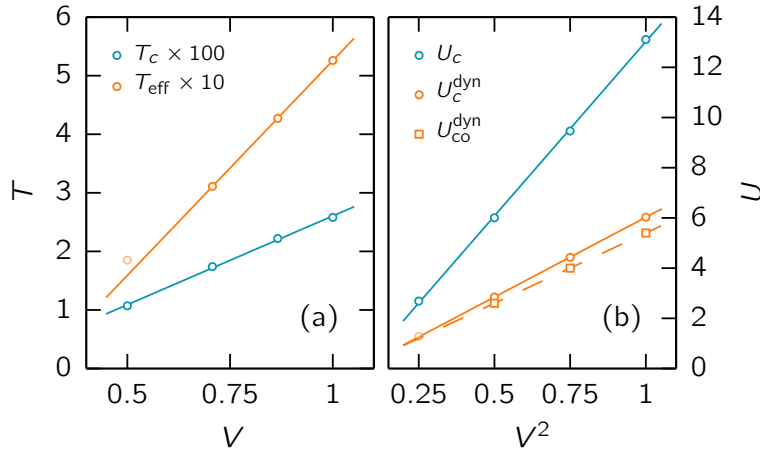
Figure 6.16: V-dependencies of (a) critical and effective temperatures and (b) critical (crossover) interactions U_c^{dyn} (U_{co}^{dyn}) both in (blue) and out of (orange) equilibrium. Circles: values for a nearest-neighbor PAM. Squares: on-site PAM. For $V = 0.5$ the effective temperature T_{eff} is not used for the linear fit and hence only plotted for completeness (plotted in pale color). Note that the results for the effective or critical temperature are rescaled by one or two orders of magnitude.

doubt that the derived scaling law trivially translates to finite temperatures.

In contrary, for the PAM with on-site hybridization, we performed calculations for temperatures down to $T \geq 2.5 \times 10^{-3}$ (i.e., $\beta \leq 400$), but could not identify any coexisting solutions, as shown in Fig. 6.17(a) for the optimal parameters V_{opt}' and for $V = 0.866$ in the original system. Starting from its noninteracting value, V_{opt}' decreases monotonically with increasing interaction, showing a steep slope around the inflection point of the curve. It is tempting to anticipate this as a precursor for some hysteresis at even smaller temperatures T, but we rather find a $1/T$-divergence of the inflection points' interaction. This is in line with a critical interaction $U_c \to \infty$ as has been suggested by linearized DMFT [233]. Moreover, the half-filled PAM with an on-site hybridization has an insulating ground state and crosses over from a hybridization band insulator at weak U to a Kondo insulator for strong interactions. As an illustration, Fig. 6.17(b) shows the gapped spectral densities for the noninteracting case. In fact, as has been pointed out by van Dongen *et al.* [234], any small on-site "perturbation" to the pure nearest-neighbor hybridization causes the transition at finite U to turn into a sharp crossover.

6.4.2 Nonequilibrium case

With the finding of an orbital selective Mott transition in the f-electron system of the PAM with nearest-neighbor hybridization, which is absent in the model with on-site hybridization, it will be interesting to analyze if and how this difference is reflected out of equilibrium. To this end, we conduct both sudden quenches and ramps of the
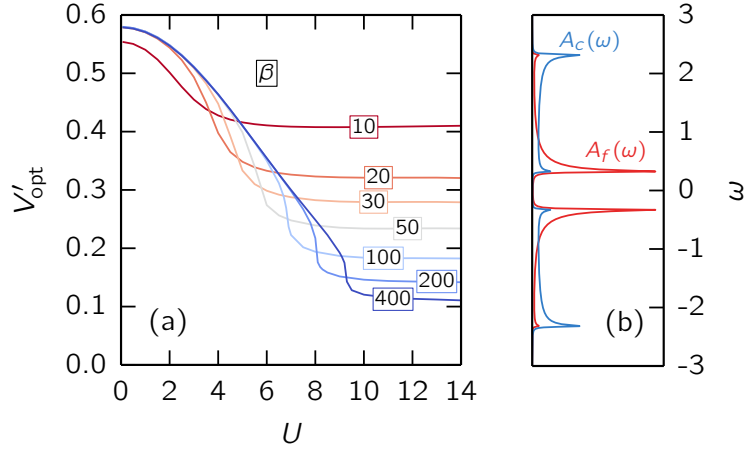
Figure 6.17: Equilibrium results for the PAM with on-site hybridization $V = 0.866$: (a) optimal parameter V'_{opt}, the point of steepest slope diverges as a function of inverse temperature, indicating a fully decoupled bath only at $T = 0$ and $U \to \infty$; (b) spectral densities for c- and f-type orbitals at $U = 0$ and $T = 0$, revealing the band-insulating character of the on-site PAM. See text for further discussion.

interaction parameter $U(t)$, starting from a "noninteracting" initial state. We have chosen a small but finite initial interaction, here $U_{\mathrm{ini}} = 0.1$, and prepared initial thermal states at inverse temperature $\beta = 10$, which as before essentially corresponds to a zero temperature state (see discussion in Sec. 6.3). As in equilibrium, we have performed calculations for different values of V, but in the following show results only for $V = 0.866$, i.e., $V^2 \approx 0.75$, if not stated otherwise.

Again, starting with the case of a nearest-neighbor hybridization, we find a *dynamical* transition for quenches ending at a critical interaction $U_c^{\mathrm{dyn}} \approx 4.43$, which sharply separates two distinct response regimes. Exemplary results for the time dependencies of the optimal parameter V'_{opt} are shown in Fig. 6.18 (top). For quenches to *weak* final interactions, i.e., $U_{\mathrm{fin}} < U_c^{\mathrm{dyn}}$, we find a quick relaxation to some smaller but positive values within about two inverse hoppings, which is followed by moderate oscillations [see Fig. 6.18 (top left)]. Contrary, as shown Fig. 6.18 (top right), for *strong* interactions $U_{\mathrm{fin}} > U_c^{\mathrm{dyn}}$ the optimal parameter drops to negative values and on top of the small and fast oscillations exhibits some pronounced, slow beating oscillations, the frequency of which increases with U_{fin}. Finally, at the critical point U_c^{dyn} the single bath site *dynamically* decouples, i.e., the optimal parameter vanishes on average for longer times, but some small regular oscillations around zero persist, as shown in Fig. 6.18 (top left). This very much resembles the situation in the Hubbard model as discussed in Sec. 6.3.1, though for the latter we found an *exact* decoupling of the bath site in the reference system.

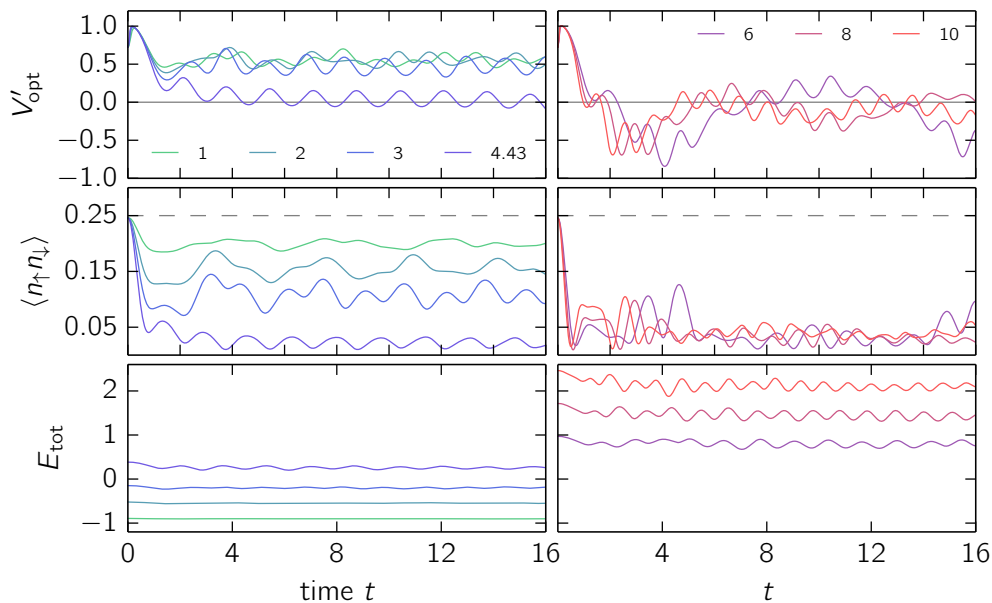Concerning the double occupancy and the energy, at least for the weak coupling case,

Figure 6.18: Time dependencies of the optimal parameters $V'_{\mathrm{opt}}(t)$, the double occupancies and the total energies for a PAM with nearest-neighbor hybridization $V = 0.866$ for quenches from $U_{\mathrm{ini}} = 0.1$ to different final interactions U_{fin} (see color labels). Left: $U_{\mathrm{fin}} \leq U_{\mathrm{c}}^{\mathrm{dyn}} \approx 4.43$. Right: $U_{\mathrm{fin}} > U_{\mathrm{c}}^{\mathrm{dyn}}$.

the overall behavior does not deviate much from that observed earlier in the Hubbard model (see Fig. 6.4). With increasing interactions, the double occupancies drop to smaller values on the same time scales as the hybridization parameter relaxes and afterward slightly oscillates (see Fig. 6.18 (left middle)), though close to the critical point, we do not find pronounced recurrences as in the case for the Hubbard model, but cannot exclude that these would appear on longer timescales for the nearest-neighbor PAM. At the same time, for all weak interactions the total energy is almost perfectly conserved and only rather small regular oscillations have to be tolerated (see Fig. 6.18 (left bottom)). For strong final interactions the dynamics of both models seemingly feature rather different dynamics: whereas in the Hubbard model on top of interaction dependent oscillations pronounced beatings and recurrences could be identified, in the present case the double occupancy rather seems to relax to almost constant values which essentially do not depend on U_{fin}. However, for the case $U_{\mathrm{fin}} = 6$ close to $t = 16$ the double occupancy, in phase with the optimal parameter's behavior, rises again and as argued before, longer times would be needed to better study this effect (see Fig. 6.18 (right middle)). Interestingly, and in contrary to the Hubbard model, the total energy also in the strong coupling regime is quite well conserved and strong oscillations are absent. In view of this, one might also speculate, whether the mentioned beatings of the double occupancy in the Hubbard model are a pure artifact of the worse energy conservation within the two-site DIA.

(a) nearest-neighbor hybridization
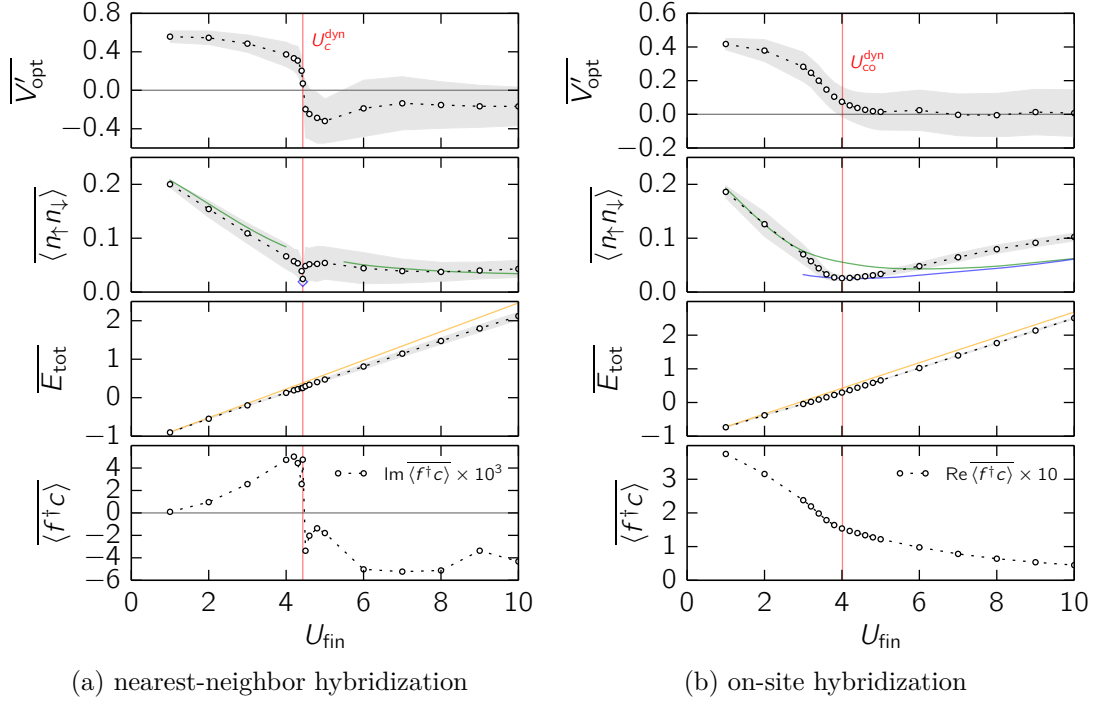(b) on-site hybridization

Figure 6.19: Long-time averages for the PAM with (a) a nearest-neighbor hybridization and (b) with an on-site hybridization, and both for $V = 0.866$. Red lines: (a) critical interaction U_c^{dyn} or rather (b) "crossover" interaction $U_{\mathrm{co}}^{\mathrm{dyn}}$. Green lines: thermal values for the double occupancy obtained from an equilibrium calculation for a two-site reference system. Blue diamond or line: same but obtained from a Hubbard-I calculation. For (a) we find $\mathrm{Re}\,\overline{\langle f^\dagger c\rangle} \approx 0$ and hence only the imaginary part $\mathrm{Im}\,\overline{\langle f^\dagger c\rangle}$ is plotted and vice versa for (b). Note that the values of the $\langle f^\dagger c\rangle$-correlation functions have been rescaled by one or three orders of magnitude.

The optimal parameter's long-time behavior is shown in Fig. 6.19(a) (top). Note that here and in the following long time averages and respective fluctuations are again calculated according to Eqs. (6.8) and (6.9). For *weak* $U_{\mathrm{fin}} < U_c^{\mathrm{dyn}}$, $\overline{V'_{\mathrm{opt}}}$ slowly decreases for increasing interactions but then rapidly drops close to the critical point where the bath site eventually decouples (on average) and relative oscillations are small. For *strong* final interactions, there is a sign change for the long-time average and considerably increased oscillations occur, which is due to the slow beating of large amplitude. Certainly, these values would improve for larger $t_{\max}$ but their overall trend seems well captured. For quenches ending at large $U_{\mathrm{fin}} > U_c^{\mathrm{dyn}}$ the absolute value of $\overline{V'_{\mathrm{opt}}}$ slowly decreases but seems to saturate for $U_{\mathrm{fin}} \gtrsim 8$. Note that the decoupling of the bath at the critical point is also reflected in the hybridization function $\langle f^\dagger c\rangle$, which reveals fully screened impurities (i.e., $\langle f^\dagger c\rangle = 0$) right at U_c^{dyn} but a finite hybridization of the f- and c-electron system off criticality [see Fig. 6.19(a) (bottom)].

The double occupancy's long-time average [see Fig. 6.19(a)] linearly decreases from its noninteracting value $\langle n_\downarrow n_\uparrow \rangle_0 = 0.25$, since the finite Coulomb repulsion energetically suppresses doubly occupied sites. Interestingly, for strong interactions $5 \leq U_{\text{fin}} \leq 10$ the double occupancy remains almost constant at around 0.05, whereas perturbative arguments, like in the Hubbard model, would suggest an increase toward larger values. Again, the two-site DIA seems to dynamically underestimate the final double occupancy for strong final interactions. This effect is even more pronounced than in the Hubbard model (therefore cf. Fig. 6.5). However, right at the critical point U_c^{dyn}, we find a similar rapid drop to almost vanishing values with only small remaining fluctuations.

Concerning the total energy, we find the same linear dependence $E_{\text{tot}}(t_0^+) = E_{\text{kin}}(t_0) + U_{\text{fin}}/4$ as discussed in Sec. 6.3 and shown in Fig. 6.19(a) (second from bottom). However, as compared to the Hubbard model, for larger times the total energy is surprisingly well conserved and only decays to long-time averages slightly smaller than $E_{\text{tot}}(t_0^+)$ accompanied by some moderate oscillations. Again, via the total energy we can ascribe an effective temperature T_{eff} to the final state, which qualitatively shows the same behavior as we plotted for the Hubbard model in Fig. 6.6 and is hence not shown again.

Finally, we have access to the thermal values for the double occupancies at T_{eff} by comparing the long-time averages of the total energies with their respective equilibrium values obtained from two-site DIA calculations at different temperatures (cf. Sec. 6.3.1). For sufficiently weak and strong interactions off U_c^{dyn} these approximately coincide with their respective long-time averages (see Fig. 6.19(a)). However, right at the critical point the long-time average deviates and rather matches the thermal value derived from a Hubbard-I approximation at $T_{\text{eff}} \approx 0.43$, i.e., from a reference system consisting of a single correlated site with no bath attached to it. Though, in total one might regard the system as thermalized in the described cases, one should consider further "meaningful" observables such as the time dependent momentum distribution. Unfortunately, the latter is dominated by severe oscillatory effects which should probably be ascribed to the small reference system, and thus proves insufficient for deciding whether the system relaxes to a thermal state or not. In conclusion, as for the equilibrium case, also the nonequilibrium dynamical transition resembles the corresponding behavior of the Hubbard model after quenches of the interaction [144] (see Sec. 6.3).

The same behavior as for the preceding exemplary case of $V = 0.866$ is essentially also found for all other values of V we considered. Interestingly, as shown in Fig. 6.16(b) we can extract a V^2-scaling of U_c^{dyn}, indicating that the nonequilibrium transition is in fact related to the equilibrium Mott behavior. The respective scaling law in equilibrium has been derived exploiting the system's properties right at criticality [233] and should hence be accounted as characteristic for the Mott transition. Moreover, the dynamical critical interactions differ by roughly a factor of two from their equilibrium counterparts, consistent with all previous results for the Hubbard model obtained by means of different methods [145–147, 229] as well as with our results presented in Sec. 6.3. Finally, as for T_c in equilibrium, we find a linear scaling of T_{eff} right at U_c^{dyn} [see Fig. 6.16(a)].

Noteworthy, besides this aforementioned accordance regarding the scaling behavior with respect to the hybridization parameter V, we again conducted ramps to trace the
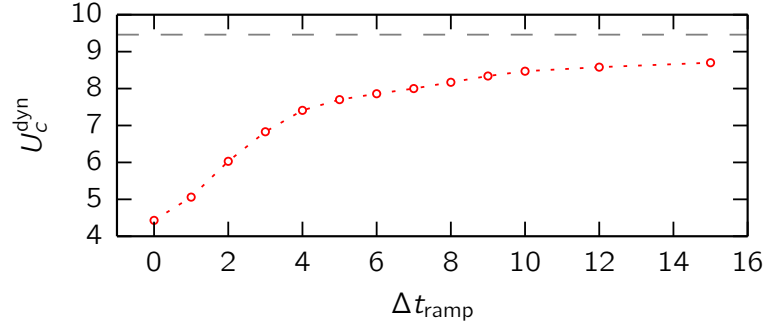
Figure 6.20: Critical dynamical interaction $U_\mathrm{c}^\mathrm{dyn}$ as a function of the ramp time Δt_ramp at $\beta_\mathrm{ini} = 10$ for a PAM with nearest-neighbor hybridization $V = 0.866$. Gray dashed line: equilibrium critical interaction $U_\mathrm{c2}(0) \approx 9.46$ at zero temperature. For comparison also consider ramps within the Hubbard model as were shown in Fig. 6.12.

crossover from the sudden quench dynamics to the adiabatic regime. We studied ramps of variable finite duration $\Delta t_\mathrm{ramp} \leq 15$ to different final interactions and for any ramp time we could identify a well defined $U_\mathrm{c}^\mathrm{dyn}(\Delta t_\mathrm{ramp})$, separating weak- and strong-coupling response regimes. For ramps with $\Delta t_\mathrm{ramp} \gtrsim 3$ the small regular oscillations observed for all quantities in the post-quench dynamics (cf. Fig. 6.18) fade out and thus e.g. the optimal parameter relaxes to constant positive values within times of the order of Δt_ramp for *weak* interactions and for *strong* interactions it performs slow collapse-and-revival oscillations around some (slightly) negative value (not plotted, but similar dynamics have been observed in the Hubbard model, as shown in Fig. 6.10). In Fig. 6.20 we show the critical interaction's dependency on Δt_ramp, which just as observed for ramps in the Hubbard model, monotonically increases toward the equilibrium value $U_c(0)$ at zero temperature.

To further support this apparent relation between the transition in and out of equilibrium, we finally question whether similar critical behavior as for the PAM with nearest-neighbor hybridization can be found in its variant where the hybridization is purely local [cf. Fig. 6.1(c)] and for which an orbital selective Mott transition is absent in equilibrium.

For weak interactions, we essentially find the same features as described for the PAM with nearest-neighbor hybridization, as may be infered from a comparison of the long-time averages [Eq. 6.8] of all observables and parameters as depicted in Figs. 6.19(b) and 6.19(a). Nevertheless, upon increasing the final interaction we could *not* identify a sharp transition. For brevity, we do not show the respective time-dependent results, but only focus on their long-time averages. Concerning the optimal hybridization, $\overline{V'_\mathrm{opt}}$ monotonically decreases and quickly approaches zero for $U_\mathrm{fin} \gtrsim 5$, but opposed to the preceding case there is no sign change. At the same time, pronounced regular oscillations persist for all $U_\mathrm{fin} \gtrsim 4$, as shown in Fig. 6.19(b). For the double occupancy, after an initial drop, we find almost constant values for all interactions, as can be seen from

the small fluctuations [cf. Eq. 6.9] in Fig. 6.19(b). After having reached a minimum at the intermediate interaction $U_{\mathrm{fin}} \approx 4$, $\overline{\langle n_\downarrow n_\uparrow \rangle}$ again increases for increasing U_{fin}, which in principle should be expected due to perturbative arguments, as has been mentioned earlier. However, as before, $\overline{\langle n_\downarrow n_\uparrow \rangle}$ does not fully rise to its noninteracting value and also for the present case seems to be underestimated by the two-site approach.

Remarkably, not only for weak, but also for strong interactions, the energy conservation is barely violated, which might be related to the strong resemblance of the "geometrical" structure of both the original and the respective reference system. Here, the on-site hybridization is present in both systems, whereas for the Hubbard model the bath site represents an additional "auxiliary" degree of freedom which is only present in the reference system and in case of the PAM with nearest-neighbor hybridization it provides an "additional link" between the f- and the c-electron system.

As before, we can deduce some effective temperature T_{eff} from $\overline{E_{\mathrm{tot}}}$, which however shows an unchanged U_{fin}^2-dependency for all final interactions (not shown), instead of two different regimes for weak and strong couplings, as observed in the case for a nearest-neighbor hybridization as well as for the Hubbard model (cf. Fig. 6.6). We again contrast the corresponding thermal values of the double occupancy with the respective long-time averages. For weak interactions, we find thermal double occupancies when compared to an appropriate grand potential calculated within the two-site DIA. For larger interactions ($U_{\mathrm{fin}} \gtrsim 3$) these start to deviate, but can again be regarded as thermal around $U_{\mathrm{fin}} \approx 4$ when compared to equilibrium results obtained with the help of a Hubbard-I reference system. This is quite remarkable, since at the same time neither the bath of the reference system decouples on average nor does the f-electron system get fully screened, as it was the case for the PAM with nearest-neighbor hybridization. For larger interactions, the double occupancy exceeds the thermal values obtained from either reference system, the latter of which converge against each other as has to be expected, since also for the two-site system the hybridization gradually vanishes close to the atomic limit.

To conclude, though both regimes are not sharply distinguished, we ascribe some dynamical "crossover" interaction $U_{\mathrm{co}}^{\mathrm{dyn}} \approx 4$ to the minimum of $\overline{\langle n_\downarrow n_\uparrow \rangle}$, in the proximity of which both $\overline{V'_{\mathrm{opt}}}$ as well as $\overline{\langle f^\dagger c \rangle}$ show an inflection point. Intriguingly, similar results are again obtained also for different values of V and as for the on-site PAM we find a V^2-scaling of $U_{\mathrm{co}}^{\mathrm{dyn}}$, which moreover almost coincides with $U_{\mathrm{c}}^{\mathrm{dyn}}$, as shown in Fig. 6.16(b). In view of $U_c = \infty$ in the equilibrium case, this is quite surprising.

6.5 Comparison of the DIA to Hamiltonian-based DMFT solvers

To conclude this chapter, let us contrast our approach with Hamiltonian-based methods which strive to exactly solve the nonequilibrium DMFT equations on short time scales by mapping the lattice model onto a single-impurity Anderson model with a *finite* number of bath sites [154]. It turns out that two different types of baths have to be carefully distinguished in such approaches, one describing correlations of the initial state which

possibly decay in the course of time and a second one which simultaneously captures the dynamically emerging correlations. For the latter, a causal scheme has been suggested for which a gradually increasing number of bath sites gets coupled to the impurity as time proceeds [154]. In practice one is limited to small systems, which sets a short maximum propagation time up to which converged results can be obtained. Recently, different implementations have been put forward, using exact-diagonalization techniques [154], the multi-configuration time-dependent Hartree method [155] as well as an approach based on the matrix-product state representation [156]. In all these studies the time evolution is started from the atomic limit, where there is no need for an initial bath. The number of bath sites needed for the final-state dynamics and the related maximum propagation time varies: With exact-diagonalization methods [154] propagation up to $t_{\max} \approx 3$ inverse hoppings has been possible by providing $L_b = 8$ bath sites at weak interactions, whereas using matrix-product states [156], $t_{\max} \approx 7$ ($t_{\max} \approx 5.5$) could be reached with $L_b = 24$ ($L_b = 18$) sites at strong (weak) interactions. It is noteworthy that the performance of both approaches depends on the interaction strength and that for later times conservation of energy is lost and additional bath sites would be needed.

Opposed to those Hamiltonian-based DMFT methods, the self-energy functional approach maps the original lattice-fermion problem onto an auxiliary model with a fixed, small number of bath sites and, in the case of the dynamical impurity approximation, a single correlated site. Rather than aiming at an exact solution of the nonequilibrium DMFT equations, the SFT provides an independent variational scheme to determine the time-dependent one-particle parameters of the reference system which only in the limit of an infinite number of bath sites recovers the DMFT. Formally, much longer propagation times with a very small number of bath sites (a single bath site only in the case considered here) are possible in this way. The present study has in fact shown that even with the most simple reference system one can make close contact with full DMFT results. The agreement between the two-site DIA and full DMFT is qualitatively satisfying and close to the critical point for the (dynamical) Mott transition even quantitative. This demonstrates that much of the essential physics can be captured with a single time-dependent variational parameter.

The general framework of the SFT ensures that variational approximations are conserving with respect to the particle number and spin. The possible violation of energy conservation, however, must be seen as a major drawback of the present implementation of the DIA. Ways to overcome this problem have been discussed in Sec. 3.9.3. Here, we could show that energy conservation is in fact violated but that, on the other hand, this violation is moderate in the weak-coupling limit after a quantum quench and even for strong interactions does not generally invalidate the results which still agree qualitatively with DMFT. Furthermore, if the dynamics is initiated by ramping the interaction, energy conservation is respected to a much higher degree.

7 Conclusions and Perspectives

Mastering the problem of strongly correlated fermions on a lattice has challenged theoreticians for more than five decades and has stimulated the development of a large number of different methods. Among these many cluster and impurity approximations could be unified and extended in the single framework of self-energy functional theory (SFT) [162]. This comprises "two-site" approximations [240] and the linearized DMFT [235], dynamical impurity approximations (DIA) [162, 171, 174], but also formally recovers the dynamical mean-field theory (DMFT) and its cluster extensions, i.e., the cellular DMFT (C-DMFT) [125, 126, 163] as well as the dynamical cluster approximation (DCA) [127, 176], and finally the cluster-perturbation theory (CPT) [158, 159] and its variational extension, the variational cluster approach (VCA) [164]. The SFT has been extended into several directions, e.g., to systems with nonlocal interactions [175], to disordered [176] and to bosonic systems [177–179].

Starting out to the unexplored grounds of physics far from equilibrium has stimulated the development of staggeringly fast and precise experimental techniques which nowadays allow experimentalists to e.g. stimulate and trace electron dynamics in real materials or to trap atoms in artificial optical lattices to unveil the properties of underlying, idealized theoretical models. On the theoretical side, considerable progress has been made to extend known methods and develop new concepts to describe real-time phenomena of many-body systems.

Nonequilibrium methodology

In this thesis, we have generalized the self-energy functional theory to the nonequilibrium case. Approximations provided within this nonequilibrium SFT address the transient dynamics of single-particle observables of lattice-fermion systems, initially prepared in a thermal state and driven out of equilibrium by sudden quenches or arbitrary time-dependent perturbations.

Though the equilibrium variant of the present approach is recovered in case of an equilibrium setup and both share the same formal structure, several important aspects without any counterpart in the equilibrium formalism emerge. For a meaningful extension of the variational principle inherent to the SFT, the space of physical parameters has to be enlarged to also incorporate *unphysical* or *transverse* variations which fix the nontrivial time-dependent solutions within the *physical* manifold. However, evaluated at a *physical* stationary point, the self-energy functional yields the grand potential of the initial thermal state and thus also in nonequilibrium retains a precise physical meaning. Another important concern exclusive only to the nonequilibrium case is the question whether microscopic conservation laws resulting from the symmetries of the original

Hamiltonian are respected within the generalized approach. Remarkably, we could show that even the simplest approximations accessible via the NE-SFT "conserve" any one-particle observables if this had to be the case for the original system. Importantly, though we adapted basic concepts and ideas of a proof on "conserving approximations" by Baym and Kadanoff, apart from DMFT, approximations constructed within the NE-SFT are not "Φ-derivable" but rather *nonperturbative*.

Regarding energy conservation, the optimization of parameters which are nonlocal in time would be required, which, however, corresponds to providing a continuous bath in the reference system. In fact, this recovers the DMFT or its cluster variants, which indeed conserve the total energy. Nevertheless, the quality of the approximations can be systematically improved by enlarging the reference system and moreover, in principle, the formal structure of the SFT allows to enforce energy conservation by means of constrained variations.

Finally, the nonequilibrium SFT has an inherently causal structure, i.e., respects the physical causality principle. Apart from being relevant on a fundamental level, this also proves important for the numerical implementation of the variational problem.

Numerical implementation

Numerically evaluating the SFT Euler equation on the real-time contour turned out to be elaborate in several aspects. Due to the necessity for *transverse* variations of the self-energy functional, its direct evaluation, which would entail *unphysical* Hamiltonians, seems to be less favorable than in the equilibrium variant of the SFT. Fortunately the involved functional derivatives could be carried out explicitly, turning the variational problem of the respective functional on an *unphysical* manifold into a root finding problem for its derivative on the space of *physical* parameters. Due to causality, a time-propagation algorithm has been proposed which allows to search for stationary points at some instant of time without altering the results at earlier stages. Disadvantageously, in practice this suffers from severe numerical instabilities which could be traced back to an inherent quadratic dependence of the Jacobian on the time step Δt. Replacing the Euler equation by its time-derivative, the corresponding Jacobian of which shows a numerically much more favorable linear-in-Δt scaling, this difficulty could eventually be evaded. By using high-order integration schemes wherever possible and with the help of Broyden's method we have finally put forward and have implemented a stable propagation algorithm for the optimal parameters of the reference system.

As a benchmark, we have applied the variational cluster approach (VCA) in its simplest, conceivable form, namely for a reference cluster consisting of two sites, to study the dynamics of a one-dimensional dimerized Hubbard model. To this end, we considered exactly solvable or slightly perturbed initial states and altered the model's hopping parameter by two different fast ramps at various but fixed interaction strengths. Tracing the time-evolution of the optimal parameters, the double occupancy, and the energy and guided by well-founded expectations on the final state dynamics, we could demonstrate that plausible and consistent results are in fact accessible.

Dynamical Mott transition

The true strengths of variational approaches encompassed by the SFT manifest themselves in situations involving e.g. broken symmetry phases or (dynamical) phase transitions. As a prime example, we studied the dynamical Mott metal-insulator transition which emerges in the real-time dynamics of the Hubbard model subsequent to quenches and ramps of its interaction parameter. As for its (possible) equilibrium counterpart, the (two-site) dynamical impurity approximation (DIA), which provides a local trial self-energy, turned out to sufficiently capture the transition's essential features.

Starting from a noninteracting initial state, we have studied the time evolutions of the double occupancy, the total energy, the momentum distribution, and the optimal hybridization parameter of the reference system for different final values of the interaction. Sharply separated by a critical interaction $U_{\mathrm{c}}^{\mathrm{dyn}}$ at which fast thermalization occurs, we have found two distinct response regimes and clear signs of prethermal, intermediate states for both weak and strong final interactions. However, this dynamical transition occurs at a highly increased effective temperature and at about half the value of the critical interaction for the equilibrium Mott transition at zero temperature. Despite the simplicity of the two-site approach, this is in surprisingly good accordance with previous nonequilibrium DMFT results [144].

Interestingly, within the DIA, right at the critical point and after a rapid relaxation, the optimal hybridization parameter vanishes for all later times. This strongly resembles the characteristic behavior in the equilibrium case, where the Mott transition is indicated by a decoupling of the bath site in the two-site approximation, emphasizing a possible link between both transitions. To further trace this presumption, we conducted ramps of different duration and found the same well-pronounced critical behavior in the entire range from the sudden quench to the limit of an adiabatically slow quasi-static process. Upon slowing down the ramp speed we could identify a monotonic increase of $U_{\mathrm{c}}^{\mathrm{dyn}}$ finally approaching the zero-temperature critical interaction in the adiabatic limit, which is qualitatively in line with earlier findings within the Gutzwiller approach [229, 239]. By means of the latter also the impact of doping was studied, and, as in the equilibrium case, the transition was found to turn into a crossover away from half-filling.

In a similar spirit, we considered the half-filled periodic Anderson model (PAM) and in particular focused on two variants with different hybridizations of the uncorrelated dispersive band and the correlated impurity degrees of freedom. This is especially interesting, since this setup allows us to "tune" between different configurations either favoring or impeding the Mott transition in equilibrium: for a spatially local hybridization the model exhibits band or Kondo insulating behavior for weak or strong interactions, whereas for a nearest-neighbor hybridization a Mott-type metal-insulator transition takes place in the correlated orbitals. By means of linearized DMFT this could be related to the Mott transition in the Hubbard model [233] and furthermore a characteristic quadratic scaling of the precise value of the critical interaction with the hybridization strength was predicted. Here, we have again studied quenches and ramps of the interaction parameter questioning whether the presence or absence of a Mott-like transition depending on the geometrical details of the model is also reflected in the respective nonequilibrium dynam-

ics. In fact, for the model with a nearest-neighbor hybridization V we found two distinct response regimes, separated by a sharp transition, sharing basically the same features as the dynamical transition in the Hubbard model. Moreover, the critical interaction obeys the same characteristic V^2-scaling as the respective value in equilibrium. On the other hand, for a local hybridization this transition turns into a dynamical crossover. These findings strongly support the existence of a possible link between both the transition in and out of equilibrium and hence justify the notion of a *dynamical* Mott transition.

Perspectives

Over a little more than the last decade the SFT has become a well established, widely used and valuable framework for various different approximation schemes to the strongly correlated many-body problem and with this thesis we hope to provide the basis for a similar recognition and success in the emerging field of nonequilibrium dynamics.

Concerning the Mott insulator, an obvious extension of the present DIA studies would comprise more bath sites, and one may speculate that some of these, representing low energy degrees of freedom, would decouple at the transition, whereas other would remain connected to the correlated impurity. Equally well interesting would be to induce the dynamical Mott transition from the "opposite" side, i.e., study the time-dependent closure of the Mott-Hubbard gap when conducting quenches or ramps into metallic states, starting from the atomic limit, for example. To the best of our knowledge only a few works have been leading in this direction so far [241, 242].

In fact, our first efforts concerning this matter revealed diverging optimal parameters at a certain time t^* and we could almost certainly exclude numerical reasons for this [priv. comm. w/ C. Gramsch]. However, so far, we did not find a fully convincing physical explanation for this phenomena but expect clarifying results in some future work. Until then, room is left for speculations. Most promisingly, the observed divergences might be linked to a recently proposed notion of a *dynamical phase transition*, which relies on the observation of nonanalytical behavior of e.g. the return probability at certain instants of time [55]. For variational approaches as constructed within the SFT, such real-time nonanalytical behavior of the thermodynamically large original system might translate into diverging optimal parameters of the small reference system.

Providing additional bath sites would furthermore allow for the study of more complex models, like two-band variants of the Hubbard model. There, an orbital selective Mott transition gives rise to a more complex phase diagram and non-Fermi liquid behavior may arise in a phase where localized and itinerant fermions coexist [243, 244]. Understanding these phenomena from a real-time perspective would clearly be an exciting task and first attempts along these lines have been made recently [245].

Moreover, incorporating nonlocal trial self-energies via cluster approximations and exploring the same questions will probably reveal further intriguing insights of the Mott transition, as is apparent from equilibrium considerations in two dimensions, where short-ranged antiferromagnetic correlations turn out to modify the topology of the phase diagram [168].

The variational cluster approximation seems particularly suited for models with hopping amplitudes alternating from site to site, i.e., which on their own suggest a "natural" tiling of the full lattice into smaller clusters by cutting along the "weaker" links (cf. Sec. 5). For Hubbard models on a checkerboard lattice, i.e., for weakly coupled square plaquettes, an extremely rich phase diagram has been found [246] and a new class of so called "fragile" Mott insulators was predicted to exist [247]. Furthermore, studies on topological transport in one-dimensional "dimerized", but effectively uncorrelated models have been performed in recent experiments with ultracold fermions [248] and bosons [249] but also theoretically for doublons in the strong coupling limit of a dimerized Hubbard model [250]. Clearly, the interplay of correlations and topological phenomena raises new questions and has become a field of active research [251]. Interaction driven topological phase transitions in the Haldane-Hubbard model on honeycomb lattices have very recently been studied in equilibrium with the help of the VCA [252, 253]. Lastly, the formation and redistribution of spin-correlations after changing the lattice geometry by ramping the hopping between certain sublattice sites of a Hubbard model has been in the focus of experiments with ultracold fermions [92, 94]. Studying the expectable complex real-time phenomenology of these systems, induced by temporal changes of the geometrical details or the interaction, might serve as a fruitful field of application for the nonequilibrium VCA.

However, since the SFT builds on one-particle quantities, directly measuring spin-spin correlations is impossible and informations on spin-order can only be gained via local spin-densities and fictitious magnetic fields in the reference system. Thus a formalism in the spirit of the SFT but with access to preferably two-particle correlation functions would be desirable. A work by van Leeuwen et al. [254] may serve as a basis for a imaginable "vertex-functional theory": analogous to Φ-derivable approximations based on the Luttinger-Ward functional, the authors derive a more general functional Ξ, from which conserving but perturbative approximations for both the self-energy as well as the four-point vertex can be derived. Exploiting universality properties of this or related functionals will allow for the same idea as in the SFT: without changing the functional dependencies a nonperturbative evaluation on a space of trial self-energies and four-point vertices obtained from a small reference system is accessible. Such a vertex-functional theory might not suffer from the same difficulties concerning energy conservation as does the SFT and will give direct access to two-particle observables.

Another technical endeavor of the SFT could target long-time evolutions. In the present formulation calculations become computationally demanding for long-times due to the evaluation of the four-point correlation functions (for three independent times) involved in the Euler equation: at any time-step a memory kernel quadratic in time has to be recalculated or updated and eventually the entire propagation algorithm scales cubically in maximum propagation time. This obstacle might be bypassed with the help of an appealing idea [161, 185]: a small correlated reference system may be replaced by a completely uncorrelated effective medium providing a Markovian propagation scheme instead of the solution of the respective Dyson equation with a memory kernel. To this end, a Lehmann representation of the nonequilibrium self-energy has been constructed,

based on which a beneficial reformulation of the SFT seems conceivable.

Appendix

A Technicalities

A.1 Prevalent commutation relations

Fermionic operators obey the following anticommuation relations

$$\left\{ c_\alpha, c_\beta^\dagger \right\} = \delta_{\alpha\beta}\,, \tag{A.1}$$

$$\left\{ c_\alpha, c_\beta \right\} = \left\{ c_\alpha^\dagger, c_\beta^\dagger \right\} = 0\,. \tag{A.2}$$

Using basic properties of (anti)commutators, we derive the following commutation relations of fermionic construction operators with one- and two-particle parts of a general Hamiltonian [see Eq. 2.1].

For $H_{\boldsymbol{\lambda},0} = \sum_{\alpha\beta} \lambda_{\alpha\beta} c_\alpha^\dagger c_\beta$:

$$
\begin{aligned}
\left[c_\alpha, H_{\boldsymbol{\lambda},0} \right] &= \sum_\beta \lambda_{\alpha\beta} c_\beta\,, \\
\left[H_{\boldsymbol{\lambda},0}, c_\alpha^\dagger \right] &= \sum_\beta c_\beta^\dagger \lambda_{\beta\alpha}\,.
\end{aligned}
\tag{A.3}
$$

For $H_{0,\boldsymbol{U}} = \frac{1}{2} \sum_{\alpha\beta\gamma\delta} U_{\alpha\beta\delta\gamma} c_\alpha^\dagger c_\beta^\dagger c_\gamma c_\delta$, with $U_{\alpha\beta\delta\gamma} = U_{\beta\alpha\gamma\delta}$:

$$
\begin{aligned}
\left[c_\alpha, H_{0,\boldsymbol{U}} \right] &= \frac{1}{2} \sum_{\beta\gamma\delta} U_{[\alpha,\beta]\delta\gamma} c_\beta^\dagger c_\gamma c_\delta\,, \\
\left[H_{0,\boldsymbol{U}}, c_\alpha^\dagger \right] &= \frac{1}{2} \sum_{\beta\gamma\delta} U_{\delta\gamma[\alpha,\beta]} c_\delta^\dagger c_\gamma^\dagger c_\beta\,,
\end{aligned}
\tag{A.4}
$$

where we used the short-hand notation $U_{[\alpha,\beta]\delta\gamma} = U_{\alpha\beta\delta\gamma} - U_{\beta\alpha\delta\gamma}$. For Coulomb-like interactions with orbital and spin indices, i.e., $\alpha = (i,\sigma)$ and so forth, and with $U_{i\sigma,j\sigma',l\lambda,k\lambda'} = U_{ijlk}\delta_{\lambda\sigma}\delta_{\lambda'\sigma'}$, Eqs. (A.4) attain the form:

$$
\begin{aligned}
\left[c_{i\sigma}, H_{0,\boldsymbol{U}} \right] &= \sum_{jkl} \sum_{\sigma'} U_{ijkl} c_{j\sigma'}^\dagger c_{l\sigma'} c_{k\sigma}\,, \\
\left[H_{0,\boldsymbol{U}}, c_{i\sigma}^\dagger \right] &= \sum_{jkl} \sum_{\sigma'} U_{klij} c_{k\sigma}^\dagger c_{l\sigma'}^\dagger c_{j\sigma'}\,.
\end{aligned}
\tag{A.5}
$$

A.2 Units of contour quantities

Since $\hbar$ is set to one, all quantities are measured in units of the energy E, i.e., in powers of $[E]$. For the following, note that the inverse of a two-point function $\boldsymbol{X}(1, 2)$ on the contour is defined by

$$\int d\bar{1}\, \boldsymbol{X}^{-1}(1, \bar{1})\boldsymbol{X}(\bar{1}, 1') = [\boldsymbol{X}^{-1} \circ \boldsymbol{X}](1, 1') = \boldsymbol{\delta}(z, z')\,. \tag{A.6}$$

The following table lists the units of typical quantities that occur in the present context as well as units of derived quantities, such as derivatives or inverses.

quantity	unit	example
z (time)	$[E]^{-1}$	
β^{-1} (temperature)	$[E]$	
$\int_{\mathcal{C}} dz\,,\int di\,,\circ\,,\mathrm{Tr}$	$[E]^{-1}$	
$\delta_{\mathcal{C}}(z, z')\,,\delta(1, 1')$	$[E]$	
∂_z	$[E]$	
$\boldsymbol{\lambda}(z)$	$[E]$	
$\boldsymbol{G}\,,\boldsymbol{G}^{(0)}$	1	
$\boldsymbol{\Sigma}$	$[E]^2$	
two-point contour functions $X(1, 2)$		
$\boldsymbol{X}^{-1}$	$[E]^2[\boldsymbol{X}]^{-1}$	$\left[\boldsymbol{G}^{(0)^{-1}}\right] = [E]^2$
$\dfrac{\delta}{\delta \boldsymbol{X}}$	$[E]^2[\boldsymbol{X}]^{-1}$	$\left[\dfrac{\delta}{\delta \boldsymbol{\Sigma}}\right] = 1$
$\widehat{F}[\boldsymbol{X}]$	different possibilities	$[\widehat{\Omega}] = [E]$
$\dfrac{\delta\widehat{F}[\boldsymbol{X}]}{\delta \boldsymbol{X}}$	$[E]^2[\boldsymbol{X}]^{-1}[\widehat{F}]$	
$f(\boldsymbol{X})$ (cf. Eq. 2.25)	$[E]$	
one-point contour functions $Y(1)$		
$\boldsymbol{Y}^{-1}$	$[E][\boldsymbol{Y}]^{-1}$	$[\boldsymbol{\lambda}(z)^{-1}] = 1$
$\dfrac{\delta}{\delta \boldsymbol{Y}}$	$[E][\boldsymbol{Y}]^{-1}$	$\left[\dfrac{\delta}{\delta \boldsymbol{\lambda}(z)}\right] = 1$

Table A.1: List of units of different contour quantities as well as derived entities such as inverses and derivatives, measured in units of energy $[E]$.

Bibliography

[1] Hutchison, C. A., R.-Y. Chuang, V. N. Noskov, N. Assad-Garcia, T. J. Deerinck, M. H. Ellisman, J. Gill, K. Kannan, B. J. Karas, L. Ma, J. F. Pelletier, Z.-Q. Qi, R. A. Richter, E. A. Strychalski, L. Sun, Y. Suzuki, B. Tsvetanova, K. S. Wise, H. O. Smith, J. I. Glass, C. Merryman, D. G. Gibson and J. C. Venter: *Design and synthesis of a minimal bacterial genome*, Science **351** (6280) aad6253 (2016).

[2] Silver, D., A. Huang, C. J. Maddison, A. Guez, L. Sifre, G. van den Driessche, J. Schrittwieser, I. Antonoglou, V. Panneershelvam, M. Lanctot, S. Dieleman, D. Grewe, J. Nham, N. Kalchbrenner, I. Sutskever, T. Lillicrap, M. Leach, K. Kavukcuoglu, T. Graepel and D. Hassabis: *Mastering the game of Go with deep neural networks and tree search*, Nature **529** (7587) 484 (2016).

[3] Mitrano, M., A. Cantaluppi, D. Nicoletti, S. Kaiser, A. Perucchi, S. Lupi, P. Di Pietro, D. Pontiroli, M. Riccò, S. R. Clark, D. Jaksch and A. Cavalleri: *Possible light-induced superconductivity in K_3C_{60} at high temperature*, Nature **530** (7591) 461 (2016).

[4] Boer, J. H. d. and E. J. W. Verwey: *Semi-conductors with partially and with completely filled 3 d -lattice bands*, Proc. Phys. Soc. **49** (4S) 59 (1937).

[5] Mott, N. F. and R. Peierls: *Discussion of the paper by de Boer and Verwey*, Proc. Phys. Soc. **49** (4S) 72 (1937).

[6] Mott, N. F.: *The Basis of the Electron Theory of Metals, with Special Reference to the Transition Metals*, Proc. Phys. Soc. (London) **A62** (7) 416 (1949).

[7] Hubbard, J.: *Electron correlations in narrow energy bands*, Proc. R. Soc. Lond. A **276** 238 (1963).

[8] Gutzwiller, M. C.: *Effect of Correlation on the Ferromagnetism of Transition Metals*, Phys. Rev. Lett. **10** (5) 159 (1963).

[9] Kanamori, J.: *Electron Correlation and Ferromagnetism of Transition Metals*, Prog. Theor. Phys. **30** (3) 275 (1963).

[10] Imada, M., A. Fujimori and Y. Tokura: *Metal-insulator transitions*, Rev. Mod. Phys. **70** (4) 1039 (1998).

[11] Dobrosavljević, V.: *Conductor-Insulator Quantum Phase Transitions*, chapter Introduction to Metal-Insulator Transitions, Oxford University Press, Oxford (2012), `arXiv:1112.6166 [cond-mat.str-el]`.

[12] Gebhard, F.: *The Mott Metal-Insulator Transition*, *Springer Tracts in Modern Physics*, volume 137, Springer, Berlin Heidelberg (1997).

[13] Anderson, P. W.: *Antiferromagnetism. Theory of Superexchange Interaction*, Phys. Rev. **79** (2) 350 (1950).

[14] Lee, P. A., N. Nagaosa and X.-G. Wen: *Doping a Mott insulator: Physics of high-temperature superconductivity*, Rev. Mod. Phys. **78** (1) 17 (2006), `cond-mat/0410445`.

[15] Dagotto, E.: *Complexity in strongly correlated electronic systems*, Science **309** (5732) 257 (2005).

[16] Steinmeyer, G., D. H. Sutter, L. Gallmann, N. Matuschek and U. Keller: *Frontiers in ultrashort pulse generation: pushing the limits in linear and nonlinear optics*, Science **286** (5444) 1507 (1999).

[17] Hentschel, M., R. Kienberger, C. Spielmann, G. A. Reider, N. Milosevic, T. Brabec, P. Corkum, U. Heinzmann, M. Drescher and F. Krausz: *Attosecond metrology*, Nature **414** (6863) 509 (2001).

[18] Cavalieri, A. L., N. Müller, T. Uphues, V. S. Yakovlev, A. Baltuska, B. Horvath, B. Schmidt, L. Blümel, R. Holzwarth, S. Hendel, M. Drescher, U. Kleineberg, P. M. Echenique, R. Kienberger, F. Krausz and U. Heinzmann: *Attosecond spectroscopy in condensed matter.*, Nature **449** (7165) 1029 (2007).

[19] Kling, M. F. and M. J. J. Vrakking: *Attosecond electron dynamics.*, Annu Rev Phys Chem **59** 463 (2008).

[20] Gallmann, L., C. Cirelli and U. Keller: *Attosecond science: recent highlights and future trends.*, Annu Rev Phys Chem **63** 447 (2012).

[21] Wall, S., D. Brida, S. R. Clark, H. P. Ehrke, D. Jaksch, A. Ardavan, S. Bonora, H. Uemura, Y. Takahashi, T. Hasegawa, H. Okamoto, G. Cerullo and A. Cavalleri: *Quantum interference between charge excitation paths in a solid-state Mott insulator*, Nat. Phys. **7** 114 (2011).

[22] Ogasawara, T., M. Ashida, N. Motoyama, H. Eisaki, S. Uchida, Y. Tokura, H. Ghosh, A. Shukla, S. Mazumdar and M. Kuwata-Gonokami: *Ultrafast Optical Nonlinearity in the Quasi-One-Dimensional Mott Insulator*, Phys. Rev. Lett. **85** (10) 2204 (2000).

[23] Iwai, S., M. Ono, A. Maeda, H. Matsuzaki, H. Kishida, H. Okamoto and Y. Tokura: *Ultrafast Optical Switching to a Metallic State by Photoinduced Mott Transition in a Halogen-Bridged Nickel-Chain Compound*, Phys. Rev. Lett. **91** (5) 057401 (2003).

[24] Perfetti, L., P. A. Loukakos, M. Lisowski, U. Bovensiepen, H. Berger, S. Biermann, P. S. Cornaglia, A. Georges and M. Wolf: *Time Evolution of the Electronic Structure of* $1\mathrm{T} - \mathrm{TaS}_2$ *through the Insulator-Metal Transition*, Phys. Rev. Lett. **97** (6) 067402 (2006).

[25] Kübler, C., H. Ehrke, R. Huber, R. Lopez, A. Halabica, R. F. Haglund and A. Leitenstorfer: *Coherent Structural Dynamics and Electronic Correlations during an Ultrafast Insulator-to-Metal Phase Transition in* VO_2, Phys. Rev. Lett. **99** (11) 116401 (2007).

[26] Nasu, K.: *Photoinduced phase transitions*, World Scientific (2004).

[27] Ichikawa, H., S. Nozawa, T. Sato, A. Tomita, K. Ichiyanagi, M. Chollet, L. Guerin, N. Dean, A. Cavalleri, S.-i. Adachi, T.-h. Arima, H. Sawa, Y. Ogimoto, M. Nakamura, R. Tamaki, K. Miyano and S.-y. Koshihara: *Transient photoinduced 'hidden' phase in a manganite.*, Nat Mater **10** (2) 101 (2011).

[28] Fausti, D., R. I. Tobey, N. Dean, S. Kaiser, A. Dienst, M. C. Hoffmann, S. Pyon, T. Takayama, H. Takagi and A. Cavalleri: *Light-induced superconductivity in a stripe-ordered cuprate.*, Science **331** (6014) 189 (2011).

[29] Polkovnikov, A., K. Sengupta, A. Silva and M. Vengalattore: *Colloquium: Nonequilibrium dynamics of closed interacting quantum systems*, Rev. Mod. Phys. **83** (3) 863 (2011), `arXiv:1007.5331 [cond-mat.stat-mech]`.

[30] Eisert, J., M. Friesdorf and C. Gogolin: *Quantum many-body systems out of equilibrium*, Nat. Phys. **11** 124 (2015), `arXiv:1408.5148 [quant-ph]`.

[31] von Neumann, J.: *Beweis des Ergodensatzes und des H-Theorems in der neuen Mechanik*, Zeitschrift für Physik **57** (1-2) 30 (1929).

[32] von Neumann, J.: *Proof of the ergodic theorem and the H-theorem in quantum mechanics. Translation of: Beweis des Ergodensatzes und des H-Theorems in der neuen Mechanik*, Eur. Phys. J. H **35** 201 (2010), `arXiv:1003.2133 [physics.hist-ph]`.

[33] Goldstein, S., J. L. Lebowitz, C. Mastrodonato, R. Tumulka and N. Zanghi: *Normal typicality and von Neumann's quantum ergodic theorem*, Royal Society of London Proceedings Series A **466** 3203 (2010), `arXiv:0907.0108 [quant-ph]`.

[34] Rigol, M. and M. Srednicki: *Alternatives to Eigenstate Thermalization*, Phys. Rev. Lett. **108** (11) 110601 (2012), `arXiv:1108.0928 [cond-mat.stat-mech]`.

[35] Deutsch, J. M.: *Quantum statistical mechanics in a closed system*, Phys. Rev. A **43** (4) 2046 (1991).

[36] Srednicki, M.: *Chaos and quantum thermalization*, Phys. Rev. E **50** (2) 888 (1994).

[37] Rigol, M., V. Dunjko and M. Olshanii: *Thermalization and its mechanism for generic isolated quantum systems.*, Nature **452** (7189) 854 (2008).

[38] De Palma, G., A. Serafini, V. Giovannetti and M. Cramer: *Necessity of Eigenstate Thermalization.*, Phys. Rev. Lett. **115** (22) 220401 (2015), `arXiv:1506.07265 [quant-ph]`.

[39] Caux, J. S. and J. Mossel: *Remarks on the notion of quantum integrability*, J. Stat. Mech. **2** (02) 02023 (2011), `arXiv:1012.3587 [cond-mat.str-el]`.

[40] Rigol, M., V. Dunjko, V. Yurovsky and M. Olshanii: *Relaxation in a Completely Integrable Many-Body Quantum System: An AbInitio Study of the Dynamics of the Highly Excited States of 1D Lattice Hard-Core Bosons*, Phys. Rev. Lett. **98** (5) 050405 (2007), `cond-mat/0604476`.

[41] Berges, J., S. Borsányi and C. Wetterich: *Prethermalization*, Phys. Rev. Lett. **93** (14) 142002 (2004), `hep-ph/0403234`.

[42] Moeckel, M. and S. Kehrein: *Interaction Quench in the Hubbard Model*, Phys. Rev. Lett. **100** (17) 175702 (2008), `arXiv:0802.3202 [cond-mat.str-el]`.

[43] Marcuzzi, M., J. Marino, A. Gambassi and A. Silva: *Prethermalization in a Non-integrable Quantum Spin Chain after a Quench*, Phys. Rev. Lett. **111** (19) 197203 (2013), `arXiv:1307.3738 [cond-mat.stat-mech]`.

[44] Gring, M., M. Kuhnert, T. Langen, T. Kitagawa, B. Rauer, M. Schreitl, I. Mazets, D. A. Smith, E. Demler and J. Schmiedmayer: *Relaxation and Prethermalization in an Isolated Quantum System*, Science **337** 1318 (2012), `arXiv:1112.0013 [cond-mat.quant-gas]`.

[45] Langen, T., T. Gasenzer and J. Schmiedmayer: *Prethermalization and universal dynamics in near-integrable quantum systems*, Journal of Statistical Mechanics: Theory and Experiment **6** 064009 (2016), `arXiv:1603.09385 [cond-mat.quant-gas]`.

[46] Kollar, M., F. A. Wolf and M. Eckstein: *Generalized Gibbs ensemble prediction of prethermalization plateaus and their relation to nonthermal steady states in integrable systems*, Phys. Rev. B **84** (5) 054304 (2011), `arXiv:1102.2117 [cond-mat.str-el]`.

[47] Anderson, P. W.: *Absence of Diffusion in Certain Random Lattices*, Phys. Rev. **109** (5) 1492 (1958).

[48] Burrell, C. K. and T. J. Osborne: *Bounds on the speed of information propagation in disordered quantum spin chains.*, Phys. Rev. Lett. **99** (16) 167201 (2007), `quant-ph/0703209`.

[49] Canovi, E., D. Rossini, R. Fazio, G. E. Santoro and A. Silva: *Quantum quenches, thermalization, and many-body localization*, Phys. Rev. B **83** (9) 094431 (2011), `arXiv:1006.1634 [cond-mat.stat-mech]`.

[50] Nandkishore, R. and D. A. Huse: *Many-Body Localization and Thermalization in Quantum Statistical Mechanics*, Annual Review of Condensed Matter Physics **6** 15 (2015), `arXiv:1404.0686 [cond-mat.stat-mech]`.

[51] Kibble, T. W. B.: *Topology of cosmic domains and strings*, J. Phys. A: Math. Gen. **9** (8) 1387 (1976).

[52] Zurek, W. H.: *Cosmological experiments in superfluid helium?*, Nature **317** 505 (1985).

[53] Zurek, W. H.: *Cosmological experiments in condensed matter systems.*, Physics Reports **276** 177 (1996), `cond-mat/9607135`.

[54] Dziarmaga, J.: *Dynamics of a quantum phase transition and relaxation to a steady state*, Adv. Phys. **59** 1063 (2010), `arXiv:0912.4034 [cond-mat.quant-gas]`.

[55] Heyl, M., A. Polkovnikov and S. Kehrein: *Dynamical Quantum Phase Transitions in the Transverse-Field Ising Model*, Phys. Rev. Lett. **110** (13) 135704 (2013), `arXiv:1206.2505 [cond-mat.stat-mech]`.

[56] Karrasch, C. and D. Schuricht: *Dynamical phase transitions after quenches in nonintegrable models*, Phys. Rev. B **87** (19) 195104 (2013), `arXiv:1302.3893 [cond-mat.str-el]`.

[57] Canovi, E., P. Werner and M. Eckstein: *First-Order Dynamical Phase Transitions*, Phys. Rev. Lett. **113** (26) 265702 (2014), `arXiv:1408.1795 [cond-mat.str-el]`.

[58] Heyl, M.: *Scaling and Universality at Dynamical Quantum Phase Transitions*, Phys. Rev. Lett. **115** (14) 140602 (2015), `arXiv:1505.02352 [cond-mat.stat-mech]`.

[59] Jaksch, D., C. Bruder, J. I. Cirac, C. W. Gardiner and P. Zoller: *Cold Bosonic Atoms in Optical Lattices*, Phys. Rev. Lett. **81** (15) 3108 (1998), `cond-mat/9805329`.

[60] Fisher, M. P. A., P. B. Weichman, G. Grinstein and D. S. Fisher: *Boson localization and the superfluid-insulator transition*, Phys. Rev. B **40** (1) 546 (1989).

[61] Jaksch, D. and P. Zoller: *The cold atom Hubbard toolbox*, Annals of Physics **315** 52 (2005), `cond-mat/0410614`.

[62] Bloch, I., J. Dalibard and W. Zwerger: *Many-body physics with ultracold gases*, Rev. Mod. Phys. **80** (3) 885 (2008), `arXiv:0704.3011`.

[63] Bloch, I., J. Dalibard and S. Nascimbène: *Quantum simulations with ultracold quantum gases*, Nat. Phys. **8** 267 (2012).

[64] Georgescu, I. M., S. Ashhab and F. Nori: *Quantum simulation*, Rev. Mod. Phys. **86** 153 (2014), `arXiv:1308.6253 [quant-ph]`.

[65] Feynman, R.: *Simulating physics with computers*, International Journal of Theoretical Physics **21** (6) 467 (1982).

[66] Feynman, R.: *Quantum mechanical computers*, Foundations of Physics **16** (6) 507 (1986).

[67] Esslinger, T.: *Fermi-Hubbard Physics with Atoms in an Optical Lattice*, Annu. Rev. Condens. Matter Phys. **1** 129 (2010), `arXiv:1007.0012 [cond-mat.quant-gas]`.

[68] Lewenstein, M., A. Sanpera and V. Ahufinger: *Ultracold Atoms in Optical Lattices: Simulating quantum many-body systems*, Oxford University Press, Oxford, 1st edition (2012).

[69] Langen, T., R. Geiger and J. Schmiedmayer: *Ultracold Atoms Out of Equilibrium*, Annual Review of Condensed Matter Physics **6** 201 (2015), `arXiv:1408.6377 [cond-mat.quant-gas]`.

[70] Altman, E.: *Non equilibrium quantum dynamics in ultra-cold quantum gases*, ArXiv e-prints (2015), `arXiv:1512.00870 [cond-mat.quant-gas]`.

[71] Greiner, M., O. Mandel, T. Esslinger, T. W. Hänsch and I. Bloch: *Quantum phase transition from a superfluid to a Mott insulator in a gas of ultracold atoms*, Nature **415** 39 (2002).

[72] Köhl, M., H. Moritz, T. Stöferle, K. Günter and T. Esslinger: *Fermionic Atoms in a Three Dimensional Optical Lattice: Observing Fermi Surfaces, Dynamics, and Interactions*, Phys. Rev. Lett. **94** (8) 080403 (2005), `cond-mat/0410389`.

[73] Jördens, R., N. Strohmaier, K. Günter, H. Moritz and T. Esslinger: *A Mott insulator of fermionic atoms in an optical lattice*, Nature **455** 204 (2008), `arXiv:0804.4009 [cond-mat.other]`.

[74] Schneider, U., L. Hackermüller, S. Will, T. Best, I. Bloch, T. A. Costi, R. W. Helmes, D. Rasch and A. Rosch: *Metallic and insulating phases of repulsively interacting fermions in a 3D optical lattice.*, Science **322** (5907) 1520 (2008).

[75] Trotzky, S., P. Cheinet, S. Fölling, M. Feld, U. Schnorrberger, A. M. Rey, A. Polkovnikov, E. A. Demler, M. D. Lukin and I. Bloch: *Time-Resolved Observation and Control of Superexchange Interactions with Ultracold Atoms in Optical Lattices*, Science **319** 295 (2008), `arXiv:0712.1853`.

[76] Cheneau, M., P. Barmettler, D. Poletti, M. Endres, P. Schauß, T. Fukuhara, C. Gross, I. Bloch, C. Kollath and S. Kuhr: *Light-cone-like spreading of correlations in a quantum many-body system*, Nature **481** 484 (2012), `arXiv:1111.0776 [cond-mat.quant-gas]`.

[77] Lignier, H., C. Sias, D. Ciampini, Y. Singh, A. Zenesini, O. Morsch and E. Arimondo: *Dynamical Control of Matter-Wave Tunneling in Periodic Potentials*, Phys. Rev. Lett. **99** (22) 220403 (2007).

[78] Eckardt, A., C. Weiss and M. Holthaus: *Superfluid-insulator transition in a periodically driven optical lattice.*, Phys. Rev. Lett. **95** (26) 260404 (2005), `cond-mat/0601020`.

[79] Zenesini, A., H. Lignier, D. Ciampini, O. Morsch and E. Arimondo: *Coherent control of dressed matter waves.*, Phys. Rev. Lett. **102** (10) 100403 (2009), `arXiv:0809.0768 [cond-mat.other]`.

[80] Struck, J., C. Ölschläger, R. Le Targat, P. Soltan-Panahi, A. Eckardt, M. Lewenstein, P. Windpassinger and K. Sengstock: *Quantum simulation of frustrated classical magnetism in triangular optical lattices.*, Science **333** (6045) 996 (2011).

[81] Struck, J., C. Ölschläger, M. Weinberg, P. Hauke, J. Simonet, A. Eckardt, M. Lewenstein, K. Sengstock and P. Windpassinger: *Tunable Gauge Potential for Neutral and Spinless Particles in Driven Optical Lattices*, Phys. Rev. Lett. **108** (22) 225304 (2012).

[82] Nelson, K. D., X. Li and D. S. Weiss: *Imaging single atoms in a three-dimensional array*, Nature Physics **3** 556 (2007).

[83] Bakr, W. S., J. I. Gillen, A. Peng, S. Fölling and M. Greiner: *A quantum gas microscope for detecting single atoms in a Hubbard-regime optical lattice.*, Nature **462** (7269) 74 (2009), `arXiv:0908.0174 [cond-mat.quant-gas]`.

[84] Sherson, J. F., C. Weitenberg, M. Endres, M. Cheneau, I. Bloch and S. Kuhr: *Single-atom-resolved fluorescence imaging of an atomic Mott insulator.*, Nature **467** (7311) 68 (2010), `arXiv:1006.3799 [cond-mat.quant-gas]`.

[85] Simon, J., W. S. Bakr, R. Ma, M. E. Tai, P. M. Preiss and M. Greiner: *Quantum simulation of antiferromagnetic spin chains in an optical lattice.*, Nature **472** (7343) 307 (2011).

[86] Billy, J., V. Josse, Z. Zuo, A. Bernard, B. Hambrecht, P. Lugan, D. Clément, L. Sanchez-Palencia, P. Bouyer and A. Aspect: *Direct observation of Anderson localization of matter waves in a controlled disorder.*, Nature **453** (7197) 891 (2008), `arXiv:0804.1621 [cond-mat.dis-nn]`.

[87] Roati, G., C. D'Errico, L. Fallani, M. Fattori, C. Fort, M. Zaccanti, G. Modugno, M. Modugno and M. Inguscio: *Anderson localization of a non-interacting Bose-Einstein condensate.*, Nature **453** (7197) 895 (2008), `arXiv:0804.2609` `[cond-mat.dis-nn]`.

[88] White, M., M. Pasienski, D. McKay, S. Q. Zhou, D. Ceperley and B. Demarco: *Strongly interacting bosons in a disordered optical lattice.*, Phys. Rev. Lett. **102** (5) 055301 (2009), `arXiv:0807.0446` `[physics.atom-ph]`.

[89] Sensarma, R., D. Pekker, E. Altman, E. Demler, N. Strohmaier, D. Greif, R. Jördens, L. Tarruell, H. Moritz and T. Esslinger: *Lifetime of double occupancies in the Fermi-Hubbard model*, Phys. Rev. B **82** (22) 224302 (2010), `arXiv:1001.3881` `[cond-mat.quant-gas]`.

[90] Strohmaier, N., D. Greif, R. Jördens, L. Tarruell, H. Moritz, T. Esslinger, R. Sensarma, D. Pekker, E. Altman and E. Demler: *Observation of Elastic Doublon Decay in the Fermi-Hubbard Model*, Phys. Rev. Lett. **104** (8) 080401 (2010), `arXiv:0905.2963` `[cond-mat.quant-gas]`.

[91] Sensarma, R., D. Pekker, A. M. Rey, M. D. Lukin and E. Demler: *Relaxation of Fermionic Excitations in a Strongly Attractive Fermi Gas in an Optical Lattice*, Phys. Rev. Lett. **107** (14) 145303 (2011), `arXiv:1105.1778` `[cond-mat.quant-gas]`.

[92] Greif, D., T. Uehlinger, G. Jotzu, L. Tarruell and T. Esslinger: *Short-Range Quantum Magnetism of Ultracold Fermions in an Optical Lattice*, Science **340** 1307 (2013), `arXiv:1212.2634` `[cond-mat.quant-gas]`.

[93] Hart, R. A., P. M. Duarte, T.-L. Yang, X. Liu, T. Paiva, E. Khatami, R. T. Scalettar, N. Trivedi, D. A. Huse and R. G. Hulet: *Observation of antiferromagnetic correlations in the Hubbard model with ultracold atoms.*, Nature **519** (7542) 211 (2015), `arXiv:1407.5932` `[cond-mat.quant-gas]`.

[94] Greif, D., G. Jotzu, M. Messer, R. Desbuquois and T. Esslinger: *Formation and Dynamics of Antiferromagnetic Correlations in Tunable Optical Lattices*, Phys. Rev. Lett. **115** (26) 260401 (2015), `arXiv:1509.00854` `[cond-mat.quant-gas]`.

[95] Anderson, P. W.: *The Resonating Valence Bond State in La2CuO4 and Superconductivity.*, Science **235** (4793) 1196 (1987).

[96] Hofstetter, W., J. I. Cirac, P. Zoller, E. Demler and M. D. Lukin: *High-temperature superfluidity of fermionic atoms in optical lattices.*, Phys. Rev. Lett. **89** (22) 220407 (2002), `cond-mat/0204237`.

[97] Haller, E., J. Hudson, A. Kelly, D. A. Cotta, B. Peaudecerf, G. D. Bruce and S. Kuhr: *Single-atom imaging of fermions in a quantum-gas microscope*, Nature Physics **11** 738 (2015), `arXiv:1503.02005` `[cond-mat.quant-gas]`.

[98] Cheuk, L. W., M. A. Nichols, M. Okan, T. Gersdorf, V. V. Ramasesh, W. S. Bakr, T. Lompe and M. W. Zwierlein: *Quantum-gas microscope for fermionic atoms.*, Phys. Rev. Lett. **114** (19) 193001 (2015), `arXiv:1503.02648 [cond-mat.quant-gas]`.

[99] Parsons, M. F., F. Huber, A. Mazurenko, C. S. Chiu, W. Setiawan, K. Wooley-Brown, S. Blatt and M. Greiner: *Site-resolved imaging of fermionic* ^{6}Li *in an optical lattice*, Phys. Rev. Lett. **114** (21) 213002 (2015), `arXiv:1504.04397 [cond-mat.quant-gas]`.

[100] Greif, D., M. F. Parsons, A. Mazurenko, C. S. Chiu, S. Blatt, F. Huber, G. Ji and M. Greiner: *Site-resolved imaging of a fermionic Mott insulator*, Science **351** (6276) 953 (2016), `arXiv:1511.06366 [cond-mat.quant-gas]`.

[101] Schreiber, M., S. S. Hodgman, P. Bordia, H. P. Lüschen, M. H. Fischer, R. Vosk, E. Altman, U. Schneider and I. Bloch: *Observation of many-body localization of interacting fermions in a quasirandom optical lattice*, Science **349** (6250) 842 (2015).

[102] Dutta, O., M. Gajda, P. Hauke, M. Lewenstein, D. S. Lühmann, B. A. Malomed, T. Sowiński and J. Zakrzewski: *Non-standard Hubbard models in optical lattices: a review*, Rep. Prog. Phys. **78** (6) 066001 (2015), `arXiv:1406.0181 [cond-mat.quant-gas]`.

[103] Cirac, J. I. and P. Zoller: *Quantum Computations with Cold Trapped Ions*, Phys. Rev. Lett. **74** (20) 4091 (1995).

[104] Brennen, G. K., C. M. Caves, P. S. Jessen and I. H. Deutsch: *Quantum Logic Gates in Optical Lattices*, Phys. Rev. Lett. **82** (5) 1060 (1999), `quant-ph/9806021`.

[105] Childs, A. M., D. Gosset and Z. Webb: *Universal Computation by Multiparticle Quantum Walk*, Science **339** 791 (2013), `arXiv:1205.3782 [quant-ph]`.

[106] Shor, P. W.: *Polynomial-Time Algorithms for Prime Factorization and Discrete Logarithms on a Quantum Computer*, SIAM J. Sci. Statist. Comput. **26** 1484 (1997), expanded version of contribution to the Proceedings of the 35th Annual Symposium on Foundations of Computer Science, 1994, `quant-ph/9508027`.

[107] Monz, T., D. Nigg, E. A. Martinez, M. F. Brandl, P. Schindler, R. Rines, S. X. Wang, I. L. Chuang and R. Blatt: *Realization of a scalable Shor algorithm.*, Science **351** (6277) 1068 (2016), `arXiv:1507.08852 [quant-ph]`.

[108] Hartmann, M. J., F. G. S. L. Brandao and M. B. Plenio: *Quantum Many-Body Phenomena in Coupled Cavity Arrays*, Laser & Photonics Reviews **2** (6) 527 (2008), `arXiv:0808.2557 [quant-ph]`.

[109] Tomadin, A. and R. Fazio: *Many-body phenomena in QED-cavity arrays*, J. Opt. Soc. Am. B **27** (6) A130 (2010), `arXiv:1005.0137 [cond-mat.str-el]`.

[110] Byrnes, T., N. Y. Kim, K. Kusudo and Y. Yamamoto: *Quantum simulation of Fermi-Hubbard models in semiconductor quantum-dot arrays*, Phys. Rev. B **78** (7) 075320 (2008), `arXiv:0711.2841 [quant-ph]`.

[111] Metzner, W. and D. Vollhardt: *Correlated Lattice Fermions in $d = \infty$ Dimensions*, Phys. Rev. Lett. **62** (3) 324 (1989).

[112] Georges, A. and G. Kotliar: *Hubbard model in infinite dimensions*, Phys. Rev. B **45** (12) 6479 (1992).

[113] Georges, A., G. Kotliar, W. Krauth and M. J. Rozenberg: *Dynamical mean-field theory of strongly correlated fermion systems and the limit of infinite dimensions*, Rev. Mod. Phys. **68** (1) 13 (1996).

[114] Kotliar, G. and D. Vollhardt: *Strongly Correlated Materials: Insights from Dynamical Mean-Field Theory*, Physics Today **57** (3) 53 (2004).

[115] Rozenberg, M. J., X. Y. Zhang and G. Kotliar: *Mott-Hubbard transition in infinite dimensions*, Phys. Rev. Lett. **69** (8) 1236 (1992).

[116] Rozenberg, M. J., G. Kotliar and X. Y. Zhang: *Mott-Hubbard transition in infinite dimensions. II*, Phys. Rev. B **49** (15) 10181 (1994).

[117] Rozenberg, M. J., R. Chitra and G. Kotliar: *Finite Temperature Mott Transition in the Hubbard Model in Infinite Dimensions*, Phys. Rev. Lett. **83** 3498 (1999), `cond-mat/9905145`.

[118] Baym, G. and L. P. Kadanoff: *Conservation Laws and Correlation Functions*, Phys. Rev. **124** (2) 287 (1961).

[119] Baym, G.: *Self-Consistent Approximations in Many-Body Systems*, Phys. Rev. **127** (4) 1391 (1962).

[120] Kotliar, G., S. Y. Savrasov, K. Haule, V. S. Oudovenko, O. Parcollet and C. A. Marianetti: *Electronic structure calculations with dynamical mean-field theory*, Rev. Mod. Phys. **78** (3) 865 (2006), `cond-mat/0511085`.

[121] Byczuk, K. and D. Vollhardt: *Correlated bosons on a lattice: Dynamical mean-field theory for Bose-Einstein condensed and normal phases*, Phys. Rev. B **77** (23) 235106 (2008), `arXiv:0706.0839 [cond-mat.other]`.

[122] Hu, W.-J. and N.-H. Tong: *Dynamical mean-field theory for the Bose-Hubbard model*, Phys. Rev. B **80** (24) 245110 (2009), `arXiv:0907.2928 [cond-mat.quant-gas]`.

[123] Anders, P., E. Gull, L. Pollet, M. Troyer and P. Werner: *Dynamical mean field solution of the Bose-Hubbard model.*, Phys. Rev. Lett. **105** (9) 096402 (2010), `arXiv:1004.0510 [cond-mat.str-el]`.

[124] Anders, P., E. Gull, L. Pollet, M. Troyer and P. Werner: *Dynamical mean-field theory for bosons*, New Journal of Physics **13** (7) 075013 (2011), `arXiv:1103.0017 [cond-mat.str-el]`.

[125] Kotliar, G., S. Y. Savrasov, G. Pálsson and G. Biroli: *Cellular Dynamical Mean Field Approach to Strongly Correlated Systems*, Phys. Rev. Lett. **87** (18) 186401 (2001).

[126] Lichtenstein, A. I. and M. I. Katsnelson: *Antiferromagnetism and d-wave superconductivity in cuprates: A cluster dynamical mean-field theory*, Phys. Rev. B **62** (14) R9283 (2000), `cond-mat/9911320`.

[127] Hettler, M. H., A. N. Tahvildar-Zadeh, M. Jarrell, T. Pruschke and H. R. Krishnamurthy: *Nonlocal dynamical correlations of strongly interacting electron systems*, Phys. Rev. B **58** R7475 (1998), `cond-mat/9803295`.

[128] Toschi, A., A. A. Katanin and K. Held: *Dynamical vertex approximation: A step beyond dynamical mean-field theory*, Phys. Rev. B **75** (4) 045118 (2007), `cond-mat/0603100`.

[129] Rubtsov, A. N., M. I. Katsnelson and A. I. Lichtenstein: *Dual fermion approach to nonlocal correlations in the Hubbard model*, Phys. Rev. B **77** 033101 (2006), `cond-mat/0612196`.

[130] Hafermann, H., C. Jung, S. Brener, M. I. Katsnelson, A. N. Rubtsov and A. I. Lichtenstein: *Superperturbation solver for quantum impurity models*, Europhys. Lett. **85** 27007 (2009), `arXiv:0809.1051 [cond-mat.str-el]`.

[131] Freericks, J. K., V. M. Turkowski and V. Zlatić: *Nonequilibrium Dynamical Mean-Field Theory*, Phys. Rev. Lett. **97** (26) 266408 (2006), `cond-mat/0607053`.

[132] Schmidt, P. and H. Monien: *Nonequilibrium dynamical mean-field theory of a strongly correlated system*, ArXiv e-prints (2002), `cond-mat/0202046`.

[133] Aoki, H., N. Tsuji, M. Eckstein, M. Kollar, T. Oka and P. Werner: *Nonequilibrium dynamical mean-field theory and its applications*, Rev. Mod. Phys. **86** 779 (2014), `arXiv:1310.5329 [cond-mat.str-el]`.

[134] Strand, H. U. R., M. Eckstein and P. Werner: *Nonequilibrium Dynamical Mean-Field Theory for Bosonic Lattice Models*, Phys. Rev. X **5** (1) 011038 (2015), `arXiv:1405.6941 [cond-mat.quant-gas]`.

[135] Tsuji, N., P. Barmettler, H. Aoki and P. Werner: *Nonequilibrium dynamical cluster theory*, Phys. Rev. B **90** (7) 075117 (2014), `arXiv:1307.5946 [cond-mat.str-el]`.

[136] Jung, C., A. Lieder, S. Brener, H. Hafermann, B. Baxevanis, A. Chudnovskiy, A. N. Rubtsov, M. I. Katsnelson and A. I. Lichtenstein: *Dual-fermion approach to non-equilibrium strongly correlated problems*, Ann. Phys. **524** (1) 49 (2012), `arXiv:1011.3264 [cond-mat.str-el]`.

[137] Tsuji, N., T. Oka and H. Aoki: *Nonequilibrium Steady State of Photoexcited Correlated Electrons in the Presence of Dissipation*, Phys. Rev. Lett. **103** (4) 047403 (2009), `arXiv:0903.2332 [cond-mat.str-el]`.

[138] Eckstein, M. and P. Werner: *Nonequilibrium dynamical mean-field calculations based on the noncrossing approximation and its generalizations*, Phys. Rev. B **82** (11) 115115 (2010), `arXiv:1005.1872 [cond-mat.str-el]`.

[139] Werner, P. and M. Eckstein: *Relaxation dynamics of the Kondo lattice model*, Phys. Rev. B **86** (4) 045119 (2012), `arXiv:1204.5418 [cond-mat.str-el]`.

[140] Amaricci, A., C. Weber, M. Capone and G. Kotliar: *Approach to a stationary state in a driven Hubbard model coupled to a thermostat*, Phys. Rev. B **86** (8) 085110 (2012), `arXiv:1106.3483 [cond-mat.str-el]`.

[141] Eckstein, M. and P. Werner: *Ultra-fast photo-carrier relaxation in Mott insulators with short-range spin correlations*, Nature Scientific Reports **6** 21235 (2016), `arXiv:1410.3956 [cond-mat.str-el]`.

[142] Strand, H. U. R., M. Eckstein and P. Werner: *Beyond the Hubbard bands in strongly correlated lattice bosons*, Phys. Rev. A **92** (6) 063602 (2015), `arXiv:1506.05609 [cond-mat.quant-gas]`.

[143] Muõz, E., C. J. Bolech and S. Kirchner: *Universal Out-of-Equilibrium Transport in Kondo-Correlated Quantum Dots: Renormalized Dual Fermions on the Keldysh Contour*, Phys. Rev. Lett. **110** (1) 016601 (2013), `arXiv:1111.4076 [cond-mat.mes-hall]`.

[144] Eckstein, M., M. Kollar and P. Werner: *Thermalization after an Interaction Quench in the Hubbard Model*, Phys. Rev. Lett. **103** (5) 056403 (2009), `arXiv:0904.0976 [cond-mat.str-el]`.

[145] Schiró, M. and M. Fabrizio: *Time-Dependent Mean Field Theory for Quench Dynamics in Correlated Electron Systems*, Phys. Rev. Lett. **105** (7) 076401 (2010), `arXiv:1005.0992 [cond-mat.str-el]`.

[146] Hamerla, S. A. and G. S. Uhrig: *Dynamical transition in interaction quenches of the one-dimensional Hubbard model*, Phys. Rev. B **87** (6) 064304 (2013), `arXiv:1302.4109 [cond-mat.str-el]`.

[147] Hamerla, S. A. and G. S. Uhrig: *Interaction quenches in the two-dimensional fermionic Hubbard model*, Phys. Rev. B **89** (10) 104301 (2014), `arXiv:1307.3438 [cond-mat.str-el]`.

[148] Gull, E., A. J. Millis, A. I. Lichtenstein, A. N. Rubtsov, M. Troyer and P. Werner: *Continuous-time Monte Carlo methods for quantum impurity models*, Rev. Mod. Phys. **83** 349 (2011), `arXiv:1012.4474 [cond-mat.str-el]`.

[149] Werner, P., T. Oka and A. J. Millis: *Diagrammatic Monte Carlo simulation of nonequilibrium systems*, Phys. Rev. B **79** (3) 035320 (2009), `arXiv:0810.2345 [cond-mat.mes-hall]`.

[150] Eckstein, M. and P. Werner: *Damping of Bloch Oscillations in the Hubbard Model*, Phys. Rev. Lett. **107** (18) 186406 (2011), `arXiv:1107.3830 [cond-mat.str-el]`.

[151] Tsuji, N., M. Eckstein and P. Werner: *Nonthermal Antiferromagnetic Order and Nonequilibrium Criticality in the Hubbard Model*, Phys. Rev. Lett. **110** (13) 136404 (2013), `arXiv:1210.0133 [cond-mat.str-el]`.

[152] Caffarel, M. and W. Krauth: *Exact diagonalization approach to correlated fermions in infinite dimensions: Mott transition and superconductivity*, Phys. Rev. Lett. **72** (10) 1545 (1994).

[153] Liebsch, A. and H. Ishida: *Temperature and bath size in exact diagonalization dynamical mean field theory*, Journal of Physics: Condensed Matter **24** (5) 053201 (2012), `arXiv:1109.0158 [cond-mat.str-el]`.

[154] Gramsch, C., K. Balzer, M. Eckstein and M. Kollar: *Hamiltonian-based impurity solver for nonequilibrium dynamical mean-field theory*, Phys. Rev. B **88** (23) 235106 (2013), `arXiv:1306.6315 [cond-mat.str-el]`.

[155] Balzer, K., Z. Li, O. Vendrell and M. Eckstein: *Multiconfiguration time-dependent Hartree impurity solver for nonequilibrium dynamical mean-field theory*, Phys. Rev. B **91** (4) 045136 (2015), `arXiv:1407.6578 [cond-mat.str-el]`.

[156] Wolf, F. A., I. P. McCulloch and U. Schollwöck: *Solving nonequilibrium dynamical mean-field theory using matrix product states*, Phys. Rev. B **90** (23) 235131 (2014), `arXiv:1410.3342 [cond-mat.str-el]`.

[157] Maier, T., M. Jarrell, T. Pruschke and M. H. Hettler: *Quantum cluster theories*, Rev. Mod. Phys. **77** (3) 1027 (2005).

[158] Gros, C. and R. Valentí: *Cluster expansion for the self-energy: A simple many-body method for interpreting the photoemission spectra of correlated Fermi systems*, Phys. Rev. B **48** (1) 418 (1993).

[159] Sénéchal, D., D. Perez and M. Pioro-Ladrière: *Spectral Weight of the Hubbard Model through Cluster Perturbation Theory*, Phys. Rev. Lett. **84** 522 (2000), `cond-mat/9908045`.

[160] Balzer, M. and M. Potthoff: *Nonequilibrium cluster perturbation theory*, Phys. Rev. B **83** (19) 195132 (2011), `arXiv:1102.3344 [cond-mat.str-el]`.

[161] Gramsch, C. and M. Potthoff: *Lehmann representation of the nonequilibrium self-energy*, Phys. Rev. B **92** (23) 235135 (2015), `arXiv:1509.05313 [cond-mat.str-el]`.

[162] Potthoff, M.: *Self-energy-functional approach to systems of correlated electrons*, Eur. Phys. J. B **32** 429 (2003), `cond-mat/0301137`.

[163] Potthoff, M., M. Aichhorn and C. Dahnken: *Variational Cluster Approach to Correlated Electron Systems in Low Dimensions*, Phys. Rev. Lett. **91** (20) 206402 (2003), `cond-mat/0303136`.

[164] Dahnken, C., M. Aichhorn, W. Hanke, E. Arrigoni and M. Potthoff: *Variational cluster approach to spontaneous symmetry breaking: The itinerant antiferromagnet in two dimensions*, Phys. Rev. B **70** (24) 245110 (2004), `cond-mat/0309407`.

[165] Potthoff, M.: *Making use of self-energy functionals: The variational cluster approximation*, in D. V. Eva Pavarini, Erik Koch and A. Lichtenstein (editors), *DMFT at 25: Infinite Dimensions*, *Modeling and Simulation*, volume 4, Forschungszentrum Jülich (2014), `arXiv:1407.4065 [cond-mat.str-el]`.

[166] Potthoff, M.: *Self-energy-functional approach: Analytical results and the Mott-Hubbard transition*, Eur. Phys. J. B **36** 335 (2003), `cond-mat/0306278`.

[167] Balzer, M., W. Hanke and M. Potthoff: *Mott transition in one dimension: Benchmarking dynamical cluster approaches*, Phys. Rev. B **77** (4) 045133 (2008), `arXiv:0709.4620 [cond-mat.str-el]`.

[168] Balzer, M., B. Kyung, D. Sénéchal, A. M. S. Tremblay and M. Potthoff: *First-order Mott transition at zero temperature in two dimensions: Variational plaquette study*, Europhys. Lett. **85** 17002 (2009), `arXiv:0808.2364 [cond-mat.str-el]`.

[169] Knap, M., W. von der Linden and E. Arrigoni: *Nonequilibrium steady state for strongly correlated many-body systems: Variational cluster approach*, Phys. Rev. B **84** (11) 115145 (2011), `arXiv:1104.3838 [cond-mat.str-el]`.

[170] Nuss, M., C. Heil, M. Ganahl, M. Knap, H. G. Evertz, E. Arrigoni and W. von der Linden: *Steady-state spectra, current, and stability diagram of a quantum dot: A nonequilibrium variational cluster approach*, Phys. Rev. B **86** (24) 245119 (2012), `arXiv:1207.5641 [cond-mat.str-el]`.

[171] Požgajčić, K.: *Quantitative aspects of the dynamical impurity approach*, ArXiv e-prints (2004), `cond-mat/0407172`.

[172] Koga, A., K. Inaba and N. Kawakami: *Mott Transitions in Two-Orbital Hubbard Systems*, Progress of Theoretical Physics Supplement **160** 253 (2005), `cond-mat/0510449`.

[173] Inaba, K., A. Koga, S. I. Suga and N. Kawakami: *Finite-temperature Mott transitions in the multiorbital Hubbard model*, Phys. Rev. B **72** (8) 085112 (2005), `cond-mat/0506150`.

[174] Eckstein, M., M. Kollar, M. Potthoff and D. Vollhardt: *Phase separation in the particle-hole asymmetric Hubbard model*, Phys. Rev. B **75** (12) 125103 (2007), `cond-mat/0610803`.

[175] Tong, N.-H.: *Extended variational cluster approximation for correlated systems*, Phys. Rev. B **72** (11) 115104 (2005), `cond-mat/0504778`.

[176] Potthoff, M. and M. Balzer: *Self-energy-functional theory for systems of interacting electrons with disorder*, Phys. Rev. B **75** (12) 125112 (2007), `cond-mat/0610217`.

[177] Koller, W. and N. Dupuis: *Variational cluster perturbation theory for Bose Hubbard models*, J. Phys.: Condens. Matter **18** 9525 (2006), `cond-mat/0511294`.

[178] Arrigoni, E., M. Knap and W. von der Linden: *Extended self-energy functional approach for strongly correlated lattice bosons in the superfluid phase*, Phys. Rev. B **84** (1) 014535 (2011), `arXiv:1103.3664 [cond-mat.quant-gas]`.

[179] Hügel, D., P. Werner, L. Pollet and H. U. R. Strand: *Bosonic self-energy functional theory*, ArXiv e-prints (2016), `arXiv:1603.01401 [cond-mat.quant-gas]`.

[180] Hofmann, F., M. Eckstein, E. Arrigoni and M. Potthoff: *Nonequilibrium self-energy functional theory*, Phys. Rev. B **88** (16) 165124 (2013), `arXiv:1306.6340 [cond-mat.str-el]`.

[181] Hofmann, F., M. Eckstein and M. Potthoff: *Nonequilibrium variational-cluster approach to real-time dynamics in the Fermi-Hubbard model*, Journal of Physics: Conference Series **696** (1) 012002 (2016), `arXiv:1510.05866 [cond-mat.str-el]`.

[182] Hofmann, F., M. Eckstein and M. Potthoff: *Nonequilibrium self-energy functional approach to the dynamical Mott transition*, Phys. Rev. B **93** (23) 235104 (2016), `arXiv:1603.07177 [cond-mat.str-el]`.

[183] Hofmann, F. and M. Potthoff: *Time-dependent Mott transition in the periodic Anderson model with nonlocal hybridization*, ArXiv e-prints (2016), `arXiv:1606.01089 [cond-mat.str-el]`.

[184] Thygesen, K. S. and A. Rubio: *Nonequilibrium GW approach to quantum transport in nano-scale contacts*, J. Chem. Phys. **126** (9) 091101 (2007), `cond-mat/0609223`.

[185] Balzer, K. and M. Eckstein: *Auxiliary Hamiltonian representation of the nonequilibrium Dyson equation*, Phys. Rev. B **89** (3) 035148 (2014), `arXiv:1312.0214 [cond-mat.str-el]`.

[186] Lipavský, P., V. Špička and B. Velický: *Generalized Kadanoff-Baym ansatz for deriving quantum transport equations*, Phys. Rev. B **34** (10) 6933 (1986).

[187] Kubo, R.: *Statistical-Mechanical Theory of Irreversible Processes. I. General Theory and Simple Applications to Magnetic and Conduction Problems*, J. Phys. Soc. Jap. **12** (6) 570 (1957).

[188] Matsubara, T.: *A New Approach to Quantum-Statistical Mechanics*, Prog. Theor. Phys. **14** (4) 351 (1955).

[189] Schwinger, J.: *Brownian Motion of a Quantum Oscillator*, J. Math. Phys. **2** (3) 407 (1961).

[190] Keldysh, L.: *Diagram technique for nonequilibrium processes*, Sov. Phys. JETP **20** 1018 (1965).

[191] Danielewicz, P.: *Quantum theory of nonequilibrium processes, I*, Ann. Phys. **152** (2) 239 (1984).

[192] Bonitz, M. (editor): *Conference: Progress in Nonequilibrium Green's Functions*, World Scientific, Rostock, Germany (1999).

[193] Bonitz, M. and D. Semkat (editors): *Conference: Progress in Nonequilibrium Green's Functions II*, World Scientific, Dresden (2002).

[194] Bonitz, M. and A. Filinov (editors): *Conference: Progress in Nonequilibrium Green's Functions III*, IOP Publishing, Kiel (2005).

[195] Bonitz, M. and K. Balzer (editors): *Conference: Progress in Nonequilibrium Green's Functions IV*, IOP Publishing, Glasgow (2009).

[196] Leeuwen, R. v., R. Tuovinen and M. Bonitz (editors): *Conference: Progress in Nonequilibrium Green's Functions V*, IOP Publishing, Jyväskylä (2012).

[197] Verdozzi, C., A. Wacker, C.-O. Almbladh and M. Bonitz (editors): *Conference: Progress in Nonequilibrium Green's Functions VI*, IOP Publishing, Lund (2016).

[198] Wagner, M.: *Expansions of nonequilibrium Green's functions*, Phys. Rev. B **44** (12) 6104 (1991).

[199] van Leeuwen, R., N. E. Dahlen, G. Stefanucci, C. O. Almbladh and U. von Barth: *Introduction to the Keldysh Formalism*, in M. A. L. Marques, C. A. Ullrich, F. Nogueira, A. Rubio, K. Burke and E. K. U. Gross (editors), *Time-Dependent Density Functional Theory*, volume 706, chapter Lecture Notes in Physics, p. 33, Springer, Berlin Heidelberg (2006).

[200] Rammer, J.: *Quantum field theory of nonequilibrium states*, Cambridge University Press (2007).

[201] Kamenev, A.: *Field theory of non-equilibrium systems*, Cambridge University Press, Cambridge, New York (2011).

[202] Kita, T.: *Introduction to Nonequilibrium Statistical Mechanics with Quantum Field*, Progress of Theoretical Physics **123** 581 (2010), `arXiv:1005.0393 [cond-mat.stat-mech]`.

[203] Sakurai, J. J.: *Modern Quantum Mechanics*, Addison Wesley (1993).

[204] Martin, P. C. and J. Schwinger: *Theory of Many-Particle Systems. I*, Phys. Rev. **115** (6) 1342 (1959).

[205] Leeuwen, R. v. and G. Stefanucci: *Equilibrium and nonequilibrium many-body perturbation theory: a unified framework based on the Martin-Schwinger hierarchy*, Journal of Physics: Conference Series **427** (1) 012001 (2013).

[206] Abrikosov, A. A., L. P. Gorkov and I. E. Dzyaloshinski: *Methods of Quantum Field Theory in Statistical Mechanics*, Dover Publications (1975).

[207] Luttinger, J. M. and J. C. Ward: *Ground-State Energy of a Many-Fermion System. II*, Phys. Rev. **118** (5) 1417 (1960).

[208] Potthoff, M.: *Non-perturbative construction of the Luttinger-Ward functional*, Condens. Mat. Phys. **9** 557 (2006), `cond-mat/0406671`.

[209] Balzer, M. and M. Potthoff: *Variational cluster approach to ferromagnetism in infinite dimensions and in one-dimensional chains*, Phys. Rev. B **82** (17) 174441 (2010), `arXiv:1007.2517 [cond-mat.str-el]`.

[210] Aichhorn, M., E. Arrigoni, M. Potthoff and W. Hanke: *Antiferromagnetic to superconducting phase transition in the hole- and electron-doped Hubbard model at zero temperature*, Phys. Rev. B **74** (2) 024508 (2006), `cond-mat/0511460`.

[211] Balzer, M., N. Gdaniec and M. Potthoff: *Krylov-space approach to the equilibrium and nonequilibrium single-particle Green's function*, J. Phys.: Condens. Matter **24** (3) 035603 (2012), `arXiv:1109.1205 [cond-mat.str-el]`.

[212] Jurgenowski, P. and M. Potthoff: *Dynamical symmetry between spin and charge excitations studied by a plaquette mean-field approach in two dimensions*, Phys. Rev. B **87** (20) 205118 (2013), `arXiv:1302.5317 [cond-mat.str-el]`.

[213] Eckstein, M.: *Nonequilibrium dynamical mean-field theory*, Ph.D. thesis, Universität Augsburg (2009).

[214] Eckstein, M., M. Kollar and P. Werner: *Interaction quench in the Hubbard model: Relaxation of the spectral function and the optical conductivity*, Phys. Rev. B **81** (11) 115131 (2010), `arXiv:0910.5674 [cond-mat.str-el]`.

[215] Brunner, H. and P. J. v. d. Houwen: *The numerical solution of Volterra equations*, North-Holland, Amsterdam (1986).

[216] Linz, P.: *Analytical and numerical methods for Volterra equations, SIAM studies in applied mathematics*, volume 7, Society for Industrial and Applied Mathematics (1987).

[217] Press, W. H., S. A. Teukolsky, W. T. Vetterling and B. P. Flannery: *Numerical Recipes. The Art of Scientific Computing*, Cambridge University Press, 3rd edition (2007).

[218] Alvermann, A. and H. Fehske: *High-order commutator-free exponential time-propagation of driven quantum systems*, J. Comput. Phys. **230** 5930 (2011), `arXiv:1102.5071 [math.NA]`.

[219] Runge, C.: *Über empirische Funktionen und die Interpolation zwischen äquidistanten Ordinaten*, Zeitschrift für Mathematik und Physik **46** 224 (1901).

[220] Epperson, J. F.: *On the Runge Example*, Am. Math. Monthly **94** (4) 329 (1987).

[221] Kelley, C. T.: *Solving nonlinear equations with Newton's method*, Fundamentals of algorithms, Society for Industrial and Applied Mathematics (1987).

[222] Broyden, C. G.: *A class of methods for solving nonlinear simultaneous equations*, Math. Comp. **19** 577 (1965).

[223] Sylvester, J.: *Sur l'equations en matrices px = xq*, C. R. Acad. Sc. Paris **99** (2) 67–71, 115–116 (1884).

[224] Rosenblum, M.: *On the operator equation $BX - XA = Q$*, Duke Math. J. **23** (2) 263 (1956).

[225] Bhatia, R. and P. Rosenthal: *How and Why to Solve the Operator Equation $AX - XB = Y$*, Bull. London Math. Soc. **29** (1) 1 (1997).

[226] Atala, M., M. Aidelsburger, J. T. Barreiro, D. Abanin, T. Kitagawa, E. Demler and I. Bloch: *Direct measurement of the Zak phase in topological Bloch bands*, Nat. Phys. **9** 795 (2013), `arXiv:1212.0572 [cond-mat.quant-gas]`.

[227] Su, W. P., J. R. Schrieffer and A. J. Heeger: *Solitons in Polyacetylene*, Phys. Rev. Lett. **42** (25) 1698 (1979).

[228] Rice, M. J. and E. J. Mele: *Elementary Excitations of a Linearly Conjugated Diatomic Polymer*, Phys. Rev. Lett. **49** (19) 1455 (1982).

[229] Sandri, M., M. Schiró and M. Fabrizio: *Linear ramps of interaction in the fermionic Hubbard model*, Phys. Rev. B **86** (7) 075122 (2012), `arXiv:1112.5063 [cond-mat.str-el]`.

[230] Werner, P. and M. Eckstein: *Field-induced polaron formation in the Holstein-Hubbard model*, Europhys. Lett. **109** 37002 (2015), `arXiv:1403.7376 [cond-mat.str-el]`.

[231] Huscroft, C., A. K. McMahan and R. T. Scalettar: *Magnetic and Thermodynamic Properties of the Three-Dimensional Periodic Anderson Hamiltonian*, Phys. Rev. Lett. **82** (11) 2342 (1999).

[232] Held, K., C. Huscroft, R. T. Scalettar and A. K. McMahan: *Similarities between the Hubbard and Periodic Anderson Models at Finite Temperatures*, Phys. Rev. Lett. **85** 373 (2000), `cond-mat/9905011`.

[233] Held, K. and R. Bulla: *Mott transition of the f-electron system in the periodic Anderson model with nearest neighbor hybridization*, EPJ B **17** 7 (2000), `cond-mat/0006418`.

[234] Dongen, P. v., K. Majumdar, C. Huscroft and F.-C. Zhang: *Quantum critical point in a periodic Anderson model*, Phys. Rev. B **64** (19) 195123 (2001), `cond-mat/0011119`.

[235] Bulla, R. and M. Potthoff: *"Linearized" dynamical mean-field theory for the Mott-Hubbard transition*, European Physical Journal B **13** 257 (2000), `cond-mat/9905075`.

[236] Lange, E.: *Renormalized Versus Unrenormalized Perturbation-Theoretical Approaches to the Mott Transition*, Modern Physics Letters B **12** 915 (1998), `cond-mat/9810208`.

[237] Strand, H. U. R., A. Sabashvili, M. Granath, B. Hellsing and S. Östlund: *Dynamical mean field theory phase-space extension and critical properties of the finite temperature Mott transition*, Phys. Rev. B **83** (20) 205136 (2011), `arXiv:1012.3829 [cond-mat.str-el]`.

[238] Bulla, R.: *Zero Temperature Metal-Insulator Transition in the Infinite-Dimensional Hubbard Model*, Phys. Rev. Lett. **83** (1) 136 (1999).

[239] Schiró, M. and M. Fabrizio: *Quantum quenches in the Hubbard model: Time-dependent mean-field theory and the role of quantum fluctuations*, Phys. Rev. B **83** (16) 165105 (2011), `arXiv:1102.1658 [cond-mat.str-el]`.

[240] Potthoff, M.: *Two-site dynamical mean-field theory*, Phys. Rev. B **64** (16) 165114 (2001), `cond-mat/0107502`.

[241] Goth, F. and F. F. Assaad: *Time and spatially resolved quench of the fermionic Hubbard model showing restricted equilibration*, Phys. Rev. B **85** (8) 085129 (2012), `arXiv:1108.2703 [cond-mat.str-el]`.

[242] Sorg, S., L. Vidmar, L. Pollet and F. Heidrich-Meisner: *Relaxation and thermalization in the one-dimensional Bose-Hubbard model: A case study for the interaction quantum quench from the atomic limit*, Phys. Rev. A **90** (3) 033606 (2014), `arXiv:1405.5404 [cond-mat.stat-mech]`.

[243] de'Medici, L., A. Georges and S. Biermann: *Orbital-selective Mott transition in multiband systems: Slave-spin representation and dynamical mean-field theory*, Phys. Rev. B **72** (20) 205124 (2005), `cond-mat/0503764`.

[244] Biermann, S., L. de'Medici and A. Georges: *Non-Fermi-Liquid Behavior and Double-Exchange Physics in Orbital-Selective Mott Systems*, Phys. Rev. Lett. **95** (20) 206401 (2005), `cond-mat/0505737`.

[245] Behrmann, M., M. Fabrizio and F. Lechermann: *Extended dynamic Mott transition in the two-band Hubbard model out of equilibrium*, Phys. Rev. B **88** (3) 035116 (2013), `arXiv:1304.6013 [cond-mat.str-el]`.

[246] Yao, H., W. F. Tsai and S. A. Kivelson: *Myriad phases of the checkerboard Hubbard model*, Phys. Rev. B **76** (16) 161104 (2007), `arXiv:0706.0761 [cond-mat.str-el]`.

[247] Yao, H. and S. A. Kivelson: *Fragile Mott Insulators*, Phys. Rev. Lett. **105** (16) 166402 (2010), `arXiv:1008.1065 [cond-mat.str-el]`.

[248] Nakajima, S., T. Tomita, S. Taie, T. Ichinose, H. Ozawa, L. Wang, M. Troyer and Y. Takahashi: *Topological Thouless Pumping of Ultracold Fermions*, Nature Physics **12** 296 (2016), `arXiv:1507.02223 [cond-mat.quant-gas]`.

[249] Lohse, M., C. Schweizer, O. Zilberberg, M. Aidelsburger and I. Bloch: *A Thouless Quantum Pump with Ultracold Bosonic Atoms in an Optical Superlattice*, Nature Physics **12** 350 (2016), `arXiv:1507.02225 [cond-mat.quant-gas]`.

[250] Bello, M., C. E. Creffield and G. Platero: *Long-range doublon transfer in a dimer chain induced by topology and ac fields*, Scientific Reports **6** 22562 (2016), `arXiv:1510.01379 [cond-mat.quant-gas]`.

[251] Hohenadler, M. and F. F. Assaad: *Correlation effects in two-dimensional topological insulators*, Journal of Physics Condensed Matter **25** (14) 143201 (2013), `arXiv:1211.1774 [cond-mat.str-el]`.

[252] Wu, J., J. P. L. Faye, D. Sénéchal and J. Maciejko: *Quantum cluster approach to the spinful Haldane-Hubbard model*, Phys. Rev. B **93** (7) 075131 (2016), `arXiv:1512.04498 [cond-mat.str-el]`.

[253] Gu, Z. L., K. Li and J. X. Li: *Topological phase transitions and topological Mott insulator in Haldane-Hubbard model*, ArXiv e-prints (2015), `arXiv:1512.05118 [cond-mat.str-el]`.

[254] van Leeuwen, R., N. E. Dahlen and A. Stan: *Total energies from variational functionals of the Green function and the renormalized four-point vertex*, Phys. Rev. B **74** (19) 195105 (2006), `cond-mat/0609694`.

List of publications and preprints

Major parts of this thesis have been published as refereed journal articles, conference contributions or preprints, which have significant overlap with some of the chapters of the present work as indicated below.

Publications related to this thesis

5. F. Hofmann and M. Potthoff: *Time-dependent Mott transition in the periodic Anderson model with nonlocal hybridization*, accepted for publication in EPJB. Copyright EDP Sciences, Società Italiana di Fisica, Springer-Verlag 2016. With kind permission of The European Physical Journal (EPJ)
   preprint: ArXiv e-prints (2016), `arXiv:1606.01089 [cond-mat.str-el]`.

   see Sections 6.1 and 6.4

4. F. Hofmann, M. Eckstein, and M. Potthoff: *Nonequilibrium self-energy functional approach to the dynamical Mott transition*, Phys. Rev. B **93** (23) 235104 (2016). Copyright (2016) by the American Physical Society. Reproduced with permission.

   see Chapter 6, especially Sections 6.1 to 6.3 and 6.5

3. F. Hofmann, M. Eckstein and M. Potthoff: *Nonequilibrium variational-cluster approach to real-time dynamics in the Fermi-Hubbard model*, Journal of Physics: Conference Series **696** (1) 012002 (2016).
   Used under CC BY 3.0

   see Chapter 4 and 5

2. F. Hofmann, M. Eckstein, E. Arrigoni, and M. Potthoff: *Nonequilibrium self-energy functional theory*, Phys. Rev. B **88** (16) 165124 (2013). Copyright (2013) by the American Physical Society. Reproduced with permission.

   see parts of Chapter 2 and Chapter 3

Unrelated publication

1. F. Hofmann and M. Potthoff: *Doublon dynamics in the extended Fermi-Hubbard model*, Phys. Rev. B **85** (20) 205127 (2012).

Technical aids

In the context of the present work extensive computer code has been developed and implemented by the author of this work within the programming language `C++`, making mainly use of the `Eigen`- and `boost`-libraries.

Solutions of the CPT equation (3.30) have been calculated with the help of a library contributed by Martin Eckstein. Karsten Balzer provided a routine to efficiently set up a many-body basis.

Post-processing and plotting of the obtained data has been done with `python` and the plotting library `matplotlib`.

All numerical calculations have been performed on the PHYSnet computing cluster at the University of Hamburg.

Eidesstattliche Versicherung

Declaration on oath

Hiermit erkläre ich an Eides statt, dass ich die vorliegende Dissertationsschrift selbst verfasst und keine anderen als die angegebenen Quellen und Hilfsmittel benutzt habe.

I hereby declare, on oath, that I have written the present dissertation by my own and have not used other than the acknowledged resources and aids.

Hamburg, den 14. April 2016   Felix Hofmann